

UiO : **University of Oslo**

Sigbjørn Grini

Band gap grading and impurities in $\text{Cu}_2\text{ZnSnS}_4$ solar cells

Thesis submitted for the degree of Philosophiae Doctor

Department of Physics

Faculty of Mathematics and Natural Sciences



2019

© Sigbjørn Grini, 2019

*Series of dissertations submitted to the
Faculty of Mathematics and Natural Sciences, University of Oslo
No. 1234*

ISSN 1234-5678

All rights reserved. No part of this publication may be
reproduced or transmitted, in any form or by any means, without permission.

Cover: Hanne Baadsgaard Utigard.
Print production: Reprosentralen, University of Oslo.

However great your dedication, you never win anything on your own.

- Rafael Nadal

Acknowledgements

This thesis would not have been possible without the support from many great people whom I have had the honor to meet, chat and collaborate with during my time as a PhD student. I want to express my gratitude to all of you. Thank you for taking parts of your time to spend time with me.

The project leading to this thesis, "Longer lifetime and higher efficiency of CZTS thin-film solar cells", was initiated by Professor Clas Persson and started up four years ago when I began this journey. The project was a collaboration between two groups at UiO (LENS and theory group at Structure Physics) and the thin film solar cell group at the Ångström Solar Center (ASC) at Uppsala University. The project consisted of two senior researchers in addition to Clas, Associate Professor Lasse Vines at LENS and Professor Charlotte Platzer-Björkman at ASC as well as post docs Dr. Nils Ross and Dr. Sergiy Zamulko in addition to me. The collaboration excelled utilizing the strength of each group, making use of the excellent solar cell fabrication and characterization facilities at Uppsala University and the competence on theoretical calculations and defect characterization at UiO. Consequently, I have been lucky to be a part of three research groups! I have thoroughly enjoyed to participate in this collaboration and I want to thank you all for your contributions.

Lasse, you have been dedicated to my work and given me steady guidance throughout this period. You are patient, understanding, skillful, persistent and a role model for young researchers. I am incredibly grateful to have had you as a my supervisor.

Clas, thank you for your supervision and enthusiasm for my work. You have a profound expertise in the field and are able to see my work in a broader context. I have greatly benefited from your collective mindset and encouragement for collaboration.

Lotten, you have made me feel like home in Uppsala and included me in the group. I appreciate that you have always taken time to listen and give me helpful advice.

Nils, thank you for having me follow you around when at ASC. I fondly remember our days in the lab. I admire your dedication and have learned a lot from you.

Sergiy, thank you for lunches, discussions and trips during our time together at UiO. Your enthusiasm have always lifted me up.

I have enjoyed collaborators from outside of the project. I want to thank Kostiantyn (Kostya) for long, but enjoyable hours preparing paper together. I thank Sven for entrusting me with measuring his samples and Xin for helping me use his annealing setup. Hisham spent an enormous amount of time preparing my samples for APT measurements, which I really appreciate. Thank you to Moises for our fruitful collaboration and Volodymyr for our efforts on electrical measurements. I had a great time collaborating with Filipe and Alireza together with Fredrik, it was a perfect match.

Acknowledgements

I want to thank all my colleagues at LENS. I was so lucky to move into the same office space as the greatest office mates Torunn, Chris and Josef. Working on quite a wide range of topics, we have still supported each other by sharing experiences, knowledge and encouragement. I want to thank Marianne for our morning chats and discussions, especially during the latter parts of my PhD. My time would not have been the same if it would not have been for the table tennis players Vegard, Mads, Heine and Nishant. I received a lot of help from others using the instruments at LENS. Thomas S. taught me how to use the SIMS and has always been a source of knowledge. Viktor is amazing, being able to fix everything that is broken, especially the SIMS. I want to thank Micke, Halvor, Per, Kristin, Cristian, Heine, Alex A., Phil and Ilia for your assistance and training. Alex H. and Thomas A. have shared my enthusiasm for Python, which I really appreciated. I want to acknowledge Klaus Magnus for many discussions and for asking me to be the step-in teaching assistant for the course "Bærekraftige energisystemer". Fredrik for accepting to have me as his supervisor during his Master's degree, which have been a great experience. Margareta for giving me advice and sharing many of her vast experiences with SIMS. Lastly, I want to thank the late Professor Bengt G. Svensson for our inspiring conversations at the coffee machine which always ended with tennis-related topics.

The lunch table is an instrumental meeting place for those working at LENS, I want to thank everyone who have been there during my time. The cabin trips have been great experiences for me. I have so many great memories of our time together at LENS. Thank you for making it so enjoyable.

My second home has been with the theory group at Structure Physics. Here, I have enjoyed lunches, dinners and seminars with Kristian, Sergiy, Sasha, Rongzhen, Priya, Gustavo, Kostya, Johannes, Mathias and Konstantina among others. Thank you for giving me great memories and guidance in this period.

My third home has been in Uppsala at the ÅSC. Here I have met great people who have provided with a good working and social environment during my many visits. Thank you! In addition to Lotten and Nils, I want to especially thank Katharina and Sven for including me in social activities such as BBQs, padel and afterwork beer. I have also benefited from discussions and/or lab assistance from Jes, Sethu, Jan, Nishant and Marika.

Finally I want to thank my friends and family. You wish me well and always have my back. Thank you to Lina for helping me improve some of my illustrations.

I want to especially thank my wife, Ane. You have become quite an expert on solar cells, listening, helping and supporting me every day throughout these years. You are one of a kind. My greatest achievement is meeting you.

• **Sigbjørn Grini**

Oslo, November 2019

Abstract

The solar energy sector is growing rapidly and solar cells are expected to be the main source of energy in the future. To ensure sustainable growth, the solar cells need to be cheap and accessible. Thin film solar cells allow for less material usage and can be used on flexible substrates, however, commercial alternatives contain either toxic or scarce elements. One promising alternative for an absorber material is copper-zinc-tin-sulfide ($\text{Cu}_2\text{ZnSnS}_4$), abbreviated CZTS, which contains only earth-abundant non-toxic elements. That said, CZTS is a complex material which makes it challenging to understand all its underlying properties and how to fabricate an efficient CZTS solar cell.

In this thesis, band gap grading by incorporation of selenium and impurities, particularly sodium and oxygen, in CZTS have been studied. Secondary ion mass spectrometry (SIMS) has been utilized in combination with complementary techniques to reveal insights into the properties of CZTS, closely related to solar cell device performance. Tools for using SIMS depth profiles and imaging to study sulfur-selenium gradients have been established. The in-diffusion and recrystallization during selenium incorporation have been observed to closely relate to the presence of sodium. Based on the results, optimization of the process lead to the fabrication high-performing CZTS-based solar cells.

Impurities play an important role for fabrication of efficient CZTS solar cells. Here, the interplay between sodium and oxygen have been identified. The close correlation between the two impurities suggest that trapping of sodium by incorporation of oxygen can be used to control the sodium distribution. The mechanism can be utilized during fabrication and postdeposition heat treatments to achieve high-performing solar cells. Nonuniformity and distribution of impurities are highlighted and shown to occur on the millimeter, micrometer and nanometer scale. The migration of the impurities is studied with heat and heavy water treatments.

List of Papers

Paper I

S. Grini, N. Ross, T. N. Sky, C. Persson, C. Platzer-Björkman and L. Vines
Secondary ion mass spectrometry as a tool to study selenium gradient in $\text{Cu}_2\text{ZnSn}(\text{S},\text{Se})_4$
Phys. Status Solidi C 14, No. 6, 1600187 (2017).

My contribution: SIMS measurements, analyzing results, discussions, writing manuscript with input from co-authors

Paper II

N. Ross, J. Larsen, S. Grini, L. Vines and C. Platzer-Björkman
Practical limitations to selenium annealing of compound co-sputtered $\text{Cu}_2\text{ZnSnS}_4$ as a route to achieving sulfur-selenium graded solar cell absorber
Thin Solid Films 623, 110–115 (2017).

My contribution: SIMS measurements, analyzing results, discussions, proof reading

Paper III

S. Grini, N. Ross, C. Persson, C. Platzer-Björkman and L. Vines
Low temperature incorporation of selenium in $\text{Cu}_2\text{ZnSnS}_4$: Diffusion and nucleation
Thin Solid Films 665, 159–163 (2018).

My contribution: SIMS, top-view SEM, XRD measurements, part of performing heat treatments, analyzing results, discussions, writing manuscript with input from co-authors

Paper IV

N. Ross, S. Grini, K. Rudisch, L. Vines and C. Platzer-Björkman
Selenium Inclusion in $\text{Cu}_2\text{ZnSn}(\text{S},\text{Se})_4$ Solar Cell Absorber Precursors for Optimized Grain Growth
IEEE Journal of Photovoltaics Vol. 8, No. 4, (2018).

My contribution: SIMS measurements, analyzing results, discussions, proof reading

Paper V

S. Grini, K. V. Sopiha, N. Ross, X. Liu, T. S. Bjørheim, C. Platzer-Björkman, C. Persson and L. Vines

Strong Interplay between Sodium and Oxygen in Kesterite Absorbers: Complex Formation, Incorporation and Tailoring Depth Distributions

Advanced Energy Materials 1900740, (2019).

My contribution: SIMS measurements, heat treatments, analyzing results, discussions, writing manuscript with input from co-authors, manuscript revision

Paper VI

Sigbjørn Grini, Hisham Aboulfadl, Nils Ross, Clas Persson, Charlotte Platzer-Björkman, Mattias Thuvander and Lasse Vines

Dynamic impurity redistributions in kesterite absorbers

Submitted.

My contribution: SIMS measurements, heat and heavy water treatments, analyzing results, discussions, writing manuscript with input from co-authors

Paper VII

S. Englund, S. Grini, O. Donzel-Gargand, V. Paneta, V. Kosyak, D. Primetzhofner, J. J. S. Scragg and C. Platzer-Björkman

TiN Interlayers with Varied Thickness in $\text{Cu}_2\text{ZnSnS}(e)_4$ Thin Film Solar Cells: Effect on Na Diffusion, Back Contact Stability, and Performance

Phys. Status Solidi A 215, 1800491 (2018).

My contribution: SIMS measurements, analyzing SIMS results, discussions, proof reading

The published papers are reprinted with permission from <publisher(s)>. All rights reserved.

Related work by the author, not presented in this thesis

1. N. Ross, J. Larsen, S. Grini, E. Sarhammar, L. Vines, and C. Platzer-Björkman, *Cu₂ZnSn(S,Se)₄ solar cell absorbers from diffusion of selenium into annealed Cu₂ZnSnS₄ absorbers*, 2016 IEEE 43rd Photovoltaic Specialists Conference (PVSC) 0492-0497, (2016).
2. N. Ross, S. Grini, L. Vines, and C. Platzer-Björkman, *Mixed sulfur and selenium annealing study of compound-sputtered bilayer Cu₂ZnSnS₄/Cu₂ZnSnSe₄ precursors*, 2017 IEEE 44th Photovoltaic Specialist Conference (PVSC) 3269-3274, (2017).
3. T. U. Nærland, S. Bernardini, H. Haug, S. Grini, L. Vines, N. Stoddard and M. Bertoni, *On the recombination centers of iron-gallium pairs in Ga-doped silicon*, Journal of Applied Physics 122(8), 085703, (2017).
4. M. Espindola-Rodriguez, D. Sylla, Y. Sánchez, F. Oliva, S. Grini, M. Neuschitzer, V. Izquierdo-Roca, E. Saucedo and M. Placidi, *Bifacial kesterite solar cells on FTO substrates*. ACS Sustainable Chemistry & Engineering 5(12), 11516-11524, (2017).
5. A. Hajjifarassar, F. Martinho, F. A. Stulen, S. Grini, S. Lopez-Marino, M. Espindola-Rodriguez, M. Döbeli, S. Canulescu, E. Stamate, M. Gansukh, S. Engberg, A. Crovetto, L. Vines, J. Schou and O. Hansen, *Monolithic Thin-Film Chalcogenide-Silicon Tandem Solar Cells Enabled by a Diffusion Barrier*, Submitted.

Contents

Acknowledgements	iii
Abstract	v
List of Papers	vii
Related work by the author, not presented in this thesis	ix
Contents	xi
1 Introduction	1
2 The $\text{Cu}_2\text{ZnSnS}_4$ solar cell	3
2.1 Solar cell principles	3
2.2 Current status of thin film solar cells	11
2.3 Current challenges and prospects for CZTS	13
3 Fabrication of $\text{Cu}_2\text{ZnSnS}_4$-based solar cells	15
3.1 Sputtering	15
3.2 The fabrication process	16
3.3 Diffusion	19
3.4 Strategies for incorporating both sulfur and selenium	21
3.5 Impurity incorporation	21
3.6 Controlling the average grain size	21
4 Characterization and modeling of $\text{Cu}_2\text{ZnSnS}_4$-based solar cells	23
4.1 Secondary ion mass spectrometry	23
4.2 X-ray diffraction	32
4.3 Scanning electron microscopy	33
4.4 Atom probe tomography	35
4.5 Density functional theory	36
5 Summary of results	39
5.1 Band gap grading with Se	39
5.2 Impurities in CZTS	46
6 Conclusions and outlook	53
6.1 Suggestions for further work	53
6.2 Outlook	54

Bibliography	55
Papers	64
I Secondary ion mass spectrometry as a tool to study selenium gradient in $\text{Cu}_2\text{ZnSn}(\text{S},\text{Se})_4$	65
II Practical limitations to selenium annealing of compound co-sputtered $\text{Cu}_2\text{ZnSnS}_4$ as a route to achieving sulfur-selenium graded solar cell absorber	73
III Low temperature incorporation of selenium in $\text{Cu}_2\text{ZnSnS}_4$: Diffusion and nucleation	81
IV Selenium Inclusion in $\text{Cu}_2\text{ZnSn}(\text{S},\text{Se})_4$ Solar Cell Absorber Precursors for Optimized Grain Growth	89
V Strong Interplay between Sodium and Oxygen in Kesterite Absorbers: Complex Formation, Incorporation, and Tailoring Depth Distributions	101
VI Dynamic impurity redistributions in kesterite absorbers	127
VII TiN Interlayers with Varied Thickness in $\text{Cu}_2\text{ZnSn}(\text{e})_4$ Thin Film Solar Cells: Effect on Na Diffusion, Back Contact Stability, and Performance	143

List of Abbreviations

<i>EQE</i>	External quantum efficiency
<i>FF</i>	Fill factor
<i>IQE</i>	Internal quantum efficiency
<i>J_{SC}</i>	Short circuit current
<i>P_{mp}</i>	Maximum power point
<i>QE</i>	Quantum efficiency
<i>RSF</i>	Relative sensitivity factor
<i>SF</i>	Sensitivity factor
<i>V_{OC}</i>	Open circuit voltage
APT	Atom probe tomography
CA	Contrast aperture
CB	Conduction band
CBM	Conduction band minimum
CdS	Cadmium sulfide
CdTe	Cadmium telluride
CIGS	Cu(In,Ga)(S,Se) ₂ - Copper indium gallium disulpho-selenide
CIS	CuInSe ₂ - Copper indium diselenide
CZTS	Cu ₂ ZnSnS ₄ - Copper zinc tin sulfide
CZTS(e)	Both CZTS and CZTSe
CZTSe	Cu ₂ ZnSnSe ₄ - Copper zinc tin selenide
CZTSSe	Cu ₂ ZnSn(S,Se) ₄ - Copper zinc tin sulfoselenide
DC	Direct current
DFT	Density functional theory
EDS	Energy dispersive X-ray spectroscopy

Contents

EDX	Energy dispersive X-ray spectroscopy
EM	Electron multiplier
ESA	Energy sector analyzer
FA	Field aperture
FC	Faraday cup
MSA	Magnetic sector analyzer
PCE	Power conversion efficiency
PVD	Physical Vapor Deposition
RF	Radio frequency
SCR	Space charge region
SEM	Scanning electron microscopy
SIMS	Secondary ion mass spectrometry
SLG	Soda-lime glass
SQ limit	Shockley-Queisser limit
STC	Standard test conditions
ToF-ERDA	Time-of-flight-energy elastic recoil detection analysis
VB	Valence band
VBM	Valence band maximum
XRD	X-ray diffraction
ZnO	Zinc oxide
ZnO:Al	Aluminium-doped Zinc oxide
ÅSC	Ångström Solar Center

Chapter 1

Introduction

The World's total electricity generation has over doubled since 1990 increasing from 11 900 TWh to 25 000 TWh in 2016 [1]. The generation will continue to increase as more of the population obtain access to electricity and electric form of transportation. Of the total electricity produced, 65 % comes from fossil fuels. This share will likely decrease as alternatives such as wind and solar are becoming the cheapest source of energy in more than two-thirds of the world [2]. Bloomberg's New Energy Outlook predicts that by 2050, nearly half of the world electricity generation will come from wind and solar, as shown in Figure 1.1, playing a vital role in the reducing the World's carbon emissions.

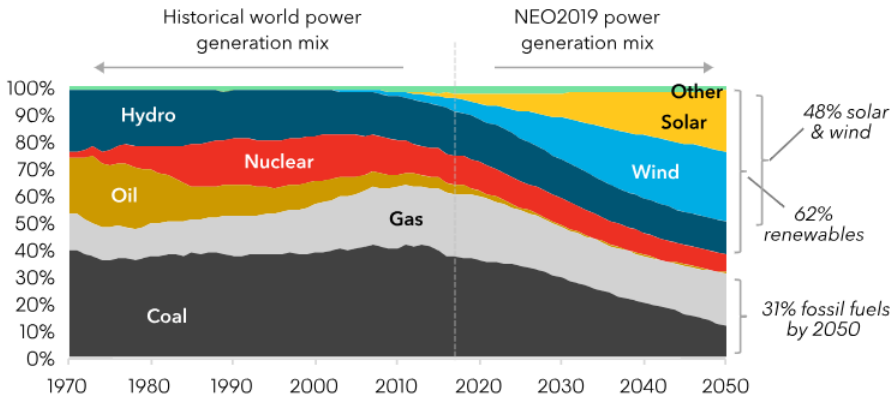


Figure 1.1: The global power mix as presented by BloombergNEF [2].

Here, solar energy is predicted to see the largest growth. For solar energies, photovoltaics (PV) or solar cells, are expected to contribute to most of the electricity generation [3]. PV technologies utilize the photovoltaic effect, which is the effect that voltage can be created in a material illuminated by light, for instance sunlight, and this effect can be used in a solar cell to produce current. Importantly, PV systems do not need any moving parts to generate electricity, minimizing maintenance costs such that most of the costs are related to fabrication and installation. PV systems are versatile and can be installed on a large-scale including in a power plant or on a small scale like when integrated on the facade or roof of buildings. Currently, most of the installed PV are made from crystalline silicon (c-Si) solar cells. Silicon is earth abundant and non-toxic, and the fabrication of c-Si is a mature technology. Purification and production of Si wafers have been developed and optimized for use in electronic devices for decades. Crystalline silicon solar cells also exhibit high solar cell efficiencies compared competing technologies. Nevertheless, c-Si does not absorb sunlight very efficiently

1. Introduction

compared to many other semiconductors due to an indirect band gap and therefore requires films that are on the order of 100 micrometer thick. Semiconductors which have direct band gaps, however, only need thin films of one micrometer. Such thin films allows for less material usage, lower production costs and handling, and flexible substrates.

For thin film solar cells to compete with c-Si, fabrication and installation costs and the efficiency need to be comparable to that of c-Si. Thin film solar cell technologies based on Cu(In,Ga)Se₂ (CIGS) and CdTe as absorbers, have been able to commercialize and contributed to 4.2 % of the total PV production in 2017 [4]. However, these two materials contain either scarce or toxic elements, which puts the sustainability of these technologies in question. Hence, in the search for potential solar cell materials that are earth-abundant and non-toxic, Cu₂ZnSnS₄ (CZTS) has been proposed as a promising candidate. CZTS solar cells have been produced with promising efficiencies using cheap and scalable deposition techniques. However, CZTS is a complex material, consisting of four different elements – copper, zinc, tin and sulfur. Additionally, elements such as sodium and selenium may be added to optimize the devices. The large number of elements raises the need for studying the elemental distribution of the elements and for understanding how to introduce these for optimal solar cell properties, which is the purpose of this thesis. Herein, band gap grading by introducing selenium into CZTS as well as the interplay and distribution of impurities are studied. Collaboration has been a central part of this thesis as it has been part of a larger collaborative project between the University of Oslo and Uppsala University. The framework of the collaboration has made it possible to successfully combine fabrication, characterization and theory. This is illustrated by the number of authors and methods used in the appended papers and related work. Thus, conclusions drawn in the thesis would not have been possible without this collaborative environment.

The thesis comprises of five more chapters. In Chapter 2, the solar cell concepts and the CZTS solar cell are introduced. In Chapter 3, the fabrication of CZTS and physical processes related to the fabrication are presented. In Chapter 4, the characterization techniques used are explained. In Chapter 5, a summary of the results obtained is presented. Lastly, in Chapter 6, conclusions, suggestions for further work and outlook are outlined.

In Papers I-IV, characterization of selenium incorporation into CZTS and the alloy containing both sulfur and selenium is in focus.

In Papers V-VII, the impurities in CZTS are studied, with new insight into the interplay between sodium and oxygen.

Chapter 2

The $\text{Cu}_2\text{ZnSnS}_4$ solar cell

2.1 Solar cell principles

2.1.1 Semiconductors

Most solar cells are composed of semiconductors. Semiconductors are materials with an energy gap, called band gap or E_g , in the electronic band structure that may be up to several eV, and where the electrical conductivity can be manipulated. In an ideal undoped (or intrinsic) semiconductor at temperature 0 K all electronic states up to the lower energy of the band gap are occupied with electrons, while the energy states above the band gap are empty. The Fermi level (E_F) denotes the energy level at which the probability of the state being filled by an electron is 1/2. For an undoped semiconductor at 0 K, the Fermi level is located in the middle of the band gap. The band that contains the energy states with energies below the band gap is known as the valence band (VB), while the band that contains the energy states with energy above the band gap is known as the conduction band (CB). Electrons can excite from the VB to the CB if sufficient energy is provided. Once located in the CB, electrons can move spatially in bands that the CB provides. These electrons are denoted as free electrons. The excited electron leaves behind an unoccupied state in the VB known as a hole. Holes in the VB are also considered free as they can move spatially in the VB. Excitation of electrons from the VB to the CB forms one electron and one hole, known as an electron-hole pair.

Any irregularity in a semiconductor crystal is known as a defect. Defects can be zero-dimensional (vacancies), one-dimensional (substitutionals and interstitials), two-dimensional (dislocations and grain boundaries) and three-dimensional (complexes and clusters). Some defects may introduce charge transition levels within the band gap. The levels are either acceptors or donors, depending on the charge carrier contribution. A charge transition level is often considered shallow if it is located close to the respective band edges and deep if it is far from the respective band edges. Defects that contribute with shallow defect levels are typically used for doping of a semiconductor. Doping is introducing a defect that adds a free electrons or hole to the semiconductor. A classical example of a dopant is boron (B) in silicon (Si). Replacing a Si atom with a B atom on the Si lattice site (substitutional defect, B_{Si}) introduces a state in the band gap close to the valence band maximum (VBM). B has one less electron than Si, hence, an electron from the VB can be trapped by the B atom leaving a free hole behind in the VB. Thus B acts as an acceptor providing a hole to the VB by accepting an electron. Dopants introduced into a semiconductor changes its conductivity. If there are more free holes than electrons, the semiconductor is categorized as p-type and if there are more free electrons than holes, the semiconductor is categorized as n-type. In a p-type semiconductor free holes are the majority carriers and free electrons the minority carriers. B is an extrinsic defect in Si, irregularities involving only the constituent elements in the lattice are called intrinsic defects.

2.1.1.1 $\text{Cu}_2\text{ZnSnS}_4$

The semiconductor studied in this thesis is copper-zinc-tin-sulfide ($\text{Cu}_2\text{ZnSnS}_4$), abbreviated CZTS. In Papers I-IV, however one objective is to alloy exchanging some S with selenium (Se), which is abbreviated CZTSSe and in Paper VII, CZTS is compared with selenide $\text{Cu}_2\text{ZnSnSe}_4$, which is abbreviated CZTSe. Herein, the term "CZTS-based" is used as a general term for all three compounds.

The two main crystal structures formed by CZTS thin films are kesterite and stannite, where kesterite structure is formed under normal processing conditions [5]. The unit cell for the kesterite structure is shown in Figure 2.1, as visualized by VESTA [6] adapted from [7, 8]. Each sulfur atom (yellow) is bonded to two Cu atoms (blue), one Zn atom (gray) and one Sn atom (purple) described by the $I\bar{4}$ space group. The formation energy required for exchanging sites between Cu and Zn is low and gives rise to Cu-Zn disorder [9–12]. The atoms marked half blue and half gray in the disordered kesterite are potentially either Cu or Zn. If there is a random distribution of Cu and Zn on these sites, the crystal is fully Cu-Zn disordered, however, if all the Cu is on 2c sites and all the Zn is on 2d sites (using Wyckoff positions), the crystal is fully Cu-Zn ordered. Cu-Zn disorder is one challenge for CZTS solar cell devices as described in Section 2.3. The kesterite structure is quite complex compared to elemental and binary compounds, opening up possibilities for many lattice defects. Stable intrinsic defects in the CZTS includes vacancies (V_{Cu} , V_{Zn} , V_{Sn} , V_{S}), antisites (Cu_{Zn} , Cu_{Sn} , Zn_{Cu} , Zn_{Sn} , Sn_{Cu} , Sn_{Zn}) and interstitials (Cu_i , Zn_i) [13, 14]. Notably, many of these defects are compensated in neutral defect pairs, such as $V_{\text{Cu}}+\text{Zn}_{\text{Cu}}$, $V_{\text{Zn}}+\text{Sn}_{\text{Zn}}$. However, the list highlights the complexity of CZTS. CZTS is p-type, which is believed to be due to the shallow defect V_{Cu} acting as an acceptor. In fact, to produce the best solar cell devices, Cu-poor stoichiometry is commonly used and it is believed that Cu-poor conditions give rise to a very high concentration of V_{Cu} . "Kesterite" is used in this thesis as a term for CZTS and CZTS-like compounds forming the kesterite crystal structure.

The band gap of CZTS is direct, meaning that no phonon interaction is needed to excite an electron from the VB maximum (VBM) to the CB minimum (CBM). The band gap of CZTS, which is about 1.5 eV, is comparable to that of CdTe, a commercially available solar cell material. CZTS exhibits a strong absorption coefficient such that only a thin layer (less than 1 μm) is needed to absorb all the sunlight [15–18]. Therefore, CZTS solar cells are classified as a thin film technology, enabling the substrate underneath the CZTS solar cell to be flexible. Flexible solar cells can, for example, be rolled together after use and moved to a new location.

The constituent elements of CZTS - copper, zinc, tin and sulfur - are all earth-abundant and non-toxic elements. Earth-abundance of the elements used in the solar cell production is important for ensuring low and stable production costs and sustainability. Non-toxicity is also considered an advantage. However, an argument can be made that toxicity of the constituent elements in the solar cell is a solvable problem. The solar cell itself is a sealed device and with appropriate recycling procedures, toxic elements will not be released. Additionally, if toxic elements are only integrated into a 1 μm thick layer, this is a tiny part of the whole solar cell construction. On the other hand, the usage

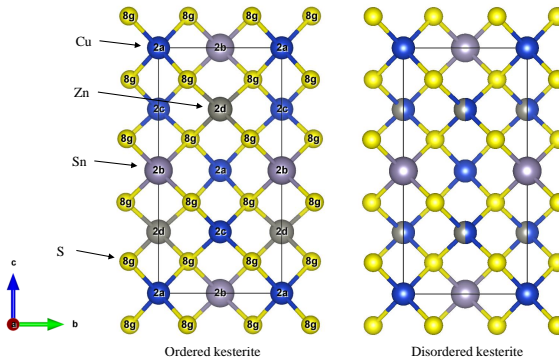


Figure 2.1: The ordered and disordered kesterite $\text{Cu}_2\text{ZnSnS}_4$ crystal structure as displayed with VESTA [6], structures adapted from [7, 8]. The labels indicate the Wyckoff positions. For the ordered kesterite, 2a and 2c sites are occupied by Cu, likewise are 2b, 2d and 8g sites occupied by Sn, Zn and S, respectively.

of toxic elements promotes mining of these elements and requires strict care during processing. One caveat with the research on CZTS is that the best devices comprise of around 50 nm thick layer of CdS as the n-type buffer layer. Alternative buffer layers are being researched and have exhibited well performing CZTS solar cells, for example $(\text{Zn},\text{Sn})\text{O}$ and $\text{Zn}(\text{O},\text{S})$ [19–21].

The band gap of CZTS may be tuned by alloying with other elements. For instance, alloying with Se reduces the band gap [15] and alloying with Ge increases the band gap [22]. Other elements for alloying have been investigated such as Li or Ag [23–25], Cd, Ba or Mn [26–28] and Si [29]. Some of these elements are not earth-abundant and also toxic, but alloying with such elements have been conducted to improve the efficiency of the solar cells as well as understanding its fundamental properties. Alloying CZTS with other elements may allow for band gap grading, i.e. a change in band gap with depth. Such a grading may result in an electrical field aiding charge carrier separation. Band gap grading has been successfully achieved with other thin film solar cell technologies, see Subsection 2.2.1.

The CZTS device structure used in this thesis is displayed in Figure 2.2. A 1 mm thick soda-lime glass (SLG) substrate is used. The SLG is cheap and contains sodium (Na) which diffuses into the CZTS layer during processing. On top of the SLG is the molybdenum (Mo) back contact, about 400 nm thick. The CZTS layer is about 1 μm thick, consisting of polycrystalline CZTS grains. The CZTS layer is where most of the incident photons are absorbed, hence it is often called the absorber. On top of the CZTS layer is a thin CdS layer (~50 nm) acting as a highly doped n-type buffer to form a pn junction (as described in Subsection 2.1.2). To extract charge carriers, a double layer of the transparent conductive oxide, ZnO (undoped (~80 nm) and doped with aluminum (Al) (~210 nm), on top the CdS layer.



Figure 2.2: The CZTS solar cell structure. Soda-lime glass substrate (1 mm), Mo back contact (~ 400 nm), CZTS absorber layer ($\sim 1 \mu\text{m}$), CdS buffer layer (~ 50 nm), ZnO (~ 80 nm) and ZnO:Al (~ 210 nm).

2.1.2 Solar cell operation

In solar cells, electron-hole pairs are created by incident photons with larger energy than the band gap. Electrons and holes are separated and extracted to provide electricity. To separate the electrons and holes in CZTS solar cells, a p-n junction is utilized. A p-n junction is a junction between a p-type and an n-type semiconductor. Once the two semiconductors join, electrons from the n-type side and holes from the p-type side move across the junctions. The charge carriers leave behind ionized donors and acceptors that form an electric field inside the depletion layer or the space charge region (SCR). If both the n-type and the p-type semiconductors consist of the same material, the p-n junction is a homojunction. If the two materials are different, it is a heterojunction. For CZTS solar cells, a heterojunction is utilized, usually with p-type CZTS and n-type CdS. For simplicity, the band diagram of a p-n homojunction is displayed in Figure 2.3. Free electrons in the CB and free holes in the VB move easily through the semiconductor junctions if the CBM is bending downwards and the VBM is bending upwards. In Figure 2.3(a) the n-type and the p-type semiconductors are in thermal equilibrium, with

a depletion layer (gray region) formed in between the two layers. However, if the p-n junction is illuminated by incident photons, electron-hole pairs are generated and moves across the junction. At steady-state conditions under illumination, as in Figure 2.3(b), the electron and hole concentrations have changed. The concentrations of each charge carrier can expressed in terms of Fermi levels, and is called the quasi-Fermi levels for the electrons and holes, F_n and F_p . The difference in quasi-Fermi levels over a p-n junction limits the voltage output of the solar cell in operation.

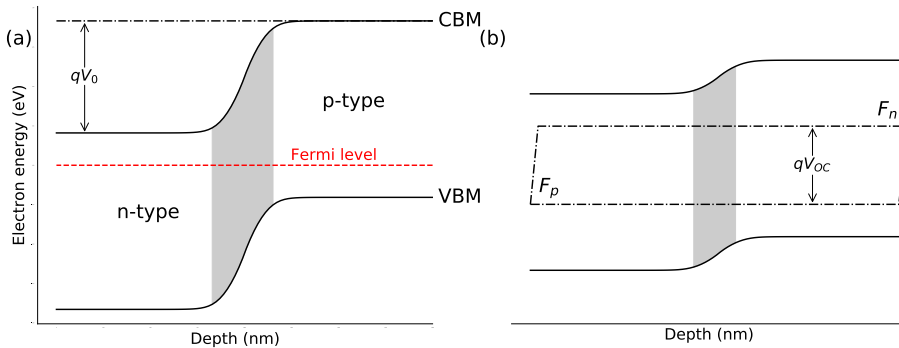


Figure 2.3: (a) Band diagram of a p-n junction at equilibrium. The n-type and the p-type semiconductors have joined. Donors and acceptors near the junction have ionized forming a depletion region (gray region). (b) Steady state condition under illumination. Electron-hole pairs are formed changing the quasi-Fermi levels, F_n and F_p , for the electrons and holes, respectively.

The band diagram of a typical CZTS solar cell at thermal equilibrium is displayed in Figure 2.4. The CBM and the VBM in CZTS have a gradient in the region near the CdS, forming the depletion region. The charge carriers from an electron-hole pair formed by incident light in the CZTS layer (blue region) are extracted at the contacts unless they recombine. Three recombination processes occurring in CZTS solar cells are shown in Figure 2.4 and listed below:

(1) *Band-to-band recombination*

- A free electron in the CB recombines with a free hole in the VB. The excess energy is released either as a photon (radiative recombination) or by transferring the energy to an existing free charge carrier that dissipate the energy as heat (Auger recombination). The band-to-band recombinations are generally not the dominating factor for the total recombination rate in chalcogenide solar cells [30].

(2) *Defect recombination*

- Defect states with charge transition levels in between the CB and the VB can act as recombination centers. The defect level, with energy above the Fermi

level, is normally unfilled (i.e with a hole). However, with the formation of electron-hole pairs, the quasi-Fermi level for the electrons increase and allows for an electron to be captured by the defect. The quasi-Fermi level for the holes is though unchanged and hence a hole from the VB will be captured and recombine with the captured electron. The energy will dissipate as heat or radiation.

(3) *Interface recombination*

- At the interface between the p-type and the n-type material in a heterojunction, a high concentration of defect states, known as interface states may be present. These states induce several energy levels in the band gap, which capture electrons and holes. Additionally, due to the large concentration of defect states, the quasi-Fermi levels may be pinned at the interface, further enhancing recombination and lowering the potential barrier. Interface recombination may also occur at the CZTS/Mo interface.

At the interface between the CZTS and the CdS, the electron affinity of CZTS is larger than that of CdS such that a "cliff-like" conduction band offset (CBO) is formed [31]. The offset allows for a cross-recombination channel between an electron in the CdS and a hole in the CZTS layer involving a tunneling process [30].

The time it takes from a minority carrier is generated to it is recombined is known as the minority carrier lifetime, τ . If the minority carrier lifetime of a solar cell device is low, the excited charge carriers will not exist long enough for them to be extracted.

The solar cell performance is evaluated by measuring the current-voltage ($J - V$) characteristics with and without illumination, where V is the voltage applied over the junction. If a positive voltage bias is applied, both sides are injected with the respective majority carriers and the depletion width is reduced, increasing the chance for carriers to move across the junction. If a negative voltage bias is applied, the respective majority carriers are drawn away from the junction interface and the depletion width increases, limiting the current flow through the device. The current density, J , through the p-n junction in dark can be described by the Diode equation

$$J = J_0 \left(e^{qV/nkT} - 1 \right) \quad (2.1)$$

where J_0 is the dark saturation current, q is the elementary charge, V is the applied voltage and n is the ideality factor. A dark $J - V$ curve is displayed in Figure 2.5 (dashed blue line) for a CZTSSe solar cell from Paper IV. When illuminated, a fraction of the generated electron-hole pairs contribute to J , such that the current-density J can be described as in Equation 2.2.

$$J_D = J_0 \left(e^{qV/nkT} - 1 \right) - J_{SC} \quad (2.2)$$

Where J_{SC} is the short-circuit current measured at zero voltage bias, assumed here to be equal to the current of photo-generated electron hole-pairs. By evaluating Equation 2.2 with $J_D = 0$, the open circuit voltage, V_{OC} , can be expressed as in Equation 2.3.

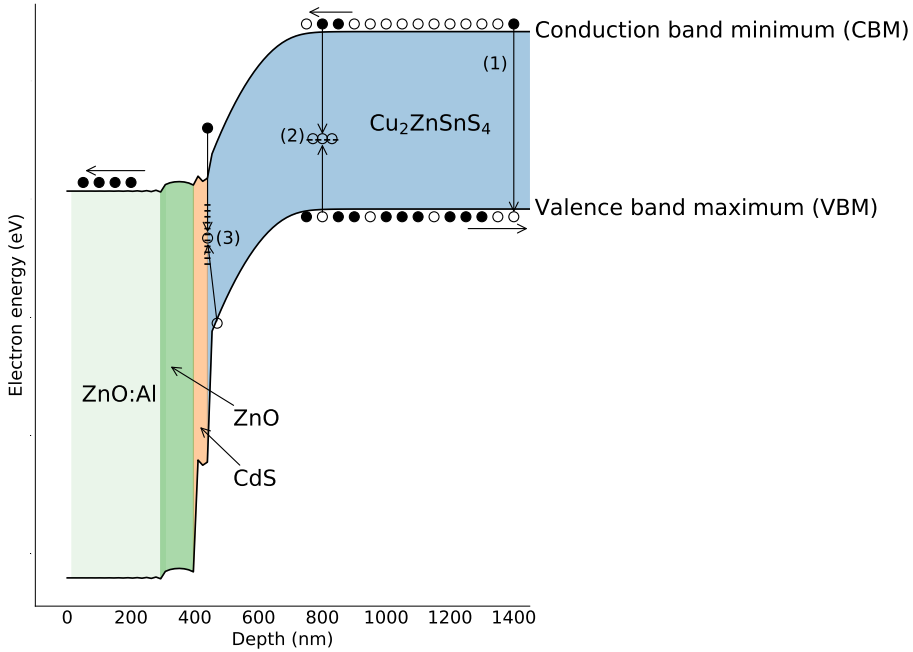


Figure 2.4: Band diagram of a typical CZTS solar cell. The three recombination processes (1) Band-to-band recombination, (2) Defect recombination and (3) Interface recombination are illustrated.

$$V_{OC} = \frac{nkT}{q} \ln \left(\frac{J_{SC}}{J_0} + 1 \right) \quad (2.3)$$

The $J-V$ characteristics for the device under illumination is displayed as a solid blue line in Figure 2.5. There are a crossover between the dark and illuminated $J-V$ curves in forward bias. The crossover is commonly seen for the cells presented in this thesis. The reason is uncertain, but is likely related to charge transport barriers at the interfaces which are neutralized during illumination [32, 33].

The J_{SC} and V_{OC} are annotated at zero voltage and zero current respectively. The power density of the device under illumination is displayed as an orange dashdotted line in Figure 2.5. The maximum power output from the solar cell under illumination is at the maximum power point and equals $P_{mp} = I_{mp}V_{mp}$. The I_{mp} and the V_{mp} represent the ideal operation conditions for the device. The fraction representing the maximum power divided by $J_{SC}V_{OC}$ represents the fill factor, FF , of the device as shown in Equation 2.4.

$$FF = \frac{I_{mp}V_{mp}}{J_{SC}V_{OC}} \quad (2.4)$$

The three parameters, J_{SC} , V_{OC} and FF are key parameters for describing the power conversion efficiency (PCE or η) of the solar cell, which is defined in Equation 2.5.

2. The $\text{Cu}_2\text{ZnSnS}_4$ solar cell

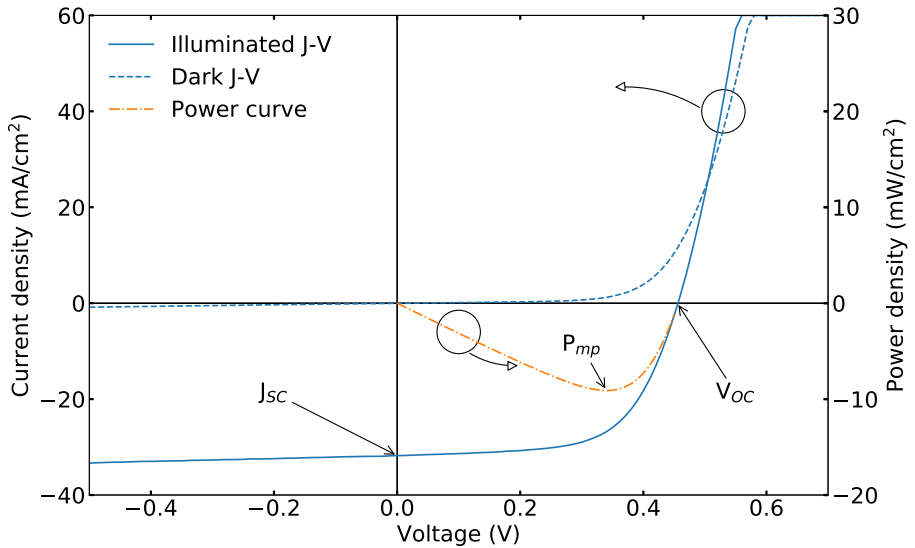


Figure 2.5: J-V curve of the best performing CZTSSe solar cell produced in Paper IV. Key parameters such as open circuit voltage (V_{OC}), short circuit current (J_{SC}) and maximum power point (P_{mp}) are annotated. The power conversion efficiency (PCE) of the device was 9.11 %. The circles indicate which lines correspond to which y-axis.

$$\eta = \frac{P_{mp}}{P_{in}} = \frac{FFJ_{SC}V_{OC}}{P_{in}} \quad (2.5)$$

Where P_{in} is usually the illumination from the Sun at standard test conditions (STC), with air mass 1.5, as illustrated in Figure 2.6 [34].

For the absorber to produce an electron-hole pair from the incident light, the photon energy must be larger than the band gap. Hence, for CZTS, all photons with energies less than 1.5 eV will not contribute to the power output. Furthermore, each photon with its potential energy larger than 1.5 eV will only produce one electron-hole pair with energy potential limited by the band gap. The residual energy is dissipated as heat. Consequently, the upper PCE limit for a single p-n junction CZTS solar cell is ~32 %, known as the Shockley-Queisser limit [35]. To circumvent this limit, solar cells comprising of multiple band gaps have to be utilized. More band gap energies can be made possible by stacking several p-n junctions, with absorbers of different band gaps, on top of each other. This concept is known as tandem or multi junction solar cells. State of the art multi junction solar cells consisting of 5 junctions have reached a record PCE of 38.8 % [36]. The prospect of CZTS as an absorber in tandem solar cells is discussed briefly in Section 2.3.

The solar cell may also have optical and electrical losses related to the response to photons with different wavelength. The probability that an incident photon will generate

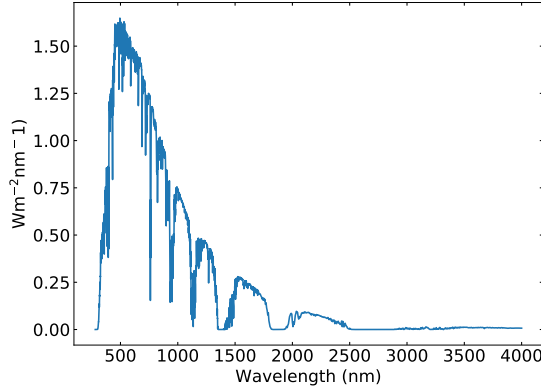


Figure 2.6: The solar energy spectrum at air mass 1.5, adopted from the ASTM G-173-03 [34].

one electron that outputted as current is called the quantum efficiency (QE). The external QE, EQE , is defined as

$$EQE(E) = (1 - R(E))\eta_{\text{coll}}(E)\alpha(E) \quad (2.6)$$

where $R(E)$, $\eta_{\text{coll}}(E)$ and $\alpha(E)$ is the reflectance, the collection efficiency and the absorbance at a given photon energy E . EQE or internal quantum efficiency (neglecting reflection losses), IQE , are commonly measured for solar cell devices.

2.2 Current status of thin film solar cells

Here, a brief overview of three thin film solar cell absorber materials is presented. The materials have been proven suited for thin film processing and have been demonstrated in solar cell devices which have reached PCEs above 20 %. Some of the advantages and disadvantages for each material are put forward.

2.2.1 Copper indium gallium diselenide

Cu(In,Ga)Se_2 (CIGS or CIS for the Ga-free compound) is a solar cell absorber material that contributed to 1.9 % of the total global PV production in 2017 [4]. CIGS-based solar cells display the same architecture as used for CZTS-based solar cells. The PCE of CIGS devices has reached over 20 %, with the current world record being 22.9 % [37]. The band gap of CIGS will vary from ~ 1.0 eV to ~ 1.6 eV depending on the $[\text{Ga}] / ([\text{Ga}] + [\text{In}])$ ratio [38]. Band gap grading, a topic discussed in this thesis, using Ga and In have been successfully applied in CIGS devices.

CZTS shares many characteristics with CIGS. Structurally they both form a crystal structure where anions surround cations with a tetrahedral coordination and vice versa.

2. The $\text{Cu}_2\text{ZnSnS}_4$ solar cell

In CZTS, Zn(II) and Sn(IV) replace the scarce element In(III) (or Ga(III)). Both are Cu-based chalcogenides and both form sulfoselenides easily. The two compounds crystallize at around 400 °C and Na facilitates the growth and improves the PCE of solar cell devices [39]. The use of a Mo back contact and a CdS buffer layer has been adapted from CIGS processing.

Advantages:

- High record PCE above 20 %
- Stable PCE over long periods of time
- Band gap grading has been achieved

Disadvantages:

- In is a scarce element
- Buffer layer usually contains Cd

2.2.2 Cadmium telluride

Cadmium telluride (CdTe) based solar cells accounted for 2.3 % of the total global PV production in 2017 [4]. CdTe has a band gap of ~1.5 eV and displayed similar PCE as for CZTS until a rapid increase in PCE was reported from 17.3 % in 2013 to 22.1 % in 2016.

Advantages:

- High record PCE above 20 %
- Stable PCE over long periods of time

Disadvantages:

- The absorber and the buffer layer contains Cd

2.2.3 Perovskites

Perovskite solar cells are quite different from aforementioned technologies. Perovskite is a crystal structure formed by compounds with the chemical composition described by ABX_3 . For high PCE, the A site is occupied by either an inorganic element or an organic molecule, the B site is primarily occupied by lead (Pb) and the X site is occupied by halides (i.e. iodine, chlorine). By choosing different halides and alloying with Pb with Sn, the band gap can be tuned from ~1.1 eV to ~2.3 eV [40]. Perovskite solar cells have seen a large increase in PCE from 3.81 % in 2009 [41] to 21.6 % in 2017 [42].

Advantages:

- High record PCE above 20 %
- Vast improvements in few years of research
- Band gap can be tuned in a large range

- Low temperature processing allows for easier integration with c-Si for tandem applications

Disadvantages:

- The absorber contains lead
- Not stable PCE of long periods of time

2.3 Current challenges and prospects for CZTS

Compared to CdTe- and CIGS-based thin film solar cells, the record PCE is only 11.0 % for CZTS [43] and 12.6 % for CZTSSe [44]. The lower PCE of CZTS-based solar cells can to some extent be attributed to a low V_{OC} . This deficiency is illustrated in Figure 2.7, where the $J-V$ characteristics normalized to their SQ limits calculated from Ref. [45] are displayed. Figure 2.7 confirms that the low V_{OC} is what distinguishes CZTS-based solar cells from CIGS and CdTe.

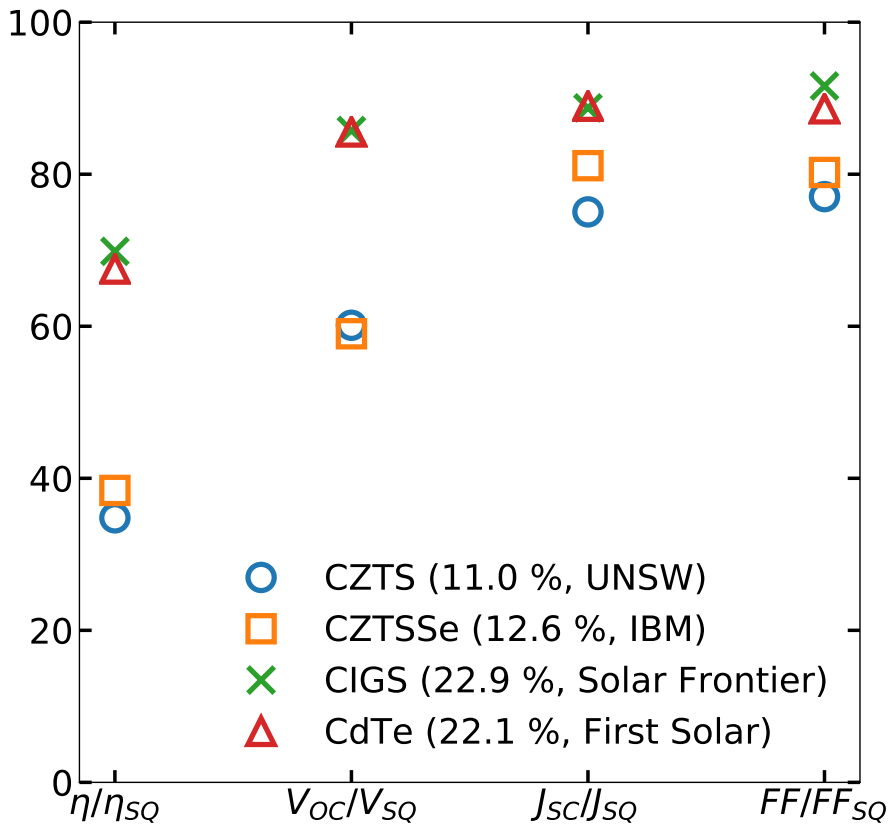


Figure 2.7: Solar cell parameters normalized to the SQ-limit for the record PCE devices of CZTS, CZTSSe, CIGS and CdTe. The CZTS-based solar cells exhibit lower PCE compared to CIGS and CdTe. Especially, the V_{OC} needs to be improved for CZTS-based solar cells to compete with CIGS and CdTe.

There are many factors contributing to V_{OC} loss in the CZTS solar cell devices [46,

47]. Some of the proposed factors are Cu-Zn disorder, low minority carrier lifetime, band misalignment, band tailing, secondary phase formations, unable to achieve band gap grading, deep defects and not optimizing impurity incorporation [12, 19, 31, 48–63]. Among these, band gap grading and impurities are the main topics in this thesis. Band gap grading is a proven method to improve the PCE. For CIGS, two successful types of band gap grading have been realized. First, an increase of the band gap towards the back contact (back grading) forms a back surface field. Since the band gap shift for Ga alloying in CIGS mainly affect the conduction band, the back surface field repels free electrons and reduces recombination at the back contact. Second, an increase of the band gap in the depletion layer (front grading) increases subsequently the V_{OC} [64, 65]. Additionally, the band gap at the interface can be modified to reduce band misalignment. In band gap graded CIGS, the band gap usually varies between 1.0 and 1.5 eV. The band gap of CZTS may be changed in the same range by varying the $[\text{S}]/([\text{S}] + [\text{Se}])$ ratio. Thus, understanding the crystallization and diffusion mechanisms between S and Se is important. Na impurities have been observed to increase the grain growth during the crystallization process and need to be addressed [63]. For semiconductors, impurity control is vital for device performance [66]. In CZTS, changes in the Na distribution with depth have been observed to correlate with changes in PCE [67, 68]. Also, oxygen (O) has been observed to reside in grain boundaries (GBs) in high PCE devices [69] and hydrogen (H) may also passivate CZTS [70]. CZTS devices are usually subjected to postdeposition heat treatments after crystallization. During this step, impurity diffusion occurs. Thus it is important to understand the role and behavior of impurities in the CZTS solar cell to improve the PCE.

Substantial research have been put into improving CZTS-based solar cells and understanding their properties. Several research groups have improved their devices and reported PCEs close to the record of 12.6 %, and even an uncertified record PCE of over 13 % has been presented [71]. The understanding of the properties of CZTS-based materials has improved significantly in the last 10 years. Indeed, several research groups have presented devices with over 10 % PCE [43, 55, 72–75]. Slow and steady increase in PCE has been the pathway for many solar cell technologies [76]. Continued dedicated research and collaborative efforts on CZTS will likely lead to further improvements in efficiency such as that made for CIGS and CdTe. Postdeposition treatments of potassium fluoride (KF) on CIGS and CdCl_2 on CdTe have yielded improved efficiencies [77–79]. Perhaps an unknown activation step based on impurity treatment is yet to be discovered for CZTS. There are also exciting prospects for the use of CZTS as the top cell in a CZTS/Si tandem solar cell. Based on a TiN diffusion barrier and temperature resilient Tunnel Oxide Passivated Contacts (TOPCon) Si structures, contamination of impurities from the CZTS sulfurization process has been limited and working devices with V_{OC} higher than that of the bottom Si cell has been achieved [80, 81]. The variety of deposition methods being used displays the versatility of reaction pathways for producing CZTS devices with good solar cell efficiency.

Chapter 3

Fabrication of $\text{Cu}_2\text{ZnSnS}_4$ -based solar cells

3.1 Sputtering

Fabrication methods as well as characterization techniques used in this thesis are based on sputtering. Sputtering is a physical process where atoms are removed from a solid or liquid by bombardment with particles which have kinetic energies in the range of 1 eV to 1 MeV [82]. These high energy particles collide with atoms on the surface and transfer their energy which triggers a collision cascade in the material. If a particle receives enough energy to be broken free from its bond at the surface, it will be ejected from the material and be sputtered. The principle of sputtering is illustrated in Figure 3.1. The incoming particle can either be back-scattered from the surface or enter into the sample causing more collision cascades. The effect of the incoming particle is dependent on its mass, incident angle, energy, the surface roughness, chemical binding and crystallinity of the sample [82]. Sputtering is an efficient method to remove particles from a material at temperatures close to room temperature. Specifically, particles removed by sputtering can for instance be used to deposit a thin film on a substrate or be analyzed in a mass spectrometer to investigate the composition of the sputtered material.

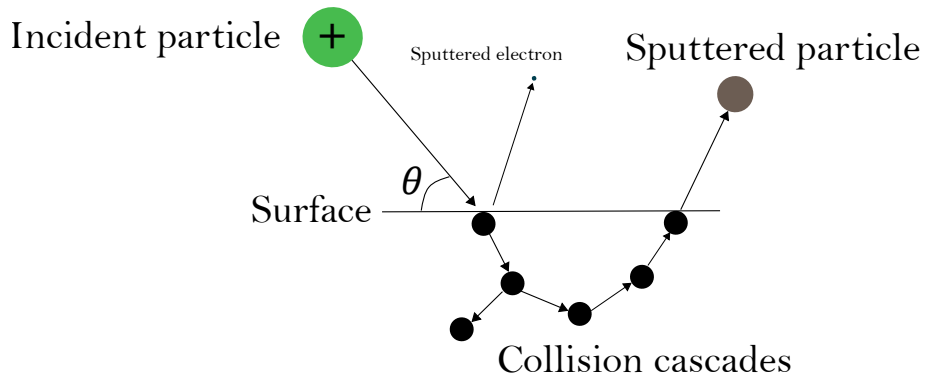


Figure 3.1: Schematic illustration of the principle of sputtering. An incident high energy particle hits the surface of a solid or liquid and triggers a collision cascade that results in a particle being ejected, i.e. sputtered from the material.

3.1.1 Thin film deposition by sputtering

Sputter deposition is a technique used to deposit a thin layer of a material or compound on top of a substrate, typically categorized as a physical vapor deposition technique (PVD) [83]. Sputter deposition requires either one or more so-called targets. Targets are lumps of material consisting of the element or compound one wants to deposit as a thin film on top of the substrate. During sputter deposition, ions accelerated towards the targets ejects its constituent elements. The ions being accelerated originate from the gas present in the chamber, (typically Ar). The gas is ionized by high energy electrons and accelerated by an electrical field, provided by a direct current (DC) or radio frequency (RF) current source depending on the resistivity of the target. For the sputtered ions to reach the sample with sufficient energy for forming high quality films, the chamber needs to be at high vacuum.

3.2 The fabrication process

The processing steps used at the Ångström Solar Center in Uppsala for fabrication of CZTS-based solar cells relevant for this thesis is described below. The process is illustrated in Figure 3.2.

The substrate and the back contact A SLG substrate was cleaned using standard cleaning procedure briefly described in Ref. [84]. The Mo back contact was deposited on top of the SLG by DC-sputtering with an in-line Materials Research Corporation sputtering system using a Mo target (99.97 % purity) with Ar (99.9995 % purity) as sputtering gas. The back contact consisted of two layers: An adhesive layer sputtered with a background pressure of 2 Pa and a conductive layer sputtered with a background pressure of 0.8 Pa. The total Mo thickness was about 400 nm. For some samples, like the ones discussed in Paper VII, a 20 - 200 nm thick TiN layer was deposited on top of the Mo using a Von Ardenne sputtering system.

The precursor The precursor layer used for CZTSSe formation was co-sputtered from the compound targets. For sulfide CZTS precursors, CuS, ZnS, SnS (99.99 % purity) were used as targets, while for selenide CZTSe precursors, CuSe, ZnSe and SnSe were used as targets. The precursor layer was deposited using a Lesker CMS-18 sputter system, with a 666 Pa Ar (99.9995 % purity) background pressure. CuS and SnS were DC-sputtered, while ZnS was RF-sputtered to prevent charging. The sputtering was performed with a substrate temperature of 250 °C. The sputtering power and substrate temperature during deposition for a typical run are displayed in Figure 3.3. The sputter deposition did not start until the substrate temperature had reached 250 °C. An SEM image¹ of a CZTS precursor layer on top of Mo is shown in in Figure 3.4(a).

The absorber formation To crystallize into solar-grade CZTS material, the SLG/Mo/precursor structure was annealed in the presence of elemental S and/or Se powders. The sample was put in a pyrolytic carbon-coated graphite box together with the powders,

¹For more information on SEM see Section 4.3

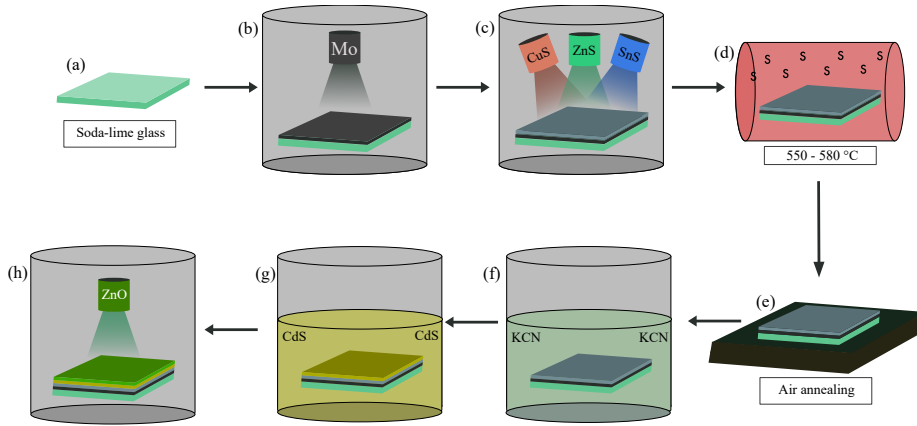


Figure 3.2: The fabrication process used at Ångström Solar Center in Uppsala for fabrication of CZTS-based solar cells relevant for this thesis. The process consisted of the following steps (a) Soda-lime glass substrate, (b) Mo sputtering, (c) co-sputtering of CZTS precursors, (d) chalcogen annealing, (e) air annealing (optional), (f) KCN treatment, (g) CdS chemical bath deposition and (h) ZnO (and ZnO:Al) sputtering.

which were placed in pockets on each side of the box. The box was placed inside a home-made tube furnace setup illustrated in Figure 3.5. The graphite box was transferred from a water-cooled cold zone to a hot zone, rapidly increasing the temperature to maximum 580 °C in about 90 seconds. Prior to the anneal, the furnace was filled with Ar with a background pressure varying between 24 and 47 kPa. Once the annealing was finished, the sample was transferred back to the cold zone and cooled down to 150 °C in about 5 minutes. Afterwards, the sample was transferred to a load-lock before being exposed to air. This chalcogen annealing is also referred to as sulfurization for only S powders, selenization for only Se powders and sulfoselenization for both S and Se powders present in the graphite box.

Solar cell fabrication In Papers IV and VII, complete solar cell structures were made. Prior to buffer layer deposition, air annealing was sometimes introduced to improve the device quality, where the absorber is typically put on a hot plate at 300 °C for 10 minutes. The low temperature anneal after absorber formation is a common step in the device process for chalcogenide technologies and was included in the baseline process at Ångström Solar Center after improvements in PCE were observed by Larsen et al. following annealing in air [85]. In the present thesis, air annealing has been utilized in Paper IV. Before buffer layer deposition, SLG/Mo/CZTS absorbers were etched in 5 wt% KCN solution for 2 minutes to remove unwanted phases, such as Na₂S [86]. The n-type CdS buffer layer was deposited on top of the structure by chemical bath deposition (CBD). Afterwards, the ZnO and ZnO:Al window layers were sputtered on top of the buffer layer using a von Ardenne sputter system. Finally, a Ni/Al/Ni grid

3. Fabrication of $\text{Cu}_2\text{ZnSnS}_4$ -based solar cells

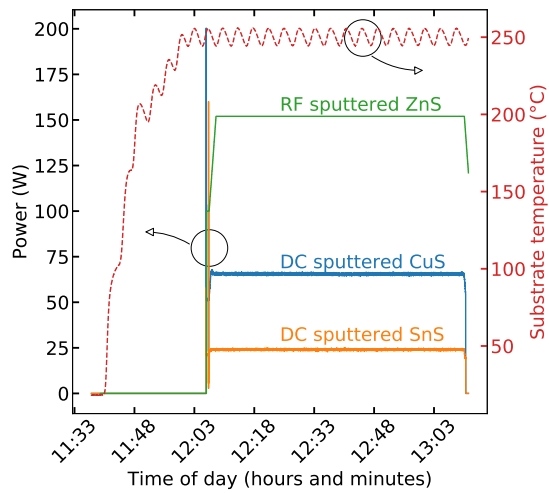


Figure 3.3: The sputtering power used for CuS, ZnS and SnS, and the substrate temperature during precursor sputter deposition. The sputtering did not start until the substrate temperature had reached 250 °C.

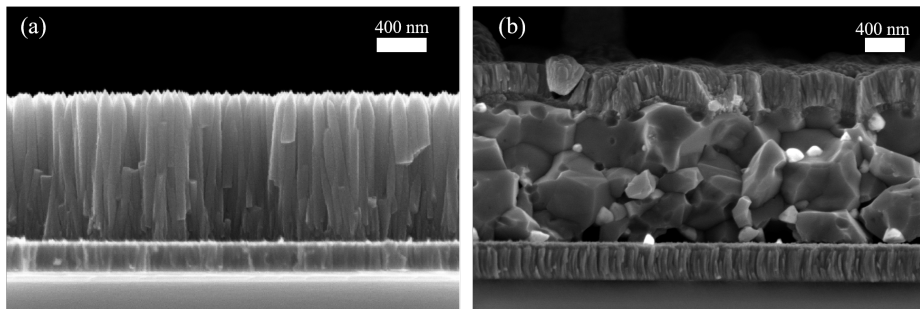


Figure 3.4: SEM images of (a) baseline CZTS sample after precursor deposition and (b) a finished solar cell device structure. The CZTS precursor consists of columnar grain structure. After the chalcogen annealing, the precursor has crystallized into more spherical grain structure.

was evaporated on top the widow layers by e-beam evaporation and individual 0.5 cm^2 cells were obtained with a mechanical scriber. A cross-section SEM image of a finished device structure is shown in Figure 3.4(b).

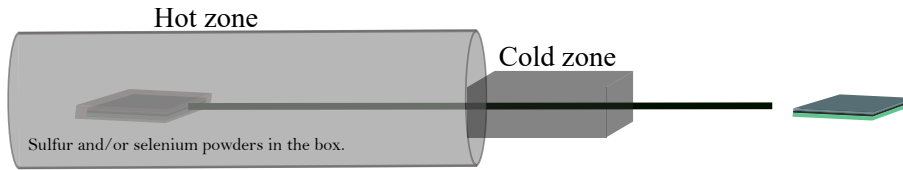


Figure 3.5: The chalcogen annealing setup at the Ångström Solar Center in Uppsala. The sample is placed in a pyrolytic carbon-coated graphite box. Sulfur and/or selenium powders were placed in pockets on each side of the box. The sample is rapidly transferred from a cold zone to a hot zone to initiate the heat treatment.

3.3 Diffusion

Atoms can migrate in solids by diffusion. Diffusion is the net movement of a species from a region of higher concentration to a region of lower concentration. The underlying microscopic process connected to diffusion is the random motion of each atom. If provided sufficient energy in the case of nonuniform concentrations, the concentrations will eventually be uniform due to diffusion. The flux of species in a one-dimensional system, J , along x , can be expressed with Fick's law.

$$J = -D \frac{\partial c}{\partial x} \quad (3.1)$$

Where D is the diffusion coefficient and c is the concentration of the species. For crystalline semiconductors and solids, the species often has to diffuse through a crystal structure. Diffusion of species in solids occurs by a direct exchange of sites between two neighboring atoms or through some point defect in the crystal [87]. The involved point defects can be vacant sites (vacancies) or interstitial sites. Diffusion can also occur along defect structures that are of higher order of dimensionality, such as dislocations, precipitates and cavities. The CZTS thin films evaluated in this thesis are polycrystalline and contain grain boundaries (GBs). Such structures are less ordered than a CZTS single crystal and can provide for more diffusion pathways. In general, the diffusivity in GBs, D' , is expected to be larger than the diffusivity in the grain interior (GI), D [88]. In 1961, Harrison presented three types of diffusion regimes characterized by the influence of GBs and dislocations on the diffusion of a species in a material: Type A, B and C [89]. The three different types are illustrated in the case of columnar GBs in Figure 3.6, inspired by Ref. [87]. In Type A $\sqrt{Dt} \gg d$ is valid, where \sqrt{Dt} is the diffusion length in the GI and d the average grain size (diameter in one dimension). Diffusion occurs both in GBs and GI. Diffusion out from the GBs into the GIs accelerate the macroscopic diffusion. In Type B $\delta \ll \sqrt{Dt} < d/2$ is valid, where δ is the GB thickness. Diffusion in the GI is slow compared to the distance between each GB and diffusion out from the GBs extends the macroscopic diffusivity markedly. In Type C $\sqrt{Dt} \ll d$ is valid. In contrast to Type A, diffusion occurs exclusively in the GBs (GI diffusion is negligible).

The categorization can be utilized when investigating the diffusion of species in thin films. If Type C diffusion, the diffusivity in the GBs can potentially be measured

3. Fabrication of $\text{Cu}_2\text{ZnSnS}_4$ -based solar cells

directly given short penetration depths compared to the thickness of the film and that the concentrations in the GBs are detectable. Type B diffusion can also be characterized by identifying two regions in the depth profile. For example, Na, K and Rb diffusion characterized by Type B and C regimes have been observed for CIGS by diffusing each element into Na-free, K-free and Rb-free CIGS thin films, respectively [90–92]. In addition, the diffusion of radiotracer isotopes of Fe, Cd, Zn, In and Ag in CIGS has been studied [93–97]. Self-diffusion of Se in CZTSe has been investigated by observing the growth of MoSe_2 at the back contact. In Paper III, Se incorporation into CZTS has been examined.

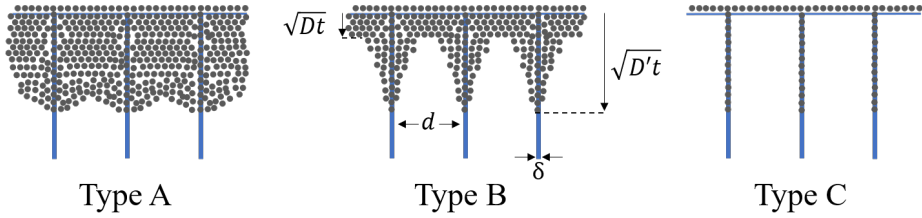


Figure 3.6: The three diffusion regimes proposed by Harrison: Type A, B and C [89]. The diffusion length in the (GI), \sqrt{Dt} , the diffusion length in the grain boundaries (GB), $\sqrt{D't}$, the average grain size, d , and the GB thickness, δ , are annotated.

3.3.1 Accumulation of impurities at grain boundaries

For polycrystalline CIGS and CZTS, impurities, such as Na and O have been observed to accumulate at GBs [69, 91, 98–104]. The relationship between the concentration of species in the GBs, C_{GB} , and the concentration of species in the GI, C_{GI} is known as the segregation factor, s .

$$s = \frac{C_{GB}}{C_{GI}} \quad (3.2)$$

The fraction of the total volume, which represents the grain boundaries, f , is

$$f = \frac{V_{GB}}{V_{GI} + V_{GB}} \approx \frac{V_{GB}}{V_{GI}} \quad V_{GI} \gg V_{GB}, \quad (3.3)$$

where V_{GB} is the volume of the GBs and V_{GI} is the volume of the GI. If a cubic grain structure is assumed, the volume fraction can be expressed as

$$f = \frac{3d^2\delta}{d^3} = \frac{3\delta}{d}, \quad (3.4)$$

where d is the average grain size, and δ is the average GB width. The average concentration in the polycrystalline material, C_{avg} , can be expressed as

$$C_{avg} = fC_{GB} + (1 - f)C_{GI}. \quad (3.5)$$

Here it is assumed that C_{GB} has the same value along all GBs and C_{GI} is uniform in all GIs. C_{avg} as presented in Equation 3.5 is not considered for the case of high densities of dislocations and clusters.

3.4 Strategies for incorporating both sulfur and selenium

Alloying CZTS with Se allows for continuously tuning the band gap between 1.0 and 1.5 eV. For alloying, both chalcogens have to be introduced during the fabrication process. S and Se may be introduced both as part of the precursor and as elemental powders in the chalcogen annealing step. In Papers I-III as well as in Ref. [105], Se is introduced by selenization after deposition of sulfide CZTS precursor and sulfurization. The use of this strategy separates the incorporation of the chalcogens, hence allows for a controlled incorporation of Se. In Paper IV and in Ref. [106], however, four kinds of precursors were evaluated: CZTS, CZTSe, CZTSe-atop-CZTS and CZTS-atop-CZTSe. Additionally, both S and Se powders were present during the chalcogen anneal.

3.5 Impurity incorporation

Na, O and H are the main impurities in most CZTS-based solar cells and were observed in the CZTS thin films relevant for this thesis. Na is introduced from the Na_2O present in the SLG and diffuse through the Mo back contact during thermal treatments [107, 108]. Na is present just 5 minutes after sulfurization at 500 °C as discussed in Paper II. Na distributes throughout the absorber reaching concentrations up to 1 at. %, accumulating especially at dislocations and grain boundaries, observed for instance in Paper VI. O is also an abundant impurity in CZTS. However, there are several sources for incorporation. Possible sources are the SLG, Mo back contact and the precursors all contain O in addition to the air during and after the processing steps. In Paper V, annealing in a sealed tube filled with the isotopic ^{18}O in a furnace after different stages of the CZTS processing allowed for tracing the O through the CZTS baseline process to evaluate the origin of O. In Paper VI, deuterium (D) was introduced by dipping the sample in heavy water. Impurity redistribution after postdeposition treatments is the topic of interest in Paper VI and is discussed briefly in Paper V.

3.6 Controlling the average grain size

As described earlier, the CZTS absorber layer is polycrystalline with grain sizes ranging from tens of nanometer to about one micrometer. Impurities tend to segregate to sites at the grain boundaries and diffusion often occurs along these defective regions. By decreasing the grain size, impurities are presented with more pathways for diffusion. Therefore, variation in the average grain size between samples can be a rewarding approach to separate between diffusion occurring along the grain boundaries and in the grain interior to corroborate findings from SIMS². The grains grow during the chalcogen annealing. By lowering the sulfurization temperature to 500 °C, the average grain size

²For more information on SIMS see Section 4.1

3. Fabrication of $\text{Cu}_2\text{ZnSnS}_4$ -based solar cells

can be controlled by varying the annealing time. This method phases been successfully utilized in Papers III and VI.

Chapter 4

Characterization and modeling of $\text{Cu}_2\text{ZnSnS}_4$ -based solar cells

4.1 Secondary ion mass spectrometry

The principal characterization technique used in this thesis is secondary ion mass spectrometry (SIMS). By sputtering the surface of the layers in the CZTS solar cell structure, spatially elemental information can be obtained for both the constituent elements and impurities. Herein, the principles of operation is explained, displaying the three measurement modes: mass spectrum, depth profile and imaging. Additionally, a careful consideration of the effects of the sputtering process and extraction of secondary ions on the depth profile is laid out, with examples from the samples utilized in this work.

4.1.1 Principles of operation

Secondary ion mass spectrometry (SIMS) is a powerful technique used to investigate the presence and distribution of elements in materials. There are two classes of SIMS instruments, static and dynamic SIMS. In general, static SIMS is used for surface analysis, while dynamic SIMS is used for bulk analysis. In this thesis, the latter is used, thus the following section focuses on dynamic SIMS. An overview over the SIMS setup used in this thesis is shown in Figure 4.1. A primary beam of high energy ions (5 - 15 keV) are directed at the sample of interest, where the impinging ions will transfer energy to the near-surface elements in the sample. The energy transfer may lead to the ejection of atoms and molecules from the material, called sputtering, leaving a crater behind.¹ Some of these particles are ionized and these secondary ions are accelerated by an electrical field towards the secondary column (in the present setup using a voltage difference of 5 kV between the sample and the immersion lens). The probability of elements ionizing positively or negatively depends on the electron affinity and the ionization potential. By changing the polarity of the electrical field, most elements can be detected. Two types of primary ion species can be used in the current setup: O_2^+ and Cs^+ . Generally, O_2^+ ions are used to when the species of interest has a low ionization potential since O is very electronegative. In contrast, Cs^+ primary ions are used when the species of interest has with a high electron affinity since it is very electropositive.

The secondary ions are separated by their mass-to-charge ratio with a mass spectrometer. For dynamic SIMS, both quadrupole or magnetic sector mass spectrometers can be used. The Cameca IMS 7f instrument used to perform SIMS measurements in this thesis uses the latter. First, particles with energies solely due to the sputtering process are filtered out, using an energy sector analyzer (ESA). The ESA is built such

¹For more information on sputtering see Section 3.1

4. Characterization and modeling of $\text{Cu}_2\text{ZnSnS}_4$ -based solar cells

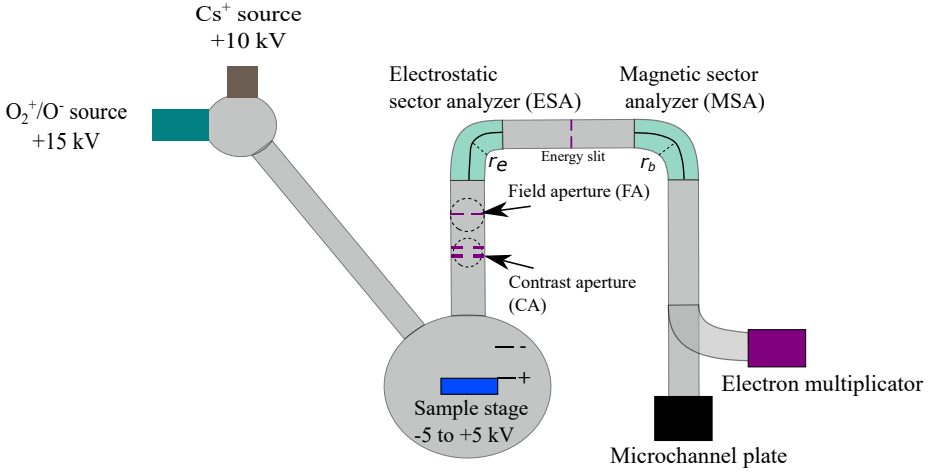


Figure 4.1: The secondary ion mass spectrometry (SIMS) setup used in this thesis, a Cameca IMS 7f instrument. A primary beam of either oxygen or cesium ions are directed onto the sample. The sputtered ions are accelerated by the electrical field provided by the secondary voltage on the sample stage and sent through an electrostatic analyzer (ESA) and a magnetic sector analyzer (MSA) to separate the ions by their mass-to-charge ratio. The separated ions are detected either with an electron multiplier (EM) or a Faraday cup (FC). The microchannel plate is used for alignment.

that an electrical field, E_0 , applies a force to charged particles. E_0 can be chosen such that only charged particles with a certain velocity, v , are sent on a trajectory with a radius, r_e , that allows them to pass the energy slit. The r_e can be expressed as

$$r_e = \frac{mv^2}{qE_0}, \quad (4.1)$$

where m and q is the mass and elementary charge of the ion respectively. After passing through the ESA, ions enter the magnetic sector analyzer (MSA). In the MSA, a magnetic field, B , is applied. The ions will experience a curved trajectory due to the magnetic field with radius, r_b , given their mass, m , elementary charge, q , and their velocity, v , as shown in Equation 4.2:

$$r_b = \frac{mv}{qB}. \quad (4.2)$$

Thus, E_0 and B can be chosen to ensure that only particles with a certain mass-to-charge ratio can pass the ESA and MSA and subsequently reach the detector. A general equation for the mass-to-charge can be deduced by combining Eqs. 4.1 and 4.2.

$$\frac{m}{q} = \frac{(r_b B)^2}{r_e E_0} \quad (4.3)$$

Usually, r_e , r_b and E_0 are kept constant, such that if B is changed, different mass-to-charge ratio will reach the detector. The mass-to-charge ratio has the SI units of kg/C. For mass spectra in SIMS, however, the mass-to-charge ratio is denoted M or m/z , where z is the number of charge in the ions. For example, singly charged $^{16}\text{O}^+$ and doubly charged $^{32}\text{S}^{++}$ have close to the same mass-to-charge ratio and can be challenging to separate, with an M of 15.9949 and 15.9860, respectively. To separate two similar mass-to-charge ratios, a high mass resolution is needed. Mass resolution is defined as the mass-to-charge ratio of the ion of interest divided by the difference in mass-to-charge with respect to the interfering ion, $M/\Delta M$. To separate $^{16}\text{O}^+$ from $^{32}\text{S}^{++}$ a $M/\Delta M > 1802$ is needed. A higher $M/\Delta M$ is obtained by narrowing the exit slit after the MSA. However, a smaller opening also limit the number of ions that pass the MSA, and hence the SIMS intensity is lowered. If the SIMS intensity of interest is orders of magnitude higher compared to that of the interfering element, often low mass resolution is preferred. The SIMS intensity can be controlled by many factors described below.

4.1.1.1 SIMS intensity

The SIMS intensity is measured as the average number of ions observed by the detector per second, and is measured with an electron multiplier (EM) or a Faraday cup (FC). An EM consists of a series of electrodes (dynodes) in a vacuum tube. Once an ion hits the first dynode, the electrode emits secondary electrons which are accelerated onto the next dynode, initiating further electron emissions. A FC is a metal cup that gathers the ions and each ion contribute to formation of one charge carrier in a circuit. The EM has higher precision and accuracy compared to the FC and hence the EM is preferred for precise measurements. However, the FC is used for high SIMS intensities to extend the lifetime of the EM. The SIMS intensity for a given species, I_s , can be expressed as

$$I_s = I_p C_s Y_s \gamma_s T \quad (4.4)$$

where I_p is the primary beam current, C_s is the concentration of the species, Y_s is the sputtering yield, γ_s is the ionization efficiency and T is the transmission of the species through the mass spectrometer. The sputtering yield, Y_s , is the number of sputtered particles per incident primary ion. Of these sputtered particles, a fraction, γ_s is ionized. The ionization efficiency, γ_s is usually expressed as $n^\pm / (n^\pm + n^0)$, where n^\pm is the number of ionized species and n^0 is the number of neutral species [109]. Importantly from Equation 4.4, the SIMS intensity is proportional to the concentration, such that if a sensitivity factor, SF , is provided, SIMS intensity can be converted to concentration as shown in Equation 4.5.

$$C_s = SF I_s \quad (4.5)$$

To account for temporal variations in the sputtering conditions in the chamber (i.e. the shape of the beam and the background pressure) a relative sensitivity factor, RSF , can be used as in Equation 4.6.

$$C_s = RSF \frac{I_s}{I_m}, \quad (4.6)$$

4. Characterization and modeling of $\text{Cu}_2\text{ZnSnS}_4$ -based solar cells

where I_m is the SIMS intensity of a matrix element. Separate *RSF* values are needed for each material, primary ion species and secondary ion polarities. *RSF* values can be obtained by measuring a reference sample where the concentration is known.

The transmission of the species through the mass spectrometer is governed by the aperture sizes of the field aperture (FA) and the contrast aperture (CA), displayed in Figure 4.1. The FA controls the size of the analyzed area, while the CA controls the image contrast.

4.1.1.2 Modes of operation

Mass spectrum A mass spectrum is measured by varying the magnetic field, B , in the mass spectrometer such that different mass-to-charge ratios are detected. A mass spectrum is a convenient method to study which elements are present in the sample. In Figure 4.2, an example of a mass spectrum of a CZTSSe sample is displayed where the mass-to-charge ratio has been varied between 195 and 270. Some selected molecules with Cs^+ and the element of interest have been labeled, often referred to as MCs^+ clusters. Some elements have different isotopes, and hence comprise of different mass-to-charge ratios. Their relative occurrences or abundances serve as a fingerprint for the corresponding element. The fingerprints can be used to identify the elements in the mass spectrum. Most noticeably in Figure 4.2 is the fingerprint of Sn, where the natural abundance of ^{116}Sn , ^{118}Sn and ^{120}Sn are 2 to 3 times higher than ^{117}Sn and ^{119}Sn . Cu and Zn are also recognized by the natural abundance at ^{63}Cu and ^{64}Zn being roughly two times the natural abundance of ^{65}Cu and ^{66}Zn , respectively.

Depth profile The depth profile is the most used mode of operation in this thesis. A selected number of mass-to-charge ratios are chosen, assumed to mainly represent a specific set of elements. While the primary beam is sputtering, B is changed sequentially covering all the selected M values. The output is thus an intensity versus sputtering time, as shown in Figure 4.3(a), where depth profiles of Na is taken from the near surface region of a CZTS sample using O_2^+ primary beam detecting $^{23}\text{Na}^+$ and using Cs^+ primary beam detecting $^{23}\text{Na}^{133}\text{Cs}^+$ and $^{23}\text{Na}^-$. The sputtering rate can also be converted to depth by measuring the depth of the crater after a measurement, or by knowing the sputtering rate or depth of the thin films. An example depth profile of common elements in CZTS is displayed in Figure 4.3(b).

Imaging By tracking the position of the primary beam on the sample, i.e. synchronizing the primary beam raster with the detector, an image can be constructed. The corresponding mode of operation is known as SIMS imaging. The image reveals lateral information about an element's distribution. In Figure 4.4(a), $^{23}\text{Na}^+$ has been measured on a $20 \times 20 \mu\text{m}^2$ grid using the smallest beam size available in the instrument, roughly $1 \mu\text{m}$ for a CZTSSe sample, presented in Paper VI. The minimal beam size achievable limits the spatial resolution which can be obtained. The grid size is 128 pixels \times 128 pixels where each pixel varies between 0 and 11 counts. The distribution of Na is nonuniform and represents the Na distribution at a depth of about 200 nm from the surface. If the images are measured continuously, a 3D image can be shown for the

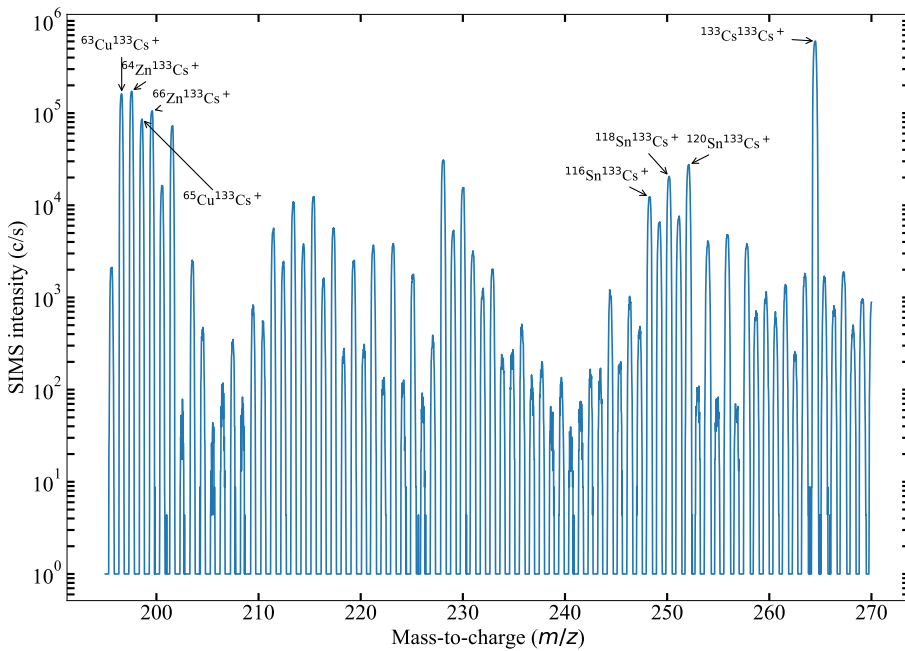


Figure 4.2: An example mass spectrum of a $\text{Cu}_2\text{ZnSn}(\text{S},\text{Se})_4$ sample over mass-to-charge ratios ranging from 195 to 270. The magnetic field, B , is varied over a range of values corresponding to different mass-to-charge ratios. Notable peaks in the spectrum have been labeled. Different isotopes serves as a fingerprint for the corresponding elements, for example Cu, Zn and Sn.

element's distribution. This is displayed in Figure 4.4(b). The 3D image reveals a spatially nonuniform Na distribution in the sample.

4.1.2 Considerations for elemental depth profiles of $\text{Cu}_2\text{ZnSnS}_4$

The SIMS intensity measured is a result of many factors, as indicated by Equation 4.4. Especially, the sputtering yield, Y_s , and the ionization efficiency, γ_s , are affected by the analysis conditions. The parameters can be influenced by the primary ion impact energy, angle and species, the sputtered material's composition, roughness and conductivity, the extraction voltage and the air ambient in the chamber. The sputtering process is very complex and is not fully understood [110]. In this subsection, common profile issues relevant to CZTS, previously reported for SIMS [109], are considered in the case of elemental depth profiles.

4.1.2.1 Matrix effects

The sputtering yield and/or the ionization efficiency depends on the material being investigated, the so-called matrix effect. The linear relation between the SIMS intensity

4. Characterization and modeling of Cu₂ZnSnS₄-based solar cells

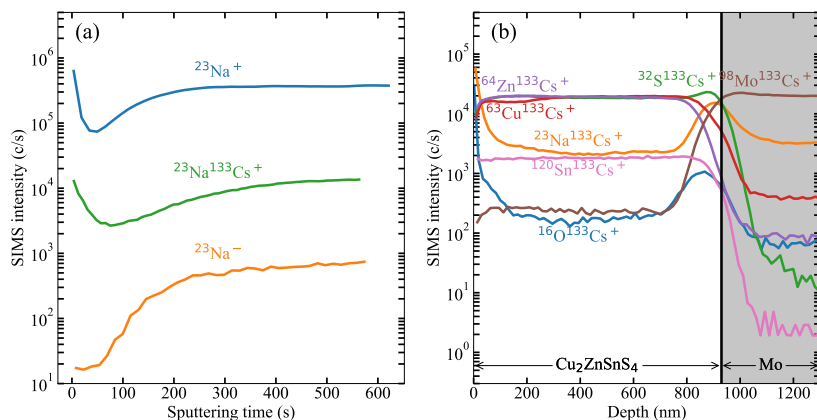


Figure 4.3: (a) SIMS intensity of Na in the near surface region of a CZTS sample versus sputtering time showing the variation between different primary ions and samples secondary polarities. ²³Na⁺ is measured with the O₂⁺ source, ²³Na¹³³Cs⁺ is measured with the Cs⁺ source detecting positive ions and ²³Na⁻ is detected with the Cs⁺ source detecting negative ions. (b) An example depth profile on CZTS and Mo detecting MCs⁺ ions from the constituent elements together with Na and O

and the concentration of an element assume that all other factors, as stated in Equation 4.4, are constant. However, this may not always be true. The species affected by the matrix effect are not only limited to the constituent elements, but also impurities. Generally, if the concentration of a non-constituent element becomes large, typically > 1 % or if there is a change of phase, matrix effects needs to be considered. Examples for CZTS are alloying with Se, off-stoichiometric conditions, secondary phase formation near the surface and the back contact. To mitigate the matrix effect, the detection of the species of interest in cluster with Cs (MCs⁺) have been successfully applied in several material systems [111–115]. Since the sample is bombarded with Cs⁺ ions, the ion cluster formation does not necessarily depend on the ionization of the M atom and hence, the number of MCs⁺ ions are independent of the matrix. Although no significant matrix effects have been observed for species measured in the samples in this work, both O₂⁺ detecting M⁺ ions and Cs⁺ primary beam detecting MCs⁺ ions have been conducted for most sample sets. The matrix effect in samples with a sulfur-selenium gradient in CZTS is one of the challenges discussed in Paper I as well as briefly in Section 5.1.

4.1.2.2 Sputter-induced and surface effects

In addition to the removal of atoms from the surface, the sputtering process induces damage to the atomic layers deeper into the sample [116]. The primary ions hit the

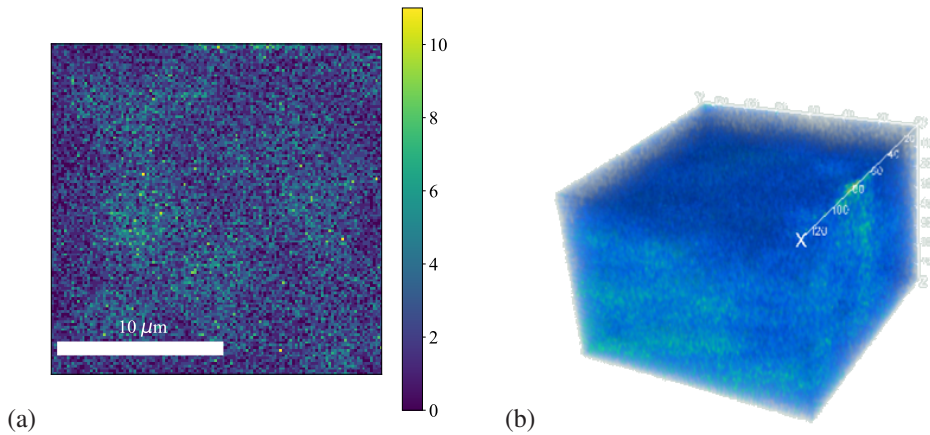


Figure 4.4: SIMS image depth profile example of Na. (a) A SIMS image with a $20 \times 20 \mu\text{m}^2$ at a depth of about 200 nm. The image indicate nonuniform Na distribution. (b) A series of continuous SIMS images accumulated into a 3D image displaying the spatial distribution of Na.

lattice atoms, causing a cascade of collisions. The sputtering process produces extrinsic defects and form a charged surface, which may drive diffusion of atoms deeper into the sample. Additionally, the sputter yield at the surface is expected to increase [109]. For CZTS and CIGS, light impurities, such as Na and O, are especially exposed to such effects due to high concentrations at the surface [98, 117]. The effect of the sputter-induced and surface effects in CZTSSe has been investigated by measuring depth profiles from both sides of the CZTSSe layer. To sputter from the backside, the CZTSSe layer was lifted off. The lift-off was conducted by applying a SLG piece on top of the CZTSSe layer with superglue in-between. After 24 hours the SLG was torn off, breaking the CZTSSe and the Mo interface. An example Na depth profiles from both sputter directions are shown in Figure 4.5. The profiles are fairly similar indicating that the profile is not distorted due to sputter-induced effects. There is, however, a higher intensity at the first couple of measurement points for both measurements, attributed to surface effects.

4.1.2.3 Interfaces

It is a challenge to measure the elemental distribution at interfaces accurately with SIMS due to the nature of the sputtering process. Surface reconstruction as well as segregation of impurities are important when comparing SIMS measurements performed in the bulk with SIMS measurements performed at an interface of a sample. Additionally, due to a mixing region and roughness of the sample, in interface regions, both matrices are being sputtered simultaneously, which may result in a significant change in the ionization efficiency. Consequently, it is more challenging to properly quantify SIMS intensities obtained from the interface compared to regions measured in the bulk. This is of particular importance for CZTS, since CZTS solar cells consist of several layers:

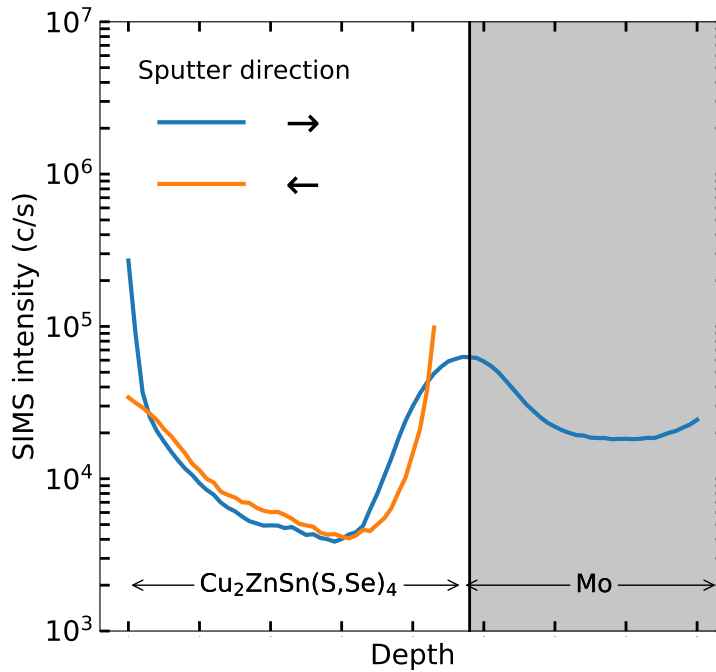


Figure 4.5: SIMS depth profile showing the intensity of Na from two sputter directions on the same sample. The profiles are similar indicating no significant distortion of the Na depth profile due to sputter-induced effects. An increased SIMS intensity at the surfaces for both measurements are attributed to surface effects.

ZnO, CdS, CZTS, Mo on top of SLG. For most of the SIMS measurements in this thesis, the CZTS layer has been of interest and thus the ZnO and CdS layers have not been deposited prior to SIMS measurements. Here, the CZTS/Mo is of interest. Figure 4.6 shows the $^{23}\text{Na}^+$, $^{120}\text{Sn}^+$ and $^{98}\text{Mo}^+$ signals for two of the samples presented in Paper VII using an O_2^+ primary beam. The sample with a rough surface exhibits a larger interface region between CZTS(e) and Mo compared to that of the sample with a smooth surface.

4.1.2.4 Uncertainties and spatial variations

Taking into account the considerations in the preceding subsections, there will always be uncertainties related to the SIMS intensity. As a benchmark, we regard this to be $\sim 10\%$. Additionally, since SIMS is a destructive technique and each measurement leave a crater behind, it impossible to remeasure the same spot. Thus, spatial variations in each sample and between samples is extremely important to keep in mind when interpreting SIMS measurements. For CZTS in particular, it is known to have spatial variations both constituent elements [118] and for sodium [119]. The CZTS samples measured in this thesis have noticeably spatial nonuniformities of impurities on the micrometer and

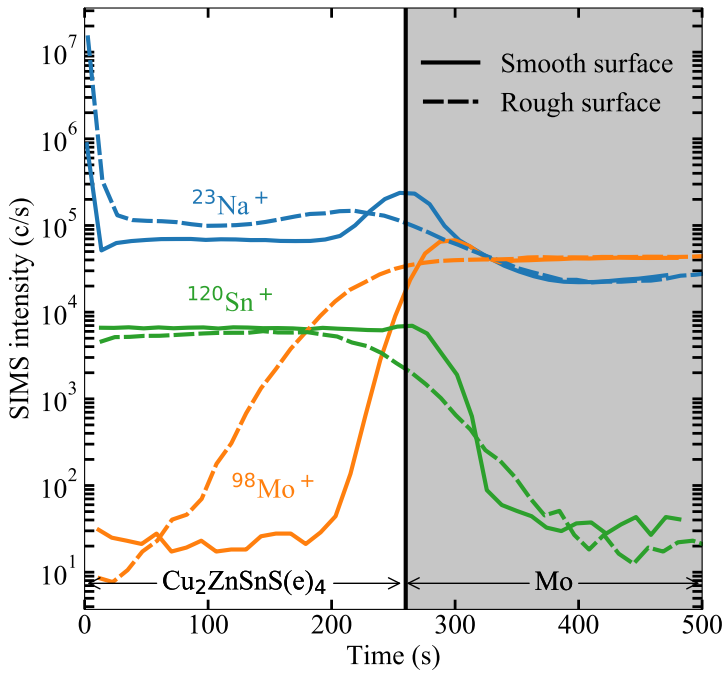


Figure 4.6: $^{23}\text{Na}^+$, $^{120}\text{Sn}^+$ and $^{98}\text{Mo}^+$ signals for two of the samples presented in Paper VII using an O_2^+ primary beam. The sample with a rough surface exhibits a larger interface region between CZTS(e) and Mo compared to that of the sample with a smooth surface.

nanometer scale, as discussed in Paper VI. To mitigate the effect these variations had on the SIMS measurements, craters were made as close as possible to each other after each treatment. In Figure 4.7, depth profiles of selected elements for three measurements on the same sample are shown, where craters are located close to each other, while the last is located roughly 1 mm away. Such observations have been observed on several samples. The origin could be inhomogeneities in the SLG as discussed in Ref [119].

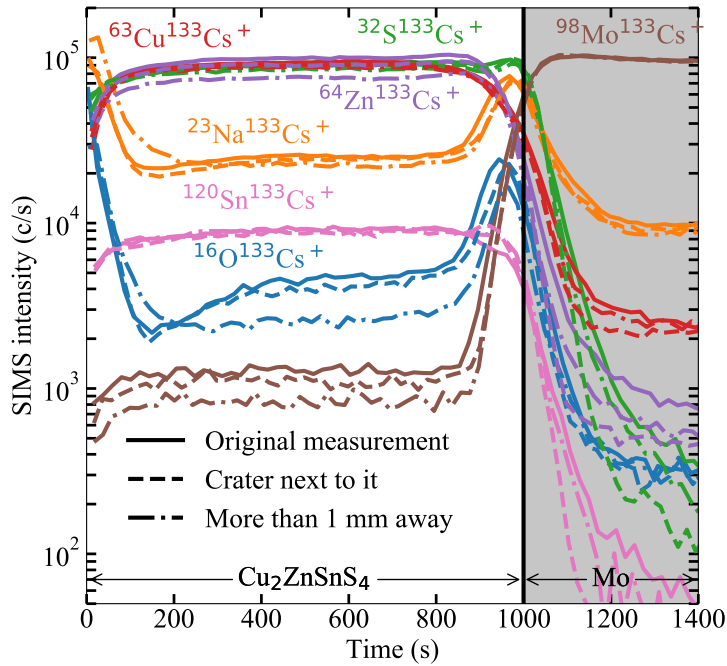


Figure 4.7: SIMS depth profile of different elements for three different craters on the same sample illustrating the existence of area to area variation. Two craters were located next to each other and resulted in very similar depth profiles for all elements, however, the measurement from the crater located >1 mm away had slightly different $^{16}\text{O}^{133}\text{Cs}^+$, $^{23}\text{Na}^{133}\text{Cs}^+$ and $^{64}\text{Zn}^{133}\text{Cs}^+$ depth profiles.

4.2 X-ray diffraction

X-ray diffraction (XRD) is a technique used to measure the crystal structure of semiconductor thin films and crystals in general. Incoming X-rays are directed at the sample and the scattered X-rays are detected. The X-rays may interact with the atoms in the crystal structure by photoionization, Compton scattering and Thomson scattering with the latter being elastic and the one made use of for XRD [120]. For certain conditions determined by the energy and angle of the incoming X-ray, the angle of the detector and the distance between lattice planes in the thin film, constructive interference between the scattered waves in the different planes occurs. Scanning over several angles reveals structural information about the sample.

The most common measurement mode for XRD is a $\theta/2\theta$ scan. Here, both the X-ray source and the detector moves such that the angle normal to the surface is kept the same during the scan. An advantage is that the scan is made over all lattice spaces. A disadvantage is that the lattice planes must be perpendicular to the surface plane. For polycrystalline thin films, several planes do not satisfy this criterion and the measurement volume is limited and hence the signal intensity is lowered. For such samples, grazing

incidence mode (GIXRD) can be utilized. For GIXRD, a chosen angle of incidence for the incoming X-ray is selected, often low angles such that the measurement volume is in the thin film. The measurement mode also allows for obtaining depth-resolved information. Grains that have only preferential orientation normal to the surface, however, cannot be detected with GIXRD, for instance SnS secondary phases observed in this thesis and similar samples fabricated at the Ångström Solar Center [121]. The XRD measurements gathered using the Siemens D5000 diffractometer was performed by N. Ross whilst those gathered with the Bruker AXS D8 Discover was performed by the author.

4.3 Scanning electron microscopy

Instead of using light as a probing source such as traditional optical microscopes, an electron microscope utilize electrons. The wavelengths of the electrons are determined by the particle-wave duality. Focused electrons are accelerated towards a sample and interacts with its atoms. As a consequence of the interaction, both photons and electrons are emitted from the sample. The secondary electrons emitted can be detected and the intensity of the signal produced by the secondary electrons is dependent on the topology and type of elements on the sample. Thus, by scanning the focused electron beam over an area and detecting the secondary electrons, topological information can be gathered. This technique is known as scanning electron microscopy (SEM). For CZTS, this can be either on top of the sample (top view) or by breaking the sample in two and scanning the side of the sample (cross-sectional view). An example SEM top-view image of a CZTS sample measured with a JEOL JSM-IT300 with a 5 kV accelerating voltage is shown in Figure 4.8.

4.3.1 Energy dispersive X-ray spectroscopy

The interaction between the electrons accelerating onto the sample does not only produce secondary electrons. For instance high energy X-rays are produced by electrons receiving enough energy to move between energy levels in the electron shells. The energies of the X-rays are determined by the constituent elements in the region where the electrons impinge. Each element's X-ray emission characteristic is determined by possible transitions between energy levels. A p-i-n semiconductor detector can be installed in the microscope, where the incoming X-rays can be absorbed producing electron-hole pairs that are separated to form a current. The number of electron-hole pairs formed (i.e. the current) corresponds to the energy of the X-ray. By counting several incoming X-rays, an energy spectrum can be obtained. This method is known as energy dispersive X-ray spectroscopy (EDS or EDX). In combination with SEM, a spatial map with a selected energy range can be extracted providing spatial elemental information of the sample studied. In Figure 4.9, an SEM cross-section image of an example CZTSSe sample is shown with the S $K\alpha 1$ (4.9(b)) and the Se $L\alpha 1/2$ (4.9(c)) transitions. $K\alpha 1$ is the de-excitation from the L to the K shell for S, while $L\alpha 1/2$ is the transition from the M to the L shell for Se [122]. In the EDX images, there is a difference in the $[S]/([S]+[Se])$ ratio between different grains. The SEM images gathered using the

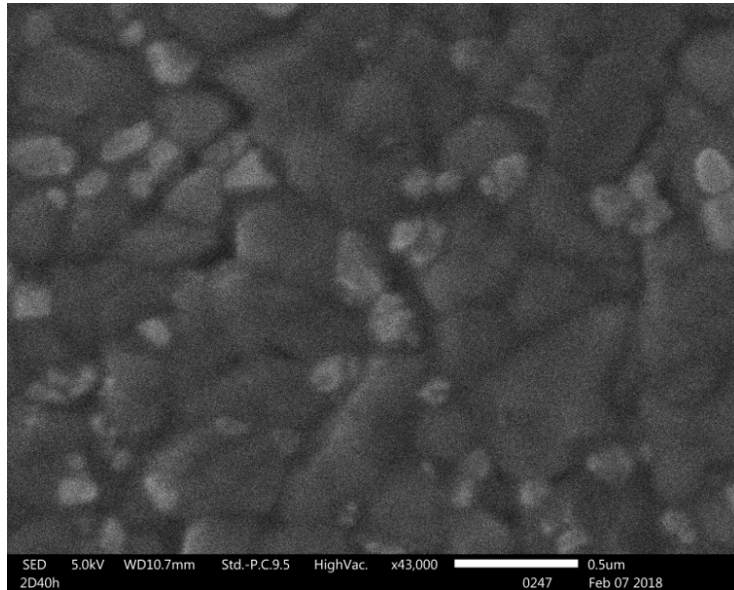


Figure 4.8: An example SEM top view image of a CZTS measured with a JEOL JSM-IT300 microscope. The SEM image shows the polycrystalline structure of CZTS, with small white grains being SnS secondary phases.

Zeiss Leo 1550 were performed by N. Ross and S. Englund, however, the measurements using the JEOL JSM-IT300 was performed by the author.

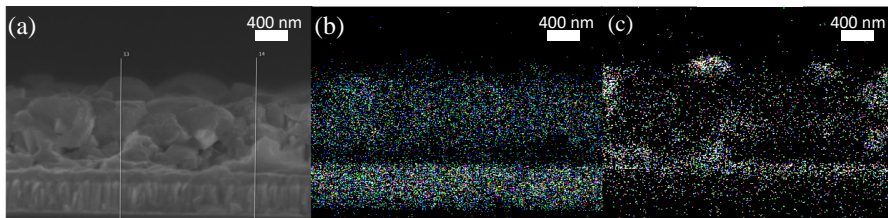


Figure 4.9: Scanning electron microscopy energy dispersive X-ray spectroscopy (SEM-EDX) image of an example CZTSSe sample. (a) SEM cross-section, (b) S $K\alpha 1$ signal and (c) Se $L\alpha 1/2$.

4.3.2 Time-of-flight-energy elastic recoil detection analysis

Time-of-flight-energy elastic recoil detection analysis (ToF-ERDA) is an ion beam technique used to acquire elemental depth profiles of thin films. The technique is in

principle absolute. Heavy ions, for instance, I^{8+} , are accelerated onto the sample from an angle hitting the surface and forward-scattering sample atoms [123]. The ionized sample atoms are sent through two carbon foil detectors measuring the time of flight of the ions to a silicon detector or a gas ionization chamber [124, 125]. The energy and ToF can be plotted to separate out the elements in the sample. With available analysis software, CONTES, the output can be converted to depth as shown in Figure 4.10 [126]. The ToF-ERDA measurements presented were performed by D. Primetzhofer with the presence of the author and the analysis itself was carried out by the author.

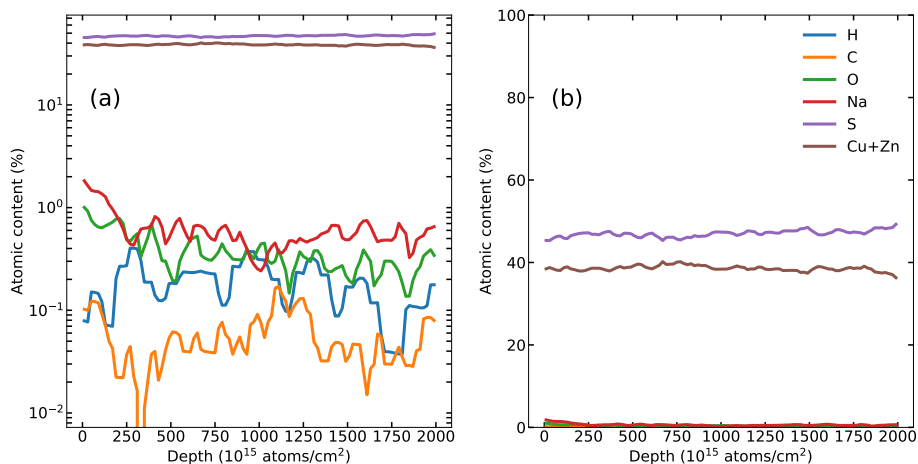


Figure 4.10: Elemental depth profile measured with ToF-ERDA at the Tandem Accelerator at Uppsala University: (a) on a logarithmic scale and (b) on a linear scale.

4.4 Atom probe tomography

Atom probe tomography (APT) provides elemental three-dimensional information of elements in materials with high spatial resolution. The technique is based on the principle of field ionization, a strong electrical field removes an electron from an atom in a gas close to a surface, hence ionizing the atom [127]. A small tip (for instance $100 \text{ nm} \times 100 \text{ nm} \times 200 \text{ nm}$) is cut out from a sample using a focused ion beam. The tip is coated, transferred to a chamber and pumped down to ultra high vacuum conditions (10^{-10} Torr) at a temperature of around 50 K. In the chamber, the front of the tip is heated with a laser. The combination of the laser and a strong electrical field present at the surface allows the atoms on the surface to desorb and ionize. The pulsing of either the laser or the electrical field allows for controlled removal of surface atoms, sending them through a time-of-flight mass spectrometer. The trajectory of the ions is determined by their original position, allowing for spatially resolved detection of atoms from a solid. The nature of the field evaporation results in many highly charged ions, such as $^{64}\text{Zn}^{+++}$, which overlaps in mass-to-charge ratio with $^{32}\text{S}^{++}$ and $^{16}\text{O}^{+}$. The overlapping mass-to-charge ratios cannot be resolved and hence these elements are

challenging to separate. The APT measurements presented in Paper VI were performed by H. Aboufadel.

4.5 Density functional theory

In Paper V, the binding energy between neutral defects Na and O in kesterite CZTS is calculated using the density functional theory (DFT). Here a brief overview of DFT and binding energy calculations are presented. More detailed overviews are given in for instance Refs. [128–130].

DFT is a method to calculate ground state properties of a full system using only the density of the electrons and it is based on the Hohenberg-Kohn theorems [131]. However, it cannot predict single-electron properties. Moreover, the Born-Oppenheimer approximation simplifies the wave function into one Schrödinger-like equation representing the electrons and one representing the nuclei. The Hartree product approximates the electronic wave function to be a product of individual electron wave functions, reducing the dimensionality down to spatial coordinates. Now, the Kohn-Sham approach can be used to solve the DFT using the auxiliary single-electron eigenfunctions. The Kohn-Sham equation [132] in conjunction with DFT can map the many-electron problem into many single electron equations with an effective potential, separating the energy functional into a known part (that one can calculate) and an exchange-correlation part. For practical purposes, the problem boils down to employing a sufficiently accurate approximation of the exchange-correlation part of the functional and find a self-consistent solution of the ground-state electron density.

To approximate the exchange-correlation functional, the well-known exchange-correlation potential for a uniform electron gas can be used, known as local density approximation (LDA). Another functional being used is the generalized gradient approximation, which depends on the local gradient in the electron density. In Paper V, the Perdew-Burke-Ernzerhof functional (PBE) was used, which is one variant of the GGA [133]. The electron density can be calculated for a chosen exchange-correlation functional. For analyzing pristine materials, one uses a single primitive unit cell and the Kohn-Sham equation is solved in the reciprocal space to include the periodic condition. For more complex system, i.e, compounds with defects, one often constructs a larger cell volume that contain the defects, but allows a periodic structures of the defects and instead tries to reduce or compensate the defect-defect interactions.

4.5.1 Binding energy

As a result of DFT calculations, the total energy of a larger cell volume (supercell) can be calculated. To find the binding energy between two defects, the total energy of four configurations need to be calculated. The binding energy is defined as the difference between the total energy of the supercell with the defects separately and the total energy with the defects and a pristine compound, where $E_{tot}(D_1)$ is the total energy of the supercell containing isolated defect 1 and $E_{tot}(D_2)$ is the total energy of the supercell

containing isolated defect 2, $E_{tot}(D_1 + D_2)$ is the total energy of the supercell containing both defects 1 and 2, $E_{tot}(\text{pristine})$ is the supercell with the pristine compound and E_b is the binding energy between the two defect in the configuration.

$$E_b = E_{tot}(D_1) + E_{tot}(D_2) - E_{tot}(D_1 + D_2) - E_{tot}(\text{pristine}) \quad (4.7)$$

A binding energy of ~ 0.8 eV, with the two defects in a neighboring configuration, indicates that clustering of the two will occur across all processing temperatures. The DFT calculations presented in Paper V was performed by K. V. Sopiha.

Chapter 5

Summary of results

In this chapter a summary of the results obtained in this thesis is presented. The majority of the summary is based on results presented in the appended papers. Here, the main scientific challenges tackled are (1) to understand Se diffusion in CZTS and identify the feasibility of establishing a $[S]/([S]+[Se])$ gradient by alloying CZTS with Se and how to measure this efficiently with SIMS and (2) to observe impurities in CZTS, understanding how they are introduced and diffuse in the solar cell structure. These fundamental challenges are motivated by the more critical question on how CZTS can be utilized most efficiently as a solar cell absorber, and thus an important aspect has been to study CZTS samples with such quality that they would produce efficient solar cells. First, efforts on band gap grading of CZTS by alloying with Se is presented, combining results from Papers I-IV. Second, impurities in CZTS are studied and the interplay between sodium and oxygen is demonstrated.

5.1 Band gap grading with Se

As described in Chapter 2, the band gap of CZTS can be modified by alloying with other elements. One possibility is to exchange S with Se, which enables band gap tuning in the range between ~ 1.5 and 1.0 eV for pure sulfide and selenide, respectively. It may be beneficial for solar cell device performance to vary the $[S]/([S]+[Se])$ ratio with depth. In this work, strategies to achieve such a band gap grading and identifying the $[S]/([S]+[Se])$ ratio using SIMS were evaluated. A strategy to achieve such a gradient is to controllably incorporate Se into grains only containing CZTS. Solar-grade CZTS absorbers are formed during a two-step process by depositing a precursor and subsequently annealing in chalcogen atmosphere.¹ The Se can potentially be incorporated by annealing in Se atmosphere either after the precursor deposition or after the sulfurization. This Se incorporation strategy was employed in Ref. [105], where the samples were annealed in Se for 10 minutes before and after sulfurization at 350, 400 and 450 °C. In addition, the 450 °C selenization after sulfurization was also performed for 20 and 30 minutes. GIXRD diffractograms showed a selenide CZTSSe (112) peak being present for shallow incident angles and a sulfide CZTS (112) peak for deeper incident angles, indicating a CZTSSe phase near the surface and a CZTS phase deeper into the sample. Cross-section SEM-EDX images revealed that the Se was distributed in some grains only, where the increase in Se corresponded with a lowering of the S signal. However, SIMS depth profiles exhibited a more gradual $[S]/([S]+[Se])$ gradient, displaying more Se towards the front and more S towards the back as one would expect from a controlled incorporation of Se.

¹The fabrication process is described in more detail in Chapter 3

5.1.1 Study $[S]/([S]+[Se])$ gradient with secondary ion mass spectrometry

In Paper I, selected samples from the experiment described above were analyzed in detail using SIMS. The impact of matrix effects on depth profiles and the use of SIMS image depth profiling were studied. Conventional SIMS depth profiles were measured using both O_2^+ primary beam detecting M^+ ions (O_2^+ depth profile) and Cs^+ primary beam detecting MCs^+ ions (MCs^+ depth profile). Interestingly, both depth profiles showed a linear dependence between the S and Se intensities in the region a few hundred nm below the surface and above the Mo back contact, displaying no evidence of matrix effects in this region. Near the interfaces, however, the linear dependence did no longer hold, and the discrepancy is attributed to either matrix effects or the formation of secondary phases. Nevertheless, the results indicate that a change in the $[S]/([S]+[Se])$ ratio does not drastically change the secondary ion yield in the SIMS measurements.

SIMS image depth profiles recorded with about a micrometer beam diameter revealed that S and Se were not uniformly distributed spatially over a $20 \times 20 \mu m^2$ area as displayed in Figure 5.1. The inhomogeneities confirmed the results from SEM cross-section images and XRD spectra that the Se in-diffusion during the selenization was not uniform [105], and corroborated that the inhomogeneity is also on the micrometer scale. SIMS image depth profiling proved to be a suitable measurement technique to reveal nonuniformities on a micrometer scale and was demonstrated to be a novel approach to study the Se incorporation into CZTS. The results from Paper I establish a foundation for SIMS to be used as a technique to study selenium gradients in CZTSSe.

5.1.2 Recrystallization rather than in-diffusion

In Paper II, the practical limitations regarding selenium annealing of co-sputtered CZTS precursors to achieve a band gap gradient were evaluated. A series of annealing experiments were conducted consisting of a sulfurization step at $500^\circ C$ followed by selenizations at $425^\circ C$ for variable duration. For short annealing times of sulfurization and selenization, samples exhibited more advanced crystallization towards the back contact, corresponding to an increase in Se and Na content, as shown with SIMS. For longer selenization times at $425^\circ C$, more Se was incorporated and $[S]/([S]+[Se])$ gradients were observed with SEM-EDX. The samples exhibited nonuniformly distributed chalcogen content between grains similar to that observed in Ref. [105] and Paper I. Consequently, there is a limitation in the chalcogen annealing setup to obtain controlled incorporation of Se during selenization before nonuniform sulfide and sulfoselenide grains are formed.

The origin of the nucleation of Se in CZTS and the crystallization of sulfoselenide grains were studied in Paper III. Low temperature selenizations at 337, 360 and $409^\circ C$ for 30 minutes were performed on CZTS absorbers with different grain sizes. After selenizations at 337 and $360^\circ C$, the SIMS intensity of Se increased slightly in the bulk and more pronounced at the CZTS/Mo interface. After selenizations at $409^\circ C$, the SIMS signals for Se increased by one order of magnitude in the bulk corresponding to a

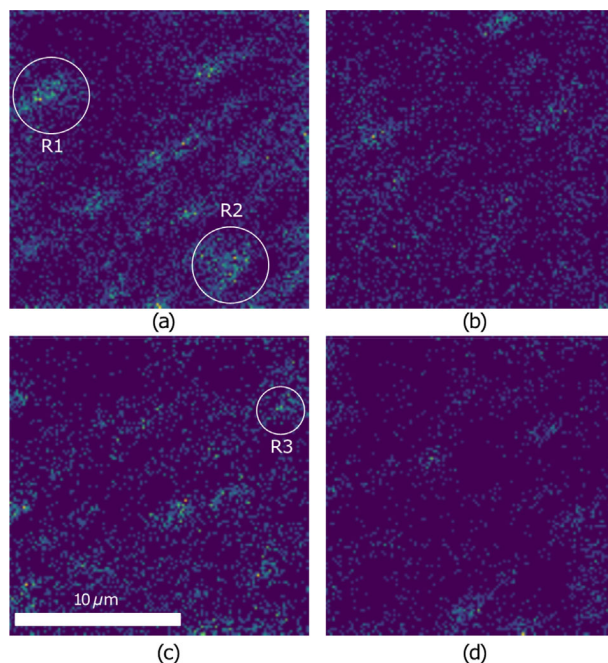


Figure 5.1: $^{80}\text{Se}^+$ signal acquired with SIMS image depth profiling at four different distances to the surface; (a) 20 nm, (b) 100 nm, (c) 250 nm and (d) 350 nm, and with a raster of $20 \times 20 \text{ nm}^2$. Reprinted from Paper I with permission from Wiley.

decrease in S signals as displayed in Figure 5.2.

The increase of Se concentration at the CZTS/Mo interface after selenization at 360°C inversely correlates with grain size corroborating that the accumulation is promoted by GB diffusion. The Se SIMS intensities were increasing with depth for all grain sizes, similar to that observed for shorter anneals at 425°C in Paper II. After the 409°C selenization, however, a two distinct peaks corresponding to the (112) of pure $\text{Cu}_2\text{ZnSnS}_4$ and $\text{Cu}_2\text{ZnSn}(\text{S}_{0.25},\text{Se}_{0.75})_4$ was observed with $\theta/2\theta$ high resolution indicating the formation of a new sulfoselenide CZTSSe phase.

Interestingly, the peak-like SIMS intensity for Na, observed at the CZTS/Mo interface before the 409°C selenization, moved a few 100 nm into the bulk, to the depth where a step in the Se intensity was observed as displayed in Figure 5.3. The behavior supports that Na promotes the crystallization of CZTSSe grains during the selenization corresponding to the behavior of Na observed in Paper II. The increased Se intensity could be related to growth of MoSe_2 at the back contact, however, no evidence for increase of MoSe_2 was found with SIMS, XRD or cross-section SEM was found to support the growth of such a layer after the 409°C selenization.

5. Summary of results

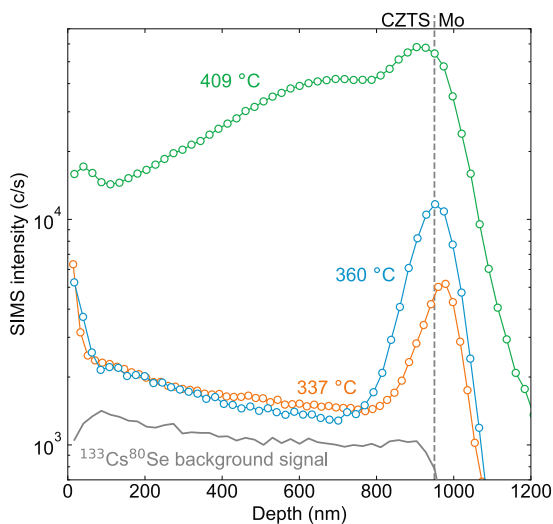


Figure 5.2: SIMS intensity for $^{80}\text{Se}^{133}\text{Cs}$ for sample B which was sulfurized at 500 °C for 20 min followed by selenization at 337 °C (orange circles), 360 (blue circles) and 409 °C (green circles) for 30 min. Se accumulates at the back contact after selenization at 337 °C and the accumulation is greater after selenization at 360 °C. After selenization at 409 °C Se has heavily been incorporated into the CZTS layer and the signal has increased by around one order of magnitude. Reprinted from Paper III with permission from Elsevier.

5.1.2.1 Discussion

For co-sputtered precursors studied in this thesis, controlled incorporation of Se into CZTS to form a band gap gradient proved challenging. During selenization, growth of sulfoselenide CZTSSe grains was dominant. The growth was promoted by the existence of Na in the CZTS layer. As such, incorporating Na into the film limits the range of temperatures where Se does not recrystallize. In Paper III, we suggest that controlled Na incorporation or sulfurization of selenide CTZSe precursors can potentially provide pathways into a more controlled band gap grading by alloying with S and Se.

5.1.3 Optimization of grain growth with S and Se

In Ref. [106] and Paper IV, optimization of solar cell devices is performed by investigating the incorporation of S and Se in the precursor and during the chalcogen anneal. Here, the purpose was not limited to the effects on the band gap grading of Se/S incorporation, but also to judge the impact on properties for solar cell device performance. Four precursor compositions were investigated: $\text{Cu}_2\text{ZnSnS}_4$, $\text{Cu}_2\text{ZnSnSe}_4$, $\text{Cu}_2\text{ZnSnSe}_4$ -atop- $\text{Cu}_2\text{ZnSnS}_4$ and $\text{Cu}_2\text{ZnSnS}_4$ -atop- $\text{Cu}_2\text{ZnSnSe}_4$. In Ref. [106], the chalcogen mass ratios, in addition to Ar pressure during the anneal and the annealing temperature, were varied. It was found that the chalcogen present in the precursors was

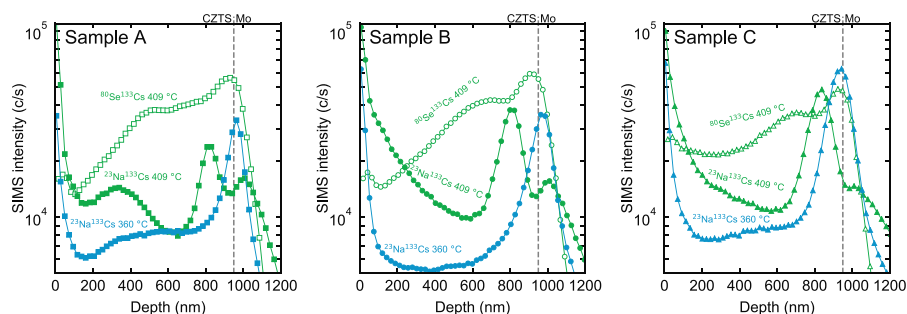


Figure 5.3: SIMS intensity for $^{23}\text{Na}^{133}\text{Cs}$ (closed markers) for samples A, B and C which was sulfurized at 500°C for 10, 20 and 40 min respectively from the same precursor followed by a selenization at 360°C (blue) and 409°C (green) for 30 min. The $^{80}\text{Se}^{133}\text{Cs}$ signals after the Se anneal at 409°C is displayed as green open markers. The peak intensity has shifted from the Mo layer close to the CZTS/Mo interface to more inside the CZTS layer where Se has a local step. Reprinted from Paper III with permission from Elsevier.

replaced by the chalcogen present during the anneal, unless the anneal atmosphere is highly sulfur deficient. The annealing condition "6", corresponding to 5 mg of S and 50 mg of Se in the graphite box, was found to yield solar cells with PCE from ~ 6.5 to 7.3 % regardless of the initial precursor. The chalcogen mass ratio was used as the baseline for further study in Paper IV. The elemental distribution during the ramp up during annealing condition "6" with a mixed CZTSe-atop-CZTS precursor was studied in ex situ with SIMS. As discussed in Section 3.2, the temperature during the chalcogen anneal ramps up to 580°C in about 90 seconds. For the present study, the samples were removed from the furnace during the ramp up at 400, 450 and 500°C and subsequently cooled down quickly. SIMS depth profiles were measured on a non-annealed precursor in addition to the three partially annealed samples as displayed in Figure 5.4.

An increase of S and a decrease of Se content were observed in the CZTSe top layer at 400°C , indicating in-diffusion of the chalcogens already at this temperature during the temperature ramping. Likewise, an increase in Se was observed in the CZTS bottom layer and at the CZTS/Mo interface. Additionally, the Na intensity at this temperature, as observed by SIMS, increases and is evenly distributed with depth except for accumulation at the CZTSe/CZTS interface as well as the CZTS/Mo interface. The SIMS depth profiles after the samples were taken out at 450 and 500°C indicate that the distinction between the two layers is nearly removed during the ramp up and corresponding SEM images reveal that the precursor starts to crystallize, most noticeably in the CZTSe precursor layer. Both chalcogen species accumulate at the CZTS/Mo interface after the ramp up to 500°C . This marks the initial stage for the formation of $\text{Mo}(\text{S},\text{Se})_2$ observed after a 3 minute anneal at 560°C in cross-sectional SEM images. The annealed CZTSe-atop-CZTS precursors produced rougher surfaces compared to the CZTS-atop-CZTSe precursors. However, the annealed CZTS-atop-CZTSe precursors promoted formation of a secondary phase $\text{Zn}(\text{S},\text{Se})$ at the

5. Summary of results

surface. Based on these observations, a model for the growth of the absorber was postulated. Further, crystallization of CZTSSe grains occurs faster in the CZTSe precursor promoting the formation of larger grains. The slower crystallization of the CZTS leads to the formation of smaller as well as flatter grains and promotes the transport of excess Zn from the CZTSe precursor to form Zn(S,Se) secondary phases. Based on the results, another model was developed for the effects of the chalcogen partial pressures during the anneal on the growth.

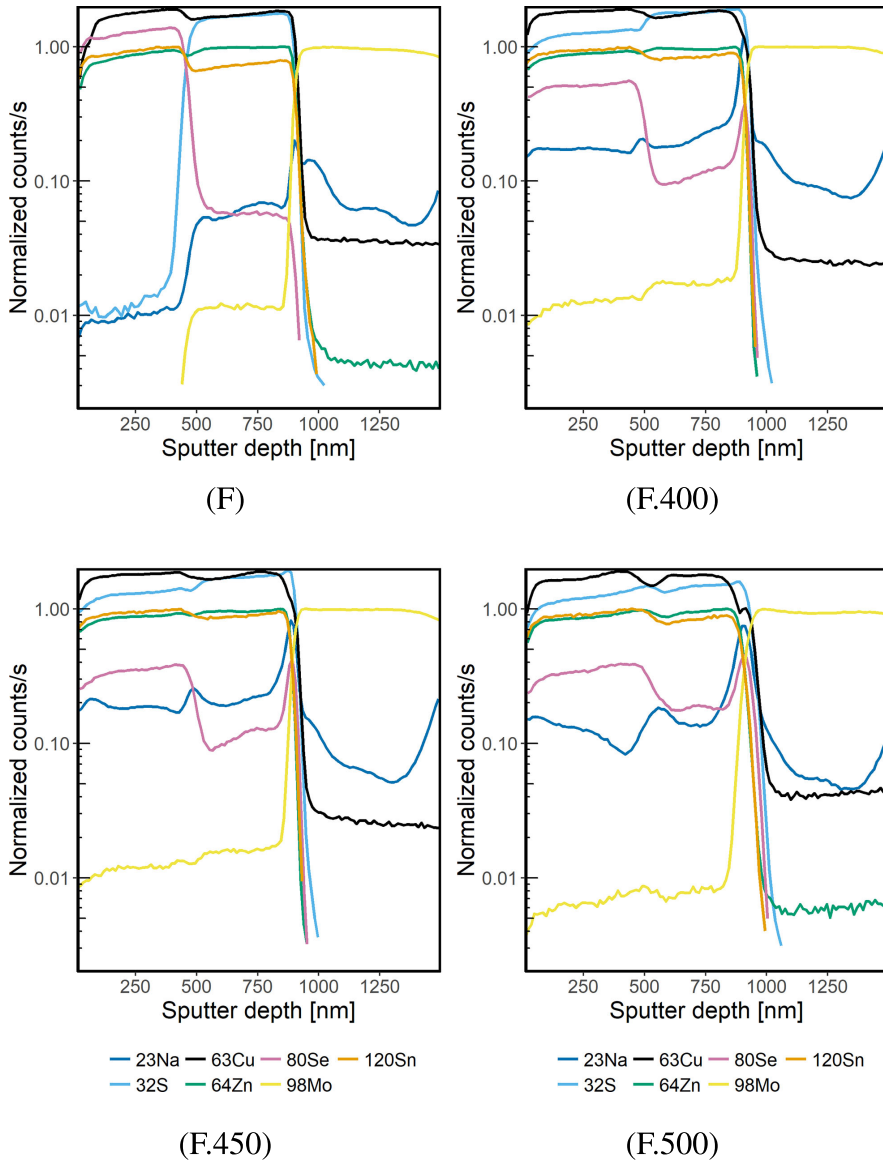


Figure 5.4: SIMS data for the precursor F bilayer ramp tests. Counts are normalized to fit a common scale. Reprinted from Paper IV with permission from IEEE (© 2018 IEEE).

5.2 Impurities in CZTS

Understanding the role of impurities in complex materials such as CZTS is challenging. The polycrystalline structure and a high density of defects opens up possibilities for a wide range of sites for the impurity be found and mechanisms to migrate. Importantly, Na is known to have a beneficial effect on the PCE. For other impurities, such as O and H, the effects are less studied and this has been an important topic in the present thesis. Here, results regarding the behavior and migration of prevalent impurities are presented.

5.2.1 Contribution from sodium in grain boundaries to the SIMS intensity

The SIMS intensity represents the average concentration of a species in the volume measured. The analyzed area is usually a circular region with 33 or 62 μm in diameter. Thus, the area covers a large number of grains, since the CZTS samples typically exhibit an average grain size of 100 to 400 nm. For impurities such as Na, segregation to line and planar defects is expected. For CIGS, the segregation factor between a GB and the GI has been observed to be 1000 [91]. Whether Na in the GBs contribute to the SIMS intensity depends on the segregation factor, the size of the grains, the chemistry of the GBs, the ionization efficiencies and the sputtering yields at the GIs and GBs. It has previously been proposed that the SIMS intensity only represents the GB density for SIMS measured on CIGS [134]. To investigate whether the SIMS intensity measured for Na in CZTS predominantly originates from GBs, three sample sets with three samples each, where the sulfurization time was 10, 20 and 40 minutes were fabricated. This leads to a range of different average grain sizes. The average grain sizes were calculated by counting the number of GBs crossed for five horizontal and five vertical equally spaced lines in two top-view SEM images (similar to that in Figure 4.8) and dividing by the length of the lines. The SIMS intensities for the nine samples are displayed in Figure 5.5.

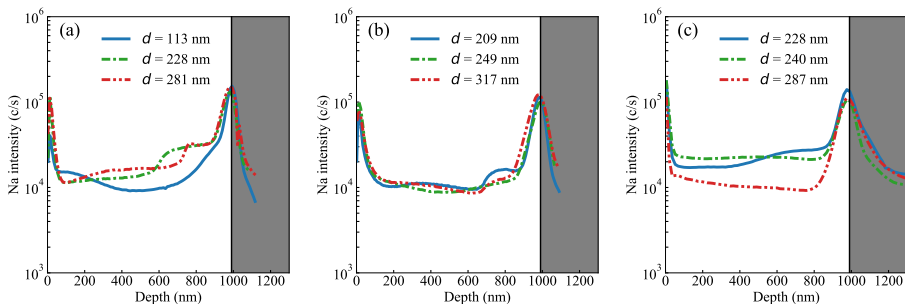


Figure 5.5: Na SIMS intensity versus depth for three samples from three different sample sets (a), (b) and (c), which have all gone through identical processing at different dates. The Na intensity varies between the samples, however, only for the samples in (c) there is a correlation between average grain size and the Na intensity.

If the SIMS intensities are purely originating from the GB, the Na intensity should increase for smaller grain sizes due to increased GB density. However, for the three sample sets there is no clear trend for the Na concentration to be dependent on the grain size. The absence of a correlation between GB density and concentration could be explained by more Na being incorporated into the GI for longer chalcogen anneals. As described in Paper VI, after low temperature air annealing, Na is expected to diffuse from the SLG into the CZTS layer. However, no clear trend of increased Na concentration with GB density after such heat treatments is observed. It has previously been reported through several APT analyses of CZTSe that Na clusters and accumulates at dislocations [43, 135, 136]. It has also been shown that the Na concentration can exhibit spatial inhomogeneities on a micrometer scale [119]. Consequently, the hypothesis that SIMS depth profiles of impurities represent only the GB density in CZTS is inadequate to explain the SIMS results obtained in this thesis. The GI, clustering of impurities and accumulation of impurities at dislocations need to be considered as well.

5.2.2 Interplay between sodium and oxygen in kesterite absorbers

Correlations between Na and O have previously been reported in studies on CIGS. Kronik et al. [137] proposed that Na is acting as a catalyst for O passivation of CIGS surfaces and grain boundaries, known as oxygenation. The passivation was directly attributed to the improved PCE observed after air annealing. For sulfide CuInS_2 , Yamamoto et al. [138] proposed direct bonding between Na and O. Correlations between Na and O SIMS intensities were also observed in this study as well as other studies on CIGS samples [139, 140]. In all samples evaluated in this thesis, a correlation between Na and O SIMS intensities has been found. Even though both elements are likely to segregate at GBs, no correlation between SIMS intensities and GB density was observed as discussed in Subsection 5.2.1. Correlations between Na and O depth profiles have also been observed for CZTSSe samples [117]. The most comprehensive studies, however, focused on either Na or O [61, 62, 69], omitting any interaction between the two impurities.

In Paper V, strong interplay between Na and O in kesterite CZTS was established using a combination of DFT and SIMS. Correlation between Na and O depth profiles were found regardless of the slope of the depth profile. The binding energy between the substitutional defects Na_{Cu} and O_{S} as a function of the distance between them was calculated using DFT². The calculated binding energy for the nearest neighbor configuration was 0.76 eV, which is unexpectedly high for two neutral defects. The calculated effective Bader charge and binding energies between O and selected elements in the nearest neighbor configuration indicated that the binding between Na and O is due to the strong ionic Na-O bond. Consequently, the strong bonding between the two impurities is likely not limited to the GI.

The source of Na is known to be the SLG substrate unless Na is intentionally added during the process. On the other hand, O observed in the CZTS absorber does not

²Binding energy and DFT is described in Section 4.5

5. Summary of results

necessarily originate from one source. One can argue that the consistently similar depth profiles are counter-intuitive if the sources of Na and O are not the same and there is no correlation between the two. In Paper V, the less abundant isotope oxygen-18 (^{18}O), was introduced during different stages of the CZTS baseline process to reveal the origin of the O present in the CZTS absorbers. A qualitative overview of the oxygen sources contributing to the O depth profile is displayed in Figure 5.6.

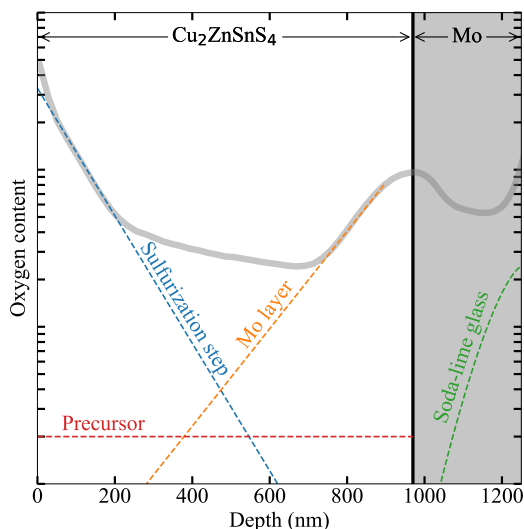


Figure 5.6: A representative O depth profile for a baseline processed CZTS absorber (gray thick line). The dashed lines illustrate a qualitative overview of oxygen sources contributing to the different parts of the depth profile based on the results from this work. Oxygen from the air exposure after processing should only contribute to the oxygen on the surface. Reprinted from Paper V.

The overview suggests that O originating from the Mo layer and the sulfurization step contribute mainly to the depth profile. Additionally, O originating from the back contact and from the atmosphere correspond well with the increased SIMS intensities near the surface and back contact. From the study we concluded that the Na depth profile is governed by the incorporation of O. Support for this hypothesis was found when O was introduced into the precursor at $400\text{ }^{\circ}\text{C}$ and resided there during the sulfurization.

Consequently, it appears that O is trapping Na, resulting in similar depth profiles. As such, Na and O are expected to be around the same order of magnitude in concentration. Another consequence is that the Na distribution and content can be engineered by controlling the O incorporation. Postdeposition heat treatments are one way to achieve this in practice. Previous studies have shown a change in the Na depth profile measured with SIMS after postdeposition heat treatments [67, 68]. We measured SIMS depth profiles on a reference sample that produced an average 4.7 % PCE and one with an air annealing step at $300\text{ }^{\circ}\text{C}$ that produced an average 9.1 % PCE. The air annealed sample

exhibited significantly lower Na and O intensities towards the surface (not shown). We propose that the controlled incorporation of O enables for tailoring the Na depth profile due to the strong interplay between Na and O. This strategy is not limited to kesterite solar cells given the generally strong Na-O bonds, but might also be a valid approach for optimizing CIGS devices.

5.2.3 Estimating quantitative depth profiles using time-of-flight-energy elastic recoil detection analysis

As discussed in Subsection 4.1.1, the SIMS intensity is proportional to the concentration of an element. Hence, the SIMS depth profiles for Na and O have been calibrated using a time-of-flight-energy elastic recoil detection analysis (ToF-ERDA) reference. The depth profiles of light elements obtained with ToF-ERDA has an uncertainty of 10-20 % [141]. Likewise, we regard the SIMS depth profiles to have an uncertainty of $\sim 10\%$. Additionally, the impinging ions from ToF-ERDA covers an area of a few millimeters, substantially larger compared to that from SIMS, increasing the uncertainty when comparing the two techniques. Ideally, a reference sample implanted with a known profile for the impurity of interest would provide for a more accurate reference. However, given the high amounts of Na and O already present in the samples the dose needs to be very high. Also, for Na implantation, contamination of the beam line is a challenge. The ToF-ERDA depth profile provides elemental atomic content. For SIMS, however, the concentration is measured as atoms/cm³, labeled cm⁻³. Thus, to convert from atomic percent to atoms/cm³ the following assumptions were made: Molar mass calculated using the cation ratios provided by XRF with 50 % of S and a density of 4.61 g/cm³ [142]. Given the assumptions and uncertainties, ToF-ERDA and SIMS depth profiles can be plotted as in Figure 5.7 for the case of Na and O.

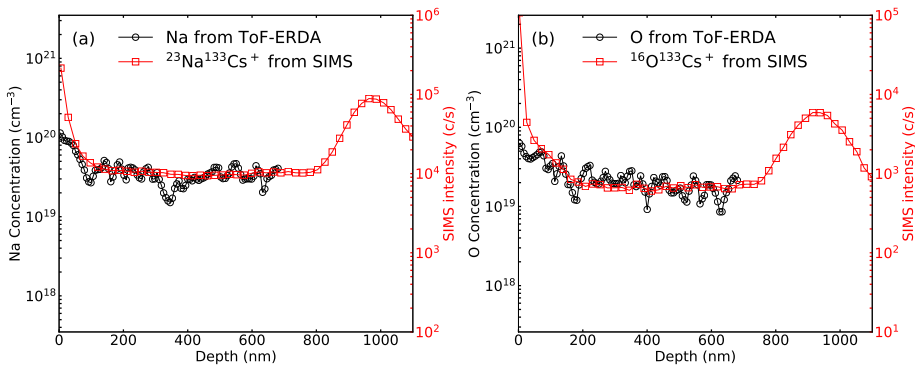


Figure 5.7: Calibration of SIMS intensity to concentration by measuring depth profiles with ToF-ERDA and SIMS on a reference sample with concentration estimated from ToF-ERDA on the left y-axes and SIMS intensity on the right y-axes. The calibrated elements are (a) sodium and (b) oxygen.

The left y-axes represent the concentrations estimated for ToF-ERDA and on the

5. Summary of results

right y-axes, the SIMS intensities for $^{23}\text{Na}^{133}\text{Cs}^+$ and $^{16}\text{O}^{133}\text{Cs}^+$ are shown, respectively. The concentrations of Na is between 10^{19} and 10^{20} cm^{-3} , which is in the upper end of what has been reported for CIGS previously [143, 144]. The depth calibration of ToF-ERDA is based on the slope of the profile. The penetration depth is less than the depth of the CZTS layer since Mo was not detected. The profiles are similar except for a higher SIMS intensity towards the surface. Note that for SIMS, the sputter yield tends to increase for the first measurement points as discussed in Subsection 4.1.2. From Figure 5.7, a relative sensitivity factor can be extracted by solving for RSF in Equation 4.6.

5.2.4 Nonuniformity and distribution of impurities

Spatial variations of Na was highlighted by Gershon et al., correlating spatial differences in light beam induced current with Na inhomogeneities measured by SIMS [119]. Similar inhomogeneities have been observed on the samples evaluated in this thesis. Millimeters apart, Na depth profiles may differ slightly, often in the first few 100 nm below the surface. In Paper VI, Na nonuniformities were also observed on the micrometer scale using SIMS image depth profiling and on the nanometer scale using atom probe tomography (APT). The three-dimensional reconstruction of the APT-tip showed that Na agglomerates at one- and two-dimensional defects. Variations of Na and Cu concentrations are observed around the defects as displayed in Figure 5.8.

The Na and O SIMS depth profiles were measured on a selected number of samples displaying the correlation between Na and O discussed in Subsection 5.2.2. Air annealing of the samples resulted in a redistribution of the impurities. For most samples, the Na and O depth profiles were more similar after the heat treatments. Long term storage in air had similar effects on the depth profiles as low temperature air annealing.

Impurity migration was also studied after heavy water treatments. By dipping the sample in heavy water, the deuterium (D) from the water can be traced. A decrease of Na was observed after the heavy water treatment and an increase in O and H, and a low signal of D. Hence, the increased H content did not originate from the heavy water, but instead from the limited exposure to air. To explain the results, the existence of an “ice-like” layer on top of the $\text{Cu}_2\text{ZnSnS}_4$ layer was proposed.

5.2.5 Secondary ion mass spectrometry to detect sodium diffusion through titanium nitride interlayers

In Paper VII, SIMS depth profiles were measured on CZTS(e)/TiN/Mo structures, using the TiN as an interlayer to prevent $\text{MoS}(\text{e})_2$ formation. This complementary SIMS study substantiates the importance of impurity diffusion in CZTS(e) and illustrates the strength of SIMS to evaluate increased sodium concentration. The SIMS depth profiles revealed a higher concentration of Na for increasing TiN thickness confirming that Na diffusion from the SLG is enhanced by TiN, as proposed in previous studies [141, 145]. The enhanced diffusion of Na is important to consider for controlling Na during processing when such interlayers are utilized. For instance, a TiN layer has been used as interlayer for successful tandem CZTS-on-Si solar cells [80, 81] and thin interlayers can be applied for bifacial solar cells [146].

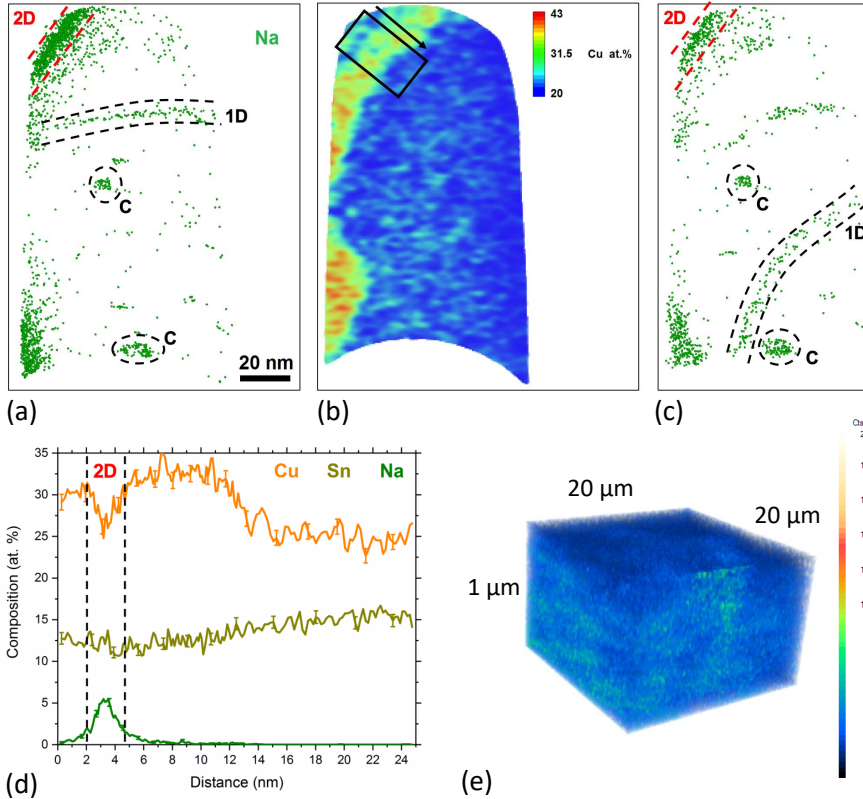


Figure 5.8: Sodium distribution on (a-d) the nm scale using atom probe tomography and on (e) the μm scale using secondary ion mass spectrometry image depth profile. (a) and (c) display two tomographic slices of 8 nm thickness within the point cloud data representing Na atoms. Clusters are marked by “C”, decorated dislocations are marked by “1D” and the two-dimensional lattice defect is marked by “2D”, respectively. (b) a two-dimensional concentration map for the Cu concentration from within the same slice of (a). (d) one-dimensional concentration profile across the two-dimensional defect, the region is marked by a black rectangle in (b), the arrow marks the direction of the profile measurement. Reprinted from Paper VI.

Chapter 6

Conclusions and outlook

Elemental distribution in kesterite $\text{Cu}_2\text{ZnSnS}_4$ absorbers closely related to parameters governing the solar cell performance has been the main focus of this thesis. SIMS as a tool to study $[\text{S}]/([\text{S}] + [\text{Se}])$ gradients have been evaluated. Both conventional depth profiling and SIMS image depth profiling have been utilized to gain information about the chalcogen and impurity migration during the fabrication of CZTSSe absorbers. It was found that recrystallization of sulfoselenide CZTSSe, instead of diffusion into existing grains, limits a controlled incorporation of Se to form a band gap gradient. The growth was promoted by the existence of Na.

Depth profiles of Na and O were found to correlate. The origin of the correlation was attributed to be a strong binding between Na and O, as corroborated by DFT. Introduction of oxygen-18 during the CZTS processing revealed the Mo back contact and the sulfurization step as the two main sources for O. The correlated depth profiles was attributed to O trapping of Na such that the Na depth profile can be controlled by controlling the O incorporation. The results may have a significant impact on the understanding of postdeposition heat treatments such as air annealing and exhibit increased control over impurity distribution in the kesterite absorbers.

Spatial Na nonuniformities were observed in CZTS, both on the millimeter, micrometer and nanometer scale. The impurity depth distributions were found to redistribute after heat treatments and water treatments.

6.1 Suggestions for further work

Important correlations and findings have been revealed in the present thesis, however, there remains further work to understand, fabricate and improve CZTS-based devices. Some suggestions for further work are listed below.

- The limitations to band gap grading with Se was observed mainly with incorporation of Se into CZTS absorbers. Here, the study could be extended to sulfurization of CZTSe absorbers. Additionally, Na free absorbers should be assessed to gain additional understanding of the diffusion and nucleation of Se in CZTS grains.
- Control of the O incorporation in CZTS processing should be performed to study its effect on solar cell parameters. For instance, O annealing of the precursors at 400°C increased the Na and O concentration as measured by SIMS. The effects of this increased impurity concentration on the PCE should be studied.
- The oxygen-18 incorporated into the CZTS samples could potentially be identified and the defect properties could be studied with Fourier transform infrared spec-

6. Conclusions and outlook

trospectroscopy (FTIR). Initial measurements on lift-off samples containing oxygen-18 yielded promising results.

- The correlation between elemental distribution and optical properties could be studied with a combination of SIMS and cathodeluminescence (CL).
- The behavior of hydrogen is not studied in CZTS. Hydrogen has passivating properties in many material systems and could play an important role in the PCE of CZTS devices. SIMS is an excellent technique used to study H distribution. D could be introduced in a similar fashion as oxygen-18 was introduced in Paper V. A study of D incorporation into CZTS with SIMS and FTIR would be very interesting.
- The interplay with Na and O is likely to be valid for other semiconductor compounds. A dedicated study of Na and O on other emerging solar cell materials would be worth investigating.

6.2 Outlook

The record PCE of CZTS-based materials has not improved during the length of this thesis, however, considerable progress has been made in understanding the complex material system. Other chalcogenide solar cell materials have seen drastic improvements solar cell PCE based on new insight. Successful band gap grading or an activation step involving impurity control are two candidates to drive the record PCE of CZTS devices. Given an increase in PCE, CZTS is promising as the top cell in a CZTS-on-Si tandem solar cell.

Impurity control is likely to be of major importance for emerging solar cell materials similar to CZTS. Here, SIMS studies will be necessary to understand the distribution and behavior of the impurities.

Bibliography

- [1] Statistics | World - Electricity Generation by Fuel (Chart), <https://www.iea.org/statistics/?country=WORLD&year=2016&category=Electricity&indicator=ElecGenByFuel&mode=chart&dataTable=ELECTRICITYANDHEAT> (visited on 06/20/2019).
- [2] Bloomberg, New Energy Outlook, **2019**.
- [3] Technology Roadmap Solar Photovoltaic Energy - 2014 Edition, p. 60.
- [4] Philipps, S., Warmuth, W., Photovoltaics Report, Fraunhofer ISE, **2018**.
- [5] Schorr, S., Gonzalez-Aviles, G., *Phys. Status Solidi (a)* **2009**, vol. 206, 1054–1058.
- [6] Momma, K., Izumi, F., *Journal of Applied Crystallography* **2011**, vol. 44, 1272–1276.
- [7] Choubrac, L., Lafond, A., Guillot-Deudon, C., Moëlo, Y., Jobic, S., *Inorg. Chem.* **2012**, vol. 51, 3346–3348.
- [8] Lafond, A., Choubrac, L., Guillot-Deudon, C., Fertey, P., Evain, M., Jobic, S., *Acta Crystallogr B Struct Sci Cryst Eng Mater* **2014**, vol. 70, 390–394.
- [9] Schorr, S., *Solar Energy Materials and Solar Cells* **2011**, vol. 95, 1482–1488.
- [10] Siebentritt, S., Schorr, S., *Prog. Photovolt: Res. Appl.* **2012**, vol. 20, 512–519.
- [11] Scragg, J. J. S., Choubrac, L., Lafond, A., Ericson, T., Platzer-Björkman, C., *Appl. Phys. Lett.* **2014**, vol. 104, 041911.
- [12] Scragg, J. J. S., Larsen, J. K., Kumar, M., Persson, C., Sendler, J., Siebentritt, S., Platzer Björkman, C., *physica status solidi (b)* **2016**, vol. 253, 247–254.
- [13] Chen, S., Walsh, A., Gong, X.-G., Wei, S.-H., *Adv. Mater.* **2013**, vol. 25, 1522–1539.
- [14] Valle Rios, L. E., Neldner, K., Gurieva, G., Schorr, S., *Journal of Alloys and Compounds* **2016**, vol. 657, 408–413.
- [15] Zhao, H., Persson, C., *Thin Solid Films* **2011**, vol. 519, 7508–7512.
- [16] Li, S.-y., Zamulko, S., Persson, C., Ross, N., Larsen, J. K., Platzer-Björkman, C., *Appl. Phys. Lett.* **2017**, vol. 110, 021905.
- [17] Zamulko, S., Chen, R., Persson, C., *physica status solidi (b)* **2017**, vol. 254, 1700084.
- [18] Zamulko, S., Berland, K., Persson, C., *Phys. Status Solidi A* **2018**, vol. 215, 1700945.

- [19] Platzer-Björkman, C., Frisk, C., Larsen, J. K., Ericson, T., Li, S.-Y., Scragg, J. J. S., Keller, J., Larsson, F., Törndahl, T., *Applied Physics Letters* **2015**, vol. 107, 243904.
- [20] Ericson, T., Larsson, F., Törndahl, T., Frisk, C., Larsen, J., Kosyak, V., Hägglund, C., Li, S., Platzer-Björkman, C., *Solar RRL* **2017**, vol. 1, 1700001.
- [21] Sun, K., Yan, C., Liu, F., Huang, J., Zhou, F., Stride, J. A., Green, M., Hao, X., *Advanced Energy Materials* **2016**, vol. 6, 1600046.
- [22] Chen, G., Wang, W., Chen, S., Whang, Z., Huang, Z., Zhang, B., Kong, X., *Journal of Alloys and Compounds* **2017**, vol. 718, 236–245.
- [23] Cabas-Vidani, A., Haass, S. G., Andres, C., Caballero, R., Figi, R., Schreiner, C., Márquez, J. A., Hages, C., Unold, T., Bleiner, D., Tiwari, A. N., Romanyuk, Y. E., *Advanced Energy Materials* **2018**, vol. 8, 1801191.
- [24] Yuan, Z.-K., Chen, S., Xiang, H., Gong, X.-G., Walsh, A., Park, J.-S., Repins, I., Wei, S.-H., *Adv. Funct. Mater.* **2015**, vol. 25, 6733–6743.
- [25] Yang, S., Wang, S., Liao, H., Xu, X., Tang, Z., Li, X., Wang, T., Li, X., Liu, D., *J Mater Sci: Mater Electron* **2019**, DOI 10.1007/s10854-019-01463-1.
- [26] Sun, J.-P., Márquez, J. A., Stange, H., Mainz, R., Mitzi, D. B., *Phys. Rev. Materials* **2019**, vol. 3, 055402.
- [27] Zhang, Q., Deng, H., Chen, L., Yu, L., Tao, J., Sun, L., Yang, P., Chu, J., *Journal of Alloys and Compounds* **2017**, vol. 695, 482–488.
- [28] Rudisch, K., Espinosa-García, W. F., Osorio-Guillén, J. M., Araujo, C. M., Platzer-Björkman, C., Scragg, J. J. S., *Phys. Status Solidi B* **2019**, 1800743.
- [29] Brammertz, G., Vermang, B., ElAnzeery, H., Sahayaraj, S., Samaneh, R., Meuris, M., Poortmans, J., *Phys. Status Solidi C* **2017**, 4.
- [30] Scheer, R., Schock, H.-W., *Chalcogenide Photovoltaics*, **2011**.
- [31] Bär, M., Schubert, B.-A., Marsen, B., Wilks, R. G., Pookpanratana, S., Blum, M., Krause, S., Unold, T., Yang, W., Weinhardt, L., Heske, C., Schock, H.-W., *Applied Physics Letters* **2011**, vol. 99, 222105.
- [32] Neuschitzer, M., Sanchez, Y., López-Marino, S., Xie, H., Fairbrother, A., Placidi, M., Haass, S., Izquierdo-Roca, V., Perez-Rodriguez, A., Saucedo, E., *Prog. Photovolt: Res. Appl.* **2015**, vol. 23, 1660–1667.
- [33] Ren, Y., PhD Thesis, Uppsala University, **2017**.
- [34] Solar Spectral Irradiance: Air Mass 1.5, <https://rredc.nrel.gov/solar//spectra/am1.5/> (visited on 06/20/2019).
- [35] Shockley, W., Queisser, H. J., *Journal of Applied Physics* **1961**, vol. 32, 11.
- [36] Chiu, P., Law, D., Woo, R., Singer, S., Bhusari, D., Hong, W., Zakaria, A., Boisvert, J., Mesropian, S., King, R., Karam, N. in 2014 IEEE 40th Photovoltaic Specialist Conference (PVSC), 2014 IEEE 40th Photovoltaic Specialists Conference (PVSC), IEEE, Denver, CO, USA, **2014**, pp. 0011–0013.

- [37] Kato, T., Wu, J.-L., Hirai, Y., Sugimoto, H., Bermudez, V., *IEEE Journal of Photovoltaics* **2019**, vol. 9, 325–330.
- [38] Alonso, M., Garriga, M., Durante Rincón, C., Hernández, E., León, M., *Applied Physics A: Materials Science & Processing* **2002**, vol. 74, 659–664.
- [39] Salomé, P., Rodriguez-Alvarez, H., Sadewasser, S., *Solar Energy Materials and Solar Cells* **2015**, vol. 143, 9–20.
- [40] Correa-Baena, J.-P., Saliba, M., Buonassisi, T., Grätzel, M., Abate, A., Tress, W., Hagfeldt, A., *Science* **2017**, vol. 358, 739–744.
- [41] Kojima, A., Teshima, K., Shirai, Y., Miyasaka, T., *J. Am. Chem. Soc.* **2009**, vol. 131, 6050–6051.
- [42] Jiang, Q., Chu, Z., Wang, P., Yang, X., Liu, H., Wang, Y., Yin, Z., Wu, J., Zhang, X., You, J., *Adv. Mater.* **2017**, vol. 29, 1703852.
- [43] Yan, C., Huang, J., Sun, K., Johnston, S., Zhang, Y., Sun, H., Pu, A., He, M., Liu, F., Eder, K., Yang, L., Cairney, J. M., Ekins-Daukes, N. J., Hameiri, Z., Stride, J. A., Chen, S., Green, M. A., Hao, X., *Nature Energy* **2018**, vol. 3, 764–772.
- [44] Wang, W., Winkler, M. T., Gunawan, O., Gokmen, T., Todorov, T. K., Zhu, Y., Mitzi, D. B., *Advanced Energy Materials* **2014**, vol. 4, 1301465.
- [45] Rühle, S., *Solar Energy* **2016**, vol. 130, 139–147.
- [46] Grenet, L., Suzon, M. A. A., Emieux, F., Roux, F., *ACS Applied Energy Materials* **2018**, vol. 1, 2103–2113.
- [47] Giraldo, S., Jehl, Z., Placidi, M., Izquierdo-Roca, V., Pérez-Rodríguez, A., Saucedo, E., *Advanced Materials* **2019**, 1806692.
- [48] Bourdais, S., Choné, C., Delatouche, B., Jacob, A., Larramona, G., Moisan, C., Lafond, A., Donatini, F., Rey, G., Siebentritt, S., Walsh, A., Dennler, G., *Adv. Energy Mater.* **2016**, vol. 6, 1502276.
- [49] Hages, C. J., Redinger, A., Levchenko, S., Hempel, H., Koeper, M. J., Agrawal, R., Greiner, D., Kaufmann, C. A., Unold, T., *Advanced Energy Materials* **2017**, vol. 7, 1700167.
- [50] Siebentritt, S., *Thin Solid Films* **2013**, vol. 535, 1–4.
- [51] Gokmen, T., Gunawan, O., Todorov, T. K., Mitzi, D. B., *Appl. Phys. Lett.* **2013**, vol. 103, 103506.
- [52] Lang, M., Zimmermann, C., Krämmer, C., Renz, T., Huber, C., Kalt, H., Heterich, M., *Physical Review B* **2017**, vol. 95, DOI 10.1103/PhysRevB.95.155202.
- [53] Kim, I., Kim, K., Oh, Y., Woo, K., Cao, G., Jeong, S., Moon, J., *Chemistry of Materials* **2014**, vol. 26, 3957–3965.
- [54] Li, J., Wang, D., Li, X., Zeng, Y., Zhang, Y., *Advanced Science* **2018**, vol. 5, 1700744.

- [55] Yang, K.-J., Son, D.-H., Sung, S.-J., Sim, J.-H., Kim, Y.-I., Park, S.-N., Jeon, D.-H., Kim, J., Hwang, D.-K., Jeon, C.-W., Nam, D., Cheong, H., Kang, J.-K., Kim, D.-H., *Journal of Materials Chemistry A* **2016**, vol. 4, 10151–10158.
- [56] Ross, N., Larsen, J., Grini, S., Vines, L., Platzer-Björkman, C., *Thin Solid Films* **2017**, vol. 623, 110–115.
- [57] Yin, L., Cheng, G., Feng, Y., Li, Z., Yang, C., Xiao, X., *RSC Adv.* **2015**, vol. 5, 40369–40374.
- [58] Levchenko, S., Just, J., Redinger, A., Larramona, G., Bourdais, S., Dennler, G., Jacob, A., Unold, T., *Physical Review Applied* **2016**, vol. 5, DOI 10.1103/PhysRevApplied.5.024004.
- [59] Kim, S., Park, J.-S., Walsh, A., *ACS Energy Lett.* **2018**, vol. 3, 496–500.
- [60] Haass, S. G., Andres, C., Figi, R., Schreiner, C., Bürki, M., Romanyuk, Y. E., Tiwari, A. N., *Advanced Energy Materials* **2018**, vol. 8, 1701760.
- [61] Gershon, T., Shin, B., Bojarczuk, N., Hopstaken, M., Mitzi, D. B., Guha, S., *Advanced Energy Materials* **2015**, vol. 5, 1400849.
- [62] Gershon, T., Lee, Y. S., Mankad, R., Gunawan, O., Gokmen, T., Bishop, D., McCandless, B., Guha, S., *Applied Physics Letters* **2015**, vol. 106, 123905.
- [63] Sutter-Fella, C. M., Stükelberger, J. A., Hagendorfer, H., La Mattina, F., Kranz, L., Nishiwaki, S., Uhl, A. R., Romanyuk, Y. E., Tiwari, A. N., *Chemistry of Materials* **2014**, vol. 26, 1420–1425.
- [64] Dullweber, T., Hanna, G., Rau, U., Schock, H. W., *Solar Energy Materials* **2001**, 6.
- [65] Frisk, C., Platzer-Björkman, C., Olsson, J., Szaniawski, P., Wätjen, J. T., Fjällström, V., Salomé, P., Edoff, M., *Journal of Physics D: Applied Physics* **2014**, vol. 47, 485104.
- [66] Sze, S. M., Ng, K. K., *Physics of Semiconductor Devices*, 3rd ed, Wiley-Interscience, Hoboken, N.J., **2007**, 815 pp.
- [67] Xie, H., López-Marino, S., Olar, T., Sánchez, Y., Neuschitzer, M., Oliva, F., Giraldo, S., Izquierdo-Roca, V., Lauer mann, I., Pérez-Rodríguez, A., Saucedo, E., *ACS Applied Materials & Interfaces* **2016**, vol. 8, 5017–5024.
- [68] Hironiwa, D., Sakai, N., Kato, T., Sugimoto, H., Tang, Z., Chantana, J., Minemoto, T., *Thin Solid Films* **2015**, vol. 582, 151–153.
- [69] Sardashti, K., Haight, R., Gokmen, T., Wang, W., Chang, L.-Y., Mitzi, D. B., Kummel, A. C., *Advanced Energy Materials* **2015**, vol. 5, 1402180.
- [70] Park, J., Huang, J., Yun, J., Liu, F., Ouyang, Z., Sun, H., Yan, C., Sun, K., Kim, K., Seidel, J., Chen, S., Green, M. A., Hao, X., *Advanced Energy Materials* **2018**, vol. 8, 1701940.
- [71] Kim, D.-H., “CZTSSe Solar Cell with over 12% Efficiency: Studies of Formation Mechanism and H₂S Effect Using Sn/ Cu/Zn Precursor”, **2018**.

- [72] Giraldo, S., Neuschitzer, M., Thersleff, T., López-Marino, S., Sánchez, Y., Xie, H., Colina, M., Placidi, M., Pistor, P., Izquierdo-Roca, V., Leifer, K., Pérez-Rodríguez, A., Saucedo, E., *Advanced Energy Materials* **2015**, vol. 5, 1501070.
- [73] Schnabel, T., Abzieher, T., Friedlmeier, T. M., Ahlswede, E., *IEEE Journal of Photovoltaics* **2015**, vol. 5, 670–675.
- [74] Taskesen, T., Neerken, J., Schoneberg, J., Pareek, D., Steininger, V., Parisi, J., Gütay, L., *Advanced Energy Materials* **2018**, vol. 8, 1703295.
- [75] Haass, S. G., Diethelm, M., Werner, M., Bissig, B., Romanyuk, Y. E., Tiwari, A. N., *Advanced Energy Materials* **2015**, vol. 5, 1500712.
- [76] Green, M. A., Hishikawa, Y., Dunlop, E. D., Levi, D. H., Hohl-Ebinger, J., Yoshita, M., Ho-Baillie, A. W., *Progress in Photovoltaics: Research and Applications* **2019**, vol. 27, 3–12.
- [77] Romeo, A., Terheggen, M., Abou-Ras, D., Bätzner, D. L., Haug, F.-J., Kälin, M., Rudmann, D., Tiwari, A. N., *Prog. Photovolt: Res. Appl.* **2004**, vol. 12, 93–111.
- [78] Laemmle, A., Wuerz, R., Powalla, M., *Phys. Status Solidi RRL* **2013**, vol. 7, 631–634.
- [79] Jackson, P., Hariskos, D., Wuerz, R., Kiowski, O., Bauer, A., Friedlmeier, T. M., Powalla, M., *physica status solidi (RRL) - Rapid Research Letters* **2015**, vol. 9, 28–31.
- [80] Hajjifarassar, A., Martinho, F., Stulen, F. A., Grini, S., Lopez-Marino, S., Espindola-Rodriguez, M., Döbeli, M., Canulescu, S., Stamate, E., Gansukh, M., Engberg, S., Crovetto, A., Vines, L., Schou, J., Hansen, O., “Monolithic Thin-Film Chalcogenide-Silicon Tandem Solar Cells Enabled by a Diffusion Barrier”, **2019**.
- [81] Stulen, F. A., Master’s thesis, University of Oslo, **2019**.
- [82] Eckstein, W., Behrisch, R., *Sputtering by Particle Bombardment*, Springer Berlin Heidelberg, Berlin, Heidelberg, **2007**.
- [83] *Handbook of Thin-Film Technology*, (Eds.: Frey, H., Khan, H. R.), OCLC: 950708027, Springer, Berlin Heidelberg, **2015**, 379 pp.
- [84] Edoff, M., Viard, N., Wätjen, T., Schleussner, S., Westin, P.-O., Leifer, K., *Proceedings of the 24th European Photovoltaic Solar Energy Conference 21-25 September 2009 Hamburg Germany* **2009**, 4.
- [85] Larsen, J., Ren, Y., Ross, N., Särhammar, E., Li, S.-Y., Platzer-Björkman, C., *Thin Solid Films* **2017**, vol. 633, 118–121.
- [86] Ren, Y., Scragg, J. J. S., Edoff, M., Larsen, J. K., Platzer-Björkman, C., *ACS Applied Materials & Interfaces* **2016**, vol. 8, 18600–18607.
- [87] Philibert, J., *Atom Movements: Diffusion and Mass Transport in Solids*, Editions de Physique, Les Ulis, France, **1991**, 577 pp.
- [88] Fisher, J. C., *Journal of Applied Physics* **1951**, vol. 22, 74–77.
- [89] Harrison, L. G., *Trans. Faraday Soc.* **1961**, vol. 57, 1191.

- [90] Laemmle, A., PhD Thesis, Karlsruhe Institute of Technology.
- [91] Laemmle, A., Wuerz, R., Schwarz, T., Cojocar-Mirédin, O., Choi, P.-P., Powalla, M., *Journal of Applied Physics* **2014**, vol. 115, 154501.
- [92] Wuerz, R., Hempel, W., Jackson, P., *Journal of Applied Physics* **2018**, vol. 124, 165305.
- [93] Stolwijk, N. A., Obeidi, S., Bastek, J., Wuerz, R., Eicke, A., *Appl. Phys. Lett.* **2010**, vol. 96, 244101.
- [94] Hiepko, K., Bastek, J., Schlesiger, R., Schmitz, G., Wuerz, R., Stolwijk, N. A., *Appl. Phys. Lett.* **2011**, vol. 99, 234101.
- [95] Bastek, J., Stolwijk, N. A., Wuerz, R., Eicke, A., Albert, J., Sadewasser, S., *Applied Physics Letters* **2012**, vol. 101, 074105.
- [96] Beckers, T., Nagarajan, L., Martin, M., *Thin Solid Films* **2015**, vol. 592, 118–123.
- [97] Wegner, M., Wilangowski, F., Wuerz, R., Stolwijk, N., *Thin Solid Films* **2017**, vol. 633, 31–34.
- [98] Niles, D. W., Al-Jassim, M., Ramanathan, K., *Journal of Vacuum Science & Technology A: Vacuum Surfaces and Films* **1999**, vol. 17, 291–296.
- [99] Su, Z., Sun, K., Han, Z., Cui, H., Liu, F., Lai, Y., Li, J., Hao, X., Liu, Y., Green, M. A., *J. Mater. Chem. A* **2014**, vol. 2, 500–509.
- [100] Yin, W.-J., Wu, Y., Wei, S.-H., Noufi, R., Al-Jassim, M. M., Yan, Y., *Advanced Energy Materials* **2014**, vol. 4, 1300712.
- [101] Cojocar-Mirédin, O., Choi, P.-P., Abou-Ras, D., Schmidt, S. S., Caballero, R., Raabe, D., *IEEE Journal of Photovoltaics* **2011**, vol. 1, 207–212.
- [102] Keller, J., Schlesiger, R., Riedel, I., Parisi, J., Schmitz, G., Avellan, A., Dalibor, T., *Solar Energy Materials and Solar Cells* **2013**, vol. 117, 592–598.
- [103] Schöppe, P., Schönherr, S., Wuerz, R., Wisniewski, W., Martínez-Criado, G., Ritzer, M., Ritter, K., Ronning, C., Schnohr, C. S., *Nano Energy* **2017**, vol. 42, 307–313.
- [104] Li, J., Mitzi, D. B., Shenoy, V. B., *ACS Nano* **2011**, vol. 5, 8613–8619.
- [105] Ross, N., Larsen, J., Grini, S., Sarhammar, E., Vines, L., Platzer-Bjorkman, C. in 2016 IEEE 43rd Photovoltaic Specialists Conference (PVSC), 2016 IEEE 43rd Photovoltaic Specialists Conference (PVSC), IEEE, Portland, OR, USA, **2016**, pp. 0492–0497.
- [106] Ross, N., Grini, S., Vines, L., Platzer-Bjorkman, C. in 2017 IEEE 44th Photovoltaic Specialist Conference (PVSC), 2017 IEEE 44th Photovoltaic Specialists Conference (PVSC), IEEE, Washington, DC, **2017**, pp. 3269–3274.
- [107] Forest, R. V., Eser, E., McCandless, B. E., Birkmire, R. W., Chen, J. G., *AIChE Journal* **2014**, vol. 60, 2365–2372.
- [108] Salome, P. M. P., Hultqvist, A., Fjallstrom, V., Edoff, M., Aitken, B. G., Zhang, K., Fuller, K., Kosik Williams, C., *IEEE Journal of Photovoltaics* **2014**, vol. 4, 1659–1664.

- [109] Stevie, F. A., Magee, C. W., Wilson, R. G., *Secondary Ion Mass Spectrometry: A Practical Handbook for Depth Profiling and Bulk Impurity Analysis*, OCLC: 20168488, Wiley, New York u.a, **1989**.
- [110] Van der Heide, P., *Secondary Ion Mass Spectrometry: An Introduction to Principles and Practices*, Wiley, Hoboken, New Jersey, **2014**, 365 pp.
- [111] Gao, Y., *Journal of Applied Physics* **1988**, vol. 64, 3760–3762.
- [112] Magee, C. W., Harrington, W. L., Botnick, E. M., *International Journal of Mass Spectrometry and Ion Processes* **1990**, vol. 103, 45–56.
- [113] Wittmaack, K., *Nuclear Instruments and Methods in Physics Research Section B: Beam Interactions with Materials and Atoms* **1992**, vol. 64, 621–625.
- [114] Wittmaack, K., *Surface Science* **2012**, vol. 606, L18–L21.
- [115] Lee, J., Kim, S. H., Lee, K.-B., Min, B. K., Lee, Y., *Applied Physics A* **2014**, vol. 115, 1355–1364.
- [116] Williams, P., Baker, J. E., *Nuclear Instruments and Methods* **1981**, vol. 182-183, 15–24.
- [117] Haight, R., Shao, X., Wang, W., Mitzi, D. B., *Applied Physics Letters* **2014**, vol. 104, 033902.
- [118] Schöppe, P., Gurieva, G., Giraldo, S., Martínez-Criado, G., Ronning, C., Saucedo, E., Schorr, S., Schnohr, C. S., *Appl. Phys. Lett.* **2017**, vol. 110, 043901.
- [119] Gershon, T., Hamann, C., Hopstaken, M., Lee, Y. S., Shin, B., Haight, R., *Advanced Energy Materials* **2015**, vol. 5, 1500922.
- [120] Birkholz, M., Fewster, P. F., Genzel, C., *Thin Film Analysis by X-Ray Scattering*, Wiley-VCH, Weinheim, **2006**, 356 pp.
- [121] Ren, Y., Richter, M., Keller, J., Redinger, A., Unold, T., Donzel-Gargand, O., Scragg, J. J. S., Platzer Björkman, C., *ACS Energy Lett.* **2017**, vol. 2, 976–981.
- [122] Tiedt, D. L. R., Pretorius, W. E., AN INTRODUCTION TO ELECTRON MICROSCOPY AND X-RAY MICROANALYSIS, LABORATORY FOR ELECTRON MICROSCOPY, **2002**, p. 32.
- [123] *Ion Beams in Nanoscience and Technology*, (Eds.: Hellborg, R., Whitlow, H. J., Zhang, Y.), OCLC: ocn310401069, Springer-Verlag, Heidelberg ; New York, **2009**, 457 pp.
- [124] Zhang, Y., Whitlow, H. J., Winzell, T., Bubb, I. F., Sajavaara, T., Arstila, K., Keinonen, J., **1999**, 13.
- [125] Ström, P., Petersson, P., Rubel, M., Possnert, G., *Review of Scientific Instruments* **2016**, vol. 87, 103303.
- [126] Janson, M., CONTES Conversion of Time-Energy Spectra a Program for ERDA Data Analysis (Internal Report, Uppsala University), Uppsala, **2004**.
- [127] *Atom Probe Microscopy*, (Ed.: Gault, B.), OCLC: ocn775406154, Springer, New York, **2012**, 396 pp.

- [128] *A Primer in Density Functional Theory*, (Eds.: Fiolhais, C., Nogueira, F., Marques, M. A. L.), Springer, Berlin ; New York, **2003**, 256 pp.
- [129] Capelle, K., *Braz. J. Phys.* **2006**, vol. 36, 1318–1343.
- [130] Giustino, F., *Materials Modelling Using Density Functional Theory: Properties and Predictions*, 1st ed, OCLC: ocn870986749, Oxford University Press, Oxford, **2014**, 286 pp.
- [131] Hohenberg, P., Kohn, W., *Phys. Rev.* **1964**, vol. 136, B864–B871.
- [132] Kohn, W., Sham, L. J., *Phys. Rev.* **1965**, vol. 140, A1133–A1138.
- [133] Perdew, J. P., Burke, K., Ernzerhof, M., *Physical Review Letters* **1996**, vol. 77, 3865–3868.
- [134] Probst, V., Karg, F., Rimmasch, J., Riedl, W., Stetter, W., Harms, H., Eibl, O., *MRS Proceedings* **1996**, vol. 426.
- [135] Schwarz, T., Cojocaru-Mirédin, O., Mousel, M., Redinger, A., Raabe, D., Choi, P.-P., *Acta Materialia* **2017**, vol. 132, 276–284.
- [136] Schwarz, T., Redinger, A., Siebentritt, S., Peng, Z., Gault, B., Raabe, D., Choi, P.-P., *Physical Review Materials* **2019**, vol. 3, DOI 10.1103/PhysRevMaterials.3.035402.
- [137] Kronik, L., Cahen, D., Schock, H. W., *Advanced Materials* **1998**, vol. 10, 31–36.
- [138] Yamamoto, T., Watanabe, T., Hamashoji, Y., *Physica B: Condensed Matter* **2001**, vol. 308-310, 1007–1010.
- [139] Rockett, A., Britt, J. S., Gillespie, T., Marshall, C., Jassim, M. M. A., Hasoon, F., Matson, R., Basol, B., *Thin Solid Films* **2000**, vol. 372, 6.
- [140] Braunger, D., Hariskos, D., Bilger, G., Rau, U., Schock, H. W., *Thin Solid Films* **2000**, 6.
- [141] Paneta, V., Englund, S., Suvanam, S., Scragg, J., Platzer-Björkman, C., Primetzhofner, D., *Nuclear Instruments and Methods in Physics Research Section B: Beam Interactions with Materials and Atoms* **2018**, S0168583X18304038.
- [142] Guen, L., Glaunsinger, W., *Journal of Solid State Chemistry* **1980**, vol. 35, 10–21.
- [143] Rockett, A., Bodegard, M., Granath, K., Stolt, L. in CONFERENCE RECORD OF THE TWENTY FIFTH IEEE PHOTOVOLTAIC SPECIALISTS CONFERENCE - 1996, 25th IEEE Photovoltaic Specialists Conference, WASHINGTON, DC, MAY 13-17, 1996, IEEE; IEEE, Electron Device Soc, **1996**, {985–987}.
- [144] Wang, L., Wang, A., Hockett, R. in 2009 34th IEEE Photovoltaic Specialists Conference (PVSC), 2009 34th IEEE Photovoltaic Specialists Conference (PVSC), IEEE, Philadelphia, PA, USA, **2009**, pp. 000494–000498.
- [145] Englund, S., Paneta, V., Primetzhofner, D., Ren, Y., Donzel-Gargand, O., Larsen, J. K., Scragg, J., Platzer Björkman, C., *Thin Solid Films* **2017**, vol. 639, 91–97.
- [146] Espindola-Rodriguez, M., Sylla, D., Sánchez, Y., Oliva, F., Grini, S., Neuschitzer, M., Vines, L., Izquierdo-Roca, V., Saucedo, E., Placidi, M., *ACS Sustainable Chem. Eng.* **2017**, vol. 5, 11516–11524.

Papers

Paper I

Secondary ion mass spectrometry as a tool to study selenium gradient in $\text{Cu}_2\text{ZnSn}(\text{S},\text{Se})_4$

**Sigbjørn Grini, Nils Ross, Thomas Neset Sky, Clas Persson,
Charlotte Platzer-Björkman, Lasse Vines**

Phys. Status Solidi C 14, No. 6, 1600187 (2017).

Secondary ion mass spectrometry as a tool to study selenium gradient in $\text{Cu}_2\text{ZnSn}(\text{S},\text{Se})_4$

Sigbjørn Grini^{*1}, Nils Ross¹, Thomas Neset Sky¹, Clas Persson¹, Charlotte Platzer-Björkman², and Lasse Vines¹

¹ Department of Physics/Centre for Materials Science and Nanotechnology, University of Oslo, P. O. Box 1048 Blindern, 0316 Oslo, Norway

² Ångström Solar Center, Solid State Electronics, Uppsala University, Box 534, 751 21 Uppsala, Sweden

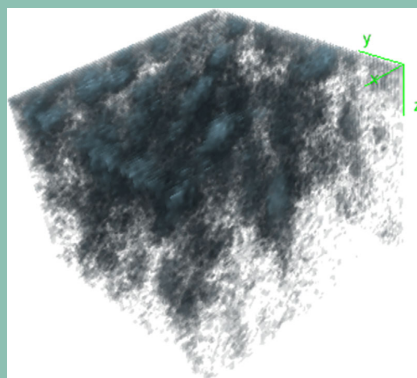
Received 31 August 2016, accepted 30 January 2017

Published online 21 February 2017

Keywords $\text{Cu}_2\text{ZnSn}(\text{S},\text{Se})_4$, kesterite, secondary ion mass spectrometry, Se gradient

* Corresponding author: e-mail sigbjorn.grini@smn.uio.no, Phone: +47 470 91 335, Fax: +47 22 85 64 22

Secondary ion mass spectrometry (SIMS) has been utilized to study compositional gradients in compound-sputtered and annealed $\text{Cu}_2\text{ZnSn}(\text{S},\text{Se})_4$ (CZTSSe). SIMS image depth profiling shows a non-uniform spatial distribution of selenium and supports a mechanism where selenization is accompanied by grain growth rather than substitution of selenium for sulfur. Furthermore, SIMS depth profiles of S and Se using O_2^+ primary ions and detecting molecular ions of the MCs^+ type using Cs^+ primary ions have been compared, where a linear relationship between the sulfur and selenium concentration suitable for compositional analysis is observed for concentrations with an Se/(S+Se) ratio in the range from 0.25 to 0.65.



3D image of the spatial Se distribution in a $20 \times 20 \mu\text{m}^2$ grid measured with SIMS image depth profiling.

© 2017 WILEY-VCH Verlag GmbH & Co. KGaA, Weinheim

1 Introduction Kesterite $\text{Cu}_2\text{ZnSn}(\text{S},\text{Se})_4$ (CZTSSe), is a promising material for the use as the p-type absorber layer for thin film solar cell applications based on earth abundant elements. One potential method to increase the efficiency of CZTSSe cells is to utilize a varying Se/(S+Se) ratio, similar to the Ga/(In+Ga) grading that has been successfully applied in $\text{Cu}(\text{In},\text{Ga})\text{Se}_2$ (CIGS) solar cells [1]. In CZTSSe, the band gap energy can be varied from that of sulfide $\text{Cu}_2\text{ZnSnS}_4$ (CZTS) of approximately 1.5 eV to that of selenide $\text{Cu}_2\text{ZnSnSe}_4$ (CZTSe) with a band gap energy of ~ 1.0 eV [2]. Several studies have reported a compositional gradient in CZTSSe [3–7], but important issues remain before a controllable band gap grading

can be implemented in commercial cells [8]. In particular, grain growth has been shown to accompany the selenization, resulting in a nonhomogeneous lateral distribution [8]. The Se/(S+Se) ratio is typically characterized using methods including scanning electron microscopy with energy dispersive X-ray spectroscopy (SEM-EDX) [3, 6, 7], grazing incidence X-ray diffraction (GIXRD) [4, 7], and secondary ion mass spectrometry (SIMS) [4, 7]. The advantage of SIMS is that it provides superior detection sensitivity and a precise depth resolution. However, the depth profile analyses rely on constant ionization efficiency with depth and are usually performed over a large area, showing the average two dimensional (2D)

distribution of each element. As a result, the lateral information is lost, which is of particular importance for multicrystalline structures such as CZTSSe, where the chemical composition within the grains may differ from the averaged composition [7]. In order to study this non-uniform distribution with SIMS one can measure the three dimensional (3D) chemical information with high spatial resolution, which can be accomplished with SIMS image depth profiling, where information on the position of the secondary ions is preserved while sputtering. The result is a set of images acquired from different depths. Moreover, the compositional gradients measured by SIMS may deviate from the actual compositional gradient. This can occur as the ionization probability of each element depends on the compositional matrix that is sputtered (hereafter called matrix effect). However, it is possible to minimize the matrix effect by detecting MCs^+ secondary ions when sputtering with Cs^+ primary ions, where M is the matrix element to be analyzed [9–12]. Previously, both positive secondary ions with O_2^+ primary ions and MCs^+ ions with Cs^+ primary ions have been utilized for SIMS analysis of CZTS(Se) [13–16]. In this article, image depth profiling is performed for CZTSSe and it is shown that a non-uniform distribution of S and Se can be detected for different depths by SIMS. Furthermore, both O_2^+ and MCs^+ depth profiles are measured and a comparison is made between each method to evaluate the impact of the matrix effect for CZTSSe.

2 Experimental The samples studied were deposited by co-sputtering of the compound precursors CuS, ZnS and SnS on a Mo-coated substrate followed by two annealing processes. O_2^+ image depth profiling was performed on a sample (Sample 1) which was annealed at 500 °C for 10 min in a sulfur-rich atmosphere. This was followed by another anneal at 425 °C for 45 min in a selenium-rich atmosphere to incorporate Se into the absorber. The O_2^+ and MCs^+ depth profiling was performed on a similar sample (Sample 2) where the first annealing temperature was 580 °C and the second was 450 °C, both for 10 min. More detailed information about the sample processing can be found elsewhere [8]. SEM-EDX images were taken with a Zeiss Leo 1550 using a 5 kV accelerating voltage on the cross-section of

the samples. The SIMS results have been obtained using a magnetic sector Cameca IMS-7f ion microprobe. Three experimental conditions were explored as listed in Table 1, where the O_2^+ ion beam was utilized for image depth profiling. The depth was calibrated from a cross-sectional SEM image and a constant erosion rate was assumed when converting sputtering time to sample depth.

3 Results and discussion The cross-sectional SEM-EDX map in Fig. 1(a) shows the distribution of Se in the film. The grain sizes as observed by SEM (not shown) are around 200 nm in diameter, and from Fig. 1(a) it is evident that the Se-rich areas are larger than the grains. The SIMS intensities of $^{32}\text{S}^+$ and $^{80}\text{Se}^+$ versus depth in Fig. 1(b), on the other hand, are proportional to average Se and S concentrations where local variations are missing. Figure 2 shows the $^{80}\text{Se}^+$ signal from the SIMS image depth profiling taken at four different depths. The images (Fig. 2) clearly show a non-uniform Se distribution, where selected regions with a higher Se signal are marked by R1, R2, and R3. The variations in SIMS intensity are likely from a set of grains, similar to that observed in Fig. 1(a). The Se-rich regions vary with depth, as the Se-rich regions R1 and R2 disappear at larger depths, while other areas contain more Se (e.g., region R3). This confirms the spatial non-uniformity of the

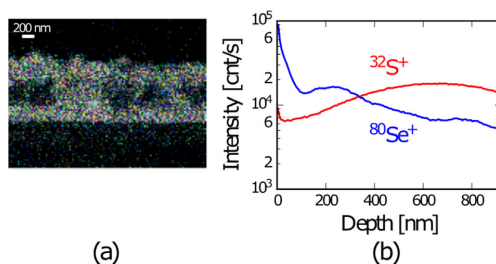


Figure 1 (a) Se $L\alpha$ SEM-EDX map of Sample 1, where white indicates Se signal and (b) corresponding SIMS depth profile.

Table 1 Experimental conditions of the three SIMS measurements performed on CZTSSe samples.

experimental conditions	O_2^+ image depth profile	O_2^+ depth profile	MCs^+ depth profile
primary ions	O_2^+	O_2^+	Cs^+
current	20 pA	100 nA	36 nA
raster size	$20 \times 20 \mu\text{m}^2$	$200 \times 200 \mu\text{m}^2$	$200 \times 200 \mu\text{m}^2$
analyzed area	$20 \times 20 \mu\text{m}^2$	62 μm^2 diameter	62 μm^2 diameter
impact energy	10 keV	10 keV	5 keV
angle of incidence (off the surface normal)	37.5°	37.5°	45°
detected ions	$^{32}\text{S}^+$ and $^{80}\text{Se}^+$	$^{32}\text{S}^+$, $^{80}\text{Se}^+$ and $^{98}\text{Mo}^+$	$^{32}\text{S}^{133}\text{Cs}^+$, $^{80}\text{Se}^{133}\text{Cs}^+$, and $^{98}\text{Mo}^{133}\text{Cs}^+$

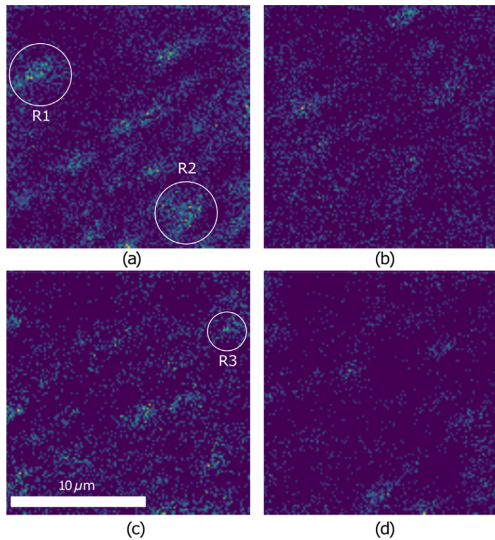


Figure 2 $^{80}\text{Se}^+$ signal acquired with SIMS image depth profiling at four different distances to the surface; (a) 20 nm, (b) 100 nm, (c) 250 nm and (d) 350 nm, and with a raster of $20 \times 20 \mu\text{m}^2$.

Se distribution and supports the notion that only some set of grains contain high amount of Se, most likely due to growth of Se rich grains. The S signals for identical depths are shown in Fig. 3, where a more uniform distribution is

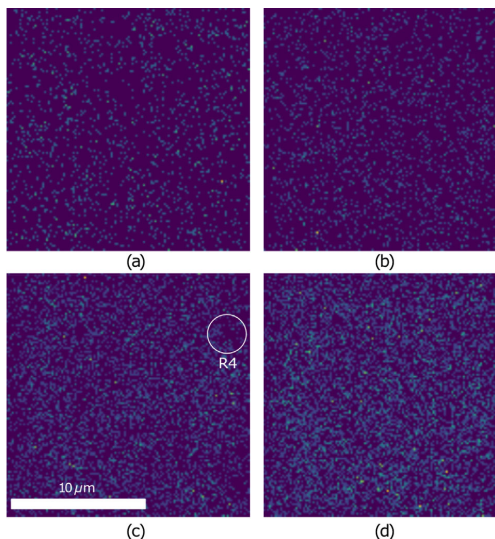


Figure 3 $^{32}\text{S}^+$ signal acquired with SIMS image depth profiling at four different distances to the surface; (a) 20 nm, (b) 100 nm, (c) 250 nm, and (d) 350 nm, and with a raster of $20 \times 20 \mu\text{m}^2$.

present and the intensities are increasing with depth. This correlates well with SEM-EDX for the S $\text{K}\alpha 1$ signal (not shown). The image depth profiles also indicate that the CZTSSe grows at the expense of CZTS. In Fig. 3(c), a dark region for the $^{32}\text{S}^+$ signal (R4) corresponds well to a high signal of $^{80}\text{Se}^+$, see region R3 in Fig. 2(c).

To overcome the dependence of the ionization efficiency of an element on the material composition (matrix effect), a Cs^+ cluster approach has successfully been applied in several materials [9–12]. Thus, to explore its potential use in CZTSSe films, both matrix elements M^+ secondary ions using O_2^+ primary beam and MCs^+ secondary ions using Cs^+ primary beam have been compared. The O_2^+ depth profile is shown in Fig. 4 and the MCs^+ depth profile is shown in Fig. 5. To simplify the analysis of the results, the measured SIMS intensity in the CZTSSe layer is divided into three sections as follows: (I) close to the surface; (II) middle of the sample; and (III) close to the Mo back contact. Both the M^+ and MCs^+ measurements show a change in S and Se signal with depth. To investigate if the SIMS intensities of S and Se correlate, the Se signal has been plotted as a function of the S signal in the insets in Figs. 4 and 5 with the O_2^+ and Cs^+ primary beam, respectively. Similar correlation plots have been made for CIGS [12] and III–V semiconductors [17]. If the signals have a linear dependence, the actual

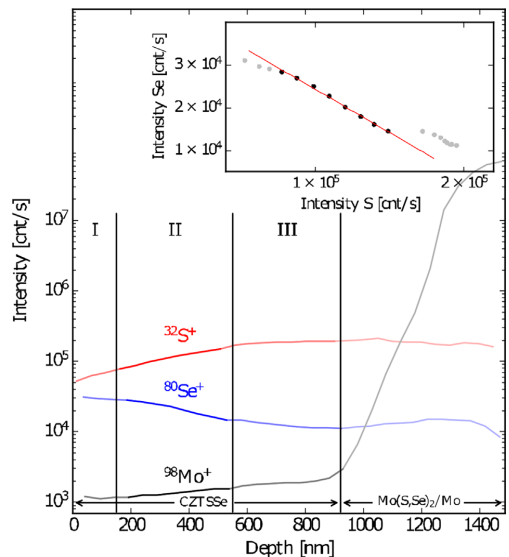


Figure 4 O_2^+ depth profile of CZTSSe and into the Mo back contact. The vertical lines at about 160 and 560 nm separate the three sections I, II, and III of the CZTSSe layer and the vertical line at 900 nm indicates the estimate for the back contact. Inset: corresponding intensity of Se as a function of intensity of S from section II (black points) and sections I and III (gray points). The solid line is the linear fit from the data points from section II.

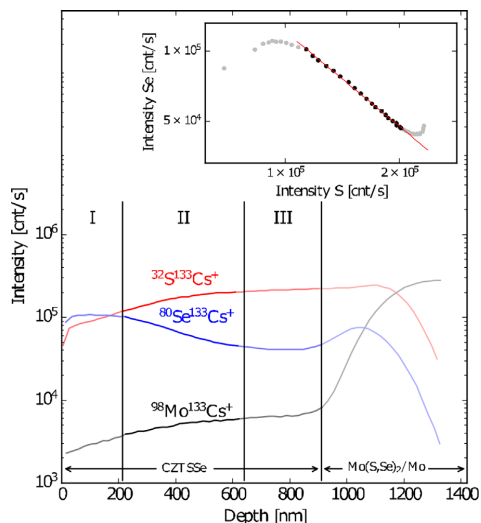


Figure 5 MCs^+ depth profile of CZTSSe and into the Mo back contact. The vertical lines at about 210 and 640 nm separate the three sections I, II, and III of the CZTSSe layer and the vertical line at 900 nm indicates the estimate for the back contact. Inset: corresponding intensity of Se as a function of intensity of S from section II (black points) and sections I and III (gray points). The solid line is the linear fit from the data points from section II.

concentration ratio between S and Se can be estimated [12]. The SIMS intensities for S and Se from section II (black points) show a linear dependence for the $\text{Se}/(\text{S}+\text{Se})$ ratio for both sources. However, the data points from sections I and III (gray points) deviate from this linear dependence. The deviation appears to be an offset for the O_2^+ depth profile while for the MCs^+ depth profile it appears to be exponential. The $\text{Se}/(\text{S}+\text{Se})$ ratios for section II are calculated using the intensities of S and Se, and the slope in the insets in Figs. 4 and 5. The ratio varies from 0.65 to 0.35 for the O_2^+ depth profile and from 0.55 to 0.25 for the MCs^+ depth profile. The deviation from linear dependence in sections I and III could be the result of two origins: (1) the high signal of selenium in section I and sulfur in section III causes a matrix effect or (2) the formation of secondary phases and elemental S or Se causes the total atomic concentration of S+Se to change and consequently the linear relationship is not valid regardless of the matrix effect. Interestingly, it has previously been reported that secondary phases form toward the back contact and the surface, supporting hypothesis (2) [13, 18, 19]. However, the deviation could also originate from the matrix effect (1). In the similar case for Ga and In in CIGS it has been shown that detecting MCs^+ ions strongly reduces the matrix effect, but not if the matrix elements, M, are detected [12, 20]. It has also been shown that the reduction of the matrix effect using MCs^+ secondary ions depends on the amount of Cs^+ ions

available compared to matrix elements and the sample material [21]. This can be achieved with a high sputtering yield by either increasing the impact angle or energy of the primary ion beam. The sputtering yield for the MCs^+ depth profile shown in Fig. 5 was calculated to be 1.8, which is lower than recommended [21]. Hence, the matrix effect cannot be excluded.

4 Conclusions The use of SIMS has been studied on a CZTSSe absorber with a Se gradient. A non-uniform spatial distribution of Se with depth has been detected with SIMS imaging depth profile, which correlates well with SEM-EDX results. This confirms that SIMS image depth profiling is a method that can be used to gain additional information about the spatial composition in CZTSSe. Furthermore, elemental ions and Cs cluster ions, detected utilizing O_2^+ and Cs^+ primary ions, respectively, have been compared in order to examine the impact of the matrix effect on the corresponding measurement modes. The results demonstrate that both configurations have low matrix effect far from the interfaces.

Acknowledgements This work has been funded from the Research Council of Norway (project 243642). We would like to thank Cameca for image processing assistance.

References

- [1] M. A. Contreras, J. Tuttle, A. Gabor, A. Tennant, K. Ramanathan, S. Asher, A. Franz, J. Keane, L. Wang, J. Scofield, and R. Noufi, in: Proc. 1994 IEEE 1st World Conf. Photovolt. Energy Convers. – WCPEC (A Jt Conf. PVSC, PVSEC PSEC) 1994, edited by Sheila Bailey, Hiroshi Sakai, and Gerhard Willeke (Waikoloa, Hawaii, 1991).
- [2] H. Zhao and C. Persson, *Thin Solid Films* **519**(21), 7508 (2011).
- [3] P. M. P. Salomé, J. Malaquias, P. A. Fernandes, M. S. Ferreira, A. F. da Cunha, J. P. Leitão, J. C. González, and F. M. Matinaga, *Sol. Energ. Mater. Sol. Cells* **101**, 147 (2012).
- [4] K. Woo, Y. Kim, W. Yang, K. Kim, I. Kim, Y. Oh, J. Y. Kim, and J. Moon, *Sci. Rep.* **3**, 3069 (2013).
- [5] T. Kato, N. Sakai, and H. Sugimoto, 2014 IEEE 40th Photovolt. Spec. Conf., 844 (2014).
- [6] Y. Qu, G. Zoppi, and N. S. Beattie, *Sol. Energy Mater. Sol. Cells*, **158**, 103–107.
- [7] N. Ross, J. Larsen, S. Grini, E. Särhammar, L. Vines, and C. Platzer-Björkman, in: Proc. 2016 IEEE 43th Photovolt. Spec. Conf. IEEE (2016), 0492–0497.
- [8] N. Ross, J. Larsen, S. Grini, E. Särhammar, L. Vines, and C. Platzer-Björkman, *Thin Solid Films*, **623**, 110–115 (2017).
- [9] Y. Gao, *J. Appl. Phys.* **64**(7), 3760 (1988).
- [10] C. W. Magee, W. L. Harrington, and E. M. Botnick, *Int. J. Mass Spectrom. Ion Process.* **103**(1), 45 (1990).
- [11] H. Gnaser and H. Oechsner, *Fresenius. J. Anal. Chem.* **341**(1–2), 54 (1991).
- [12] K. Kaufmann, S. Wahl, S. Meyer, and C. Hagendorf, *Surf. Interface Anal.* **45**(1), 434 (2013).

- [13] A. Redinger, K. Hönes, X. Fontané, V. Izquierdo-Roca, E. Saucedo, N. Valle, A. Pérez-Rodríguez, and S. Siebentritt, *Appl. Phys. Lett.* **98**(10), 101907 (2011).
- [14] J. J. Scragg, T. Kubart, J. T. Wätjen, T. Ericson, M. K. Linnarsson, and C. Platzer-Björkman, *Chem. Mater.* **25**(15), 3162 (2013).
- [15] S. P. Harvey, I. Repins, and G. Teeter, *J. Appl. Phys.* **117**(7), 074902 (2015).
- [16] T. Gershon, B. Shin, N. Bojarczuk, M. Hopstaken, D. B. Mitzi, and S. Guha, *Adv. Energy Mater.* **5**(2), 1 (2015).
- [17] H. Gnaser, *J. Vac. Sci. Technol. A* **12**(2), 452 (1994).
- [18] J. J. Scragg, J. T. Wätjen, M. Edoff, T. Ericson, T. Kubart, and C. Platzer-Björkman, *J. Am. Chem. Soc.* **134**(47), 19330 (2012).
- [19] C. Platzer-Björkman, J. Scragg, H. Flammersberger, T. Kubart and M. Edoff, *Sol. Energy Mater. Sol. Cells* **98**, 110 (2011).
- [20] J. Lee, S. H. Kim, and Y. Lee, *Surf. Interface Anal.* **46** (10–11), 1099 (2014).
- [21] K. Wittmaack, *Surf. Sci.* **606**(3–4), L18 (2012).

Paper II

**Practical limitations to selenium
annealing of compound
co-sputtered $\text{Cu}_2\text{ZnSnS}_4$ as a route
to achieving sulfur-selenium
graded solar cell absorber**

**Nils Ross, Jes Larsen, Sigbjørn Grini, Lasse Vines, Charlotte
Platzer-Björkman**

Thin Solid Films 623, 110–115 (2017).



Practical limitations to selenium annealing of compound co-sputtered $\text{Cu}_2\text{ZnSnS}_4$ as a route to achieving sulfur-selenium graded solar cell absorbers



N. Ross^{a,*,a,b}, J. Larsen^b, S. Grini^a, L. Vines^a, C. Platzer-Björkman^b

^aDepartment of Physics, Centre for Materials Science and Nanotechnology, University of Oslo, P. O. Box 1048 Blindern, Oslo N-0316, Norway

^bÅngström Laboratory, Div. Solid State Electronics, Department of Engineering Science, Uppsala University, Box 534, Uppsala SE-75121, Sweden

ARTICLE INFO

Article history:

Received 10 November 2016

Received in revised form 16 December 2016

Accepted 23 December 2016

Available online 3 January 2017

Keywords:

CZTSSe
Diffusion
Crystallisation
Sodium
Band gap gradient

ABSTRACT

The suitability of selenium annealing as a technique to introduce energy band gap gradients via sulfur-selenium substitution in $\text{Cu}_2\text{ZnSnS}_4$ (CZTS) films is evaluated. Compound co-sputtered CZTS precursors are annealed in selenium atmosphere at 425°C, either as-deposited or after a short time sulfur pre-anneal. The films are investigated by Raman spectroscopy and X-ray diffractometry, and the spatial distribution of elemental species measured by secondary ion mass spectrometry and energy dispersive X-ray spectroscopy. Sulfur-selenium gradients are not achieved for the as-deposited precursor. Sulfur-selenium gradients are achieved in the early stages of annealing for pre-anneal samples, where $\text{Cu}_2\text{ZnSn(S,Se)}_4$ (CZTSSe) formation is found to be correlated spatially with sodium distribution. These gradients are lost as the annealing progresses. Selenisation occurs by CZTSSe grain growth, rather than by direct substitution of selenium for sulfur. The spatial correlation of high sodium concentration with CZTSSe formation suggests that liquid-phase sodium selenide facilitates selenium incorporation during recrystallisation, limiting the practicality of anion-grading of CZTSSe during the annealing step as a means of establishing a graded band gap.

© 2017 Elsevier B.V. All rights reserved.

1. Introduction

The copper-zinc-tin-sulfide/selenide quaternary semiconductor material (hereafter CZTSSe or CZTS for the pure sulfide) is seen as a potential replacement for the mature copper-indium-gallium-selenide (CIGS) system as the absorber material in thin film solar cells. Although its record device sunlight-to-power efficiency remains 12.6% [1], CZTS absorbers are composed of earth-abundant materials, and show promise for future solar cell applications and as model systems for the improvement of other technologies. High efficiency CIGS solar cells employ In-Ga gradients through the thickness of the absorber film to modify the band gap and minimise recombination [2]. It is reasonable to expect the necessity of such band gap engineering in CZTSSe devices as one of the steps to improve efficiencies to compete with existing market technologies. It is also necessary to study how the peculiarities of the quaternary system such as band misalignment [3], deep defects within the absorber [4], band gap fluctuations from cation disorder defects [5], secondary-phases [6], and back-contact issues [7] might affect the

efficacy of and fabrication steps necessary for such a band gap grading. This provides motivation for studies into band gap grading in CZTSSe.

The band gap of pure selenide CZTSSe is 0.96 eV, and for the pure sulfide CZTS, 1.5 eV [8]. Substitution of one chalcogen for the other scales the band gap in an approximately linear fashion, with the majority of the change in the conduction band [9]. Increasing the sulfur proportion of the anion towards the front could result in a wider front band gap—a 'front grading'. Increasing the selenium proportion from low Se content towards the back to high Se content towards the front could yield a wider back band gap—a 'back grading'. A front S-Se grading was recently reported for CZTSSe from a stacked metallic precursor and the use of SeS_2 as the chalcogen source [10], but the mechanism of the gradient formation was not fully investigated. Back Se-S gradings have been reported for sequentially deposited compound-sputtered and metallic precursors [11], where it was noted that Se incorporation was less inhibited for stacked precursors than for CZTS films. A back grading has also been reported from solvent-based ink precursors sequentially annealed in sulfur then selenium [12], with preferential selenisation at the surface exposed directly to the selenium gas phase postulated as the mechanism responsible for the reported back grading. Good device properties were also reported for a CZTSSe sub-module and attributed to a back

* Corresponding author.

E-mail address: nilsross@smn.uio.no (N. Ross).

grading [13], but the mechanism of gradient formation was not made clear.

It is also known that diffusion of selenium in CZTSe is rapid [14], and that for nanoparticle precursors CZTSe crystallisation is dependent on nucleation and growth processes rather than surface-down reaction of the existing precursor with the gas phase [15]. We have also reported that for recrystallised CZTS films, selenisation results in rapid diffusion of selenium via grain boundaries, and that growth is limited by processes other than selenium diffusion through the film, resulting in phase segregation between the CZTS sulfide and the CZTSe selenide [16]. These studies call into question how annealing in selenium atmosphere has been sufficient to establish simple front-back chalcogen gradients in CZTSe, and how such processes might be controlled. Fine control over material grading is important for the analogous CIGS system, especially in the case of front band gap grading [2,17]. Modelling of CZTSe systems indicates sensitivity to the type, position, and extent of band gap grading [18].

Control of a simple 'back graded' band gap in CZTSe must require fine control of both the recrystallisation of the absorber and the chalcogen distribution within that absorber. The selenium-to-sulfur gradient must exist within single grains in a continuous manner to have a device-positive impact on collection and recombination. The mechanisms governing chalcogen substitution and crystal growth must therefore be understood in order to design and improve processes to form such chalcogen gradients. In this study, we study progressive selenisation of CZTSe starting from compound sputtered precursors in which SnS, ZnS, and CuS are co-sputtered rather than sequentially layered. In doing so we hope to minimise cation-specific effects such as differing chalcogen affinities, chalcogen diffusion coefficients, or sequential crystallisation through non-CZTS intermediates such as CuSn_2Se_3 . We also investigate the effect of sulfur pre-annealing prior to selenisation, in order to determine if there is some 'middle state' of CZTS formation which restricts selenisation sufficiently to form a chalcogen gradient without significant sulfide/selenide phase segregation.

2. Experimental details

Bilayer molybdenum back contacts were sputtered onto soda-lime glass substrates. $\text{Cu}_2\text{ZnSnS}_4$ precursor material was co-sputtered using a Lesker CMS-18 sputter system, in a 666 Pa argon atmosphere from sulfur-compound targets CuS, SnS, and ZnS. CuS and SnS were DC-sputtered at power densities 1.54 W cm^{-2} and 0.66 W cm^{-2} , respectively, and ZnS RF-sputtered at 3.3 W cm^{-2} . Three separate sets of $2.5 \text{ cm} \times 2.5 \text{ cm}$ precursors were fabricated, all with slightly different cation ratios. Elemental compositions for the three precursor families were determined by Rutherford back scattering-calibrated X-ray fluorescence measurements. These compositions are listed in Table 1 along with the other experimental conditions. Some changes in experimental conditions within each series are printed in colour for ease of reading.

For the annealing, precursors were either selenised directly or underwent a sulfur anneal prior to selenisation. Annealing was performed in a pyrolytic carbon coated graphite box. Sulfur annealing was performed with 40 mg of elemental sulfur, at 500°C and an argon pressure of $4.66 \times 10^4 \text{ Pa}$. Both the sulfur-annealed films and precursors were selenised with elemental selenium at 425°C , to promote slow incorporation of selenium into the absorbers. Selenisations were performed for various times at an argon pressure of $3.53 \times 10^4 \text{ Pa}$, using 40 mg of elemental selenium. The untreated precursor is denoted sample 'P'. After selenisation for 10 min, the suffix 'Se10' is added, so that sample is called 'PSe10'. Five minute sulfur annealed samples were 'S' and its subsequent 10-min selenisation 'SSe10'. Ten minute sulfur annealed samples were selenised

Table 1

Table of sample cation concentration ratios and sulfur (S, 500°C) and selenium (Se, 425°C) annealing conditions. Important differences in experimental conditions are marked with bold font.

Film	Cation conc. ratio		Time [min.]	
	$\frac{[\text{Cu}]}{[\text{Sn}]}$	$\frac{[\text{Zn}]}{[\text{Cu}]+[\text{Sn}]}$	S	Se
P	1.88	0.34	-	-
PSe10	1.88	0.34	-	10
S	1.88	0.34	5	-
SSe10	1.88	0.34	5	10
2SSe10	1.90	0.33	10	10
2SSe20	1.90	0.33	10	20
2SSe30	1.90	0.35	10	30
2SSe45	1.90	0.35	10	45

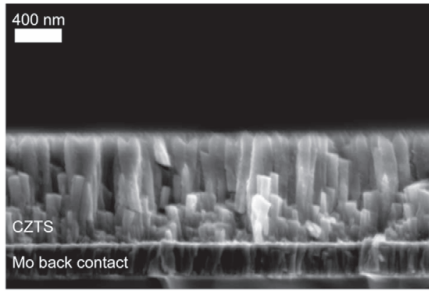
for 10, 20, 30, and 45 min. These samples are prefixed '2S' to indicate their longer sulfurisation, and have suffixes 'Se' which show their selenisation times: the samples are '2SSe10', '2SSe20', '2SSe30', and '2SSe45'. The list of samples with their preparation conditions is given in Table 1.

Grazing incidence X-ray diffraction (GIXRD) characterisation was performed in a Siemens D5000 diffractometer. Raman spectroscopy was performed using a Renshaw Invia equipped with 532 nm laser. Raman measurement of the back side of samples was achieved via a destructive lift off procedure. Films were glued top-down to a slide of clean glass and allowed to dry. Once adhesion was complete, the film substrate was removed by force, leaving a fragment of the film on the glass, cleaved along the interface between the film and the Molybdenum back contact. Scanning electron microscopy (SEM) images and energy dispersive X-ray spectroscopy (EDX) linescans were obtained using a Zeiss Leo 1550 with a 5 kV accelerating voltage. Low voltage was used to minimise the interaction volume and improve the spatial resolution of the EDX. Lines analysed were Cu-L, S-K, Se-L, Zn-L and Sn-L. Cu-L and Zn-L overlap but were deconvolved using Oxford Instruments' AZtec software. Sn-L had a low signal-to-noise. Cation lines could be resolved to the extent that measured cation elemental ratios were as expected. The Mo-L line overlaps the S-K line heavily and was not deconvolved: the back Mo contact of the film can be identified by the sudden rise in the S signal. Secondary ion mass spectrometry (SIMS) depth profile measurements were performed using a Cameca IMS 7f instrument with a primary beam of 5 keV Cs^+ ions. The beam was scanned across a raster of $200 \times 200 \text{ um}$ and an analyzed area with a diameter of 62 um . In order to minimize the potential matrix effects due to a change in $[\text{S}] / ([\text{S}] + [\text{Se}])$ ratio, MCS^+ clusters were detected in SIMS.

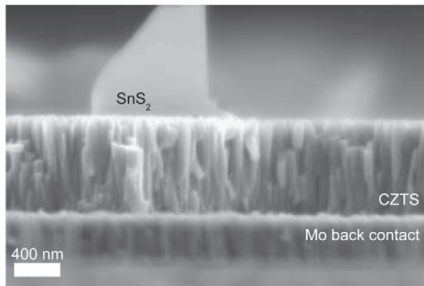
3. Results

A survey of sulfur anneal conditions was performed to find a state between the CZTS precursor and large-grain CZTS for which subsequent selenisation might produce either chalcogen gradients or variations in the profile of selenisation to facilitate further investigation. Even at the relatively low temperature of 500°C , large CZTS grains crystallised after 20 min or more, and produced sulfide/selenide grain segregation on selenisation. However, films sulfur-annealed at 500°C for less than 20 min remained morphologically similar to precursors, and selenised differently to both large grain CZTS and un-sulfurised precursor samples.

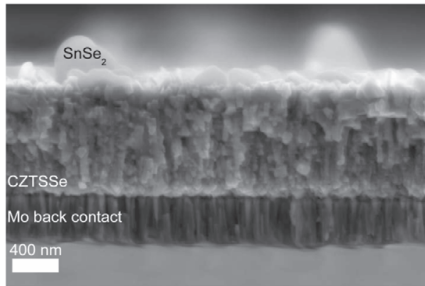
In the first instance, the effects of a 10-min 425°C selenisation on both precursor (sample 'P') and 5-minute, 500°C sulfur annealed (sample 'S') films were investigated. In the cross-sectional SEM images shown in Fig. 1, the morphology of the sulfur pre-annealed 'S' is very similar to the untreated precursor 'P'. The main observable difference is the presence of large surface structures on 'S', identified later by GIXRD as SnS_2 . A 425°C selenium anneal produced samples



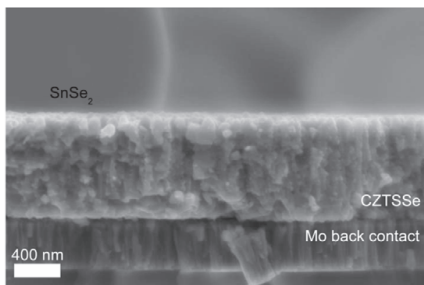
(a, P)



(b, S)

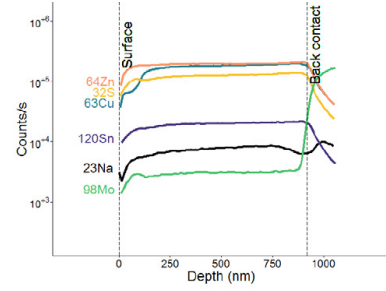


(c, PSe10)

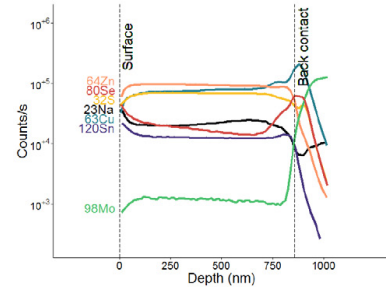


(d, SSe10)

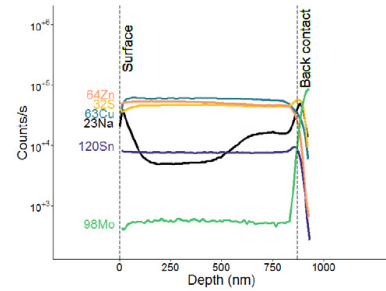
Fig. 1. Cross-sectional SEM images for samples (a) P; (b) PSe10; (c) S; (d) SSe10. Samples 'P' and 'S' have very similar morphology, but recrystallisation at the back contact in SSe10 is more advanced than in PSe10.



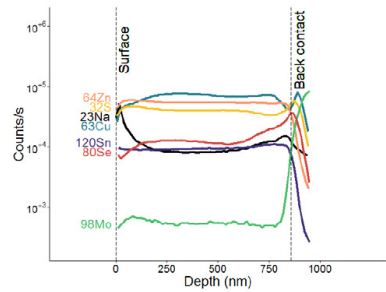
(a, P)



(b, PSe10)



(c, S)



(d, SSe10)

Fig. 2. MCs⁺ SIMS profiles for samples (a) P; (b) PSe10; (c) S; (d) SSe10.

PSe10 from the precursor 'P' and 'SSe10' from the sulfur-annealed 'S'. The morphology within the absorbers is very similar between the selenised samples, with one subtle exception: crystallisation very

close to the back contact is significantly more advanced in the sulfur-annealed sample, SSe10. The structure at the back contact is more smooth and laterally continuous than in PSe10.

Secondary ion mass spectrometry was used for elemental analysis in depth. MCs⁺ SIMS profiles are shown in Fig. 2 for samples 'P', 'S', PSe10, and SSe10. For selenised precursor PSe10, selenium is spread throughout the CZTSSe, with a slight selenium gradient from the front surface, but no complementary sulfur gradient. Sulfur- and selenium-annealed SSe10 shows an increase in selenium immediately at the back contact, tapering off several hundred nanometres into the film. This selenium extends further into the film than the back contact MoSe₂ peak of PSe10, and indicates the formation of a CZTSSe selenide near the back contact. These data match the higher degree of back contact crystallisation seen by SEM.

The ²³Na distributions in the SIMS data in Fig. 2 are of interest. Due to the possibility of ⁷⁸Se⁷⁸Se interference with the ²³Na¹³³Cs signal, these profiles were verified with O₂+ SIMS. The precursor 'P' has a very low level of sodium: either there is no sodium present, or a very small amount distributed through the film. Following 10-min selenisation in PSe10, a higher amount of sodium is distributed evenly through the film, with a small accumulation at the front and back of the CZTSSe layer. In contrast, the sodium distribution in 'S' has been changed dramatically by the sulfur pre-anneal: there is an accumulation of sodium in the first several hundred nanometres at the back of the film, as well as an accumulation near the front surface of the film. Selenisation spreads this sodium gradient out in SSe10 while simultaneously segregating the selenium in a pattern that correlates well with the preceding sodium distribution: the selenide crystallises more completely near the back contact.

The pre-annealed film underwent more complete selenide crystallisation towards the back contact than the precursor. A longer sulfuration of 10 min was used to attempt to increase the back-contact effect without crystallising large grains in the sulfur anneal. Selenisations were performed for 10, 20, 30, and 45 min: samples 2SSe10, 2SSe20, 2SSe30, and 2SSe45, respectively. EDX was used to probe the uniformity of the selenisation for all samples, but for brevity only the EDX line scans for samples 2SSe10–45 are shown in Fig. 3. The EDX profiles for the other samples reproduced similar details as the SIMS data reported in Fig. 2, but showed a uniform selenium distribution in the CZTSSe layer for PSe10. The EDX profile of the 10-min selenised film 2SSe10 reveals the familiar preferential selenisation towards the back contact. With increasing selenisation time, more selenium is incorporated towards the front of the film. As selenisation time increases to 30 min (2SSe30) and 45 min (2SSe45), the selenium distribution becomes less uniform, with some locations showing the kind of initially desired back-to-front selenium grading as in Fig. 3 (c), and others showing sulfide and selenide grain segregation as in Fig. 3 (d). EDX density maps (not included) confirmed that at 30 min of selenation anneal and beyond, the lateral uniformity of the selenium distribution is compromised, and distinct sulfide and selenide-rich grains are formed. From a previous study [16], it is known that continuing to selenise such structures results in the growth of the selenide grains via removal of cations from the sulfide grains, so longer selenisations were not attempted.

Raman spectra were recorded for both the front-side and back-side after lift-off of the CZTS/CZTSSe layers, and are shown in Fig. 4. Sn(S,Se)₂ surface structures were excluded from the beam spot if possible. Front side SnSe₂ structures were too small to avoid for sample PSe10. In the precursor 'P', the CZTS peak at 338 cm⁻¹ [19] is present, and there is no CZTSe peak. For the back side Raman measurements, all selenised samples show a CZTSSe peak between the CZTSe position at ~197 cm⁻¹ [11] and the CZTS peak. For the front side measurements, there is no CZTSSe detected for sample SSe10, and only a small peak for 2SSe10, indicating only a small quantity of selenide is within the laser penetration depth near the surface. The back/front contrast exists for short time selenisations, and is lost as

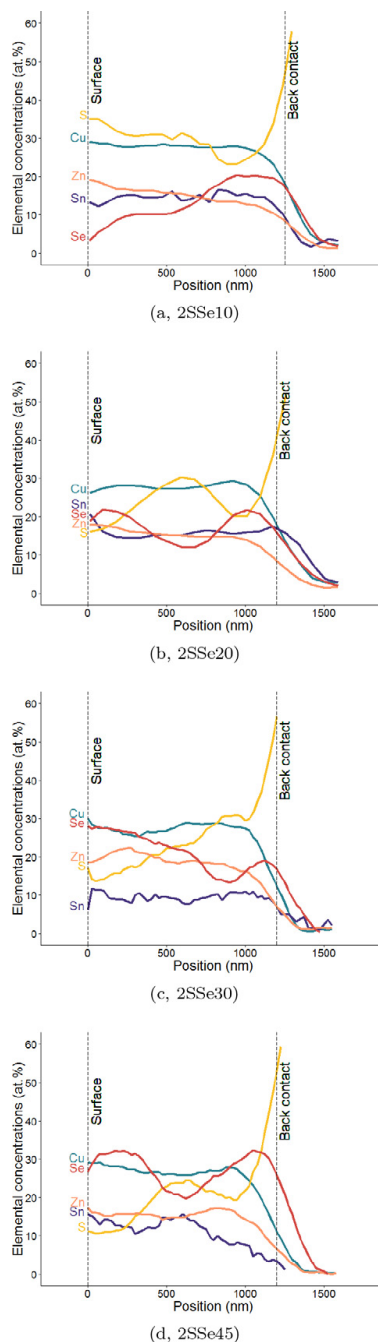


Fig. 3. Surface-to-back contact EDX line scans for (a) 2SSe10, (b) 2SSe20, (c) 2SSe30, and (d) 2SSe45, showing that the initial back contact sulfur-selenium gradient is lost as selenisation progresses. Accelerating voltage is 5kV and maximum diameter of interaction volume was estimated to be 170nm. The Mo-L line and S-K lines cannot be resolved: the back Mo contact of the film can be identified by the sudden rise in the S signal.

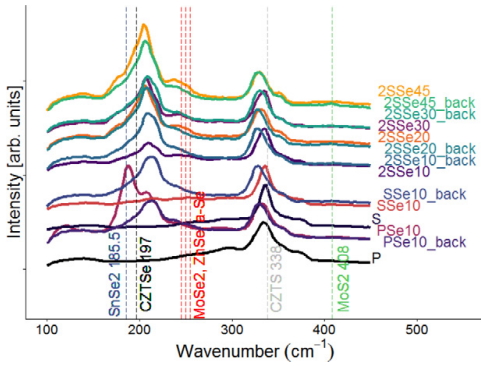


Fig. 4. Raman spectra for all samples, for both the front and back surfaces. The CZTSe peak is strong for the back side but weak for the front side in samples SSe10 and 2SSe10.

selenide grows throughout the film in the longer selenisations. An increase in selenisation is always accompanied by a blue shift and broadening of the CZTS peak. These Raman results corroborate the SIMS results from Fig. 2 and EDX results from Fig. 3: for precursors, the selenide forms throughout the thickness of the film; for the sulfur pre-annealed samples, the CZTSe selenide crystallises first near the back contact of the film, and forms throughout the film as the anneal progresses.

The 1.5° incidence angle GIXRD patterns for all samples are shown in Fig. 5, separated along the vertical axis for clarity. Of particular note are the CZTS 112 peak at $\sim 28.44^\circ$ [20] and the CZTSe 112 peak between this peak and the selenide-only CZTSe position $\sim 27.16^\circ$ [21]; selenised samples show both peaks, indicating the existence of both CZTS and CZTSe crystal structures. The spectra for 'P' and 'S' are close to identical: both show a broad peak between 45° and 60° , characteristic of precursor 'pre-kesterite' samples that are not yet properly crystallised kesterite. This match in the samples' crystallinity as measured by GIXRD corroborates the similarity of their structure as observed by SEM, and indicates that any subsequent differences in selenisation are not the result of differing input crystal properties. The 'pre-kesterite' peak reduces steadily in amplitude with increasing selenisation time for samples 2SSe10 through 2SSe45, being replaced by the 204 and 116 peaks of CZTS and associated CZTSe peaks. This reduction in amplitude from 'pre-kesterite' to well resolved CZTS peaks indicates an increase in the

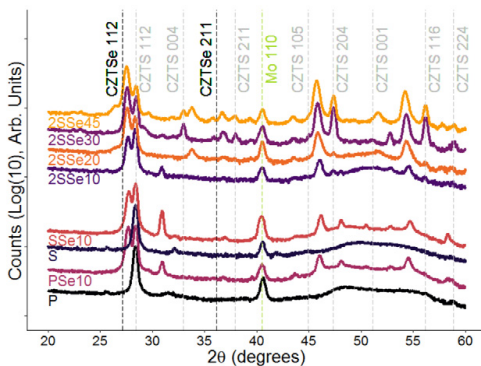


Fig. 5. GIXRD patterns for all samples, for an incident angle of 1.5° .

degree of crystallinity of the film, and shows that the increasing degree of selenisation of the films observed by EDX is accompanied by recrystallisation.

4. Discussion

SIMS (Fig. 2), Raman spectroscopy (Fig. 4), and EDX showed that compound co-sputtered precursors selenise uniformly throughout the thickness of the film, even for very mild selenisation conditions. The slight gradient in selenium content measured by SIMS was not observed in EDX line scans, and not accompanied by a corresponding sulfur gradient. The slight SIMS gradient may merely be the result of lateral non-uniformity of the measurement [22]. In contrast to this chalcogen uniformity in depth, Qu et al. produced a sulfide-selenide gradient in CZTSe by selenisation of nanoparticle precursors and ascribed the gradient to the preferential selenisation of the surface exposed to the gas phase [15]. Furthermore, in our previous study of fully recrystallised CZTS, CZTSe selenide grains nucleated around surfaces and CZTS grain boundaries, growing by removal of cations and sulfur from surrounding CZTS material [16]. Selenium gradients which could be clearly observed by EDX and X-ray diffractometry were produced by Salomé et al. for stacked compound and metallic precursors [11]. These differences imply that the primary factors controlling the distribution of selenium in the CZTSe resulting from selenium annealing are properties of the precursor, rather than only the of proximity of the surface of that precursor to the selenium gas phase.

Short time 425°C selenisations of sulfur pre-annealed films showed preferential crystallisation of the CZTSe selenide near the back contact (Fig. 1). Sulfur-selenium gradients near the back contact were observed by SIMS (Fig. 2) and EDX (Fig. 3), and confirmed by back and front side Raman spectroscopy (Fig. 4). This gradient was selenide rich at the back to selenide-poor at the front, and if maintained in a fully recrystallised absorber would result in a quasi-electric field directing electrons away from the junction, hindering carrier collection. Upon further annealing, the chalcogen gradient was lost. At the longest annealing times studied, there was evidence of segregation of sulfide and selenide grains. GIXRD (Fig. 5) showed that progressive selenisation of the film was always associated with an increasing degree of crystallinity. Given the clear increase in back contact crystallinity and selenisation of sulfur pre-annealed then selenised films, the implication was that selenium was introduced in the recrystallisation itself, rather than by substitution into either the metastable precursor or CZTS grains.

Although the morphology as measured by SEM and crystallinity as measured by GIXRD for the precursor and sulfur pre-annealed samples were similar, SIMS showed a difference in distribution of sodium at the back contact. The CZTSe crystallisation was more rapid in parts of the film with higher sodium concentration. Sodium-assisted sintering of CZTSe has been observed by other workers in solution processed films [23]. The mechanism proposed in that study was that of a liquid phase Na_2Se_x species supplying selenium to the growing CZTSe crystal. The initial back-contact CZTSe growth observed in the sulfur pre-annealed samples with high levels of sodium near the back contact suggests a similar sodium-assisted growth mechanism was dominant in this study. Since the selenium diffusion into the film is very rapid, selenium is available everywhere; but it is only in the presence of excess sodium that the rate of selenide crystal formation is increased.

The importance of this sodium assisted selenisation places practical restrictions on the introduction of chalcogen gradients in CZTSe films starting from compound co-sputtered precursors. To make a useful band gap graded absorber layer, the precursor must fully recrystallise with an appropriate anion gradient, without segregation of sulfide and selenide phases into separate grains. If the introduction

of sodium via NaF layers is used to guide the selenisation, sodium will diffuse through the film faster than the CZTSSe selenide will recrystallise, spreading the anion gradient out before the annealing is complete. CZTS sulfide and CZTSSe selenide grains may segregate during the annealing, requiring high temperatures and long annealing times to resolve completely into selenide grains. Furthermore, the distribution of sodium is important for the device performance itself, as it has been shown to enhance device performance by increasing the hole density and moving the acceptor level closer to the conduction band [24], consistent with the conjecture that its presence in the anneal enhances the concentration of V_{Cu} intrinsic shallow acceptors, as it is hypothesised to do in CIGS [25]. Any method of arresting the sodium spread during annealing to preserve the chalcogen gradient will likely have undesirable electronic effects. Reconciling the different contributions of sodium, the requirement for full absorber recrystallisation, and the necessity to imprint a chalcogen gradient likely places too many restrictions on the annealing process. These restrictions limit the potential for a chalcogen gradient to be introduced solely during the annealing step in the case of compound co-sputtered CZTS.

In this study, pure sulfide CZTS precursors and annealed films annealed in selenium produced CZTSSe selenides with approximately 20–40% sulfur, with the only supply of sulfur in the anneal coming from the film itself. This suggests that some precursor chalcogen is retained through crystallisation, although this study provided no information about its mobility during annealing. An alternative approach to obtain chalcogen gradings in compound-sputtered CZTSSe without the need to control so many different factors in the anneal may be to sputter a sulfur-selenium gradient or step into the precursor. We believe such a ‘control of precursor’ approach to be a potentially more productive path for future investigations of chalcogen gradient formation in compound co-sputtered CZTSSe than attempting to introduce the gradient in the annealing step.

5. Conclusion

In this study, compound co-sputtered CZTS precursors and precursor-like films were annealed in selenium atmospheres. By doing so, we have gained some information about the factors limiting control of chalcogen gradients introduced in the annealing step of compound co-sputtered precursors. Selenisation and recrystallisation of the absorber occur in the same process, and this process is affected by the presence of sodium. The mechanism coupling sodium and selenide recrystallisation was tentatively identified as incorporation of selenium into the growing crystal via sodium selenide compounds. The difficulties in simultaneously controlling sodium distribution, selenium incorporation, and crystallisation in the annealing phase were discussed, and the production of graded precursors as an alternative approach recommended as the way forward to achieving chalcogen gradings in compound sputtered CZTSSe.

Acknowledgement

Funding from the Research Council of Norway (project 243642), Swedish Foundation for Strategic Research, and Wallenberg Academy Fellows program is gratefully acknowledged.

References

- [1] W. Wang, M.T. Winkler, O. Gunawan, T. Gokumen, T.K. Todorov, Y. Zhu, D.B. Mitzi, Device characteristics of CZTSSe thin-film solar cells with 12.6% efficiency, *Adv. Energy Mater.* 4 (2014) 1301465.
- [2] C. Frisk, C. Platzer-Björkman, J. Olsson, P. Szañlawski, J.T. Wätjen, V. Fjällström, P. Salomé, M. Edoff, Optimizing Ga-profiles for highly efficient $Cu(In,Ga)Se_2$ thin film solar cells in simple and complex defect models, *J. Phys. D* 47 (2014) 485104.
- [3] M. Bär, B.A. Schubert, B. Marsen, R.G. Wilks, S. Pookpanratana, M. Blum, S. Krause, T. Unold, W. Yang, L. Weinhardt, C. Heske, H.W. Schock, Cliff-like conduction band offset and KCN-induced recombination barrier enhancement at the CdS/Cu_2ZnSnS_4 thin-film solar cell heterojunction, *Appl. Phys. Lett.* 99 (2011) (222105–1222105-3).
- [4] S. Chen, A. Walsh, X. Gong, S. Wei, Classification of lattice defects in the kesterite Cu_2ZnSnS_4 and $Cu_2ZnSnSe_4$ earth-abundant solar cell absorbers, *Adv. Mater.* 25 (2013) 1522–1539.
- [5] J. Scragg, J. Larsen, M. Kumar, C. Persson, J. Sandler, S. Siebentritt, C. Platzer-Björkman, Cu–Zn disorder and band gap fluctuations in $Cu_2ZnSn(S,Se)_4$: Theoretical and experimental investigations, *Phys. Status Solidi B* 253 (2013) 247–254.
- [6] J.T. Wätjen, J. Engman, M. Edoff, C. Platzer-Björkman, Direct evidence of current blocking by ZnSe in $Cu_2ZnSnSe_4$ solar cells, *Appl. Phys. Lett.* 100 (2012) 173510.
- [7] J. Scragg, J.T. Wätjen, M. Edoff, T. Ericson, T. Kubart, C. Platzer-Björkman, A detrimental reaction at the molybdenum back contact in $Cu_2ZnSn(S,Se)_4$ thin-film solar cells, *J. Am. Chem. Soc.* 134 (2012) 19330–19333.
- [8] A. Walsh, S. Chen, S. Wei, X. Gong, Kesterite thin-film solar cells: advances in materials modelling of Cu_2ZnSnS_4 , *Adv. Energy Mater.* 2 (2012) 400–409.
- [9] S. Chen, A. Walsh, J. Yang, X.G. Gong, L. Sun, P. Yang, J. Chu, S. Wei, Compositional dependence of structural and electronic properties of $Cu_2ZnSn(S,Se)_4$ alloys for thin film solar cells, *Phys. Rev. B* 83 (2011) 125201.
- [10] K. Yang, D. Son, S. Sung, J. Sim, Y. Kim, S. Park, D. Jeon, J. Kim, D. Hwang, C. Jeon, D. Nam, H. Cheong, J. Kang, D. Kim, A band-gap-graded CZTSSe solar cell with 12.3% efficiency, *J. Mater. Chem. A* 4 (2016) 10151.
- [11] P.M.P. Salomé, J. Malaquias, P.A. Fernandes, M.S. Ferreira, A.F. da Cunha, J.P. Leitão, J.C. González, F.M. Matinaga, Growth and characterization of $Cu_2ZnSn(S,Se)_4$ thin films for solar cells, *Sol. Energy Mater. Sol. Cells* 101 (2012) 147–153.
- [12] K. Woo, Y. Kim, W. Yang, K. Kim, I. Kim, Y. Oh, J.Y. Kim, J. Moon, Band-gap-graded $Cu_2ZnSn(S_{1-x}Se_x)_4$ solar cells fabricated by an ethanol-based, particulate precursor ink route, *Sci. Rep.* 3 (2013) 3069.
- [13] T. Kato, N. Sakai, H. Sugimoto, Efficiency improvement of $Cu_2ZnSn(S,Se)_4$ submodule with graded bandgap and reduced backside ZnS segregation, *Proc. IEEE PVSC 41* (2014) 0844–0846.
- [14] S.P. Harvey, I. Repins, G. Teeter, Defect chemistry and chalcogen diffusion in thin-film $Cu_2ZnSnSe_4$ materials, *J. Appl. Phys.* 117 (2015) 074902.
- [15] Y. Qu, G. Zoppi, N.S. Beattie, Selenization kinetics in $Cu_2ZnSn(S,Se)_4$ solar cells prepared from nanoparticle inks, *Sol. Energy Mater. Sol. Cells* 158 (2016) 130–137.
- [16] N. Ross, J. Larsen, S. Grini, E. Särhammar, L. Vines, C. Platzer-Björkman, $Cu_2ZnSn(S,Se)_4$ solar cell absorbers from diffusion of selenium into annealed Cu_2ZnSnS_4 absorbers, *Proc. IEEE PVSC 43* (2016) 0492–0497.
- [17] M. Gloecker, J.R. Sites, Band-gap grading in $Cu(In,Ga)Se_2$ solar cells, *J. Phys. Chem. Solids* 66 (2005) 1891–1894.
- [18] D. Hironiwa, M. Murata, N. Ashida, Z. Tang, T. Minemoto, Simulation of optimum band-gap grading profile of $Cu_2ZnSn(S,Se)_4$ solar cells with different optical and defect properties, *Jpn. J. Appl. Phys.* 53 (2014) 071201.
- [19] M. Altonsaar, J. Raudoja, K. Timmo, M. Danilson, M. Grossberg, J. Krustok, E. Melnikov, $Cu_2Zn_{1-x}Cd_xSn(S_{1-y}Se_y)_4$ solid solutions as absorber materials for solar cells, *Phys. Status Solidi A* 205 (2008) 167–170.
- [20] 04-005-0388, Cu_2ZnSnS_4 , International Centre for Diffraction Data. 2007.
- [21] 04-010-6295, $Cu_2ZnSnSe_4$, International Centre for Diffraction Data. 2002.
- [22] S. Grini, N. Ross, T. Sky, C. Platzer-Björkman, C. Persson, L. Vines, Secondary ion mass spectrometry as a tool to study selenium gradient in $Cu_2ZnSn(S,Se)_4$, *Phys. Status Solidi C* (2017) (in print).
- [23] C.M. Sutter-Fella, J.A. Stückelberger, H. Hagendorfer, F.L. Mattina, L. Kranz, S. Nishiwaki, A.R. Uhl, Y.E. Romanyuk, A.N. Tiwari, Sodium assisted sintering of chalcogenides and its application to solution processed $Cu_2ZnSn(S,Se)_4$ thin film solar cells, *Chem. Mater.* 26 (2014) 1420–1425.
- [24] J.V. Li, D. Kucuskas, M.R. Young, I.L. Repins, Effects of sodium incorporation in Co-evaporated $Cu_2ZnSnSe_4$ thin-film solar cells, *Appl. Phys. Lett.* 102 (2013) 163905.
- [25] Z. Yuan, S. Chen, Y. Xie, J. Park, H. Xiang, X. Gong, S. Wei, Na-diffusion enhanced p-type conductivity in $Cu(In,Ga)Se_2$: a new mechanism for efficient doping in semiconductors, *Adv. Energy Mater.* (2016) 1601191.

Paper III

Low temperature incorporation of selenium in $\text{Cu}_2\text{ZnSnS}_4$: Diffusion and nucleation

Sigbjørn Grini, Nils Ross, Clas Persson, Charlotte Platzer-Björkman, Lasse Vines

Thin Solid Films 665, 159–163 (2018).





Low temperature incorporation of selenium in $\text{Cu}_2\text{ZnSnS}_4$: Diffusion and nucleation

Sigbjørn Grini^{a,*}, Nils Ross^{a,b}, Clas Persson^a, Charlotte Platzer-Björkman^b, Lasse Vines^a

^a Department of Physics, Center for Materials Science and Nanotechnology, University of Oslo, P.O.Box 1048, Blindern, N-0316 Oslo, Norway

^b Ångström Solar Center, Division of Solid State Electronics, Uppsala University, Uppsala, Uppland 75120, Sweden



ARTICLE INFO

Keywords:

$\text{Cu}_2\text{ZnSnS}_4$
Selenium diffusion
Band gap grading
Nucleation
Recrystallization
Grain boundary diffusion
Diffusion
Secondary ion mass spectrometry

ABSTRACT

Band gap grading of $\text{Cu}_2\text{ZnSn}(\text{S},\text{Se})_4$ (CZTSSe) solar cells can be achieved by varying the $S_r = [\text{S}]/([\text{S}] + [\text{Se}])$ ratio in the absorber layer with depth. One approach is a two-step annealing process where the absorber is first sulfurized to $\text{Cu}_2\text{ZnSnS}_4$ (CZTS) followed by selenization to form CZTSSe. However, once nucleation of CZTSSe initiates, the rapid interchange of S and Se limits the control over the S_r ratio with depth. Here, we have studied incorporation of Se into CZTS and observed the behavior of Se below and up to the nucleation temperature of CZTSSe. Se diffusion at 337 and 360 °C is dominated by grain boundary diffusion while some increase of Se is also seen in the region from 100 to 800 nm from the surface. After selenization at 409 °C, recrystallization is observed and CZTSSe grains are formed. The recrystallization is more rapid for a smaller average grain size and is facilitated by diffusion of Na from the back contact. The grain boundary diffusion is identified with secondary ion mass spectrometry measurements by measuring the accumulation in the CZTS/Mo interface for three samples with different average grain size.

1. Introduction

The best $\text{Cu}_2\text{ZnSn}(\text{S},\text{Se})_4$ (CZTSSe) devices produced to date have introduced the chalcogens S and Se either as part of the precursor or as gas during the crystallization process [1–5]. By including both chalcogens in the complex crystallization process, control of their diffusion and nucleation is limited, and it is difficult to obtain a controlled $S_r = [\text{S}]/([\text{S}] + [\text{Se}])$ ratio with depth. Nevertheless, there are pathways to achieve an S_r gradient in the CZTSSe layer by having S and Se annealed in two steps or through non-symmetric annealing conditions [2,6–8]. If the anneals are performed at low crystallization temperatures, partial recrystallization of the absorber may occur which results in a lateral non-homogeneous distribution of S and Se [9], which can falsely be interpreted as an S_r gradient with grazing incident X-ray diffraction (GIXRD) or conventional secondary ion mass spectrometry (SIMS) depth profile [10]. Previously, we have discussed the practical limitations of chalcogen control in the crystallization process, where sodium assists grain growth [11]. To achieve a controlled S_r gradient a possible approach is to complete a full crystallization with either S or Se and subsequently diffuse in the other chalcogen without triggering nucleation. The challenge is that the energy required to diffuse Se into the existing grains is similar or perhaps higher than the energy required to start to nucleate new grains. In this work we evaluate the diffusion of Se

into CZTS at temperatures up to nucleation by annealing in a selenium ambient at 337, 360 and 409 °C for three samples with different average grain size.

2. Experimental details

Bilayer molybdenum back contact was sputtered onto a soda-lime glass substrate. $\text{Cu}_2\text{ZnSnS}_4$ precursors were co-sputtered using CuS, ZnS and SnS targets in a Lesker CMS-18 sputter system. Elemental compositions in the precursors were determined with Rutherford back-scattering calibrated X-ray fluorescence (XRF) measurements. The samples were sulfurized into $\text{Cu}_2\text{ZnSnS}_4$ for 10, 20 and 40 min at 500 ± 10 °C in a tube furnace within a pyrolytic carbon coated graphite box with 80 mg of elemental sulfur placed in a small hole on each side of the box and an argon pressure in the furnace of 35 kPa. The temperature was chosen to avoid secondary phase formation and loss of sulfur as have previously shown to occur at higher temperatures for our furnace [12]. After sulfurization and initial characterization, each sample was subjected to an anneal in the same tube furnace with 90 mg Se in the graphite box and an argon pressure of 35 kPa at 337 ± 10 , 360 ± 10 and 409 ± 10 °C for 30 min, from now on called “selenization”. The cation ratios and sulfurization conditions are described in Table 1.

* Corresponding author.

E-mail address: sigbjorn.grini@smn.uio.no (S. Grini).

<https://doi.org/10.1016/j.tsf.2018.09.024>

Received 15 June 2018; Received in revised form 10 August 2018; Accepted 12 September 2018

Available online 13 September 2018

0040-6090/ © 2018 Elsevier B.V. All rights reserved.

Table 1

Cation ratios measured with X-ray fluorescence of the precursor and sulfurization conditions in the tube furnace.

Sample name	Cation ratios		Sulfurization conditions	
	[Cu]/[Sn]	[Zn]/([Cu] + [Sn])	Temperature (°C)	Time (minutes)
A	1.92 ± 0.02	0.35 ± 0.02	500 ± 10	10
B	1.92 ± 0.02	0.35 ± 0.02	500 ± 10	20
C	1.92 ± 0.02	0.35 ± 0.02	500 ± 10	40

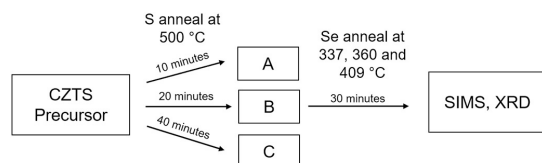


Fig. 1. Overview over the experiment. CZTS precursors were sulfurized at 500 °C for 10, 20 and 40 min and produced samples A, B and C respectively. Each sample was subsequently selenized at 337, 360 and 409 °C and characterized with secondary ion mass spectrometry (SIMS) and X-ray diffraction (XRD).

A Bruker AXS D8 Discover X-ray diffraction (XRD) system was used to study structural properties of the samples before and after selenization. Each sample was surveyed with a $\theta/2\theta$ scan ranging from 10° to 65° with an increment of 0.01° and a high-resolution scan from 27° to 29° with an increment of 0.002° to study the (112) reflection in detail. Cross-sectional scanning electron microscopy (SEM) images were obtained using a Zeiss Leo 1550 with a 5 kV accelerating voltage. Top-view SEM images were obtained with JEOL JSM-IT300 with a 5 kV accelerating voltage. The samples were studied with secondary ion mass spectrometry (SIMS) using a Cameca IMS 7f magnetic sector instrument. 5 keV Cs⁺ primary ions were mainly used, and the beam was rastered over an area of 150 × 150 μm² with a current of 20 nA. Secondary MCs⁺ cluster ions were detected from the central part of the crater (33 μm in diameter), where “M” is the element of interest. The ionization of MCs⁺ cluster ions is suggested to be less influenced by a change in concentration of matrix elements compared to that of M⁺ ions since the Cs⁺ ions are previously ionized as the primary beam [13]. The cluster ⁸⁰Se ¹³³Cs was considered most suited to observe Se given its abundance and ²³Na ¹³³Cs was used to track Na. Control measurements were also carried out on selected samples by detecting negative ions with a 15 keV Cs⁺ primary beam and positive ions with 10 keV O₂⁺ primary beam to confirm that no significant interference occurred. The sputter time was converted to depth by measuring the depth of the crater with a Stylus profilometer. For measurements on the same sample after heat treatment the depth was calibrated with the inflection point of the ⁹⁸Mo ¹³³Cs signal at the interface between CZTS and Mo. An overview over the experiment is displayed in Fig. 1.

3. Results and discussion

Fig. 2 displays cross sectional SEM images of the samples A, B and C

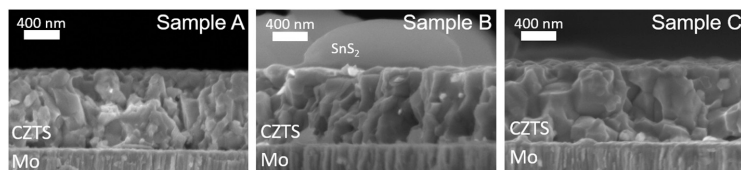


Fig. 2. Cross-sectional scanning electron microscopy (SEM) images of the CZTS samples A, B and C which was sulfurized at 500 °C for 10, 20 and 40 min respectively from the same precursor. Some SnS₂ is observed on the SEM image of sample B but was also seen on top of all samples with an optical microscope.

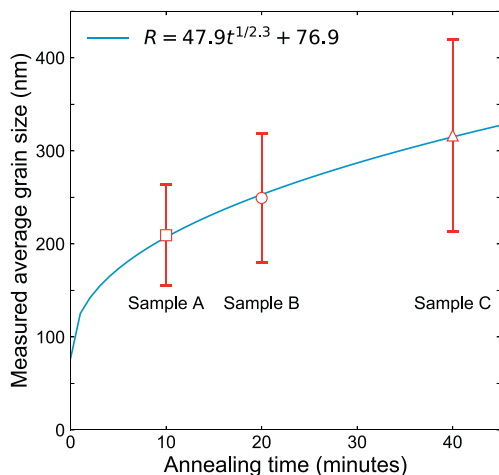


Fig. 3. Extracted average grain size, R , (red markers) and the variation (red bars), as a function of annealing temperature for the samples A, B and C which was sulfurized at 500 °C for 10, 20 and 40 min respectively from the same precursor. R was estimated using top view SEM images (not shown). 5 horizontal and 5 vertical equally spaced lines were drawn for two images for each sample. The blue line illustrates fitting equation for $R \propto t^{1/2.3}$, adapted from Ren et al. [12], and the parameters are shown in the legend. (For interpretation of the references to colour in this figure legend, the reader is referred to the web version of this article.)

which was sulfurized at 10, 20 and 40 min at 500 °C, respectively. The images show a ~1 μm CZTS layer on top of a Mo back contact, in addition to secondary phase formation of SnS₂ (in sample B). However, the amount of secondary phase formation was sufficiently low, so that it did not interfere with subsequent measurements. The variation in sulfuration time results in different average grain sizes as previously demonstrated with the same furnace and sputtering system, and where the average grain size, R , is dependent on annealing time, t , with $R \propto t^{1/n}$ where n is between 2.2 and 2.4 [12]. The average grain size was estimated by counting the number of grain boundaries over a line drawn across the image and divided by its length, as shown in Fig. 3, where the extracted average and variation in grain size, in addition to the estimate with $R \propto t^{1/2.3}$, are displayed. Indeed, Fig. 3 demonstrates that the average grain size increases with approximately 50% from the sample annealed for 10 min compared to that annealed for 40 min. Thus, one can expect that the influence of grain boundary diffusion is different for different sulfuration times.

Fig. 4 shows the ⁸⁰Se ¹³³Cs signals measured with SIMS for sample B after selenizations at 337, 360 and 409 °C for 30 min. Similar temperature dependencies are observed for samples A and C. The background signal (solid gray line) was obtained prior to the Se heat treatments. Selenization at 337 °C resulted in a considerable increase of Se signal at the CZTS/Mo interface, and a minor increase in the region between 100 and 800 nm from the surface, hereafter called “bulk”. The Se content close to the surface is about 2.5 times higher than that in the

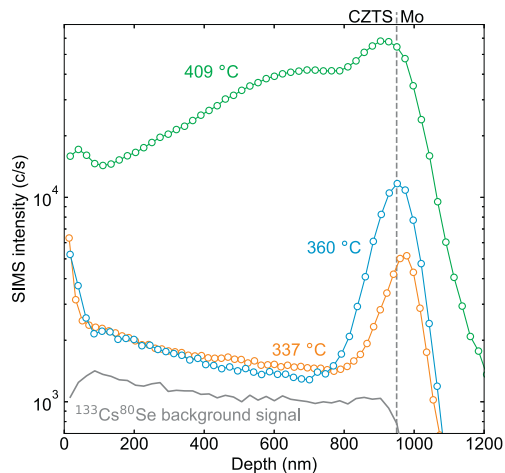


Fig. 4. Secondary ion mass spectrometry (SIMS) $^{80}\text{Se}^{133}\text{Cs}$ signals for sample B which was sulfurized at 500°C for 20 min followed by selenization at 337°C (orange circles), 360°C (blue circles) and 409°C (green circles) for 30 min. Se accumulates at the back contact after selenization at 337°C and the accumulation is greater after selenization at 360°C . After selenization at 409°C Se has heavily been incorporated into the CZTS layer and the signal has increased by around one order of magnitude. (For interpretation of the references to colour in this figure legend, the reader is referred to the web version of this article.)

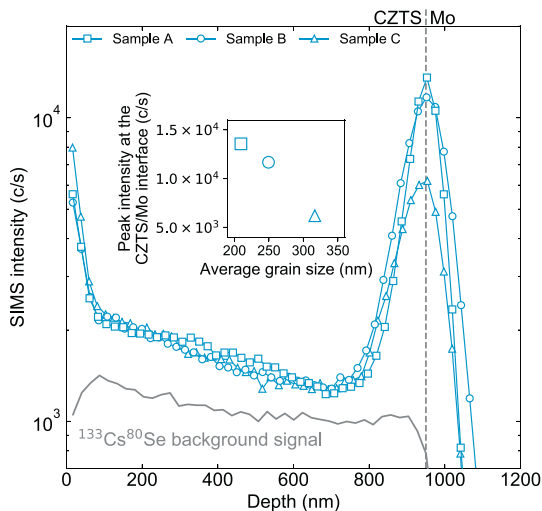


Fig. 5. Secondary ion mass spectrometry (SIMS) $^{80}\text{Se}^{133}\text{Cs}$ signals for samples A (squares), B (circles) and C (triangles) which was sulfurized at 500°C for 10, 20 and 40 min respectively from the same precursor followed by selenization at 360°C for 30 min. Se accumulates at the CZTS/Mo interface for all samples which inversely correlate with average grain size and solidifies that Se diffuses through grain boundaries at 360°C . Inset: Peak intensity at the CZTS/Mo interface from each SIMS depth profile versus the average grain size, R , estimated from top-view SEM images.

bulk, e.g. (Fig. 4), indicating that the surface acts as a source for the Se, as expected. However, after selenization at 360°C , the bulk Se signal is unchanged. This may indicate that the grain boundaries become saturated with Se at 337°C . Hence, migration of Se may still occur, but the

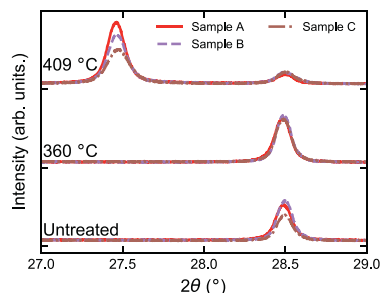


Fig. 6. X-ray diffraction (XRD) $\theta/2\theta$ high resolution scan from 27° to 29° with an increment of 0.002° for three $\text{Cu}_2\text{ZnSnS}_4$ samples (A, B and C) which was sulfurized at 500°C for 10, 20 and 40 min respectively from the same precursor. The patterns show as-deposited and after selenizations at 360 and 409°C for each sample. The peaks at 28.49° correlates with the (112) reflection of a pure sulfide $\text{Cu}_2\text{ZnSnS}_4$. After the 409°C anneal, a peak at 27.48° appears for all samples which correlates with the (112) reflection of a new phase $\text{Cu}_2\text{ZnSn}(\text{S}_x\text{Se}_{1-x})_4$ where $x = 0.25$ [6].

concentration will not increase further. This is substantiated by an increase in Se at the CZTS/Mo interface of a factor 2. After selenization at 409°C , the Se signal has increased by around one order of magnitude in the bulk and the signal is increasing with depth. The increase in Se correlates with a significant decrease in the S signal (not shown). The Se signals for all three samples after selenization at 360°C for 30 min are displayed in Fig. 5. The figure shows that the sample with the largest average grain size, i.e. sample C, displays a lower Se signal at the CZTS/Mo interface compared to that of samples A and B. Hence, the Se accumulation at the CZTS/Mo interface inversely correlates with grain size and corroborates that the accumulation is promoted by grain boundary diffusion. The inset displays the relationship between the maximum intensity of Se at the CZTS/Mo interface and the estimated average grain size. Fig. 6 shows X-ray diffraction (XRD) patterns of high resolution $\theta/2\theta$ scans from 27° to 29° with an increment of 0.002° for the three samples as-deposited, after selenizations at 360 and 409°C for 30 min. The peaks at 27.48° correlate with the (112) reflection of $\text{Cu}_2\text{ZnSn}(\text{S}_x\text{Se}_{1-x})_4$ (CZTSSe) where $x \approx 0.25$ [6] and the peaks 28.49° correlate with the (112) reflection of sulfide $\text{Cu}_2\text{ZnSnS}_4$. All samples, as-deposited as well as after a selenization at 360°C , have a strong signal at the sulfide CZTS position and no signal attributed to CZTSSe. After the selenization at 409°C the sulfide CZTS signal is reduced and a CZTSSe peak has appeared, indicating that two separate phases occur. The recrystallization process is likely to be inhomogeneous with depth which explains why the Se signal after selenization at 409°C from Fig. 4 may indicate the presence of a gradient as previously observed using similar annealing conditions [9].

Fig. 7 shows the normalized $^{23}\text{Na}^{133}\text{Cs}$ signals (closed markers) from SIMS for samples A, B and C after selenizations at 360°C (blue) and 409°C (green). The $^{80}\text{Se}^{133}\text{Cs}$ signal after selenization at 409°C is shown as open markers. Like the behavior of Se after the selenization at 409°C in sample B (Fig. 5), sample A and C shows a plateau in the Se concentration at around 4×10^4 counts/s, and extending ~ 550 , ~ 400 , and ~ 300 nm towards the surface for sample A, B and C, respectively. This is in good agreement with the formation of a CZTSSe phase observed by XRD (Fig. 6), indicating that the CZTSSe is formed close to the Mo back contact. This contrasts with reports on CZTSSe formation at higher temperatures where recrystallization has occurred towards the front [11,14]. Since recrystallization is initiated close to the Mo back contact after selenization at 409°C , this suggests that the grain boundary diffusion and agglomeration at the back contact is an important vehicle for the CZTSSe formation at reduced temperatures. For the behavior of Na, in both the as-deposited (not shown) and the

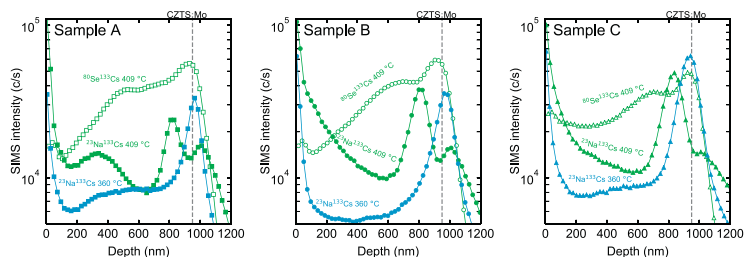


Fig. 7. Secondary ion mass spectrometry (SIMS) $^{23}\text{Na}^{133}\text{Cs}$ signals (closed markers) for samples A, B and C which was sulfurized at 500 °C for 10, 20 and 40 min respectively from the same precursor followed by a selenization at 360 °C (blue) and 409 °C (green) for 30 min. The $^{80}\text{Se}^{133}\text{Cs}$ signals after the Se anneal at 409 °C is displayed as green open markers. The peak intensity has shifted from the Mo layer close to the CZTS/Mo interface to more inside the CZTS layer where Se has a local step. (For interpretation of the references to colour in this figure legend, the reader is referred to the web version of this article.)

selenization at 360 °C, Na is found at and around the CZTS/Mo interface, with some Na diffused into the CZTS layer. However, at 409 °C, the peak intensity of the Na signal shifts from the CZTS/Mo interface and 150–200 nm into the bulk of the CZTS for all samples. Interestingly, the position of this peak aligns with a local step in the Se signal. Moreover, the peak intensity of the Na signal after selenization at 409 °C increases from sample A to C, i.e. increases with grain size, and hence inversely proportional to the Se concentration observed by SIMS and CZTSSe phase as observed by XRD (Fig. 6). Since both Se and Na are expected to migrate in the grain boundaries it points towards that there is a limited amount of grain boundary sites for Se and Na to occupy, and where Se appear to replace Na in the grain boundaries at this temperature. Here it should be noted that the samples are quenched by being transferred quickly out of the hot zone to the cold zone which suggests that the observed Na accumulation represents the situation at the end of the anneal.

In previous studies it has been reported that Na is mainly found in the grain boundaries in CZTS [14] and that Na diffuses more easily in the grain boundaries for $\text{Cu}(\text{In,Ga})\text{Se}_2$ (CIGS) [15]. If the vast transportation of Na from the back contact into the CZTS layer displayed in Fig. 7 for all samples has transpired through the grain boundaries and into new grains (likely via liquid Na_2Se_x [16]), this would suggest a substantially higher flux of atoms in the grain boundaries at 409 °C compared to the situation at 360 °C. Consequently, the diffusivity of Se increases and Se is easily transported throughout the absorber which means that the recrystallization is not limited by the availability of Se, but rather by the most energetically favorable location where Na is present in sufficient amounts. This would explain the increased Se signal towards the Mo back contact during recrystallization where more recrystallization has occurred closer to the source of Na. However, this behavior is different to previous studies where sulfurized absorbers have been selenized at 425 °C and 450 °C, and where Se have formed grains also towards the front of the absorber [10,11]. We believe the higher temperature annealing condition has caused more favorable recrystallization conditions towards the front which is also accompanied by quick Na diffusion from the back contact. Importantly, for all selenized CZTS absorbers we observe a correlation between increased Na signal and increased Se signal. A suggestion for further work is to diffuse Se into Na-free CZTS to observe the effect of not having Na present on Se diffusion and nucleation. Additionally, low temperature diffusion of S into selenide $\text{Cu}_2\text{ZnSnSe}_4$ (CZTSe) absorbers should be investigated further [17].

4. Conclusions

In this paper we demonstrate that Se diffuses into sulfide CZTS grain boundaries during selenization at 337 and 360 °C for 30 min. While some increased signal of Se is observed in the bulk region from 100 to 800 nm from the surface, the diffusion can be explained by an increased concentration of Se in the grain boundaries. Once the samples are subjected to a selenization at 409 °C for 30 min, nucleation of CZTSSe causes recrystallization of CZTSSe grains and a great increase of Se

signal from SIMS is observed in the CZTS layer. The recrystallization dominates the incorporation of Se into CZTS and suppresses the possible in-diffusion into grains to form a band gap gradient. At sufficient temperatures Na diffuses from the back contact and into the CZTS layer, facilitates the recrystallization and enhances Se grain boundary diffusion. These results show that a controlled diffusion of Se in sulfide CZTS grains to form a band gap gradient is not feasible suggesting that the energy required to recrystallize new CZTSSe grains is lower compared to diffusion into existing grains. While this conclusion should be valid for most systems, the recrystallization could potentially be suppressed by controlling the Na incorporation or by low temperature incorporation of S into CZTSe grains.

Acknowledgements

This work has been funded by the Research Council of Norway (project 243642) and the Swedish Foundation for Strategic Research. The Research Council of Norway is also acknowledged for the support to the Norwegian Micro and Nano-Fabrication Facility, NorFab, project number 245963/F50. S. G. would like to thank G. C. Vasquez for assistance with SEM top-view measurements.

References

- [1] T.K. Todorov, J. Tang, S. Bag, O. Gunawan, T. Gokmen, Y. Zhu, D.B. Mitzi, Beyond 11% efficiency: characteristics of state-of-the-art $\text{Cu}_2\text{ZnSn}(\text{S,Se})_4$ solar cells, *Adv. Energy Mater.* 3 (2013) 34–38.
- [2] S. Wu, C. Chang, H. Chen, C. Shih, Y. Wang, C. Li, S. Chan, High-efficiency $\text{Cu}_2\text{ZnSn}(\text{S,Se})_4$ solar cells fabricated through a low-cost solution process and a two-step heat treatment, *Prog. Photovolt. Res. Appl.* 25 (2017) 58–66.
- [3] J.K. Larsen, Y. Ren, N. Ross, E. Särhammar, S.-Y. Li, C. Platzer-Björkman, Surface modification through air annealing $\text{Cu}_2\text{ZnSn}(\text{S,Se})_4$ absorbers, *Thin Solid Films* 633 (2017) 118–121.
- [4] D.-K. Hwang, B.-S. Ko, D.-H. Jeon, J.-K. Kang, S.-J. Sung, K.-J. Yang, D. Nam, S. Cho, H. Cheong, D.-H. Kim, Single-step sulfo-selenization method for achieving low open circuit voltage deficit with band gap front-graded $\text{Cu}_2\text{ZnSn}(\text{S,Se})_4$ thin films, *Sol. Energy Mater. Sol. Cells* 161 (2017) 162–169.
- [5] S.G. Haass, M. Diethelm, M. Werner, B. Bissig, Y.E. Romanyuk, A.N. Tiwari, 11.2% Efficient solution processed Kesterite solar cell with a low voltage deficit, *Adv. Energy Mater.* 5 (2015) 1–7.
- [6] P.M.P. Salomé, J. Malaquias, P.A. Fernandes, M.S. Ferreira, A.F. da Cunha, J.P. Leitão, J.C. González, F.M. Matinaga, Growth and characterization of $\text{Cu}_2\text{ZnSn}(\text{S,Se})_4$ thin films for solar cells, *Sol. Energy Mater. Sol. Cells* 101 (2012) 147–153.
- [7] K.-J. Yang, D.-H. Son, S.-J. Sung, J.-H. Sim, Y.-I. Kim, S.-N. Park, D.-H. Jeon, J. Kim, D.-K. Hwang, C.-W. Jeon, D. Nam, H. Cheong, J.-K. Kang, D.-H. Kim, A band-gap-graded CZTSSe solar cell with 12.3% efficiency, *J. Mater. Chem. A* 4 (2016) 10151–10158.
- [8] K. Woo, Y. Kim, W. Yang, K. Kim, I. Kim, Y. Oh, J.Y. Kim, J. Moon, Band-gap-graded $\text{Cu}_2\text{ZnSn}(\text{S}_{1-x}\text{Se}_x)_4$ solar cells fabricated by an ethanol-based, particulate precursor ink route, *Sci. Rep.* 3 (2013) 3069.
- [9] N. Ross, J. Larsen, S. Grini, E. Särhammar, L. Vines, C. Platzer Björkman, $\text{Cu}_2\text{ZnSn}(\text{S,Se})_4$ solar cell absorbers from diffusion of selenium into annealed CZTS absorbers, *Proceedings 2016 IEEE 43th Photovolt. Spec. Conf.*, 2016, pp. 492–497.
- [10] S. Grini, N. Ross, T.N. Sky, C. Persson, C. Platzer-Björkman, L. Vines, Secondary ion mass spectrometry as a tool to study selenium gradient in $\text{Cu}_2\text{ZnSn}(\text{S,Se})_4$, *Phys. Status Solidi C* 14 (2017) 1600187.
- [11] N. Ross, J. Larsen, S. Grini, L. Vines, C. Platzer-Björkman, Practical limitations to selenium annealing of compound co-spun $\text{Cu}_2\text{ZnSnS}_4$ as a route to achieving sulfur-selenium graded solar cell absorbers, *Thin Solid Films* 623 (2017) 110–115.
- [12] Y. Ren, N. Ross, J.K. Larsen, K. Rudisch, J.J.S. Scragg, C. Platzer-Björkman, Evolution of $\text{Cu}_2\text{ZnSnS}_4$ during non-equilibrium annealing with quasi-in situ

- monitoring of sulfur partial pressure, *Chem. Mater.* 29 (2017) 3713–3722.
- [13] C.W. Magee, W.L. Harrington, E.M. Botnick, On the use of CsX⁺ cluster ions for major element depth profiling in secondary ion mass spectrometry, *Int. J. Mass Spectrom. Ion Process.* 103 (1990) 45–56.
- [14] S. Tajima, R. Asahi, D. Isheim, D.N. Seidman, T. Itoh, K.I. Ohishi, Sodium distribution in solar-grade Cu₂ZnSnS₄ layers using atom-probe tomographic technique, *Jpn. J. Appl. Phys.* 54 (11) (2015).
- [15] A. Laemmler, R. Wuerz, T. Schwarz, O. Cojocaru-Mirédin, P.-P. Choi, M. Powalla, Investigation of the diffusion behavior of sodium in Cu(In,Ga)Se₂ layers, *J. Appl. Phys.* 115 (2014) 154501.
- [16] C.M. Sutter-Fella, J.A. Stückelberger, H. Hagendorfer, F. La Mattina, L. Kranz, S. Nishiwaki, A.R. Uhl, Y.E. Romanyuk, A.N. Tiwari, Sodium assisted sintering of chalcogenides and its application to solution processed Cu₂ZnSn(S,Se)₄ thin film solar cells, *Chem. Mater.* 26 (2014) 1420–1425.
- [17] S.P. Harvey, I. Repins, G. Teeter, Defect chemistry and chalcogen diffusion in thin-film Cu₂ZnSnSe₄ materials, *J. Appl. Phys.* 117 (2015) 074902.

Paper IV

Selenium Inclusion in $\text{Cu}_2\text{ZnSn}(\text{S},\text{Se})_4$ Solar Cell Absorber Precursors for Optimized Grain Growth

**Nils Ross, Sigbjørn Grini, Katharina Rudisch, Lasse Vines,
Charlotte Platzer-Björkman**

IEEE Journal of Photovoltaics Vol. 8, No. 4, (2018).

IV

Paper V

Strong Interplay between Sodium and Oxygen in Kesterite Absorbers: Complex Formation, Incorporation, and Tailoring Depth Distributions

Sigbjørn Grini, Kostiantyn V. Sopiha, Nils Ross, Xin Liu, Tor S. Bjørheim, Clas Persson, Charlotte Platzer-Björkman, Lasse Vines

Advanced Energy Materials 1900740, (2019).

V

Strong Interplay between Sodium and Oxygen in Kesterite Absorbers: Complex Formation, Incorporation, and Tailoring Depth Distributions

Sigbjørn Grini,* Kostiantyn V. Sopiha, Nils Ross, Xin Liu, Tor S. Bjørheim, Charlotte Platzer-Björkman, Clas Persson, and Lasse Vines

Sodium and oxygen are prevalent impurities in kesterite solar cells. Both elements are known to strongly impact performance of the kesterite devices and can be connected to efficiency improvements seen after heat treatments. The sodium distribution in the kesterite absorber is commonly reported, whereas the oxygen distribution has received less attention. Here, a direct relationship between sodium and oxygen in kesterite absorbers is established using secondary ion mass spectrometry and explained by defect analyses within the density functional theory. The calculations reveal a binding energy of 0.76 eV between the substitutional defects Na_{Cu} and O_{S} in the nearest neighbor configuration, indicating an abundance of Na–O complexes in kesterite absorbers at relevant temperatures. Oxygen incorporation is studied by introducing isotopic ^{18}O at different stages of the $\text{Cu}_2\text{ZnSnS}_4/\text{Mo}$ /soda-lime glass baseline processing. It is observed that oxygen from the Mo back contact and contaminations during the sulfurization are primary contributors to the oxygen distribution. Indeed, unintentional oxygen incorporation leads to immobilization of sodium. This results in a strong correlation between sodium and oxygen, in excellent agreement with the theoretical calculations. Consequently, oxygen availability should be monitored to optimize postdeposition heat treatments to control impurities in kesterite absorbers and ultimately, the solar cell efficiency.

efficiency (PCE).^[1] In recent years, several groups have achieved over 10% efficiency with control over fabrication and doping as key factors.^[2–8] However, control over impurities during processing in kesterite and other chalcogenide technologies is challenging. Although the effects of impurities on solar cell device performance have been discussed extensively, a complete understanding of their behavior and impact is still lacking. For chalcogenide thin film solar cells, Na and O are the prevalent impurities,^[6,9–13] where both are often found to accumulate at grain boundaries (GBs).^[14,15] Importantly, moderate amounts of Na present during fabrication are almost exclusively regarded as beneficial for device performance,^[9] whereas the effect of O is more ambiguous. For instance, the champion CZTSSe cell from Wang et al.^[1] exhibited low C and O concentrations. Early studies on $\text{Cu}(\text{In,Ga})\text{Se}_2$ (CIGS), however, implied that an interplay between Na and O affects the PCE because O may passivate Se vacancies at grain boundaries with Na acting as a catalyst.^[16–18] Indeed, further studies confirmed that Na and O can coexist on the surface and GBs.^[19,20] Moreover, for both CIGS and CZTSSe, postdeposition heat treatments were shown to yield improved device performance.^[21] For kesterite solar cells, these treatments have been performed in air, inert atmosphere, and vacuum.^[10,22–25] The heat treatments have been observed to change the photoluminescence intensity and peak position,^[22,24] the sodium distribution,^[10,24] the bandgap,^[22,25] surface properties^[22] as well as oxidize the surface and grain boundaries.^[14,25] Consequently, impurities such as Na and O can be a critical factor influencing the device performance. On one hand, Na incorporation is achieved by using soda-lime glass substrates (SLG) and suppressing other Na sources. On the other hand, O is not as easily controlled since multiple potential sources may exist. For example, commonly used glass substrates, such as SLG, are composed of oxides. Furthermore, the Mo back contact is polycrystalline and usually contains significant amounts of O.^[26] Additionally, the precursors may contain O and all process stages are performed in low-to-medium vacuum conditions, under which O may also be present.

In this work, a correlation between Na and O distribution in kesterite absorbers is identified using secondary ion

1. Introduction

Earth-abundant kesterite $\text{Cu}_2\text{ZnSn}(\text{S,Se})_4$ (CZTSSe) is a promising solar cell absorber with a record 12.6% power conversion

S. Grini, Dr. X. Liu, Dr. T. S. Bjørheim, Prof. C. Persson, Prof. L. Vines
Department of Physics/Centre for Materials Science and Nanotechnology
University of Oslo
P.O. Box 1048, Blindern N-0316, Oslo, Norway
E-mail: sigbjorn.grini@smn.uio.no

Dr. K. V. Sopiha, Dr. N. Ross, Prof. C. Platzer-Björkman
Ångström Solar Center
Division of Solid State Electronics
Uppsala University
Uppsala 75120, Sweden

The ORCID identification number(s) for the author(s) of this article can be found under <https://doi.org/10.1002/aenm.201900740>.

© 2019, The Authors. Published by WILEY-VCH Verlag GmbH & Co. KGaA, Weinheim. This is an open access article under the terms of the Creative Commons Attribution License, which permits use, distribution and reproduction in any medium, provided the original work is properly cited.

DOI: 10.1002/aenm.201900740

mass spectrometry (SIMS) and explained by defect analyses within the density functional theory (DFT), where a model with complex formation and subsequent trapping of Na is proposed. The model is experimentally explored by introducing the less abundant ^{18}O isotope into different stages of the CZTS baseline process. Further, the ^{18}O investigation reveals the sources of O that contribute to the final O distribution observed in the absorber.

2. Results and Discussion

2.1. Interplay between Na and O Impurities in Kesterite Absorbers

Figure 1 shows SIMS depth profiles for two CZTSSe absorbers chosen from our previous study of high-performance devices.^[27] The lines represent Na (red) and O (black) distribution in the absorbers which yielded PCEs of 8.5% (solid lines) and 7.2% (dashed lines), respectively. SIMS depth profiles of the constituent elements are shown in Figure S1 (Supporting Information). For both samples, the Na and O profiles are correlated, which is a trend previously observed for CZTSSe and CIGS.^[28–30] Interestingly, the correlation persists regardless of the shape of the profile. This is exemplified in Figure 1 for the 7.2% PCE device where an abnormal accumulation for both Na and O is observed at about 500 nm into the sample. The fact that the accumulation is in the middle of the absorber cannot be easily explained by the SIMS intensity only representing GB density.^[31] Indeed, none of our scanning electron microscopy cross-section images showed an increase of GB density in this region. To understand the correlation between Na and O in kesterite absorbers at the atomic level, first-principles DFT was employed to study the point defects formed by these impurities in CZTS. The sole defects and possible complexes can be

formed in the grain interior, but it is also known that both sodium and oxygen often accumulate at GBs of both CZTS^[14,32] and CIGS.^[15,33,34] In recent studies, alkali impurities were even shown to segregate at specific GBs,^[35] marking a new stage in understanding the impact of Na on polycrystalline Cu-based solar cells. In this work, we analyze defect physics in bulk CZTS, and thus, we do not try to describe more complex situations for GBs.^[36–42]

For bulk CZTS, Na-related defects are already relatively well investigated in the literature. It is known that Na prefers to occupy Cu site in CZTS to form Na_{Cu} ,^[43–45] although formation of interstitial Na_i is possible during diffusion.^[46,47] The substitutional Na_{Cu} is an isovalent defect, and since the ionic radius of Na is about 0.4 Å larger than that of Cu, it does not yield any local reconstruction of the crystal.^[48] These results were confirmed by our calculations. On the other hand, the O impurities have only been addressed by a few first-principles studies,^[36,49] which hypothesized the dominant role played by substitutional O_S defect. Conversely, we found that O_S induces a substantial local lattice distortion due to significant differences in both size and electronegativity between the O^{2-} and S^{2-} ions.

While the calculated Cu–S, Zn–S, and Sn–S bond lengths in CZTS are 2.32, 2.37, and 2.47 Å, the Cu(2a)–O, Cu(2c)–O, Zn–O, and Sn–O distances for the O_S defect are 3.23, 2.18, 1.99, and 2.02 Å, respectively. This change in the coordination for O_S can be interpreted as breaking the Cu(2a)–O and shortening the remaining bonds by 0.14–0.45 Å, in accordance with a general tendency for stabilizing shorter bonds between atoms with smaller ionic radii.^[48] These optimized configurations for substitutional defects were further used as reference systems to compute binding energy between Na_{Cu} and O_S .

Apart from the isolated defects, Na and O impurities in CZTS may interact through formation of defect complexes. Now, consider that the NaO complex is formed by Na_{Cu} and O_S . The binding energy for such defect complex can be computed as

$$E_b = E_{\text{tot}}(\text{Na}) + E_{\text{tot}}(\text{O}) - E_{\text{tot}}(\text{Na+O}) - E_{\text{tot}}(\text{pristine}) \quad (1)$$

where $E_{\text{tot}}(\text{Na})$, $E_{\text{tot}}(\text{O})$, $E_{\text{tot}}(\text{Na+O})$, and $E_{\text{tot}}(\text{pristine})$ are the total energies of CZTS supercells containing isolated Na_{Cu} , isolated O_S , both Na_{Cu} and O_S , and pristine supercell, respectively. Similar expressions can also be written for the larger Na–O complexes using the supercell with NaO complex as a reference system, hence, the binding energy computed in such a way defines strength of the subsequent Na–O bonds. It was found that Na–O binding energy of the NaO complex strongly depends on distance between the defects, as shown in Figure 2a.

The highest computed binding energy of 0.76 eV corresponds to the NaO complex where Na_{Cu} and O_S are nearest neighbors. This binding energy is remarkably high considering that both Na_{Cu} and O_S are isovalent substitutional defects. In case of the Na_2O complex, binding energy for the second Na_{Cu} with the existing NaO complex is 0.56 eV (i.e., total binding energy of $0.76 + 0.56 = 1.32$ eV), which is comparable to that for the NaO complex. Further, since Na diffusion in CZTS can be mediated by the interstitial defects,^[46] binding energy was also computed for interstitial Na_i and substitutional O_S , demonstrating qualitatively similar results. In fact, the most stable complex formed by neutral Na_i and O_S has binding energy of 1.19 eV, which is even higher than that for Na_{Cu} and O_S . More

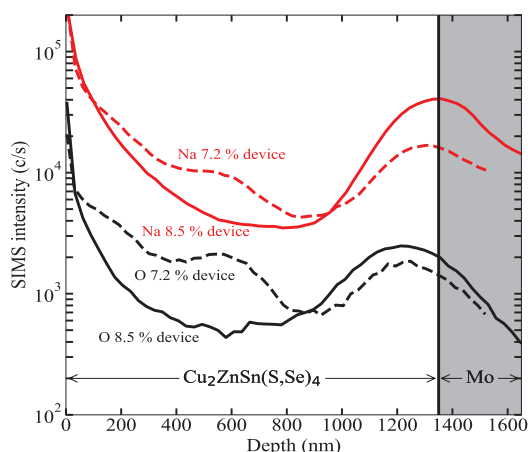


Figure 1. SIMS depth profiles of Na (red lines) and O (black lines) measured on two CZTSSe absorbers where the mean device produced an 8.5% PCE (solid lines) and a 7.2% PCE (dashed lines). The Na and O depth profiles correlate for both samples and represent a trend observed for all our measured kesterite absorbers.

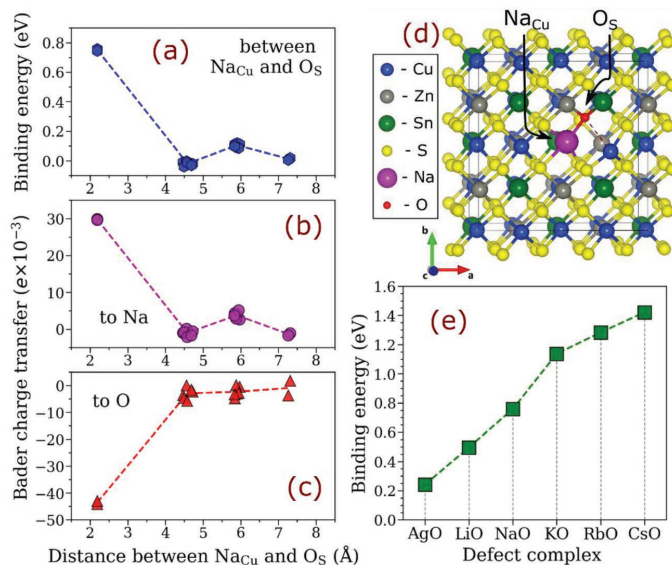


Figure 2. First-principles analysis of interaction between Na_{Cu} and O_S defects in CZTS. a) Binding energy of Na_{Cu} and O_S in 64-atom supercell versus distance between them. b,c) Bader charge transfer to Na and to O atoms versus distance between them; the separated defects in 64-atom CZTS supercells were used as reference systems for the binding energy and Bader charge transfer calculations. d) Structure of the most stable nearest-neighbor NaO complex; the broken Cu–O bond is illustrated by the red dashed line; the corresponding .CIF file is given in the Supporting Information. e) Binding energy for complexes formed between O_S and different isovalent substitutional defects on the Cu site; only the most stable configurations of the complexes are presented. The dashed lines in all graphs are to guide the eye.

detailed analysis of the defect interaction in the Na₂O complex and for Na_i with O_S is given in the Supporting Information. This strong tendency for binding suggests that Na atoms introduced into O-containing CZTS grains can be kinetically trapped by forming the nearest neighbor complexes.

To explain the origin of the remarkably strong binding, we analyze in detail the most stable configuration of the NaO complex between Na_{Cu} and O_S (see Figure 2d). First, it is notable that the Na–O bond of 2.19 Å is very close to the corresponding Cu–O bond for the isolated O_S defect (2.18 Å), suggesting relatively small contribution of the lattice relaxation. Indeed, we found that binding energy of NaO complex where both Na_{Cu} and O_S occupy the ideal lattice sites (without atomic relaxation) is 0.67 eV. Second, effective (Bader) charges were calculated for Na and O with respect to the distance between them, as shown in Figure 2b,c. Evidently, the charges transferred to Na and O correlate with the binding energy, that is, charge transfers are significant in the nearest neighbor configurations only. This behavior suggests that binding in the complexes is determined by ionicity of the Na–O bond and justifies why the binding energy causing formation of the second Na–O bond in Na₂O complex (0.56 eV) is almost as high as that for NaO (0.76 eV). Third, the binding energies for five other isovalent XO (X = Ag, Li, K, Rb, Cs) defect complexes were also computed. As can be observed in Figure 2e, the binding energy correlates with electronegativity of the X atom, affirming that bonding between Na and O in bulk CZTS

is indeed determined by the ionic bond, and thus, qualitatively similar interaction between the defects at the GBs can be expected. Fourth, the binding energies were calculated for the complexes formed by O_S and interstitial X_i defect (X = Ag, Li, Na, K, Rb, and Cs), as shown in Figure S3 (Supporting Information), further evincing that the interaction between the alkali elements and oxygen is driven by the ionic bonding. These results corroborate the conclusion that Na and O concentrations in CZTS are indeed correlated, as seen in the SIMS depth profiles in Figure 1, and that the origin of this correlation is indeed Na–O defect complexes.

Although the calculations show a clear tendency for binding between Na_{Cu} and O_S in CZTS, the binding energy alone does not guarantee the formation of the complexes at the processing and/or operating temperatures. The concentration of AB complexes at temperature *T* can be estimated from the law of mass action as

$$C_{AB} = C_A \times C_B \times GF \times \exp(E_b/kT) \quad (2)$$

where *C_A* and *C_B* are concentrations of isolated A and B defects, respectively; *GF* is a factor accounting for both the lattice symmetry and the complex geometry.^[50] The law of mass action can be applied to all other complexes as well and should be collectively satisfied for all defects in equilibrium.

Equation (2) is strictly valid in the dilute limit, but for this study it would be a reasonable approximation for the defect concentrations below 1 at% because the Na–O interaction is very short-ranged and the change in entropy is insufficient to out-compete the strong Na–O bond. In our CZTS samples, the total concentrations of Na and O impurities were estimated using elastic recoil detection analysis (ERDA) to be 0.8 and 0.5 at%, respectively. Based on this stoichiometry, one could expect NaO and Na₂O to be dominant. Assuming no influx of the impurities upon heating, their total concentrations are constrained as $C_A^{tot} = C_A + C_{AB} + 2C_{A_2B}$ and $C_B^{tot} = C_B + C_{AB} + C_{A_2B}$. Hence, by solving the system of equations with $E_b = 0.76$ eV and $GF = 8$ representing the NaO complex and $E_b = 0.56$ eV and $GF = 4$ for the Na₂O complex in CZTS, the temperature dependence for the defect concentrations can be obtained, as shown in Figure 3a (solid lines). As one can see, these high binding energies ensure the formation of both complexes at all temperatures of CZTS baseline processing (below 600 °C). In a wider range of compositions, however, the dominant type of complexes depends on the ratio of the defects introduced, as shown in Figure 3b. Thus, when concentration of O is closer to that of Na, formation of NaO would be dominant (e.g. dotted lines in Figure 3a). Contrary, when concentration of Na is about twice that of O, predominant formation of Na₂O can be expected. In the intermediate regime, both types of complexes would coexist. These results as such demonstrate that Na and

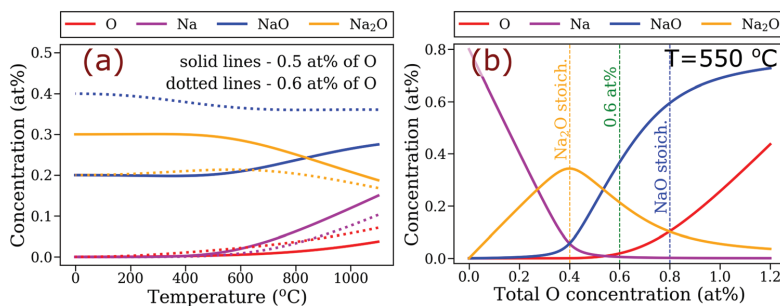


Figure 3. Estimated concentrations of Na_{Cu} , O_{S} , NaO , and Na_2O complexes a) with respect to temperature for CZTS containing 0.8 at% of Na with 0.5 at% (solid lines) and 0.6 at% (dotted lines) of O, and b) with respect to total O concentration at 550 °C and 0.8 at% of Na.

O impurities primarily coexist in the form of defect complexes throughout the typical temperature interval adopted in CZTS processing. At the same time, they do not exclude the possibility of clustering between the NaO complexes forming even larger complexes. Most importantly, however, the tendency for binding between Na and O in CZTS ensures that these impurities do interplay and cluster owing to the strong ionic Na–O bonding, and therefore, must be considered together for developing high-performance CZTS solar cells.

To control the formation of Na–O complexes, however, the origins of Na and O incorporation in kesterite processing must be identified. While Na is incorporated from Na_2O present in SLG,^[51] concurrent diffusion of O from the substrate is also possible, even though the diffusivities of alkali elements are much higher in SLG compared to that of O.^[52] Additionally and different to Na, O in kesterite absorbers has several additional potential sources: outdiffusion from the Mo back contact, from the precursors as well as from the air during and after processing.

2.2. Evaluation of Sources of O in Kesterite Processing by Isotopic ^{18}O Diffusion

To further study the relationship between Na and O in kesterite absorbers, controlled O incorporation during processing

is needed. To evaluate possible sources of O, isotope ^{18}O was introduced at different stages of the CZTS baseline processing by heat treatments in an ^{18}O -rich atmosphere ($[^{18}\text{O}]$: 97.1%, $[^{16}\text{O}]$: 2.9%) at 100, 200, 300, and 400 °C for 30 min (hereafter called ^{18}O anneal). The heat treatments were performed (Ⓐ) on the SLG substrate, (Ⓑ) after the Mo sputtering, (Ⓒ) after the CZTS precursor sputtering, and (Ⓓ) after the sulfurization, as shown in **Figure 4**. The SLG was only heat treated at 400 °C since no significant diffusion was expected at lower temperatures.^[52] The isotopic ratio $C_{^{18}\text{O}} = [^{18}\text{O}]/([^{16}\text{O}] + [^{18}\text{O}])$ versus depth after the ^{18}O anneals and for untreated CZTS absorbers measured with SIMS are shown in **Figure 5**. The cation ratios, processing steps, and annealing conditions are summarized in **Table 1**.

In **Figure 5a**, the depth profile for “SLG 400 °C” (Ⓐ, brown dashed line) has increased isotopic ratio in the Mo back contact. The increased ^{18}O concentration demonstrates that O can diffuse from the SLG into the Mo layer during the CZTS processing. However, since the isotopic ratio in the treated and untreated CZTS layers are at the same level, SLG can be excluded from the list of potential sources of O in CZTS for baseline processing conditions.

Additionally, **Figure 5a** shows that ^{18}O diffuses into the Mo back contact during the ^{18}O anneal (Ⓑ, solid lines). The

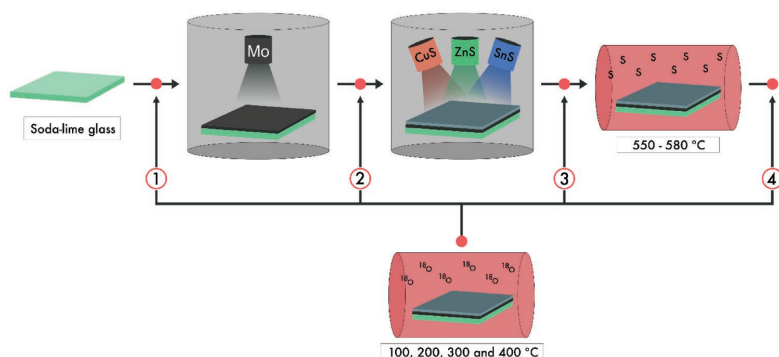


Figure 4. ^{18}O introduction into different stages of the CZTS processing; (Ⓐ) on the soda-lime glass substrate, (Ⓑ) after the Mo sputtering, (Ⓒ) after the CZTS precursor (CuS , ZnS , and SnS) sputtering, and (Ⓓ) after the sulfurization.

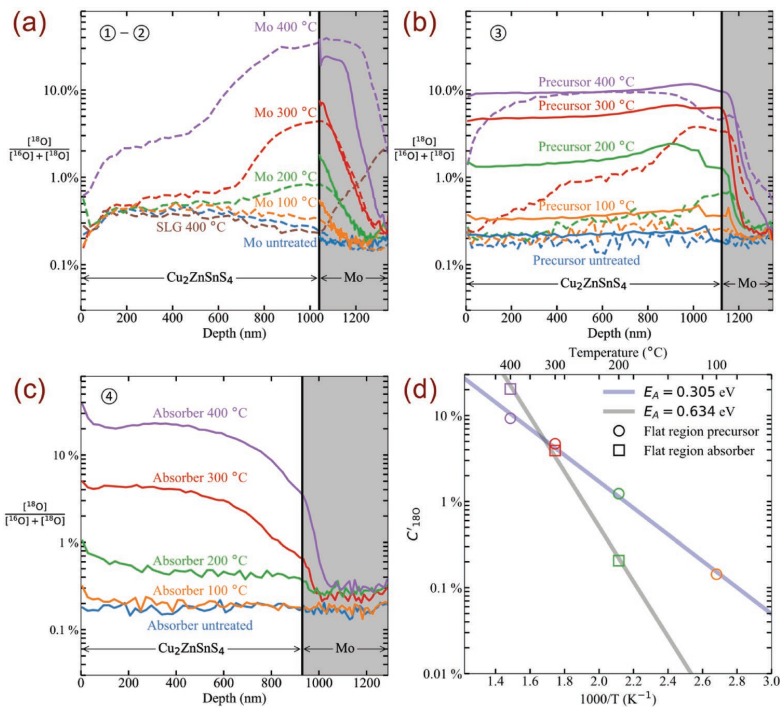


Figure 5. The isotopic ratio $C_{18O} = [^{18}O]/([^{16}O] + [^{18}O])$ measured with SIMS at different stages of the CZTS baseline process. The solid lines in (a)–(c) represent depth profiles measured after a heat treatment in an ^{18}O -rich atmosphere for 30 min. The dashed lines in (a) and (b) represent depth profiles after the samples have been processed to CZTS absorbers. “Untreated” indicates a reference sample not heat treated in the ^{18}O -rich atmosphere but processed in the same conditions otherwise. The number(s) in the upper left corner refers to the process stages shown in Figure 4. Thus, the heat treatment in the ^{18}O -rich atmosphere is performed a) before and after the Mo sputtering, b) after the CZTS precursor sputtering, and c) after the sulfurization. d) Arrhenius behavior between the ^{18}O fraction corrected for the isotopic background level of ^{18}O and for the isotope fraction in an ^{18}O -rich atmosphere, C_{18O} , for the ^{18}O inclusion into the precursor and the CZTS absorber. The circles and squares represent average for the flat regions in the depth profiles of the ^{18}O annealed precursors and absorbers, respectively.

isotopic ratio increases with annealing temperature up to 20% for “Mo 400 °C”. During the precursor deposition and sulfurization, ^{18}O from the Mo back contact diffuses into the CZTS layer (dashed lines), indicating that O from the Mo back contact inevitably ends up in the CZTS layer. The isotopic ratio is higher near the Mo back contact, suggesting that O diffusion in the CZTS layer is not fast enough to uniformly distribute O throughout its thickness. From 100 nm to about 600 nm from the surface, the isotopic ratio is nearly constant, while the isotopic ratio approaches the background natural abundance level, $C_{bg} = 0.2\%$, near the surface. Surprisingly, a small increase in the isotopic ratio above the background level is found in all profiles, including that for the untreated sample. This feature can be attributed to a minor ^{18}O exchange effect caused by keeping all the samples in the same graphite box during the sulfurization. Indeed, a follow-up control experiment for an untreated sample in a separate box (not shown) revealed only the natural abundance of ^{18}O , confirming the exchange mechanism causing the abnormality in the isotopic profiles.

After the ^{18}O anneal (ⓐ) of “Mo 400 °C”, the Mo layer turned from metallic to dark red and X-ray diffraction data unveiled the presence of MoO_2 (Figure S5, Supporting Information). The formation of oxide phase should not affect the isotopic ratio, even though it causes an increase in SIMS intensity for both ^{16}O and ^{18}O due to higher ionization yield in MoO_2 compared to that of Mo. Here, it should be noted that high SIMS intensities require a faraday cup detector to be used to protect the normal electron multiplier, which yields an uncertainty in the isotopic ratio. This effect may explain the higher ratio measured after the precursor deposition and sulfurization for “Mo 400 °C” (Figure 5a, purple dashed line).

In this work, the CZTS baseline processing employs CuS, ZnS, and SnS sputtering targets with 99.99% purity in chamber with an Ar (99.9995% purity) background pressure of 666 Pa. Despite the high purities, noticeable O concentrations are detected by SIMS in the samples prior to sulfurization (not shown). Hence, ^{18}O anneals were performed before the sulfurization to study whether the O from the precursors eventually ends up in the CZTS absorber.

Table 1. The sample names, the cation ratios, and when the samples were annealed in an ^{18}O -rich atmosphere.

Sample name	Cation ratios		^{18}O annealed
	[Cu]/[Sn]	[Zn]/([Cu]+[Sn])	
SLG 400 °C	1.78 ± 0.02	0.41 ± 0.02	400 °C on the soda-lime glass substrate
Mo untreated	1.78 ± 0.02	0.41 ± 0.02	–
Mo 100 °C	1.78 ± 0.02	0.41 ± 0.02	100 °C after Mo sputtering
Mo 200 °C	1.78 ± 0.02	0.41 ± 0.02	200 °C after Mo sputtering
Mo 300 °C	1.78 ± 0.02	0.41 ± 0.02	300 °C after Mo sputtering
Mo 400 °C	1.78 ± 0.02	0.41 ± 0.02	400 °C after Mo sputtering
Precursor untreated	1.95 ± 0.02	0.38 ± 0.02	–
Precursor 100 °C	1.95 ± 0.02	0.38 ± 0.02	100 °C after cosputtering of precursors
Precursor 200 °C	1.95 ± 0.02	0.38 ± 0.02	200 °C after cosputtering of precursors
Precursor 300 °C	1.95 ± 0.02	0.38 ± 0.02	300 °C after cosputtering of precursors
Precursor 400 °C	1.95 ± 0.02	0.38 ± 0.02	400 °C after cosputtering of precursors
Absorber untreated	1.83 ± 0.02	0.34 ± 0.02	–
Absorber 100 °C	1.83 ± 0.02	0.34 ± 0.02	100 °C after sulfurization
Absorber 200 °C	1.83 ± 0.02	0.34 ± 0.02	200 °C after sulfurization
Absorber 300 °C	1.83 ± 0.02	0.34 ± 0.02	300 °C after sulfurization
Absorber 400 °C	1.83 ± 0.02	0.34 ± 0.02	400 °C after sulfurization

Figure 5b illustrates that the isotopic ratio in the samples after the ^{18}O anneals (⊙) is roughly constant throughout the precursor layer followed by a decrease in the Mo layer (solid lines). Additionally, the isotopic ratio increases with annealing temperature. After the sulfurization, the isotopic ratio in the CZTS layer for “Precursor 300 °C” and “Precursor 200 °C” drop significantly. The reductions are from about 4 to 1% for “Precursor 300 °C” and from about 1.4 to 0.3% for “Precursor 200 °C”. Interestingly, these depth profiles in the CZTS layer resemble those after ^{18}O was introduced in the Mo layer (Figure 5a). Consequently, the isotopic profiles are likely to be formed by ^{18}O diffusing through the CZTS precursor and into the Mo during the ^{18}O anneal (solid lines in the Mo region).

Conversely, for “Precursor 400 °C”, the majority of the ^{18}O remains in the CZTS layer. The total O concentration is also higher for this sample (not shown), which indicates that the precursor oxidizes to an extent such that outdiffusion during the sulfurization process is prevented. An effort was made to fabricate devices from the precursor-annealed samples. However, most of them flaked off during the chemical bath deposition. Interestingly though, “Precursor untreated” and “Precursor 400 °C” flaked off the least. Some small sub-cells were fabricated from these films, but their PCE was low presumably due to nonideal cation stoichiometry and no difference in PCE was observed between the untreated and heat-treated samples. For close to ideal stoichiometric cation ratios, one could expect that air anneal of the precursors at 400 °C increases the O concentration in the CZTS layer and may affect the solar cell performance. Ultimately, apart from “Precursor 400 °C”, the O from the precursor accounts for only a miniscule part of the O concentration found in the CZTS absorber.

To investigate how likely O is to be introduced into crystallized absorbers, ^{18}O anneals were also performed after the sulfurization (⊙). SIMS depth profiles in Figure 5c show that after ^{18}O anneals above 100 °C, ^{18}O diffused into the CZTS layer and the Mo back contact. In the CZTS layer, the isotopic ratio is nearly constant for the “Absorber 200 °C”, while for higher temperatures the isotopic ratio starts to decline toward the Mo layer at a depth of about 650 nm.

Interestingly, the ^{18}O anneals starting from 200 °C for the absorbers (⊙) and from 100 °C for the precursors (⊙) yielded a depth profile with distinct regions of constant isotopic ratio. These constant profiles define regions where shapes of the ^{16}O and ^{18}O concentration profiles are identical. This correlation is expected from a direct exchange between ^{18}O and ^{16}O during the ^{18}O anneal. Provided O diffuses fast in CZTS, the incorporation of O from the atmosphere might be limited by the rate of surface exchange reactions. Adapting the procedure used for studying $^{18}\text{O}/^{16}\text{O}$ isotopic exchange and O transport in oxides,^[53] the isotopic ratio can

be corrected for the C_{bg} and for the ^{18}O isotopic ratio in the ^{18}O -rich atmosphere, C_g . This parameter is defined here as

$$C'_{^{18}\text{O}} = \frac{C_{^{18}\text{O}} - C_{\text{bg}}}{C_g - C_{\text{bg}}} \quad (3)$$

From the flat regions in the depth profiles in Figure 5b,c, the $C'_{^{18}\text{O}}$ can be calculated and plotted with respect to the annealing temperature, as shown in Figure 5d. As one can see, the ^{18}O isotopic ratio follows an Arrhenius behavior for both the precursor and the absorber. The activation energy for O incorporation into the precursor is half of that into the absorber. Indeed, the Arrhenius behavior indicates a negligible (<0.01%) increase in $C'_{^{18}\text{O}}$ during the 100 °C anneal of the absorber, which is less than the natural abundance and is not detectable with SIMS. Consequently, it can be concluded that prolonged room-temperature air exposure, such as storage, does not incorporate significant amounts of O into the CZTS absorbers. Nonetheless, the O partial pressure in air is about ten times higher compared to the O partial pressure in the ^{18}O anneals and hence the activation energies in Figure 5d could be underestimated as for ambient storage. Since O within few hundred nanometers from the surface cannot originate from the precursor, the Mo back contact, the SLG, or air exposure at less than 100 °C, the remaining possibility is that it arises from contaminations during the sulfurization or postsulfurization treatments. For example, during the sulfurization, a drop in sulfur partial pressure in the furnace has been previously observed,^[54] indicating possible air leakage causing O contamination. Additionally, possible exchange between the SLG, which is close to temperatures where the glass starts to soften, and the atmosphere cannot be ruled out. These possible contamination sources are aggregated as the “Sulfurization step”. Figure 6 shows a

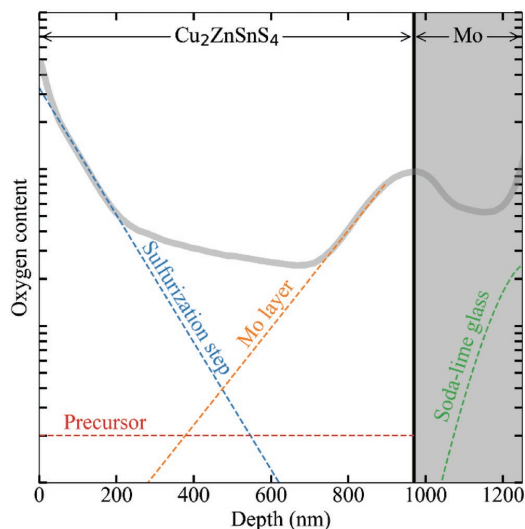


Figure 6. A representative O depth profile for a baseline processed CZTS absorber (gray thick line). The dashed lines illustrate a qualitative overview of oxygen sources contributing to the different parts of the depth profile based on the results from this work. Oxygen from the air exposure after processing should only contribute to the oxygen on the surface.

proposed assignment of the contributions to a typical O depth profile from a baseline processed CZTS absorber derived from the results given in Figure 5. The gray thick line represents the O depth profile for a baseline processed absorber (“Absorber untreated”), while the dashed lines illustrate a qualitative overview over which regions each oxygen source contributes mainly to. Based on the conducted analysis, we conclude that the sulfurization step and Mo layer account for the majority of O in the CZTS absorber. In addition, trace amounts of oxygen from the precursor may persist in the absorber as well. Conversely, O from the SLG does not diffuse sufficiently far to enter the CZTS layer during baseline processing. These results as such outline the strategies to tailor the O concentration in the kesterite absorbers.

2.3. Implications of O Incorporation and Trapping of Na

Based on the results presented in Sections 2.1 and 2.2, a deeper understanding of the mechanisms behind the correlation and the overall shape of the depth profiles for Na and O in Figure 1 can be deduced. The computed binding energy of 0.76 eV for Na–O complexes and the distinct ionic bonding nature evince that Na and O impurities in CZTS inevitably cluster together, whether it be in the bulk, surface, or grain boundary of the absorber. Na is known to be a fast diffuser in CIGS^[15,55] and evidently CZTS,^[10] where it promotes crystallization of the absorber layer.^[56,57]

Consequently, the correlation between Na and O profiles observed in the kesterite absorbers can be explained by relatively slow O diffusion from the Mo back contact and the

atmosphere during the sulfurization, as shown in Figure 6, and subsequently immobilizing the fast-diffusing Na via extensive formation of Na–O defect complexes. Hence, provided Na and O concentrations are of the same order, their depth profiles would appear correlated, as seen in Figure 1. Indeed, for “Precursor 400 °C”, where the majority of the ¹⁸O remained after the sulfurization, the depth profile exhibits an unusual but gradual increase in the total O concentration from the near-surface to the in-depth region of the sample (Figure S6, Supporting Information). Accordingly, for this sample, the Na and O profiles are also correlated throughout the sample, except for the CZTS/Mo interface region yields increased Na intensity.

Further, the proposed mechanism of O incorporation and interplay with Na can provide new insight into the Na redistribution occurring during postdeposition heat treatments. The Na distribution near the surface is likely to depend on the O₂ partial pressure in the atmosphere. Indeed in previous studies where postdeposition heat treatments were performed in N₂ atmosphere, the PCE was observed to reach a minimum between 100 and 200 °C and a maximum between 145 and 400 °C, with the optimum temperature depending on the N₂ pressure.^[10,24,58] These temperatures are sufficient to cause extensive O incorporation in kesterite absorbers, as evident from our results shown in Figure 5c. Therefore, the change in PCE may also be influenced by in-diffusion of trace O from the atmosphere, in addition to the purely thermal effects emphasized in the original studies. As such, extensive care must be taken to tightly control O incorporation during the kesterite processing.

3. Conclusions

A general tendency for correlation and clustering between Na and O in kesterite absorbers formed by cosputtering was established by SIMS measurements. The atomistic mechanism behind the correlation was further explained using defect analyses within the DFT. A strong tendency for binding between Na and O impurities mediated by the strong ionic bonding was demonstrated. The computed total binding energies of 0.76 eV for NaO and 1.32 eV for Na₂O were proven to trigger formation of the nearest neighbor complexes of Na_{Cu} and O_S at all temperatures of baseline kesterite processing. The contributions from various O sources were evaluated by incorporation of the less abundant isotope ¹⁸O at different stages of the CZTS baseline process. Based on these results, a model was proposed where the sulfurization step and the Mo layer are the main contributors of O in CZTS. Hence, the correlation between Na and O distributions can be explained by O immobilizing Na. Consequently, the redistribution of Na during postdeposition heat treatments of kesterites is strongly dependent on the availability of O. The observed interplay between Na and O in kesterite absorbers provides a foundation for more accurate impurity control needed for fabricating high-performance solar cell devices.

4. Experimental Section

The samples were processed through baseline processing steps for Cu₂ZnSnS₄ absorbers. Mo (99.97% purity) bilayer was DC sputtered

with Ar (99.9995% purity) as sputtering gas on top of soda-lime glass substrates. The bilayer consists of an adhesive layer sputtered at 2 Pa and a conductive layer sputtered at 0.8 Pa. CuS (99.99% purity), ZnS (99.99% purity), and SnS (99.99% purity) were cosputtered using a Lesker CMS-18 sputter system, with a 666 Pa Ar background pressure at a substrate temperature of 250 °C. Sulfurization was performed with 60–80 mg of sulfur in a pyrolytic carbon coated graphite box in a tube furnace at 550–580 °C for 13 min. The precursor compositions were determined with Rutherford backscattering-calibrated X-ray fluorescence measurements. At every step of the process, four pieces were taken out and annealed in an ^{18}O -rich atmosphere ($[\text{O}]: 97.1\%$, $[\text{O}]: 2.9\%$ with 20 mbar pressure at room temperature). The cation ratios vary to a degree which could impact diffusion mechanisms. Nevertheless, for all four samples, each temperature series exhibits identical cation ratios. The samples were characterized with SIMS using a Cameca IMS 7f magnetic sector instrument. Cs^+ primary ions were utilized and both negative M^- and positive MCs^+ ions were detected, where “M” is the element of interest. Impact energies were 15 and 5 keV, respectively. The beam was rastered over an area of $150 \times 150 \mu\text{m}^2$ with a beam current of 20 nA. One sample was also measured with time-of-flight-energy elastic recoil detection analysis (ToF-E ERDA) with $^{18}\text{F}^+$ ions with 36 MeV primary energy to provide as a reference for SIMS calibration.^[59,60] The depth was estimated by measuring the depth of each layer using a Dektak 8 Stylus profilometer. The first-principles calculations were carried out using the Vienna Ab initio Simulation Package (VASP).^[61–63] The Perdew–Burke–Ernzerhof (PBE) functional^[64] was employed to describe the exchange–correlation interaction and the projector augmented wave (PAW) pseudopotentials^[65,66] were adopted to model the effect of core electrons. The pseudopotentials with Cu $3d^{10}4s^1$, Zn $3d^{10}4s^2$, Sn $4d^{10}5s^25p^2$, S $3s^23p^4$, O $2s^22p^4$, Li $2s^1$, Na $3s^1$, K $3p^64s^1$, Rb $4p^65s^1$, Cs $5s^25p^66s^1$, and Ag $4d^{10}5s^1$ valence electron configurations were chosen for the study. The cutoff energy threshold for the plane-wave basis was set to 350 eV. All the defect calculations were conducted on the orthorhombic CZTS supercell containing 64 atoms. The Brillouin-zone integrations were done on Γ -centered $4 \times 4 \times 4$ Monkhorst–Pack grids.^[67] Initial configurations for the defect pairs were created by placing Na at the equilibrium Cu site and O at the S equilibrium sites, followed by random perturbation of all atoms in the supercell. This approach yielded a total of 16 nonequivalent configurations for the considered defect pair, which accounts for Na substitution on both 2a and 2c Wyckoff sites in the kesterite CZTS. To optimize the defect geometries, the atomic relaxations were performed until reaching 0.01 eV \AA^{-1} threshold for the Hellmann–Feynman forces. The charge transfer to the X atom was defined as $\Delta Q(X) = Q(X) - Q_{\text{ref}}(X)$, where $Q(X)$ and $Q_{\text{ref}}(X)$ are Bader charges on X atom in the systems containing the defect pair and the corresponding isolated defect, respectively. Importantly, since all except the interstitial defects were formed by substitution of isovalent elements, the first-principles investigation was constrained to the neutral supercell calculations. All the obtained DFT results were analyzed using Visualization for Electronic and Structural Analysis (VESTA)^[68] and Python Materials Genomics (pymatgen).^[69]

Supporting Information

Supporting Information is available from the Wiley Online Library or from the author.

Acknowledgements

This work was funded by the Research Council of Norway (Project No. 243642) and the Swedish Foundation for Strategic Research. The Research Council of Norway is also acknowledged for the support to the Norwegian Micro and Nano-Fabrication Facility, NorFab (Project No. 245963/F50). The authors acknowledge the Swedish

National Infrastructure for Computing for providing access to supercomputer resources. S.G. would like to acknowledge J. K. Larsen, N. Saini, and S. Englund for assistance with sample preparation and processing, K. Rudisch for guidance on processing of ERDA data, and D. Primetzhofer for ERDA measurements. K.V.S. would like to thank O. I. Malý and J. J. Scragg for the fruitful discussions of the results. X.L. and T.S.B. acknowledge funding from the Research Council of Norway (“SURKINOX” 258875) through the M-ERA.NET Joint Call 2016.

Conflict of Interest

The authors declare no conflict of interest.

Keywords

defect complexes, depth distributions, kesterite, oxygen, sodium

Received: March 5, 2019

Revised: April 30, 2019

Published online:

- [1] W. Wang, M. T. Winkler, O. Gunawan, T. Gokmen, T. K. Todorov, Y. Zhu, D. B. Mitzi, *Adv. Energy Mater.* **2014**, *4*, 1301465.
- [2] S. G. Haass, M. Diethelm, M. Werner, B. Bissig, Y. E. Romanyuk, A. N. Tiwari, *Adv. Energy Mater.* **2015**, *5*, 1500712.
- [3] K.-J. Yang, D.-H. Son, S.-J. Sung, J.-H. Sim, Y.-I. Kim, S.-N. Park, D.-H. Jeon, J. Kim, D.-K. Hwang, C.-W. Jeon, D. Nam, H. Cheong, J.-K. Kang, D.-H. Kim, *J. Mater. Chem. A* **2016**, *4*, 10151.
- [4] S. Giraldo, M. Neuschitzer, T. Thersleff, S. López-Marino, Y. Sánchez, H. Xie, M. Colina, M. Placidi, P. Pistor, V. Izquierdo-Roca, K. Leifer, A. Pérez-Rodríguez, E. Saucedo, *Adv. Energy Mater.* **2015**, *5*, 1501070.
- [5] T. Taskesen, J. Neerken, J. Schöneberg, D. Pareek, V. Steininger, J. Parisi, L. Gütay, *Adv. Energy Mater.* **2018**, *8*, 1703295.
- [6] C. Yan, J. Huang, K. Sun, S. Johnston, Y. Zhang, H. Sun, A. Pu, M. He, F. Liu, K. Eder, L. Yang, J. M. Cairney, N. J. Ekins-Daukes, Z. Hameiri, J. A. Stride, S. Chen, M. A. Green, X. Hao, *Nat. Energy* **2018**, *3*, 764.
- [7] A. Cabas-Vidani, S. G. Haass, C. Andres, R. Caballero, R. Figi, C. Schreiner, J. A. Márquez, C. Hages, T. Unold, D. Bleiner, A. N. Tiwari, Y. E. Romanyuk, *Adv. Energy Mater.* **2018**, *8*, 1801191.
- [8] S. Giraldo, Z. Jehl, M. Placidi, V. Izquierdo-Roca, A. Pérez-Rodríguez, E. Saucedo, *Adv. Mater.* **2019**, *31*, 1806692.
- [9] C. M. Sutter-Fella, J. A. Stükelberger, H. Hagendorfer, F. La Mattina, L. Kranz, S. Nishiwaki, A. R. Uhl, Y. E. Romanyuk, A. N. Tiwari, *Chem. Mater.* **2014**, *26*, 1420.
- [10] H. Xie, S. López-Marino, T. Olar, Y. Sánchez, M. Neuschitzer, F. Oliva, S. Giraldo, V. Izquierdo-Roca, I. Lauerermann, A. Pérez-Rodríguez, E. Saucedo, *ACS Appl. Mater. Interfaces* **2016**, *8*, 5017.
- [11] Z.-K. Yuan, S. Chen, Y. Xie, J.-S. Park, H. Xiang, X.-G. Gong, S.-H. Wei, *Adv. Energy Mater.* **2016**, *6*, 1601191.
- [12] T. Gershon, Y. S. Lee, R. Mankad, O. Gunawan, T. Gokmen, D. Bishop, B. McCandless, S. Guha, *Appl. Phys. Lett.* **2015**, *106*, 123905.
- [13] T. Gershon, B. Shin, N. Bojarczuk, M. Hopstaken, D. B. Mitzi, S. Guha, *Adv. Energy Mater.* **2015**, *5*, 1400849.
- [14] K. Sardashti, R. Haight, T. Gokmen, W. Wang, L.-Y. Chang, D. B. Mitzi, A. C. Kummel, *Adv. Energy Mater.* **2015**, *5*, 1402180.
- [15] A. Laemmle, R. Würz, T. Schwarz, O. Cojocar-Mirédin, P.-P. Choi, M. Powalla, *J. Appl. Phys.* **2014**, *115*, 154501.

- [16] L. Kronik, D. Cahen, H. W. Schock, *Adv. Mater.* **1998**, *10*, 31.
- [17] D. Cahen, R. Noufi, *Appl. Phys. Lett.* **1989**, *54*, 558.
- [18] D. Cahen, R. Noufi, *Sol. Cells* **1991**, *30*, 53.
- [19] D. W. Niles, M. Al-Jassim, K. Ramanathan, *J. Vac. Sci. Technol., A* **1999**, *17*, 291.
- [20] Z. Su, K. Sun, Z. Han, H. Cui, F. Liu, Y. Lai, J. Li, X. Hao, Y. Liu, M. A. Green, *J. Mater. Chem. A* **2014**, *2*, 500.
- [21] U. Rau, D. Braunger, R. Herberholz, H. W. Schock, J.-F. Guillemoles, L. Kronik, D. Cahen, *J. Appl. Phys.* **1999**, *86*, 497.
- [22] J. K. Larsen, Y. Ren, N. Ross, E. Särhammar, S.-Y. Li, C. Platzer-Björkman, *Thin Solid Films* **2017**, *633*, 118.
- [23] I. Repins, C. Beall, N. Vora, C. DeHart, D. Kuciauskas, P. Dippo, B. To, J. Mann, W.-C. Hsu, A. Goodrich, R. Noufi, *Sol. Energy Mater. Sol. Cells* **2012**, *101*, 154.
- [24] D. Hironiwa, N. Sakai, T. Kato, H. Sugimoto, Z. Tang, J. Chantana, T. Minemoto, *Thin Solid Films* **2015**, *582*, 151.
- [25] J. H. Kim, S.-Y. Choi, M. Choi, T. Gershon, Y. S. Lee, W. Wang, B. Shin, S.-Y. Chung, *Adv. Energy Mater.* **2016**, *6*, 1501902.
- [26] R. V. Forest, E. Eser, B. E. McCandless, R. W. Birkmire, J. G. Chen, *AIChE J.* **2014**, *60*, 2365.
- [27] N. Ross, S. Grini, K. Rudisch, L. Vines, C. Platzer-Bjorkman, *IEEE J. Photovoltaics* **2018**, *8*, 1132.
- [28] R. Haight, X. Shao, W. Wang, D. B. Mitzi, *Appl. Phys. Lett.* **2014**, *104*, 033902.
- [29] A. Rockett, J. S. Britt, T. Gillespie, C. Marshall, M. M. A. Jassim, F. Hasoon, R. Matson, B. Basol, *Thin Solid Films* **2000**, *372*, 212.
- [30] T. Yamamoto, T. Watanabe, Y. Hamashoji, *Phys. B* **2001**, *308*, 1007.
- [31] V. Probst, F. Karg, J. Rimmasch, W. Riedel, W. Stetter, H. Harms, O. Eibl, *MRS Proc.* **1996**, *426*, 165.
- [32] T. Schwarz, O. Cojocar-Mirédin, P. Choi, M. Mousel, A. Redinger, S. Siebentritt, D. Raabe, *Appl. Phys. Lett.* **2013**, *102*, 042101.
- [33] O. Cojocar-Mirédin, P.-P. Choi, D. Abou-Ras, S. S. Schmidt, R. Caballero, D. Raabe, *IEEE J. Photovoltaics* **2011**, *1*, 207.
- [34] J. Keller, R. Schlesiger, I. Riedel, J. Parisi, G. Schmitz, A. Avellan, T. Dalibor, *Sol. Energy Mater. Sol. Cells* **2013**, *117*, 592.
- [35] P. Schöppe, S. Schönherr, R. Würz, W. Wisniewski, G. Martínez-Criado, M. Ritzer, K. Ritter, C. Ronning, C. S. Schnorr, *Nano Energy* **2017**, *42*, 307.
- [36] W.-J. Yin, Y. Wu, S.-H. Wei, R. Noufi, M. M. Al-Jassim, Y. Yan, *Adv. Energy Mater.* **2014**, *4*, 1300712.
- [37] J. Li, D. B. Mitzi, V. B. Shenoy, *ACS Nano* **2011**, *5*, 8613.
- [38] M. Wong, K. Tse, J. Zhu, *J. Phys. Chem. C* **2018**, *122*, 7759.
- [39] C. Persson, A. Zunger, *Phys. Rev. Lett.* **2003**, *91*, 266401.
- [40] C. Persson, A. Zunger, *Appl. Phys. Lett.* **2005**, *87*, 211904.
- [41] Y. Yan, C.-S. Jiang, R. Noufi, S.-H. Wei, H. R. Moutinho, M. M. Al-Jassim, *Phys. Rev. Lett.* **2007**, *99*, 235504.
- [42] S. Siebentritt, M. Igalson, C. Persson, S. Lany, *Prog. Photovoltaics* **2010**, *18*, 390.
- [43] T. Maeda, A. Kawabata, T. Wada, *Phys. Status Solidi C* **2015**, *12*, 631.
- [44] E. Ghorbani, J. Kiss, H. Mirhosseini, M. Schmidt, J. Windeln, T. D. Kühne, C. Felsler, *J. Phys. Chem. C* **2016**, *120*, 2064.
- [45] K. Tse, M. Wong, Y. Zhang, J. Zhang, M. Scarpulla, J. Zhu, *J. Appl. Phys.* **2018**, *124*, 165701.
- [46] M. Han, X. Zhang, Z. Zeng, *Phys. Chem. Chem. Phys.* **2017**, *19*, 17799.
- [47] L. E. Oikonen, M. G. Ganchenkova, A. P. Seitsonen, R. M. Nieminen, *J. Appl. Phys.* **2013**, *114*, 083503.
- [48] R. D. Shannon, *Acta Crystallogr., Sect. A: Found. Adv.* **1976**, *32*, 751.
- [49] C. Tablero, *Thin Solid Films* **2012**, *520*, 5011.
- [50] C. G. Van de Walle, J. Neugebauer, *J. Appl. Phys.* **2004**, *95*, 3851.
- [51] H. Mehrer, A. W. Imre, E. Tanguet-Nijokep, *J. Phys.: Conf. Ser.* **2008**, *106*, 012001.
- [52] N. P. Bansal, R. H. Doremus, *Handbook of Glass Properties*, Elsevier, Amsterdam **2013**.
- [53] R. A. De Souza, J. A. Kilner, *Solid State Ionics* **1999**, *9*.
- [54] Y. Ren, N. Ross, J. K. Larsen, K. Rudisch, J. J. S. Scragg, C. Platzer-Björkman, *Chem. Mater.* **2017**, *29*, 3713.
- [55] R. V. Forest, B. E. McCandless, X. He, A. A. Rockett, E. Eser, K. D. Dobson, R. W. Birkmire, *J. Appl. Phys.* **2017**, *121*, 245102.
- [56] S. Grini, N. Ross, C. Persson, C. Platzer-Björkman, L. Vines, *Thin Solid Films* **2018**, *665*, 159.
- [57] N. Ross, J. Larsen, S. Grini, L. Vines, C. Platzer-Björkman, *Thin Solid Films* **2017**, *623*, 110.
- [58] T. Ericson, F. Larsson, T. Törndahl, C. Frisk, J. Larsen, V. Kosyak, C. Hägglund, S. Li, C. Platzer-Björkman, *Sol. RRL* **2017**, *1*, 1700001.
- [59] S. Englund, V. Paneta, D. Primetzhofner, Y. Ren, O. Donzel-Gargand, J. K. Larsen, J. Scragg, C. Platzer-Björkman, *Thin Solid Films* **2017**, *639*, 91.
- [60] M. S. Janson, *Contes Conversion of Time-Energy Spectra: A Program for ERDA Data Analysis*, Internal Report, Uppsala University, Uppsala, **2004**.
- [61] G. Kresse, J. Furthmüller, *Comput. Mater. Sci.* **1996**, *6*, 15.
- [62] G. Kresse, J. Hafner, *Phys. Rev. B* **1993**, *47*, 558.
- [63] G. Kresse, J. Furthmüller, *Phys. Rev. B* **1996**, *54*, 11169.
- [64] J. P. Perdew, K. Burke, M. Ernzerhof, *Phys. Rev. Lett.* **1996**, *77*, 3865.
- [65] P. E. Blöchl, *Phys. Rev. B* **1994**, *50*, 17953.
- [66] G. Kresse, D. Joubert, *Phys. Rev. B* **1999**, *59*, 1758.
- [67] H. J. Monkhorst, J. D. Pack, *Phys. Rev. B* **1976**, *13*, 5188.
- [68] K. Momma, F. Izumi, *J. Appl. Crystallogr.* **2011**, *44*, 1272.
- [69] S. P. Ong, W. D. Richards, A. Jain, G. Hautier, M. Kocher, S. Cholia, D. Gunter, V. L. Chevrier, K. A. Persson, G. Ceder, *Comput. Mater. Sci.* **2013**, *68*, 314.

ADVANCED ENERGY MATERIALS

Supporting Information

for *Adv. Energy Mater.*, DOI: 10.1002/aenm.201900740

Strong Interplay between Sodium and Oxygen in Kesterite Absorbers: Complex Formation, Incorporation, and Tailoring Depth Distributions

*Sigbjørn Grini, * Kostiantyn V. Sopiha, Nils Ross, Xin Liu, Tor S. Bjørheim, Charlotte Platzer-Björkman, Clas Persson, and Lasse Vines*

Supporting Information

Strong Interplay between Sodium and Oxygen in Kesterite Absorbers: Complex Formation, Incorporation and Tailoring Depth Distributions

Sigbjørn Grini*, Kostiantyn V. Sopiha, Nils Ross, Xin Liu, Tor S. Bjørheim, Charlotte Platzer-Björkman, Clas Persson and Lasse Vines

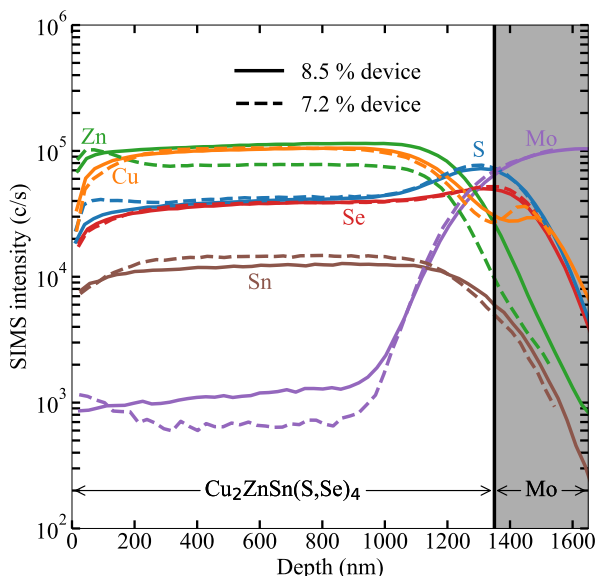


Figure S1. SIMS depth profiles of Cu, Zn, Sn, S, Se and Mo measured on two CZTSSe absorbers where the mean device produced an 8.5 % PCE (solid lines) and a 7.2 % PCE (dashed lines). The samples are chosen from our previous study of high performance devices.^[1] The Zn and S signals from the depth profile of the 7.2 % PCE sample are increased near the surface due to the presence of Zn-rich secondary phases.

Configurations of Na_i defects in CZTS

In this work, seven different configurations for Na_i in CZTS were analyzed, as shown in **Figure S2**. Three of them (see Figure S2a-c) were previously reported elsewhere^[2-4], with the most stable being Na_i coordinated with four cations (tc site). The other four configurations identified herein form when the inserted Na kicks out Cu atom into interstitial site and occupies its place forming $\text{Cu}_i\text{-Na}_{\text{Cu}}$ complex (see Figure S2d-g). The most stable among such

complexes has 0.04 eV lower energy than Na_i at tc site (see Figure S2d), which makes it the most stable configuration reported to date. Furthermore, we found that it takes practically no energy to separate the Na_{Cu} and Cu_i , suggesting that the $\text{Cu}_i\text{-Na}_{\text{Cu}}$ complexes do not reside together in equilibrium CZTS at finite temperatures.

Configurations of X_i interstitial defect in CZTS

To identify the most stable configuration for interstitial X_i defects ($X=\text{Ag}, \text{Li}, \text{K}, \text{Rb}, \text{Cs}$), we investigated all seven configurations identified for Na_i by substituting Na with the X element. We found that most elements prefer to form $\text{Cu}_i\text{-Na}_{\text{Cu}}$ complexes (see Figure S2d), except for Li, which favors interstitial site shown in Figure S2b instead. These most stable configurations for interstitial X_i defects were further used as reference systems for calculating the binding energy of complexes formed by X_i and O_s .

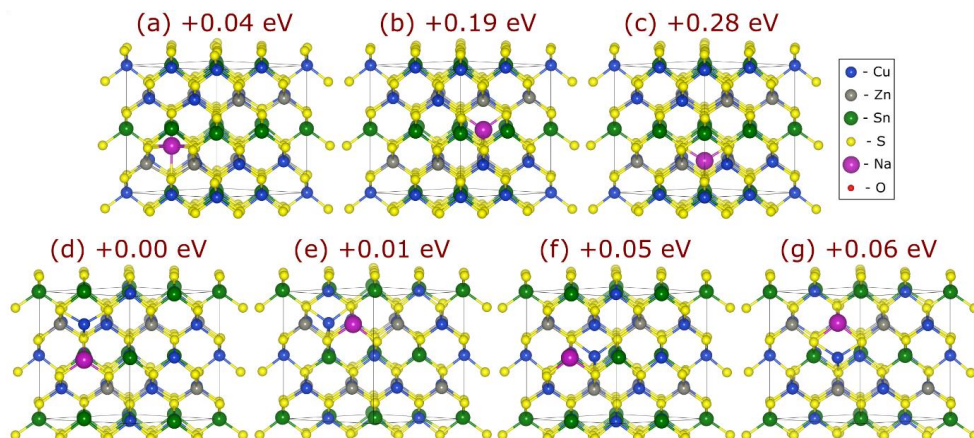


Figure S2. Seven different configurations for Na_i in a 64-atom CZTS supercell; the numbers give the defect energies with respect to that of the most stable configuration. (a) Na inserted into the interstitial site coordinated with four cations (tc site); this configuration was previously reported to be the most stable. (b) and (c) Na insertion into the interstitial sites coordinated by six cations and located in the Zn and Sn layers, respectively. (d-g) different configurations for $\text{Cu}_i\text{-Na}_{\text{Cu}}$ complexes formed when Na_i kicks out Cu into the interstitial site and occupies its place; the most stable $\text{Cu}_i\text{-Na}_{\text{Cu}}$ complex has 0.04 eV lower energy than Na_i at tc site.

Complexes of Na_i and O_s

To obtain the distance dependence of the binding energy for the Na_i and O_s defects, we investigated all inequivalent defect pairs that can be formed by replacing S with O in the 64-

atom CZTS supercell containing a Na_i defect. This procedure was performed for all seven Na_i configurations shown in Figure S2, and therefore, a total of 153 different defect pairs were analyzed. As one can see in **Figure S3a**, Na_i and O_s exhibit a clear tendency for binding into NaO complexes, with the largest binding energy of 1.19 eV, which is even higher than 0.76 eV computed for the substitutional Na_{Cu} and O_s defect complex. The most stable configuration (see Figure S3d) is characterized by a significant lattice relaxation in the vicinity of the NaO complex. Specifically, while the inserted Na atom binds to O with 2.13 Å bond, it kicks out two neighboring Cu atoms toward the interstitial positions, thus breaking two Cu-O bonds. Interestingly, this coordination differs significantly from all seven configurations for sole Na_i defect shown in Figure S2. Further, similar to the substitutional defects, the binding energy between Na_i and O_s was found to correlate with Bader charges transferred to Na and O atoms, further evincing ionic bonding nature between the impurities.

Complexes of X_i and O_s

To identify the most stable complexes of X_i and O_s , we sorted out and analyzed all systems with Na_i and O_s defect pairs separated by less than 3.0 Å. The total number of such systems amounts to 13 for each X element. Here, the most stable XO complexes were found to have geometries close to that found for NaO complex shown in Figure S3d, except for Li and Ag which shifted slightly away from the equilibrium Na_i position. Despite the small differences in geometries, the binding energy of the XO complexes was found to correlate with electronegativity of the X element, in agreement with the results for the substitutional defects presented in the main text.

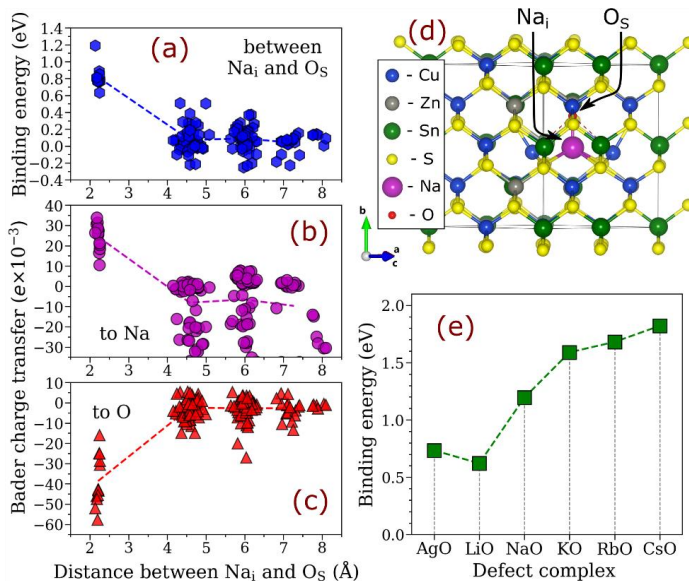


Figure S3. First-principles analysis of the interaction between Na_i and O_s defects in CZTS. (a) Binding energy of Na_i and O_s in a 64-atom supercell *versus* distance between them. Bader charge transfer (b) to Na and (c) to O atoms *versus* distance between them; the separated defects in 64-atom CZTS supercells were used as reference systems for the binding energy and Bader charge transfer calculations. (d) The structure of the most stable nearest-neighbor NaO complex; the broken Cu-O bonds are illustrated by the red dashed lines; the corresponding .CIF file is given in **Supporting Information** below. (e) Binding energies for complexes formed between O_s and different isovalent interstitial defects; only the most stable configurations of the complexes are presented. The dashed lines in all graphs above are to guide the eye.

Complexes of NaO and Na_{Cu}

The tendency for binding between NaO and Na_{Cu} was also studied by introducing Na_{Cu} defect at different positions in the 64-atom supercell containing the most stable NaO defect complex. The total binding energy was computed as:

$$E_b = 2 \cdot E_{tot}(Na) + E_{tot}(O) - E_{tot}(NaO + Na) - 2 \cdot E_{tot}(pristine)$$

where $E_{tot}(Na)$, $E_{tot}(O)$, $E_{tot}(NaO + Na)$ and $E_{tot}(pristine)$ are the total energies of CZTS supercells containing isolated Na_{Cu}, isolated O_s, both NaO complex and Na_{Cu}, and pristine supercell, respectively. The total binding energy of the most stable Na₂O complex in

the nearest neighbor position is $0.76 + 0.56 = 1.32$ eV. As one can see in Figure S4, the trends for binding energy and Bader charge transfers are similar to those observed for NaO, which reflects that both Na-O bonds in Na₂O complex are of the same highly ionic nature as that in NaO.

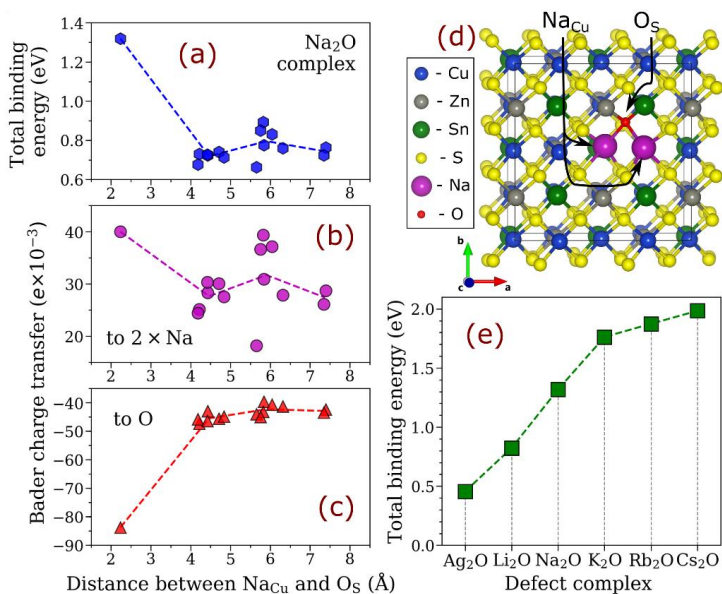


Figure S4. First-principles analysis of the interaction between the most stable NaO complex and Na_{Cu} in CZTS. (a) Total binding energy of Na₂O in 64-atom supercell *versus* distance between the NaO complex and Na_{Cu} defect. Bader charge transfer (b) to two Na atoms (aggregated) and (c) to O atom *versus* distance between O_S and the second Na_{Cu} defect; the separated defects in 64-atom CZTS supercells were used as reference systems for the binding energy and Bader charge transfer calculations. (d) Structure of the nearest-neighbor Na₂O complex; the corresponding .CIF file is given in the **Supporting Information** below. (e) Binding energy for X₂O complexes formed between O_S and different isovalent substitutional X defects on the Cu sites; only the most stable configurations of the complexes are presented. The dashed lines in all graphs above are to guide the eye.

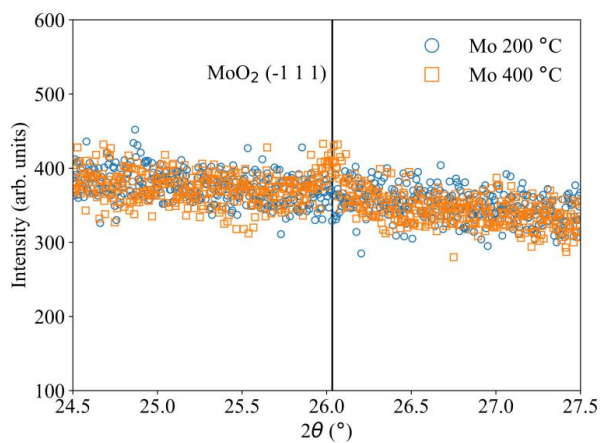


Figure S5. X-ray diffractogram of the MoO_2 (-1 1 1) peak (PDF #00-003-0671). The increased signal is observed after heat treatment in ^{18}O rich atmosphere at 400 °C for 30 minutes.

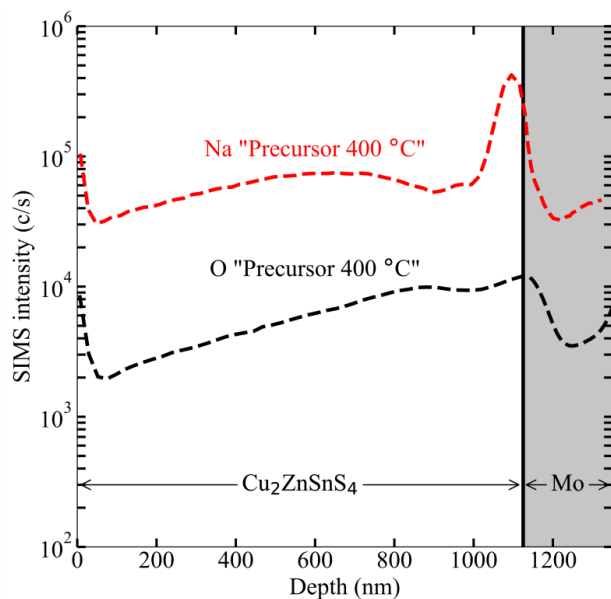


Figure S6. SIMS depth profiles of Na (dashed red lines) and O (dashed black lines) measured on the sample “Precursor 400 °C” after the sulfurization.

Structure (.CIF format) of the most stable complex formed by Na_{Cu} and O_8 , as shown in Figure 2d.

```
_cell_length_a      10.94865
_cell_length_b      10.94865
_cell_length_c      10.94131
_cell_angle_alpha   90
_cell_angle_beta    90
_cell_angle_gamma   90
_space_group_name_H-M_alt 'P 1'
```

```
loop_
  _atom_site_fract_x
  _atom_site_fract_y
  _atom_site_fract_z
  _atom_site_type_symbol
0.522687  0.755435  0.738088  Zn
0.500225  0.246579  0.751349  Zn
0.004719  0.754166  0.751040  Zn
0.006980  0.254327  0.752230  Zn
0.755387  0.503695  0.253561  Zn
0.753675  0.003036  0.251002  Zn
0.253027  0.505149  0.251538  Zn
0.253939  0.002534  0.250208  Zn
0.501820  0.004788  0.500181  Cu
0.004918  0.507361  0.499640  Cu
0.004741  0.002659  0.500946  Cu
0.779039  0.477699  0.775879  Cu
0.757467  0.007930  0.753582  Cu
0.253533  0.508931  0.754121  Cu
0.253642  0.001005  0.750591  Cu
0.752576  0.753856  0.003029  Cu
0.753087  0.255310  0.001778  Cu
0.258522  0.750674  0.997578  Cu
0.254236  0.253775  0.001583  Cu
0.504762  0.754543  0.251615  Cu
0.502012  0.252230  0.248715  Cu
0.000881  0.751139  0.253394  Cu
0.004446  0.253132  0.250405  Cu
0.748159  0.759199  0.511931  Sn
0.756005  0.249224  0.499410  Sn
0.252939  0.755912  0.499751  Sn
0.251157  0.251998  0.500367  Sn
0.503495  0.506302  0.000922  Sn
0.504586  0.001235  0.000971  Sn
0.004404  0.503401  0.002840  Sn
0.004494  0.003018  0.001630  Sn
0.625778  0.119290  0.630238  S
0.125385  0.622352  0.630278  S
0.124328  0.119253  0.630697  S
0.884815  0.889268  0.633130  S
```

0.885280	0.385369	0.627411	S
0.383788	0.885677	0.629528	S
0.372019	0.375888	0.640163	S
0.640919	0.876792	0.872182	S
0.631906	0.372124	0.871052	S
0.137125	0.873409	0.872676	S
0.137827	0.376882	0.873504	S
0.871637	0.633626	0.873636	S
0.873531	0.135529	0.873983	S
0.381287	0.637161	0.863599	S
0.369659	0.128781	0.874331	S
0.875228	0.870475	0.130793	S
0.875136	0.371545	0.131083	S
0.375503	0.869737	0.129578	S
0.374513	0.372702	0.129783	S
0.633582	0.636060	0.131990	S
0.632616	0.135402	0.129052	S
0.132576	0.637930	0.129272	S
0.133313	0.136144	0.130244	S
0.880389	0.628106	0.378739	S
0.888860	0.122299	0.370705	S
0.381750	0.629561	0.369127	S
0.385276	0.125111	0.370767	S
0.620959	0.883836	0.372677	S
0.627345	0.374593	0.367385	S
0.119806	0.882683	0.370892	S
0.119801	0.383401	0.371687	S
0.533474	0.525046	0.537758	Na
0.636243	0.672322	0.625734	O

Structure (.CIF formal) of the most stable complex formed by Na_i and O_s, as shown in Figure S2d.

```
_cell_length_a          10.94865
_cell_length_b          10.94865
_cell_length_c          10.94131
_cell_angle_alpha       90
_cell_angle_beta        90
_cell_angle_gamma       90
_space_group_name_H-M_alt 'P 1'
```

loop_

```
_atom_site_fract_x
_atom_site_fract_y
_atom_site_fract_z
_atom_site_type_symbol
0.519491  0.763516  0.734558  Zn
0.497883  0.243560  0.746996  Zn
0.004351  0.754015  0.747200  Zn
0.009567  0.255774  0.753343  Zn
0.755682  0.508859  0.251422  Zn
0.754476  0.005269  0.245566  Zn
0.250930  0.505401  0.246939  Zn
0.253843  0.002528  0.246796  Zn
0.453467  0.459736  0.450361  Cu
0.500141  0.007727  0.496294  Cu
0.001701  0.509019  0.499199  Cu
0.006888  0.002076  0.499395  Cu
0.801926  0.457590  0.804084  Cu
0.757943  0.008439  0.752512  Cu
0.256840  0.510198  0.750390  Cu
0.251851  0.001933  0.749842  Cu
0.752956  0.755407  0.000494  Cu
0.757308  0.259022  0.999551  Cu
0.259555  0.752198  0.993934  Cu
0.254602  0.254420  0.000176  Cu
0.508014  0.758422  0.246108  Cu
0.502059  0.258574  0.251061  Cu
0.001071  0.753325  0.252925  Cu
0.005206  0.253879  0.247633  Cu
0.745184  0.765026  0.506758  Sn
0.759980  0.242102  0.499099  Sn
0.254236  0.755004  0.500610  Sn
0.246439  0.251332  0.493774  Sn
0.501317  0.510026  0.000021  Sn
0.506425  0.005245  0.999554  Sn
0.009584  0.504493  0.003571  Sn
0.004776  0.003302  0.999862  Sn
0.622620  0.115556  0.630142  S
0.124338  0.620506  0.628921  S
0.123807  0.120484  0.630184  S
```


0.885121	0.890632	0.630914	S
0.886928	0.386952	0.630017	S
0.382682	0.891388	0.627131	S
0.378032	0.382847	0.627906	S
0.641555	0.878251	0.871469	S
0.628608	0.370627	0.870128	S
0.136453	0.873203	0.869719	S
0.142715	0.378082	0.871076	S
0.874926	0.634468	0.875915	S
0.874155	0.136962	0.871911	S
0.381672	0.640290	0.859177	S
0.367986	0.130818	0.871741	S
0.875119	0.870460	0.128750	S
0.875577	0.374134	0.131317	S
0.375833	0.871381	0.126086	S
0.373359	0.373214	0.127558	S
0.635038	0.638468	0.129194	S
0.633561	0.141752	0.128506	S
0.134937	0.642436	0.128743	S
0.134409	0.137311	0.127842	S
0.879779	0.630707	0.377815	S
0.893520	0.119122	0.364799	S
0.385501	0.628885	0.362601	S
0.384979	0.126197	0.366493	S
0.619316	0.889509	0.367365	S
0.626249	0.382684	0.371020	S
0.122035	0.882901	0.369077	S
0.115693	0.387461	0.368527	S
0.625228	0.488779	0.630196	Na
0.631657	0.683445	0.621111	O

Structure (.CIF formal) of the most stable Na₂O complex shown in Figure S3d.

```
_cell_length_a      10.94865
_cell_length_b      10.94865
_cell_length_c      10.94131
_cell_angle_alpha   90
_cell_angle_beta    90
_cell_angle_gamma   90
_space_group_name_H-M_alt 'P 1'
```

```
loop_
  _atom_site_fract_x
  _atom_site_fract_y
  _atom_site_fract_z
  _atom_site_type_symbol
0.516052  0.750258  0.982428  Zn
0.498771  0.239992  0.999440  Zn
0.006510  0.748800  0.997954  Zn
0.004612  0.244526  0.996441  Zn
0.753667  0.495635  0.496774  Zn
0.751638  0.995329  0.495814  Zn
0.248453  0.496062  0.495671  Zn
0.251432  0.995213  0.494954  Zn
0.499520  0.999525  0.745185  Cu
0.001149  0.497808  0.745181  Cu
0.001113  0.995717  0.747917  Cu
0.754159  0.999818  0.999328  Cu
0.251165  0.499917  0.998484  Cu
0.253426  0.994453  0.995044  Cu
0.750010  0.748756  0.251216  Cu
0.752278  0.245257  0.249274  Cu
0.256373  0.742153  0.241723  Cu
0.251146  0.246103  0.246937  Cu
0.502501  0.748910  0.493642  Cu
0.500708  0.244887  0.494671  Cu
0.999598  0.742770  0.499006  Cu
0.001928  0.245943  0.496329  Cu
0.745118  0.754201  0.753552  Sn
0.754870  0.239936  0.743832  Sn
0.247317  0.748982  0.744239  Sn
0.249351  0.244754  0.745929  Sn
0.499218  0.495461  0.247622  Sn
0.502150  0.994307  0.245640  Sn
0.003689  0.496202  0.247633  Sn
0.002497  0.994910  0.246984  Sn
0.623284  0.112154  0.875759  S
0.122329  0.614233  0.875189  S
0.123540  0.110534  0.875587  S
0.881656  0.880780  0.878977  S
0.886224  0.369886  0.868378  S
0.380807  0.878430  0.872466  S
```

0.372071	0.368849	0.884577	S
0.637686	0.867918	0.117128	S
0.626341	0.359928	0.123887	S
0.138200	0.868504	0.118067	S
0.135135	0.368376	0.117705	S
0.879816	0.636378	0.128097	S
0.871107	0.126931	0.119513	S
0.379075	0.627730	0.108651	S
0.366985	0.121377	0.119496	S
0.873611	0.863634	0.378087	S
0.874128	0.364134	0.375668	S
0.372420	0.863072	0.373283	S
0.370724	0.363664	0.376779	S
0.630146	0.627657	0.376509	S
0.630074	0.126726	0.375519	S
0.131248	0.629917	0.374672	S
0.130420	0.128717	0.375651	S
0.877866	0.620033	0.623842	S
0.886316	0.113601	0.615180	S
0.374305	0.626947	0.608562	S
0.382621	0.117914	0.615522	S
0.616588	0.877367	0.616835	S
0.626509	0.367152	0.612947	S
0.115935	0.876694	0.615955	S
0.117819	0.375418	0.616941	S
0.519800	0.523943	0.769285	Na
0.731249	0.524342	0.978015	Na
0.631412	0.664088	0.867845	O

References

- [1] N. Ross, S. Grini, K. Rudisch, L. Vines, C. Platzer-Bjorkman, *IEEE J. Photovolt.* **2018**, *8*, 1132.
- [2] T. Maeda, A. Kawabata, T. Wada, *Phys. Status Solidi C* **2015**, *12*, 631.
- [3] E. Ghorbani, J. Kiss, H. Mirhosseini, M. Schmidt, J. Windeln, T. D. Kühne, C. Felser, *J. Phys. Chem. C* **2016**, *120*, 2064.
- [4] K. Tse, M. Wong, Y. Zhang, J. Zhang, M. Scarpulla, J. Zhu, *J. Appl. Phys.* **2018**, *124*, 165701.

Paper VI

Dynamic impurity redistributions in kesterite absorbers

**Sigbjørn Grini, Hisham Aboulfadl, Nils Ross, Clas Persson,
Charlotte Platzer-Björkman, Mattias Thuvander, Lasse Vines**

Submitted

Dynamic impurity redistributions in kesterite absorbers

Sigbjørn Grini^{1}, Hisham Aboulfadl², Nils Ross^{1,3}, Clas Persson^{1,4}, Charlotte Platzer-Björkman³, Mattias Thuvander² and Lasse Vines¹*

¹Department of Physics/Centre for Materials Science and Nanotechnology, University of Oslo, P.O.Box 1048, Blindern, N-0316 Oslo, Norway

²Department of Physics, Chalmers University of Technology, 41296 Göteborg, Sweden

³Ångström Solar Center, Division of Solid State Electronics, Uppsala University, Uppsala, 75120, Sweden

⁴Department of Materials Science and Engineering, KTH Royal Institute of Technology, 10044 Stockholm, Sweden

*E-mail: sigbjorn.grini@smn.uio.no

Abstract

$\text{Cu}_2\text{ZnSn}(\text{S},\text{Se})_4$ is a promising non-toxic earth-abundant solar cell absorber. To optimize the thin films for solar cell device performance, post deposition treatments at temperatures below the crystallization temperature are normally performed, which alter the surface and bulk properties. The polycrystalline thin films contain relatively high concentrations of impurities, such as sodium, oxygen and hydrogen. During the treatments, these impurities will migrate and likely agglomerate at lattice defects or interfaces. In this work, impurity redistribution after air annealing for temperatures up to 200 °C and short heavy water treatments have been studied. In addition, nonuniformities of the sodium distribution on a nanometer and micrometer scale have been characterized by atom probe tomography and secondary ion mass spectrometry, respectively. Sodium and oxygen correlate to a greater extent after heat treatments, supporting strong binding between the two impurities. Redistributions of these impurities occur even at room temperature over longer time periods. Heavy water treatments confirm out-diffusion of sodium with more incorporation of oxygen and hydrogen. It is observed that the increased hydrogen content does not originate from the heavy water. The existence of an “ice-like” layer on top of the $\text{Cu}_2\text{ZnSnS}_4$ layer is proposed.

Keywords: CZTS, kesterite, air annealing, impurities, sodium, oxygen

Introduction

Impurities are of vital importance for the performance of semiconductor devices.^{1,2} This holds particularly true for $\text{Cu}_2\text{ZnSn}(\text{S},\text{Se})_4$, called CZTSSe or kesterite, a promising absorber material for solar cell applications. For CZTSSe thin films, there are several intrinsic defects,³ but also many extrinsic impurities such as sodium (Na), oxygen (O) and hydrogen (H). Na is intentionally introduced via the soda-lime glass (SLG) substrate, or added during the fabrication process, for instance through NaF treatment.⁴ Na has been proposed to passivate grain boundaries and deep defects, increase the carrier concentration as well as contribute to crystal growth of CZTSSe.⁴⁻⁷ Na has been commonly observed to segregate at the grain boundaries, but also a significant amount usually resides inside the grains⁸. Additionally, cluster formations have been observed.^{9,10} Other alkalis may also be added and yield a positive effect on the device performance.¹¹ Oxygen, on the other hand, is unintentionally introduced into CZTSSe and may originate from the Mo layer and through contaminations during the processing.¹² O has been observed in grain boundaries and on the surface, either correlated with Na^{13} or as SnO_x .^{14,15} Hydrogen has also been reported to have a passivating effect.¹⁶

It is well known that air annealing of CZTSSe samples during processing can improve the power conversion efficiency (PCE). However, air annealing at certain temperatures may also be detrimental for the PCE. Air annealing is typically performed below the crystallization temperature and the effects on the performance can be attributed to redistribution of impurities^{15,17,18} or modification of the surface.^{19,20} If the PCE improvements are related to the former, the diffusion mechanisms of the involved is of utmost importance. Na diffusion has been extensively studied in $\text{Cu}(\text{In},\text{Ga})\text{Se}_2$,²¹⁻²⁴ however, less is known about the diffusion in CZTSSe.^{17,18} To the best of our knowledge, no study has been dedicated to study diffusivity of O in kesterite thin films. We have previously identified the correlation between Na and O in CZTS and shown that O can be used to trap Na due to the strong Na-O bond.²⁵ Hence, a necessary aspect is to study Na and O depth profiles after low temperature heat treatments, which can reveal their diffusion mechanisms.

Here we report on the redistribution of three prevalent impurities in CZTS during air annealing and wet chemical treatments. To better distinguish diffusion inside grains and at grain boundaries one can vary the average size of the grains. To accomplish this, we prepared two sample sets of sulfide CZTS on top of Mo where we varied the sulfurization time at a lower-than-baseline temperature resulting in a total of six samples (a)-(f). The average grain sizes were estimated to vary between roughly 100 nm for sample (a) to 300 nm for sample (f). Fortuitously, after the sulfurization a nonuniform Na and O distribution with depth was produced for all samples (shown below). With isothermal air annealing treatments from 50 to 200 °C, Na and O diffuse in the CZTS absorbers. Additionally, post deposition “wet chemical cleaning” treatments are commonly used to remove unwanted phases on the surface of

the CZTS absorber before the buffer layer deposition.^{11,26,27} Water (H₂O) treatments can remove such phases.²⁸ The origin of the H in-diffusion is evaluated by using heavy water (D₂O) treatments.

Experimental details

The Mo (99.97 % purity) bilayer was DC sputtered on top of soda-lime glass substrates with Ar (99.9995 % purity) as the sputtering gas. No extra sodium was added at this stage, nor any diffusion barrier was employed. CuS, ZnS and SnS precursors (all 99.99 % purity) were co-sputtered using a Lesker CMS-18 sputter system. The precursors were sputtered with a 666 Pa Ar background pressure at a substrate temperature of 250 °C. Sulfurization was performed with 80 mg of sulfur in a pyrolytic carbon coated graphite box in a tube furnace at 500 ± 10 °C for 10, 20 and 40 minutes for two sample sets. The precursor compositions were determined with Rutherford backscattering-calibrated X-ray fluorescence measurements. The sample sets had both a $[\text{Cu}]/[\text{Sn}] = 1.92$, with dissimilar $[\text{Zn}]/([\text{Sn}]+[\text{Cu}])$ of 0.32 (samples (a), (c) and (e)) and 0.35 (samples (b), (d) and (f)), respectively. Isothermal heat treatments were performed on the samples using a hot plate at 50, 100, 150 and 200 °C for 30 minutes each in air ambience. Samples from a third sample set were treated in heavy water (D₂O). All samples were characterized with secondary ion mass spectrometry (SIMS) using a Cameca IMS 7f magnetic sector instrument before and after the treatments. Cs⁺ primary ions were utilized. For estimation of Na and O concentrations from the air annealing series, the cluster ions ²³Na¹³³Cs⁺ and ¹⁶O¹³³Cs⁺ were detected and calibrated against a time-of-flight-energy elastic recoil detection analysis (ToF-ERDA) reference sample using the ⁹⁸Mo¹³³Cs⁺ signal in the Mo layer to produce the relative sensitivity factor. The ToF-ERDA measurement was performed using I⁸⁺ primary ions with an impact energy of 36 MeV. The impinging ions covered an area of a few millimeters, which is substantially larger compared to SIMS such that the estimated concentrations are considered to be indicative. For the samples treated in D₂O, the negative ions ¹H⁻, ²H⁻ (D⁻) and ¹⁸O⁻ were also detected. The matrix signal detected for the negative ions was ¹²⁰Sn⁻, however, variations in the Sn signal for the reference sample was observed leading to uncertainties in the concentration estimation and, thus, only the SIMS intensity is presented. Cs⁺ impact energies were 15 keV and 5 keV for negative and positive secondary ions, respectively. The beam was always rastered over an area of $150 \times 150 \mu\text{m}^2$ collecting secondary ions from a circular region in the middle of the crater with diameter of 33 μm . The primary beam current was 20 nA. The depth of the CZTS layer was estimated by comparing with cross-section SEM images and the CZTS/Mo interface was defined by the inflection point of the Mo signal. For SIMS image depth profiling O₂⁺ primary ions with 10 keV impact energy using a beam current of 100 pA were utilized for increased spatial resolution. One sample from the first sample set was chosen for atom probe tomography (APT) analysis with the goal of studying the Na distribution on a finer scale. APT specimens were prepared using a dual-beam focused ion-beam/scanning electron microscopy

(FIB/SEM) workstation (FEI Versa 3D). A standard lift-out technique was implemented for specimen preparation,²⁹ having the main axis of the needle-shaped specimens oriented perpendicular to the substrate. An approximately 200 nm thick Pt layer was deposited on top, using the electron beam as a protective coating. Furthermore, 2 kV acceleration voltage was used for the final shaping of the specimens to reduce Ga implantation. APT measurements were carried out in a LEAPTM 3000X-HR (ImagoTM) system in laser pulsing mode with a repetition rate of 100 kHz, 0.05 nJ laser power and base temperature of ~50 K. The data were reconstructed and analyzed using CAMECATM IVAS 3.6.14 software. Analyzing sulfide CZTS with APT is accompanied with some limitations in the composition quantifications stemming from peak overlaps in the mass spectrum for sulfur, oxygen, and zinc elements, respectively. The overlaps occur at the peaks at 16 Da for $^{32}\text{S}^{+2}$ and $^{16}\text{O}^{+1}$, at 32 Da for $^{32}\text{S}^{+1}$, $^{16}\text{O}_2^{+1}$, and $^{64}\text{Zn}^{+2}$, as well as at 34 Da for $^{34}\text{S}^{+1}$ and $^{68}\text{Zn}^{+2}$. Correction using natural isotope abundance ratios is rather difficult, especially for the 32 Da peak.³⁰ Hence, the chemical quantification using this technique will only focus here on Na, Cu and Sn.

Results and discussion

Spatial nonuniformity of Na in $\text{Cu}_2\text{ZnSnS}_4$

Spatial variations of sodium are prevalent in the samples of this study, in agreement with previous studies on CZTSSe.^{9,10,31-33} Figure 1 shows the spatial sodium distribution of two CZTS absorbers on the nm and μm scale using APT and SIMS image depth profiling. Two tomographic slices of the three-dimensional reconstruction of the APT-tip (Figure 1a,c), highlight the Na spatial distribution's nonuniformity. A two-dimensional (2D) defect is observed at the upper left part of the reconstruction which exhibits Na agglomeration. Solely from the APT data, the nature of 2D defects cannot be identified, which here could be either a grain boundary or a stacking fault. The APT reconstruction volume exhibits several features which display not only Na segregations, but also Cu inhomogeneities, as shown in Figure 1b. A 2D concentration map for the Cu concentration within a tomographic slice in the point cloud reconstruction highlights the inhomogeneity of Cu. Figure 1d displays a profile across the two-dimensional defect (marked with a rectangle in Figure 1b), which reveals lower concentrations of Cu inside grains. Moreover, at the proximity of the interface, the Cu concentration rises to ~ 6 at. % above the average concentration detected at further distances from the defect correlating with slight increase of Na in this region (~ 0.5 at. %). Such Na increase in Cu-rich regions was also reported by Schwarz et al using APT on selenide CZTSe¹⁰. Other areas in the reconstruction show similar behavior (i.e. bottom left region in Figure 1b) where Cu enrichment relates to slight increase in Na concentration. Furthermore, in the region of the 2D defect shown in Figure 1d, a strong increase in Na concentration is observed, reaching up to ~ 6 at. %. The concentration of the matrix elements, Cu and Sn, decrease in this region, supporting that the 2D defect consists of segregated Na. Here, a secondary phase containing Na could be formed. Indeed, the Cu concentration is lowered in the 2D defect comparable to the increase of Na indicating that Cu has been replaced with Na on the substitutional site. Only slight compositional variations are observed for Sn at or near the 2D lattice defect.

SIMS image depth profile measurements of Na reveal a nonuniform spatial distribution of the SIMS intensity on the μm scale (Figure 1e). The nonuniformity is present both laterally with a $20 \times 20 \mu\text{m}^2$ raster and throughout the depth of the $1 \mu\text{m}$ thick CZTS layer, indicating that the Na rich regions are not limited to regions on a nm scale. In fact, inhomogeneities of Na on a mm scale has also been observed by performing SIMS at several locations (not shown). This has already been identified by Gershon et al. and has been attributed to inhomogeneities in the SLG³³. To limit the effects of these inhomogeneities, SIMS depth profiles are measured as close as possible to each other after heat treatments and heavy water treatments.

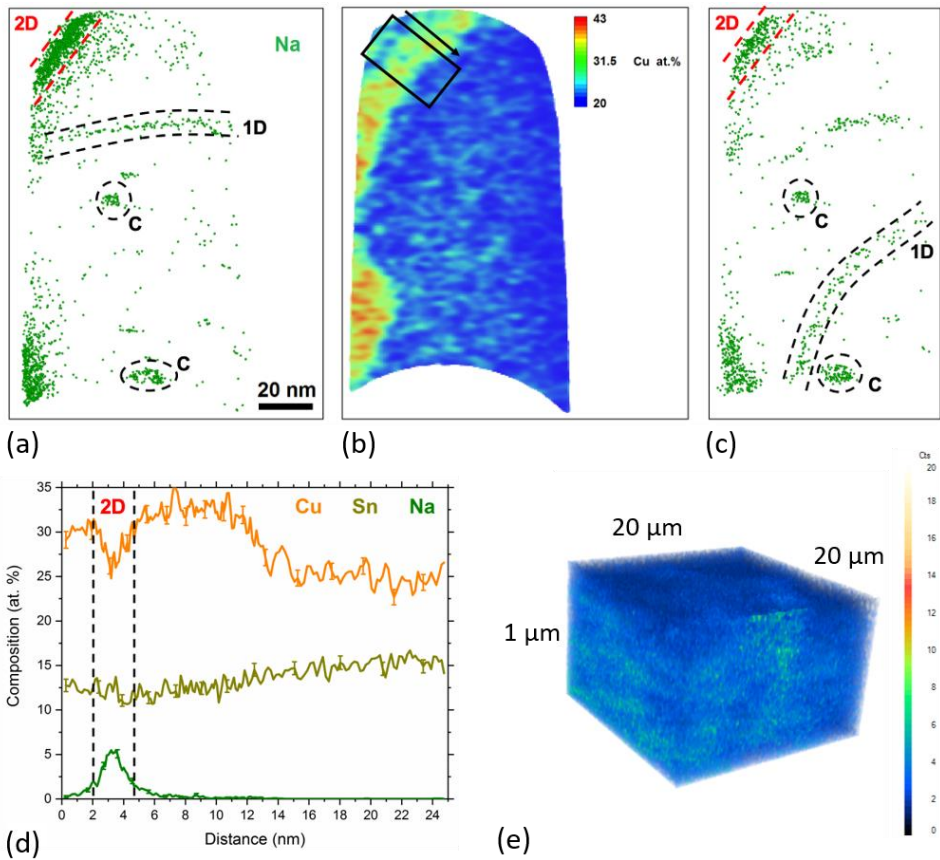


Figure 1: Sodium distribution on (a-d) the nm scale using atom probe tomography and on (e) the μm scale using secondary ion mass spectrometry image depth profile. (a) and (c) display two tomographic slices of 8 nm thickness within the point cloud data representing Na atoms. Clusters are marked by “C”, decorated dislocations are marked by “1D” and the two-dimensional lattice defect is marked by “2D”, respectively. (b) a two-dimensional concentration map for the Cu concentration from within the same slice of (a). (d) one-dimensional concentration profile across the two-dimensional defect, the region is marked by a black rectangle in (b), the arrow marks the direction of the profile measurement.

Redistribution of Na and O

Six samples with different grain sizes were annealed on a hot plate in air at 50, 100, 150 and 200 °C for 30 minutes. For each sample, SIMS depth profiles were measured, and ERDA-calibrated Na and O concentrations were estimated. The results are represented in Figures 2 and 3, where the estimated average grain size for each sample increases from about 100 nm for (a) to about 300 nm for (f). Initially, the depth profiles (blue lines) display an average estimated concentration of Na and O for all samples between 1×10^{19} and 1×10^{20} atoms/cm³, showing no correlation between measured concentration with SIMS and the grain size. However, the Na and O concentrations correlate for all samples over all temperatures. The concentrations are increased at the air/surface and the CZTS/Mo interfaces for all samples, indicating segregation of Na and O at these interfaces. The increased SIMS intensity may also be caused by a change in sputter yield and ionization efficiency at these interfaces, making quantitative assessment challenging.³⁴ To a greater extent than that of O, accumulation of Na is observed in the regions from 600 to 900 nm from the surface, near the back contact. This accumulation of Na after the sulfurization is not commonly observed in conventional CZTS samples. Different from conventional processing, these samples are processed at lower-than-baseline temperatures of about 500 °C and with a longer sulfurization time. The unconventional sulfurization conditions may have caused the abnormal Na accumulation in the region near the back contact for all samples studied. As the samples are air annealed, Na appears to diffuse from this region and redistribute to sites closer to the surface. Indeed, after the 100 and 150 °C anneals, each sample exhibited a substantially more uniform Na distribution with depth. While Na redistributes in the CZTS layer, Na from the SLG is expected to act as a source and diffuse through the Mo at these temperatures,^{17,35} which could explain the increased Na concentration for all depths as observed in (c) and (d). Evidently, the extent of the redistribution of Na after the 50 °C anneal correlates with grain size suggesting that diffusion through grain boundaries are preferred, as expected. However, the Na concentrations for the sample with the smallest grain size (a) do not redistribute further at higher temperatures. In fact, the sample with the smallest grain size has the lowest overall concentration of Na in the CZTS layer after heat treatments of the six samples, suggesting that the Na occupy sites inside the grain interior. The O depth profiles (Figure 3) show that the O concentration is increased for all samples after heat treatments to a larger extent than that of Na. Indeed, the depth profiles and concentration levels are much more similar after air annealing treatments compared to that prior to annealing, suggesting that O diffuses in from both the air and the Mo layer, where it is the rate limiting factor for the formation of Na-O complexes²⁵.

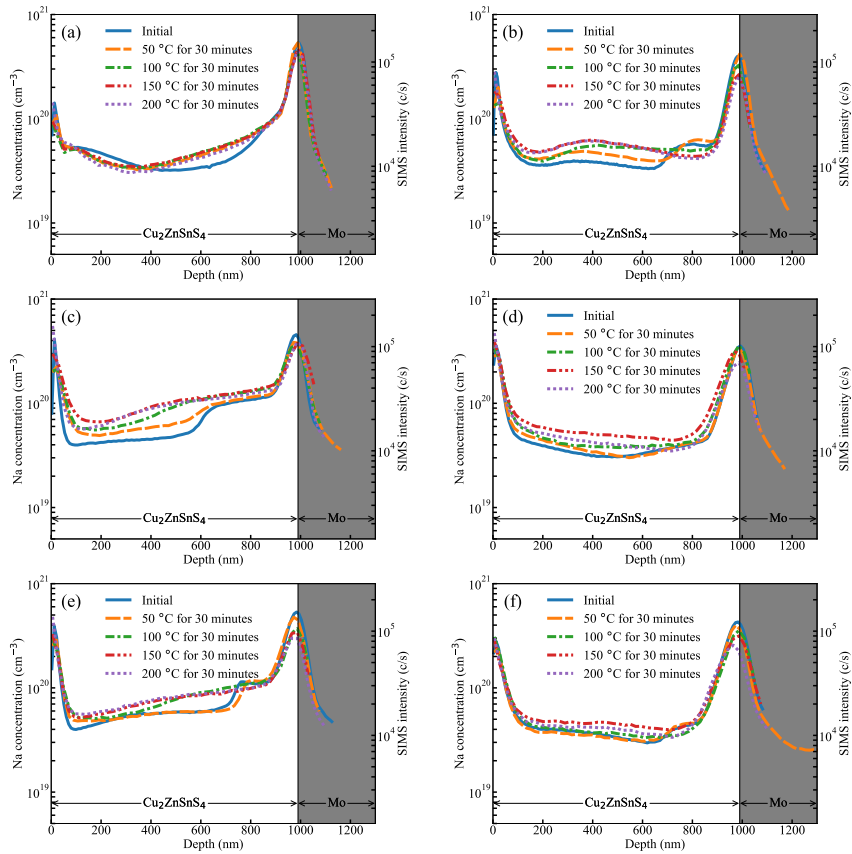


Figure 2: ERDA calibrated SIMS Na depth profiles for six samples (a)-(f) initially and after air annealing treatments at 100, 150 and 200 °C for 30 minutes. The average CZTS grain size increases from about 100 nm to about 300 nm in the samples from (a) to (f).

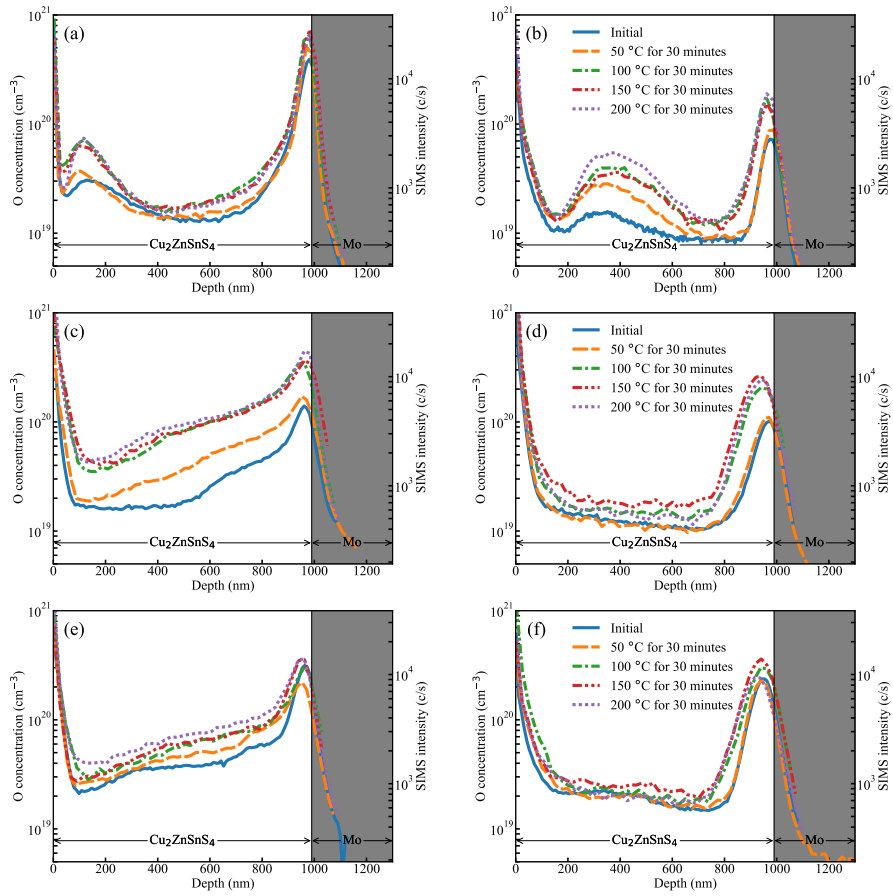


Figure 3: ERDA calibrated SIMS O depth profiles for six samples (a)-(f) initially and after air annealing treatments at 100, 150 and 200 °C for 30 minutes. The average CZTS grain size increases from about 100 nm to about 300 nm in the samples from (a) to (f).

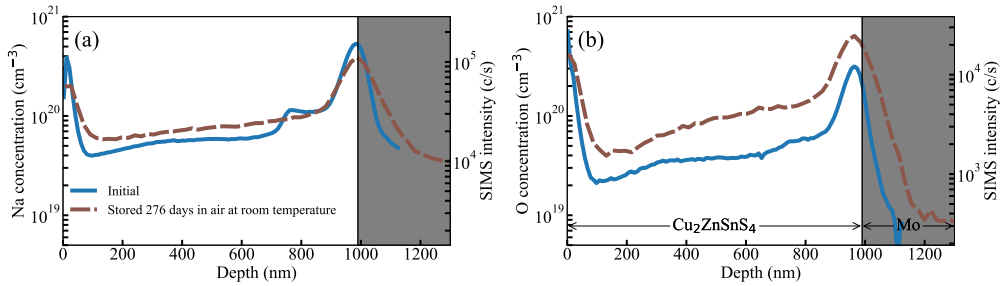


Figure 4: (a) Na and (b) O concentrations measured by SIMS for sample (e) from Figure 2 initially and after the sample was stored at room temperature for 276 days. The Na and O depth profiles after storage (dashed lines) are comparable to what was observed after the 150 °C air annealing treatment (Figure 2e).

From Figure 2, significant Na redistribution and an increase in O concentration are observed after the heat treatments. The rapid diffusion of Na at low temperatures suggests that Na may be mobile at or slightly above room temperature. In this case, long-term storage at room temperature would be sufficient for Na to migrate. Hence, a reference piece from the sample (e) was measured 276 days after the initial SIMS measurement. The measured depth profiles as well as the initial depth profiles are shown in Figure 4. Clearly, Na and O have redistributed over the depth of the CZTS layer after long-term storage confirming the low migration barrier for Na in CZTS. The depth profile is remarkably similar to that of the depth profiles measured after the 150 °C air anneal, proposing that the long-term storage has similar effects on the Na and O distributions as the short anneals at elevated temperatures. The similarity between Na and O depth profiles might be indicative of comparable solar cell properties. Thus, an interesting study would be to explore whether long-term storage in air before the buffer layer deposition produces effects on PCE comparable to shorter low-temperature air anneals.

Impurity migration after heavy water treatment

Water treatments have been shown to remove Na and O on the surface²⁸. Indeed, a reference SIMS measurement of a CZTS absorber treated in regular deionized water (H₂O) indicated out-diffusion of Na from the bulk (not shown). A likely candidate to replace Na is H. Thus to distinguish possible in-diffusion of H from the water with the H in the air and that already present in the CZTS, samples from a third series were treated in heavy water (D₂O) for 40 seconds and SIMS depth profiles of Na, O, H and D were measured before and after the procedure. Figure 5 shows the depth profiles from a representative sample of the four species before (solid lines) and after (dashed lines) the D₂O treatment. The Na intensity has decreased, most noticeably in the region near the surface. The H intensity, meanwhile, has increased after the D₂O treatment with more H introduced in the near-surface region, correlating inversely with Na suggesting a kick-out of Na by H. A significant signal from D is observed after the D₂O treatment, although it is several orders of magnitude lower than the increase in H. Although the intensity of D is low compared to that of H, the diffusion is fast as D is detected throughout the CZTS absorber and into the Mo back contact. Interestingly, the SIMS intensity from D was equal for all samples regardless of grain size, indicating that the sites occupied by D is not limited to grain boundaries. However, the SIMS intensity from D in the Mo back contact correlates with increased grain size, suggesting that the diffusion is mediated by grain boundaries.

Surprisingly, the increase in SIMS intensity for H is greater than for D after the D₂O treatment. The immediate possible source of H is from H₂O in the ambient air. The in-diffusion of H would be expected to occur during the D₂O dip where the out-diffusion of Na most likely occurs. Interestingly, a similar observation has been reported in porous materials, where an “ice-like” layer has been identified with conductivity measurements.³⁶⁻³⁸ The thickness of the layer was governed by the humidity when exposed to air. Thus, one may propose a similar explanation to why limited amounts of D diffuse from the D₂O during the 40 second treatment, i.e. that an “ice-like” layer of H₂O is formed on top of the CZTS. The CZTS sample represented in Figure 5 was exposed to air during transport and storage, supporting that such a layer could form. Accordingly, the H from the “ice-like” layer diffuse in and exchange sites with Na, much like the proposed diffusion of Na from the SLG to the CZTS layer. The “ice-like” layer may also act as a source for O, even though the increase is more significant near the Mo back contact.

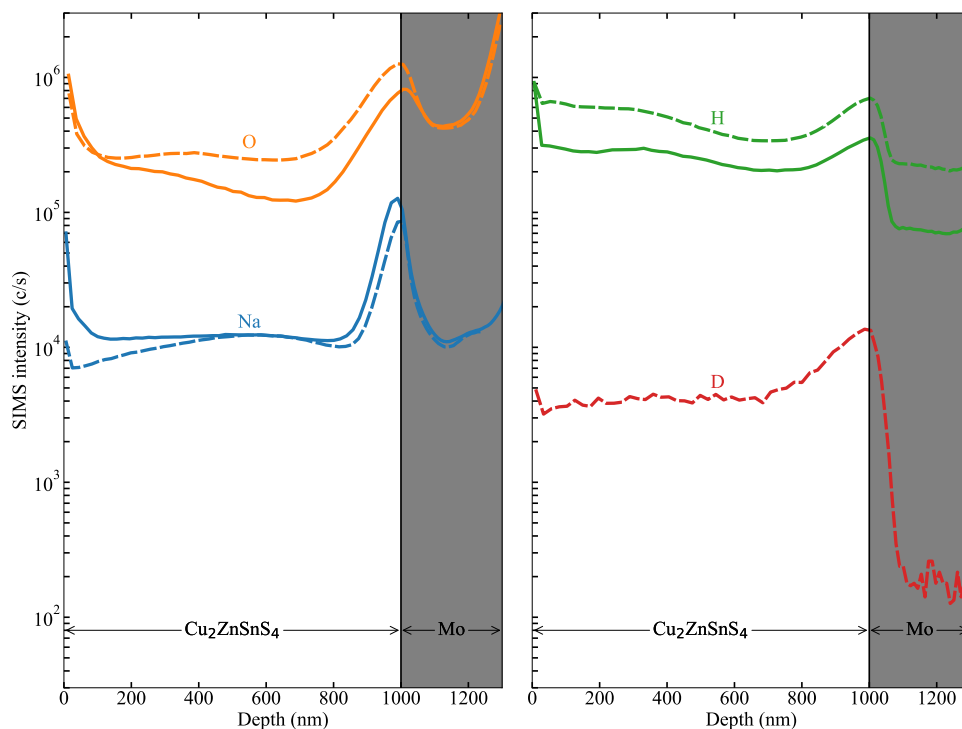


Figure 5: SIMS measurements of Na, O, H and D (deuterium) on a representative CZTS absorber before (solid lines) and after (dashed lines) the sample has been treated in D_2O for 40 seconds. The elements are separated in two plots for easier interpretation. A decrease in the Na intensity and an increase in the O and H intensities are observed. Trace amounts of D have diffused from the D_2O into the CZTS and the Mo layer.

Conclusions

Nonuniform Na distributions on the nanometer and micrometer scale have been identified in our CZTS samples by APT and SIMS image depth profile measurements. The APT measurement reveals that Na is accumulated in defect regions, corresponding to a decrease in Cu concentration. Consequently, Na likely replaces Cu on the substitutional site. Around the defects, however, the Cu concentration rises to ~6 at. % above the average concentration correlating with slight increase of Na. Further, redistribution of Na and O have been observed after air annealing at temperatures up to 200 °C for CZTS samples with varying average grain size. The low migration barriers for Na and O allow for redistribution of these impurities to occur, even at room temperature. Diffusion of impurities in CZTS is likely grain boundary mediated, however, the redistribution appears to occur at sites in the grain interior. Out-diffusion of Na and in-diffusion of H is identified by treatment in D_2O , demonstrating that water treatments do not only remove Na from the surface. It is proposed that the

increase of H in contrast to D could be explained by an existing “ice-like” layer on the CZTS surface preventing abundant amounts of D to diffuse into the sample during the D₂O treatment.

Acknowledgements

This work has been funded by the Research Council of Norway (project 243642) and the Swedish Foundation for Strategic Research. The Research Council of Norway is also acknowledged for the support to the Norwegian Micro and Nano-Fabrication Facility, NorFab, project number 245963/F50.

References

- ¹ R. Scheer and H.W. Schock, *Chalcogenide Photovoltaics: Physics, Technologies, and Thin Film Devices* (Wiley-VCH, Weinheim, Germany, 2011).
- ² S.M. Sze and M.K. Lee, *Semiconductor Devices, Physics and Technology*, 3rd ed (Wiley, Hoboken, N.J, 2012).
- ³ S. Chen, A. Walsh, X.-G. Gong, and S.-H. Wei, *Adv. Mater.* **25**, 1522 (2013).
- ⁴ P.M.P. Salomé, H. Rodriguez-Alvarez, and S. Sadewasser, *Sol. Energy Mater. Sol. Cells* **143**, 9 (2015).
- ⁵ C.M. Sutter-Fella, J.A. Stückelberger, H. Hagedorfer, F. La Mattina, L. Kranz, S. Nishiwaki, A.R. Uhl, Y.E. Romanyuk, and A.N. Tiwari, *Chem. Mater.* **26**, 1420 (2014).
- ⁶ T. Prabhakar and N. Jampana, *Sol. Energy Mater. Sol. Cells* **95**, 1001 (2011).
- ⁷ K. Sun, F. Liu, C. Yan, F. Zhou, J. Huang, Y. Shen, R. Liu, and X. Hao, *Sol. Energy Mater. Sol. Cells* **157**, 565 (2016).
- ⁸ S. Tajima, R. Asahi, D. Isheim, D.N. Seidman, T. Itoh, and K. Ohishi, *Jpn. J. Appl. Phys.* **54**, 112302 (2015).
- ⁹ C. Yan, J. Huang, K. Sun, S. Johnston, Y. Zhang, H. Sun, A. Pu, M. He, F. Liu, K. Eder, L. Yang, J.M. Cairney, N.J. Ekins-Daukes, Z. Hameiri, J.A. Stride, S. Chen, M.A. Green, and X. Hao, *Nat. Energy* **3**, 764 (2018).
- ¹⁰ T. Schwarz, A. Redinger, S. Siebentritt, Z. Peng, B. Gault, D. Raabe, and P.-P. Choi, *Phys. Rev. Mater.* **3**, (2019).
- ¹¹ S.G. Haass, M. Diethelm, M. Werner, B. Bissig, Y.E. Romanyuk, and A.N. Tiwari, *Adv. Energy Mater.* **5**, 1500712 (2015).
- ¹² S. Grini, K.V. Sopiha, N. Ross, X. Liu, T.S. Bjørheim, C. Platzer-Björkman, C. Persson, and L. Vines, *Adv. Energy Mater.* 1900740 (2019).
- ¹³ R. Haight, X. Shao, W. Wang, and D.B. Mitzi, *Appl. Phys. Lett.* **104**, 033902 (2014).
- ¹⁴ K. Sardashti, R. Haight, T. Gokmen, W. Wang, L.-Y. Chang, D.B. Mitzi, and A.C. Kummel, *Adv. Energy Mater.* **5**, 1402180 (2015).
- ¹⁵ K. Sardashti, D. Paul, C. Hitzman, J. Hammond, R. Haight, and A.C. Kummel, *J. Mater. Res.* **31**, 3473 (2016).
- ¹⁶ J. Park, J. Huang, J. Yun, F. Liu, Z. Ouyang, H. Sun, C. Yan, K. Sun, K. Kim, J. Seidel, S. Chen, M.A. Green, and X. Hao, *Adv. Energy Mater.* **8**, 1701940 (2018).
- ¹⁷ H. Xie, S. López-Marino, T. Olar, Y. Sánchez, M. Neuschitzer, F. Oliva, S. Giraldo, V. Izquierdo-Roca, I. Lauer mann, A. Pérez-Rodríguez, and E. Saucedo, *ACS Appl. Mater. Interfaces* **8**, 5017 (2016).
- ¹⁸ D. Hironiwa, N. Sakai, T. Kato, H. Sugimoto, Z. Tang, J. Chantana, and T. Minemoto, *Thin Solid Films* **582**, 151 (2015).

- ¹⁹ J.K. Larsen, Y. Ren, N. Ross, E. Särhammar, S.-Y. Li, and C. Platzer-Björkman, *Thin Solid Films* **633**, 118 (2017).
- ²⁰ M. Neuschitzer, Y. Sanchez, T. Olar, T. Thersleff, S. Lopez-Marino, F. Oliva, M. Espindola-Rodriguez, H. Xie, M. Placidi, V. Izquierdo-Roca, I. Lauermann, K. Leifer, A. Pérez-Rodriguez, and E. Saucedo, *Chem. Mater.* **27**, 5279 (2015).
- ²¹ A. Laemmle, R. Wuerz, T. Schwarz, O. Cojocar-Mirédin, P.-P. Choi, and M. Powalla, *J. Appl. Phys.* **115**, 154501 (2014).
- ²² R.V. Forest, B.E. McCandless, X. He, A.A. Rockett, E. Eser, K.D. Dobson, and R.W. Birkmire, *J. Appl. Phys.* **121**, 245102 (2017).
- ²³ R.V. Forest, E. Eser, B.E. McCandless, J.G. Chen, and R.W. Birkmire, *J. Appl. Phys.* **117**, 115102 (2015).
- ²⁴ A. Rockett, J.S. Britt, T. Gillespie, C. Marshall, M.M.A. Jassim, F. Hasoon, R. Matson, and B. Basol, *6* (2000).
- ²⁵ S. Grini, K.V. Sopiha, N. Ross, X. Liu, T.S. Bjørheim, C. Platzer-Björkman, C. Persson, and L. Vines, *Adv Energy Mater* **9** (2019).
- ²⁶ M. Bär, B.-A. Schubert, B. Marsen, R.G. Wilks, S. Pookpanratana, M. Blum, S. Krause, T. Unold, W. Yang, L. Weinhardt, C. Heske, and H.-W. Schock, *Appl. Phys. Lett.* **99**, 222105 (2011).
- ²⁷ G. Brammertz, M. Buffière, S. Oueslati, H. ElAnzeery, K. Ben Messaoud, S. Sahayaraj, C. Köble, M. Meuris, and J. Poortmans, *Appl. Phys. Lett.* **103**, 163904 (2013).
- ²⁸ Y. Ren, J.J.S. Scragg, M. Edoff, J.K. Larsen, and C. Platzer-Björkman, *ACS Appl. Mater. Interfaces* **8**, 18600 (2016).
- ²⁹ K. Thompson, D. Lawrence, D.J. Larson, J.D. Olson, T.F. Kelly, and B. Gorman, *Ultramicroscopy* **107**, 131 (2007).
- ³⁰ B. Gault, editor, *Atom Probe Microscopy* (Springer, New York, 2012).
- ³¹ T. Schwarz, O. Cojocar-Mirédin, P. Choi, M. Mousel, A. Redinger, S. Siebentritt, and D. Raabe, *Appl. Phys. Lett.* **102**, 042101 (2013).
- ³² T. Schwarz, O. Cojocar-Mirédin, P. Choi, M. Mousel, A. Redinger, S. Siebentritt, and D. Raabe, *J. Appl. Phys.* **118**, 095302 (2015).
- ³³ T. Gershon, C. Hamann, M. Hopstaken, Y.S. Lee, B. Shin, and R. Haight, *Adv. Energy Mater.* **5**, 1500922 (2015).
- ³⁴ F.A. Stevie, C.W. Magee, and R.G. Wilson, *Secondary Ion Mass Spectrometry: A Practical Handbook for Depth Profiling and Bulk Impurity Analysis* (Wiley, New York u.a, 1989).
- ³⁵ R.V. Forest, E. Eser, B.E. McCandless, R.W. Birkmire, and J.G. Chen, *AIChE J.* **60**, 2365 (2014).
- ³⁶ B. Scherrer, M.V.F. Schlupp, D. Stender, J. Martynczuk, J.G. Grolig, H. Ma, P. Kocher, T. Lippert, M. Prestat, and L.J. Gauckler, *Adv. Funct. Mater.* **23**, 1957 (2013).
- ³⁷ S.Ø. Stub, E. Vøllestad, and T. Norby, *J. Mater. Chem. A* **6**, 8265 (2018).
- ³⁸ S.Ø. Stub, K. Thorshaug, P.M. Rørvik, T. Norby, and E. Vøllestad, *Phys. Chem. Chem. Phys.* **20**, 15653 (2018).

Paper VII

TiN Interlayers with Varied Thickness in $\text{Cu}_2\text{ZnSnS(e)}_4$ Thin Film Solar Cells: Effect on Na Diffusion, Back Contact Stability, and Performance

Sven Englund, Sigbjørn Grini, Olivier Donzel-Gargand, Valentina Paneta, Volodymyr Kosyak, Daniel Primetzhofer, Jonathan J. S. Scragg, Charlotte Platzer-Björkman

Phys. Status Solidi A 215, 1800491 (2018).

TiN Interlayers with Varied Thickness in $\text{Cu}_2\text{ZnSnS}(\text{e})_4$ Thin Film Solar Cells: Effect on Na Diffusion, Back Contact Stability, and Performance

Sven Englund,* Sigbjørn Grini, Olivier Donzel-Gargand, Valentina Paneta, Volodymyr Kosyak, Daniel Primetzhofer, Jonathan J. S. Scragg, and Charlotte Platzer-Björkman

In this study, interlayers with varied thickness of TiN between $\text{Cu}_2\text{ZnSnS}(\text{e})_4$ (CZTS(e)) absorbers and Mo on soda-lime glass substrates are investigated for CZTS(e) thin film solar cells. Na diffusion is analyzed using Secondary Ion Mass Spectrometry and it is found that the use of thick TiN interlayers facilitates Na diffusion into the absorbers. The CZTS(e)/TiN/Mo interfaces are scrutinized using Transmission Electron Microscopy (TEM) Electron Energy Loss Spectroscopy (EELS). It is found that diffusion of chalcogens present in the precursor occurs through openings, resulting from surface roughness in the Mo, in the otherwise chemically stable TiN interlayers, forming point contacts of $\text{MoS}(\text{e})_2$. It is further established that both chalcogens and Mo diffuse along the TiN interlayer grain boundaries. Solar cell performance for sulfur-annealed samples improved with increased thickness of TiN, and with a 200 nm TiN interlayer, the solar cell performance is comparable to a typical Mo reference. Pure TiN bulk contacts are investigated and shown to work, but the performance is still inferior to the TiN interlayer back contacts. The use of thick TiN interlayers offers a pathway to achieve high efficiency CZTS(e) solar cells on highly inert back contacts.

increase from today's levels.^[1,2] The resulting demands on resources have triggered the interest in research on solar cells made by earth abundant materials. For this reason, $\text{Cu}_2\text{ZnSn}(\text{S}_x\text{Se}_{1-x})_4$ CZTS(e) has gained much attention during the last decade, reaching a record efficiency of 12.6% in 2012.^[3] Three main challenges that need to be addressed to reach higher efficiencies are understanding and improvement of i) the back contact (BC)/CZTS(e) interface; ii) the CZTS(e) bulk quality; and iii) the CZTS(buffer layer interface).^[4–7] The interface between the BC/CZTS(e) has gained much attention and the standard material Mo as BC has been questioned due to the formation of $\text{MoS}(\text{e})_2$ which limits the process control and the processing window and consequently also hinders optimization of the anneal process. It has been suggested that the introduction of interlayers, to work as, e.g., chemical- and/or electrical passivation

1. Introduction


Electricity generated by photovoltaics is anticipated to become a substantial source of electricity by 2050 with a nearly 9-folded

layer between the Mo BC and the absorber layer, could be a route to overcome these issues. Many materials have been investigated to date, e.g., ZnO ,^[8] Ag ,^[9–11] TiB_2 ,^[12] Au , W , Pd , Pt , Ni ,^[13] TiW , Cr , Ti , Al ,^[14] C ,^[15] Bi ,^[16] Al_2O_3 ,^[17,18] MoO_x ,^[19,20] TiN ,^[21] SnS ,^[22] a-SiC ,^[23] MoN ,^[24] and S_xNi_y .^[25] The BC must supply sufficient adhesion to the absorber to avoid delamination, especially during critical processing steps as annealing and etching, it is therefore beneficial if it is chemically inert. It must make a good electrical contact to the absorber layer and enable current/hole extraction. Na is nowadays considered as a vital constituent in CZTS(e) and affects the absorber quality as well as the interface properties.^[26] How the BC affects the Na diffusion from the SLG is often overlooked in studies on alternative BC configurations. Na diffusion from the SLG may be an important contribution for observed improved solar cell performances. Recently, Englund et al.^[27] investigated how the thickness of TiN, deposited on bilayer Mo, affected Na transport after annealing in either S, or Se atmosphere. A key finding was that increased thickness of TiN interlayer also increased the amount of Na that diffused to the surface of the BC. The result is expected to have impact on the solar cell performance, and in this paper, the results of a

S. Englund, O. Donzel-Gargand, Dr. V. Kosyak, Dr. J. J. S. Scragg, Prof. C. Platzer-Björkman
Division of Solid State Electronics
Department of Engineering Sciences, Uppsala University
Ångströmlaboratoriet, Ångströmvägen 1, 752 37 Uppsala, Sweden
E-mail: sven.englund@angstrom.uu.se

S. Grini
Department of Physics
Centre for Material Science and Nanotechnology
University of Oslo, Kristen Nygaards hus, Gaustdalleen 23 A, 0316 Oslo, Norway

Dr. V. Paneta, Dr. D. Primetzhofer
Department of Physics and Astronomy
Applied Nuclear Physics, Uppsala University
Ångströmlaboratoriet, Ångströmvägen 1, 752 37 Uppsala, Sweden

 The ORCID identification number(s) for the author(s) of this article can be found under <https://doi.org/10.1002/pssa.201800491>.

DOI: 10.1002/pssa.201800491

study on CZTS(e) solar cells with the identical TiN interlayer stacks as in England et al.^[27] are presented.

2. Experimental Section

Mo was deposited on soda-lime glass (SLG) substrate by DC magnetron sputtering in an in-line sputtering system from Material Research Corporation using Ar (purity 99.9995%) as sputtering gas and a planar Mo target (99.97%) with dimensions $120 \times 378 \text{ mm}^2$. The Mo films have a bilayer stack. It was made by first sputtering a highly adhesive layer at 2 Pa and 2000 W (4.4 W cm^{-2}) and then a highly conductive layer at 0.8 Pa and 2000 W. The total bilayer Mo thickness was approximately 350 nm.

TiN interlayers were reactively sputtered in a von Ardenne CS 730 S sputter system using DC magnetron sputtering from a 152 mm circular Ti target (99.995%) in Ar (99.9995%) and N_2 (99.9999%) atmosphere. The background pressure was 10^{-9} Pa and total pressure during sputtering was 0.8 Pa with Ar flow set to 20 sccm and N_2 to 45 sccm ($\text{N}_2/\text{Ar} = 2.25$), power of 1000 W (4.3 W cm^{-2}) and current of 2.2 A. The deposition rate was 1.64 nm s^{-1} . TiN interlayers with thicknesses of 20, 50, and 200 nm were prepared. The thicknesses were validated with profilometer (Veeco Instruments, Dektak 150). Similar procedures were later used for the 350 nm TiN bulk back contacts, but with varied N_2/Ar flow ratios, namely 8/40 sccm, 13/40 sccm, and 45/20 sccm. Sheet resistance was measured by using a 4-point probe (AIT model CMT-SR200N). Residual stress was calculated using Stoney's formula (see Thornton and Hoffman^[28] and Ericson^[29]) and measurement of curvature in profilometer (Dektak 150) of films deposited on thin microscope slides that were sputtered with the samples used for the experiments.

Two sets of CZTS (pure S) precursors were co-sputtered in a Kurt J. Lesker CMS-18 sputter system with binary compound targets. The background pressure was 10^{-5} Pa. The holder was heated to 250 °C and the Ar sputter pressure was kept to 666 Pa. For the first set, that later was annealed in sulfur, the CuS/SnS targets were sputtered with DC power of 77/22 W and ZnS with RF sputtering with a power of 135 W. In the second set, that later was selenized, the CuS/SnS-targets were set to 78/23 W and the ZnS to 144. The thicknesses were in all cases close to 1 μm . Precursor compositions were determined from Rutherford backscattering-calibrated X-ray fluorescence measurements and presented in Table 1.

The CZTS/TiN/Mo/SLG samples were then annealed in a pyrolytic carbon (PyC) coated graphite box with a volume of 15 cm^3 inserted into a preheated tube furnace with a central hot zone and an outer water-cooled zone/loading area. Fast heating and cooling were achieved by transferring the sample box from the cold zone into the hot furnace using a rod. Two separate annealing experiments were performed, one in S atmosphere and one in Se atmosphere, with four samples with the size of $25 \times 25 \text{ mm}^2$ in each anneal. The thickness of the TiN layer (0, 20, 50, and 200 nm) on top of the Mo is the only variable within each annealing batch. The sample temperature was monitored by a thermocouple placed on the back side of the sample plate. For annealing in sulfur excess environment, the sample

Table 1. Sample stack components, their thicknesses, and precursor compositions.

Sample id	Mo [nm]	TiN [nm]	CZTS [μm]	Cu/Sn	Zn/(Cu + Sn)	Anneal
Mo_S	350	0	1	1.91	0.30	S
20S	350	20	1	1.91	0.30	S
50S	350	50	1	1.91	0.30	S
200S	350	200	1	1.91	0.30	S
Mo_Se	350	0	1	1.86	0.33	Se
20Se	350	20	1	1.86	0.33	Se
50Se	350	50	1	1.86	0.33	Se
200Se	350	200	1	1.86	0.33	Se

temperature was 550–580 °C, the background Ar pressure was set to 47 kPa and the annealing time was 13 min, with 80 mg of solid S placed in the PyC coated graphite box as sulfur source. For the anneal in selenium excess environment, the sample temperature was 550–556 °C at 35 kPa and the annealing time was 4 min, with 85 mg of solid Se placed in the box. Different boxes were used for the different anneals to minimize cross-contamination and the furnace was baked between the anneals. No air annealing was used. The samples were cut in two parts to use one part for material investigation and one part for device processing and current–voltage (JV) and quantum efficiency (QE) analysis. Device processing included etching in KCN, chemical bath deposition (CBD) of a 60 nm CdS, sputtering a window layer of 80 nm intrinsic ZnO and 210 nm Al-doped ZnO. The devices were finished by evaporation of Ni/Al/Ni front contact grids, mechanical scribing to define 0.5 cm^2 .

The morphology of the samples was analyzed by scanning electron microscopy (SEM) in a Zeiss Merlin system with a high resolution Schottky FEG and an inlens detector. Acceleration voltage was 3 keV to minimize the interaction volume for both cross-sectional and top-view analysis.

Transmission Electron Microscopy (TEM) lamellae were prepared using a Focused Ion Beam (FIB) (FEI Strata DB235 FIB-SEM), following the in situ lift-out method.^[30] The Scanning Transmission Electron Microscopy (STEM) and the Electron Energy Loss Spectroscopy (EELS) analyses were realized in a FEI Tecnai F30 ST at 300 keV equipped with a Tridiem filter. A probe corrected FEI Titan Themis 200 equipped with SuperEDS detection system was used for STEM-Energy-Dispersive X-ray Spectroscopy (EDS) analysis.

Elemental depth profiles were acquired by Secondary Ion Mass Spectrometry (SIMS) using a Cameca IMS 7f instrument with a primary beam of 10 keV O^{2+} ions and positive ions were detected. O^{2+} primary ions were used for increased detection limit of $^{23}\text{Na}^+$ ions. A control measurement was also performed with Cs^+ primary ions where MCs^+ cluster ions were detected with “M” being the element of interest. The beam was scanned across a raster of $150 \times 150 \mu\text{m}^2$, where a central region with a diameter of 33 μm was used for analysis. The profiles are presented normalized to the intensities of ^{63}Cu .

Time-of-Flight Medium Energy Ion Scattering (ToF-MEIS), the system is described in detail by Linnarsson et al.^[31] was

performed with in-situ annealing in ultra-high vacuum (UHV) chamber at a pressure of 10^{-4} Pa (base pressure 10^{-6} Pa). He^+ ions were accelerated to 80 keV with a 350 kV Danfysik implanter and scattered ions were detected by a large solid angle Microchannel Plate (MCP) detector at 155° in respect to the beam direction. The temperature was controlled and increased to around 595°C using a Panmure Instruments Electron Bombardment Heater.

The surfaces of the annealed TiN back contacts were analyzed by X-ray Photoelectron Spectroscopy (XPS), with an information depth of few nanometer. The system was a Quantera II Scanning XPS microprobe from Physical Electronics. Monochromatic Al K_α radiation (1486.7 eV) was used, and the measured spot size on the sample was $100\ \mu\text{m}$ in diameter. Time between annealing and XPS analysis were kept below 2 h, and time outside N_2 storage was below 15 min to minimize oxidation. No etching was used.

Current–voltage measurements (JV) were performed in a one-sun solar simulator (Newport, ABA) with a halogen lamp. Quantum efficiency (QE) measurements were performed without light-bias in a home-made setup calibrated by externally measured Hamamatsu Si and InGaAs solar cells.

3. Results and Discussion

Samples are summarized in Table 1. The precursor composition for the S-annealed set differs somewhat from the commonly used Cu poor/Zn rich to a more Zn poor composition. The experiment was repeated with Zn rich composition, and the very same trends but a slightly lower solar cell performance was achieved, therefore only the results for the Zn poor samples are presented here.

In previous experiments on annealed back contacts by Englund et al.,^[27] one key finding was the increase of Na diffusion with increased TiN interlayer thickness. In the present study, SIMS depth profiling was therefore performed to investigate and compare the amount of Na in the absorber layers after annealing. No reference calibration samples were used, so no absolute values could be obtained, but the profiles can be compared since the matrices of CZTS(e) are expected to be identical for the respective S-annealed and Se-annealed samples. The results can be seen in Figure 1a and b, S-annealed and Se-annealed, respectively. In the subfigures the same trends are observed as in the previous experiments, i.e., increase of Na-diffusion for the thickest TiN interlayer. For the S-annealed samples, the profiles show a 30% increase in the Na signal for the 200S sample, but this is still within the error of the method, so this result is not significant. For the Se-annealed samples however, the increase of Na in the 200Se sample compared to the other Se-annealed samples is $\approx 100\%$ and by far exceeding the margin of error. This correlates with the findings in Englund et al.^[27] and further indicate that TiN interlayers tend to increase the Na in the absorber layer after anneal, at least when 200 nm TiN is used. The phenomenon has recently also been seen for some other interlayers, e.g., MoO_3 by Park et al.^[32] and Al_2O_3 by Liu et al.,^[33] contrary to the notion that interlayers may inhibit Na.

It can be noticed that the apparent thickness of the annealed absorber layers is much smaller for Se-annealed samples: Ti (TiN) profiles start to appear after around 130–160 s in this case,

while for S-annealed samples they start to appear around 220–250 s. The less steep slopes of the Ti signal show that the roughness is much higher for the Se-annealed samples and limits the depth resolution. This can be further understood in the following section and by examination of the morphology in SEM.

SEM analysis was performed to investigate how the presence and thickness of the TiN interlayer, and the increase of Na as indicated by SIMS affect the film morphology. The SEM cross-sections are shown in Figure 2 and the SEM top-view images are shown in Figure 3. The images show that the Se-anneal, even for a lower temperature and shorter anneal time (565°C for 4 min for Se, 585°C for 13 min for S) is more “aggressive” than the S-anneal, possibly due to the S-Se anion replacement. High surface roughness and deep valleys between the grains explain why the Se-annealed samples appear thinner than the S-annealed in the SIMS. These deep valleys, which also are apparent in Figure 3 for the Se-annealed samples, increase the risk of shunting paths, which also was reflected in the JV measurement. To reduce the risk of creating shunting paths one could reduce the annealing time or temperature for the Se-annealed samples. However, the anneal conditions were chosen to be comparable to the conditions used in Englund et al.^[27] On macroscopic scale, the S-annealed samples are shiny, while the roughness of the Se-samples results in a non-reflective surface. For the S-annealed samples, the SEM analysis indicates improved crystallization and larger grains for samples with TiN than without, but no significant difference with increased TiN thickness. Rather, the top view SEM observations indicates that the 20S (and 50S) samples had the largest average grain sizes. The longer anneal time for the S-annealed samples, compared to the Se-annealed samples, might even out differences in grain size, and to draw any clear conclusions it would have been necessary to study the development of the grains on a finer time scale. For the Se-annealed samples in Figure 2d–f and especially in Figure 3d–f it can be discerned that the Mo reference has the largest grains. Then, with increasing TiN thickness the “valley area” increase at the expense of large crystals. From the SIMS and the cross-sections it can be understood that the morphology must have evolved due to enhanced crystallization and not inhibited crystallization. This could be understood as a result of the higher supply of Na, known for its effect on crystallization of the CZTS(e) grains (see e.g., Yang et al.^[34] and Li et al.^[35]).

To investigate the stability of the TiN interlayer and the BC/absorber interface regarding diffusion of chalcogenides, STEM-EELS analysis were performed; images of Mo₂S, 20S, and 200S are shown in Figure 4. Bright regions indicate signal of the element studied. Similar results as reported in the annealing of back contact stacks in Englund et al.^[27] could be observed also when absorber layers are used. The TiN interlayers are greatly reducing the formation of MoS(e), but for thin interlayers (20 nm), reaction still occurs through the interlayer around discontinuities or openings, as seen in the S-map of 20S in Figure 4. The openings occur as a result of the surface roughness of the Mo, which in itself is a result of the columnar growth of the Mo grains and the valleys created in between them. In fact, the TiN interlayer itself is an effective barrier, hence why a continuous MoS₂ layer is not seen, but since the TiN is not fully covering the Mo, reactions still occur. The very same results

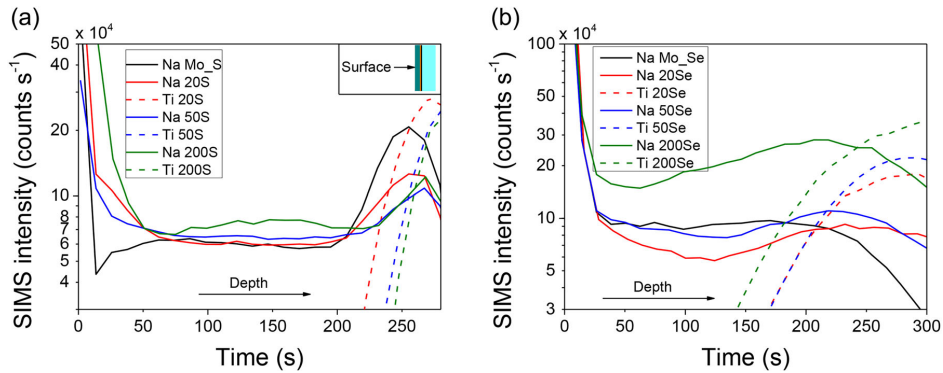


Figure 1. SIMS profiles of Na (solid lines) and Ti (dashed lines). The steep increase of Ti signal indicates the interface between CZTS(e) and TiN. S-annealed samples are shown in (a) and Se-annealed samples are shown in (b). In both cases the thickest (200 nm) TiN show higher intensity of Na in the absorber, but it is significant only for the Se-annealed samples due to the error margins in the measurement.

were found for the selenized 20Se (and therefore not shown here), S (not Se) reacts with Mo in the discontinuities, i.e., it is solely the chalcogen present in the precursor that reacts with the Mo independent on chalcogen used in the annealing atmosphere. This could be understood from the discussion in Shin et al.^[36] and Scragg et al.^[37], namely that CZTS/Mo start to react as soon as the annealing starts, while it will always take some time for the externally added chalcogen to diffuse through the absorber and reach the back contact. At the time when the diffused chalcogen reaches the back contact, the discontinuities are already “plugged” by MoS₂ and further reaction will occur at a much slower rate. In the Mo₂Se sample without TiN on the other hand, Se had diffused through the absorber layer and also reacted with the Mo, forming MoS(e)₂. After the annealing of the BC in Englund et al.^[28] Mo was found in substantial amount also above the TiN interlayer. This is not the case here, likely because of the reduced supply and partial pressure of chalcogen

at the CZTS(e)/TiN interface compared to direct annealing of the BC. The behavior for the thinner TiN interlayer here resembles recent reports when other interlayers has been used, e.g., Al₂O₃ by Liu et al.^[33] where “self-organized nano-patterns” were reported as the Al₂O₃, just as the TiN in the present study, reduced the formation of MoS(e)₂ while point contacts of MoS(e)₂ formed at the CZTS/Mo interface. However, while the thickness of Al₂O₃ in their study had to be limited to 5 nm due to delamination, no tendency of delamination could be seen even when using 200 nm TiN. On the contrary, the adhesion improved significantly with thicker TiN (noticed by the increased force needed to scribe the CZTS). When the thickness of TiN is increased, the amount of S below the TiN layer is reduced. However, in this case, S can be seen in the grain boundaries of the TiN all the way down in the Mo. To rule out the possibility that this was a result of the FIB lamellae preparation, additional careful SIMS analysis confirmed the presence of S in the TiN

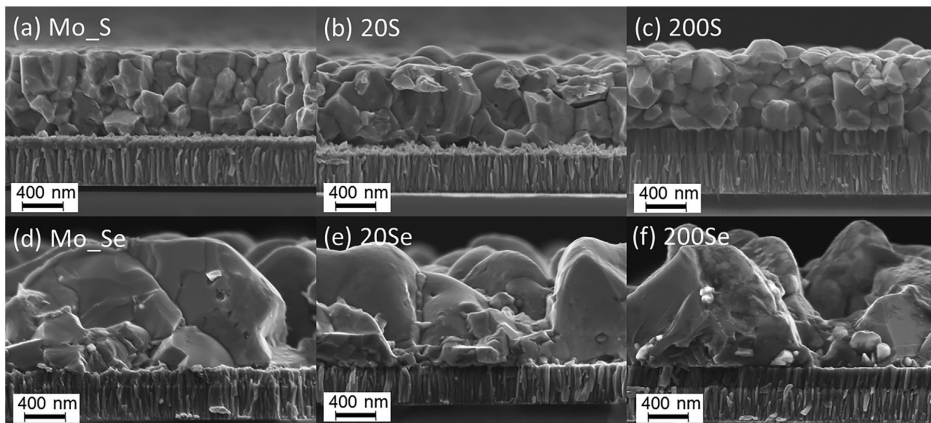


Figure 2. SEM images of cross-section of annealed absorbers. a) Mo₂S; b) 20S; and c) 200S. d) Mo₂Se; e) 20Se; and f) 200Se.

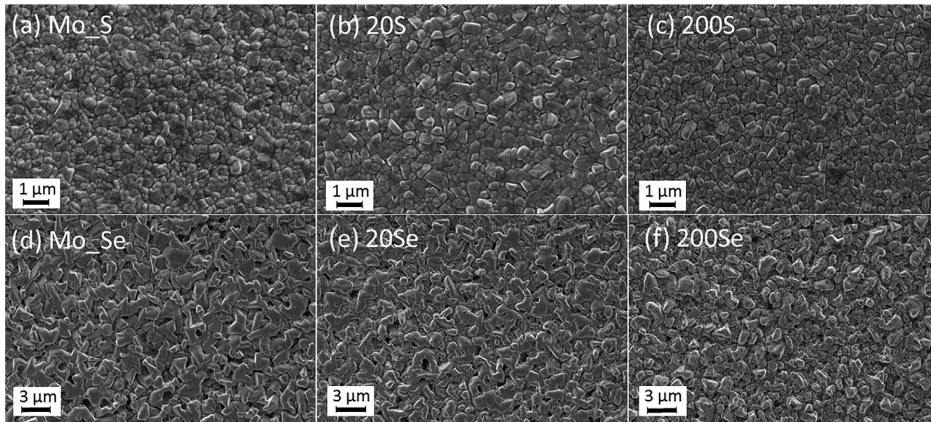


Figure 3. SEM top view images of surfaces of annealed absorbers. a) Mo₂S₃; b) 20S; c) 200S; d) Mo₂Se₃; e) 20Se; and f) 200Se.

layer. However, it can be seen that diffusion of Mo takes place, pointed out by the blue arrows in the Mo map of 200S in Figure 4. Also in this case, the diffusion follows the grain boundaries in the TiN layer. A spike of Ti was observed, marked by the red ring, which overlaps with the O rich area, and it is assumed that this can occur due to the low formation energy of TiO_x, as discussed in Englund et al.^[27] This reaction, however, seems to be very limited and probably affect neither the chemical nor the electrical properties of the layer on a larger scale. Altogether this shows the chemical stability of TiN that does not degrade under the tough chemical environment during the high temperature annealing in the presence of CZTS(e).

To investigate the coverage of TiN on SLG/Mo as a function of temperature, ToF-MEIS with in situ annealing were performed with focus on the observed Mo signal. The hypothesis to be

tested was that the TiN interlayer gets stretched out during the anneal due to thermal expansion of the substrate, and enhances reaction through the openings in the TiN interlayer. As a result, the coverage would temporarily decrease during annealing, giving rise to the Mo-signal. An untreated SLG/Mo + 20 nm TiN sample was heated up in the MEIS chamber and MEIS spectra were recorded at different temperatures sequentially. An initial experiment was done with temperature increase up to 700 °C (whereupon the glass deformed/melted) and the results are presented in Paneta et al.^[38] For the present study, however, the aim was to get a better understanding of the behavior of the TiN layer and its coverage during and after annealing at a typical anneal temperature. Time-to-energy converted ToF-MEIS spectra for 80 keV He⁺ particles were obtained at the temperatures and in the sequence shown in Figure 5a. The Mo signal (at

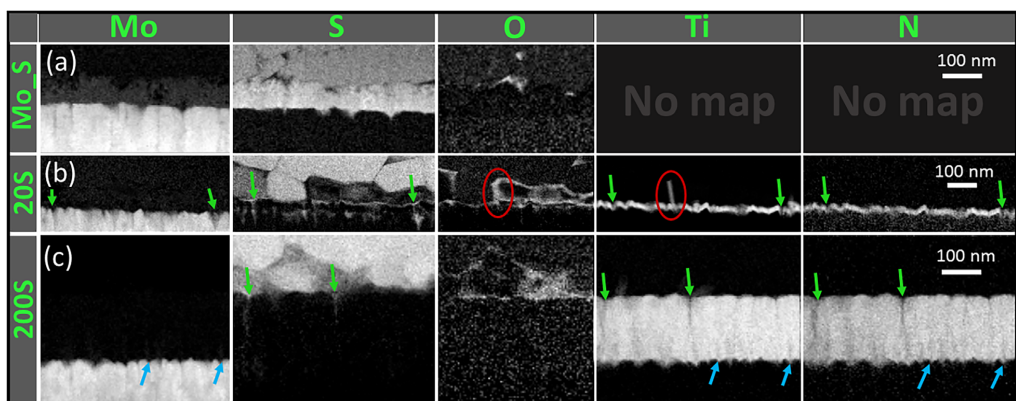


Figure 4. TEM-EELS chemical composition maps (Mo, S, O, Ti, and N) of three different sulfurized samples: a) Mo₂S₃; b) 20S; and c) 200S. The green arrows highlight valleys/openings in the TiN interlayer where chalcogen- and Mo diffusion occurs. The blue arrows highlight valleys/openings where diffusion of Mo was observed. The red circles highlight the presence of TiO_x.

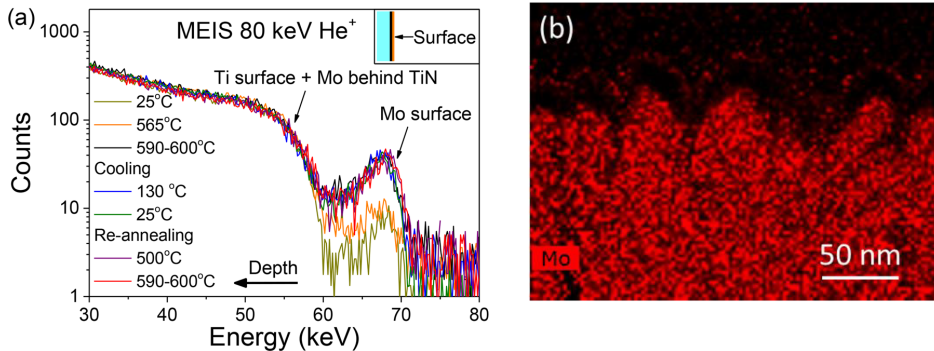


Figure 5. a) Time-to-energy converted ToF-MEIS spectra of SLG/Mo+20 nm TiN measured at different temperatures in situ in UHV chamber. b) Mo map from TEM EDS of annealed Mo+20 nm TiN BC.

around 68 keV) is seen to increase as the temperature increases. But after reducing the temperature again, the Mo signal does not change as expected if the Mo-signal was a result of reversible “opening up” of the TiN layer. The heating and cooling was repeated, but the signal did not change significantly. The shape of the MEIS spectra, with the higher concentration of Mo at the surface of the TiN layer followed by the decreased signal around 68–60 keV, clearly suggest that there is an accumulation of Mo at the surface rather than an increased exposure of bulk Mo. To get a complementing picture, TEM-EDS was performed on the same sample to track the origin of Mo detected at the surface of the TiN layer, displayed in Figure 5b. The image shows the very same as the MEIS spectra, an accumulation of Mo onto the upper TiN surface. Diffusion of Mo, has now been seen both under typical anneal conditions (with absorber layer as shown in Figure 4, and without absorber layer as shown in Englund et al.^[27]) and in vacuum, as shown in Figure 5. The mechanisms for the diffusion of Mo is not investigated in depth, but is likely to exist as some kind of compound, e.g., it is noticed that the Na 1s peak energy at 1071.8 eV in Englund et al.^[27] (which is assumed to be present also in this case) could contain signal from Na₂MoO₄.^[39]

For discussion of electrical properties, the focus is on the S-annealed samples, mainly due to the already observed poor absorber quality of the Se-annealed and the expected high number of shunts. JV and EQE were measured and the curves of the best S-annealed cells are shown in Figure 6 and the corresponding solar cell parameters in Table 2. Table 3 shows the electrical parameters extracted by fitting the one-diode model to both dark and light JV measurement are presented using the procedure described by Hegedus and Shafarman.^[40] Dark curves give a more reliable fit, but since the solar cell parameters in Table 2 are extracted from the light measurements, the numbers from the light curves are more of interest for discussion. The solar cell parameters for both S- and Se-annealed devices are summarized in boxplots in Figure 7. It was observed that the S-annealed reference performs poorly compared to typical in-house references, and the reason for this is not known (the very same happened when the experiment was repeated). Important findings can be discussed despite this. For the S-annealed solar cells, the trend is improved solar cell efficiency when the thickness of the TiN increases. The open circuit voltage (V_{oc}) is approximately constant for the best cells, but reduced for the

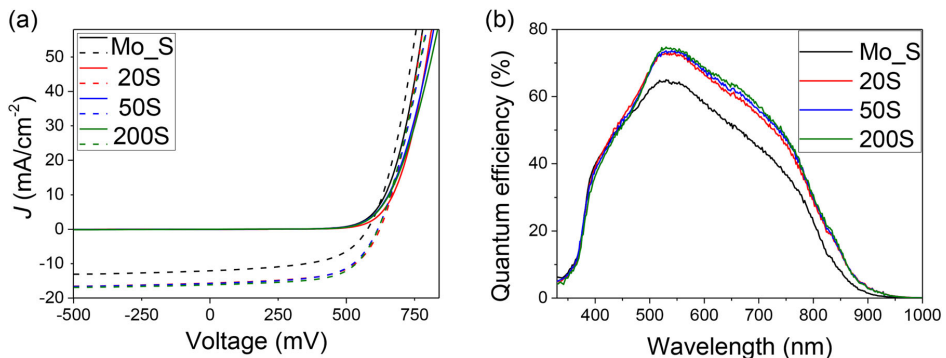


Figure 6. a) JV curves, solid lines show dark JV, dashed lines show light JV. b) EQE spectra.

Table 3. Electrical properties of the best cells of the S-annealed samples.

	Ideality factor		J_0 [mA cm^{-2}]		R_s [Ωcm^2]		R_{shunt} [$\text{k}\Omega \text{cm}^2$]	
	Dark	Light	Dark	Light	Dark	Light	Dark	Light
Mo_S	2.0	2.6	4.0E-5	1.7E-3	0.8	0.8	11.1	0.3
20S	1.9	2.5	1.2E-5	0.9E-3	1.3	0.9	7.5	0.4
50S	1.9	2.7	2.1E-5	1.9E-3	1.9	1.2	6.2	0.4
200S	1.7	2.5	7.1E-6	0.9E-3	2.4	1.3	4.0	0.8

200S on average. The short circuit current (J_{sc}) and fill factor (FF) are increased, resulting in the higher efficiency (η). The increased current is reflected also in the EQE, with an overall increased collection over most of the spectrum with increased TiN thickness. The J_{sc} differs slightly between light JV- and the low intensity QE measurement, this is sometimes observed for our CZTS devices and could be due to light induced metastabilities. The series resistance (R_s) increase only slightly, which is not enough to affect the FF as the trend is opposite. The increase of FF can at least partly be attributed to the increased shunt resistance (R_{shunt}) with TiN thickness under light conditions. The FF for the best cell here (62.21% for 200S) is comparable or even high also when comparing to a good typical Mo reference (e.g., as 60.0% in Scragg et al.^[41]). In some of the earlier studies on reactively sputtered thin TiN interlayers, one crucial drawback assigned to TiN interlayers in CZTS is increased series resistance resulting in dramatic decrease of fill factor.^[41] It was suggested that TiN possibly forms a barrier for majority carriers similar to what has been suggested for ZrN for CIGS.^[42] In this study it can first of all be seen that “point contacts” of MoS₂ exist in thin TiN interlayers, so one might not expect significantly increased contact resistance in that case.

Table 2. Solar cell parameters and electrical properties of the best cells of the S-annealed samples.

Sample	V_{OC} [mV]	J_{sc} [mA cm^{-2}]	FF [%]	η [%]
Mo_S	577	12.1 (13.9) ^{a)}	54.3	3.8
20S	622	15.7 (16.2)	60.4	5.9
50S	616	15.8 (16.4)	60.3	5.9
200S	615	16.2 (16.5)	62.2	6.2

^{a)} J_{sc} from QE.

More interesting is the absence of dramatic increase of series resistance and FF loss for the 200S sample, since in that case no or negligible existence of MoS(e)₂ is expected. In other words, there is no visible problem of contact resistance between TiN and CZTS. The trend of the best cells is visible also for all cells on the samples seen in Figure 7a. All solar cell parameters except the V_{OC} increases with increased TiN thickness.

Examination of the Se-annealed cells was limited due to the poor absorber quality. The JV (not shown here) shows shunted and highly resistive cells, although there is still a rectifying behavior. Also in this case, the Mo reference (Mo₂Se₃) performs worse than the cells with TiN, but in contrast to the S-annealed samples, the trend is negative with increased TiN thickness. This can likely be related to the morphology and increased Na diffusion as discussed above. In this case it is hard to compare with typical cells, since no air anneal was employed.

As it was found that the solar cell performance improved with increased TiN thickness for sulfide CZTS, additional experiments were performed on bulk TiN back contacts. In earlier attempts, the use of 1 μm bulk TiN back contacts failed.^[41] The reasons were not investigated in depth, but poor adhesion and limited grain growth led to the assumption that TiN blocked Na.

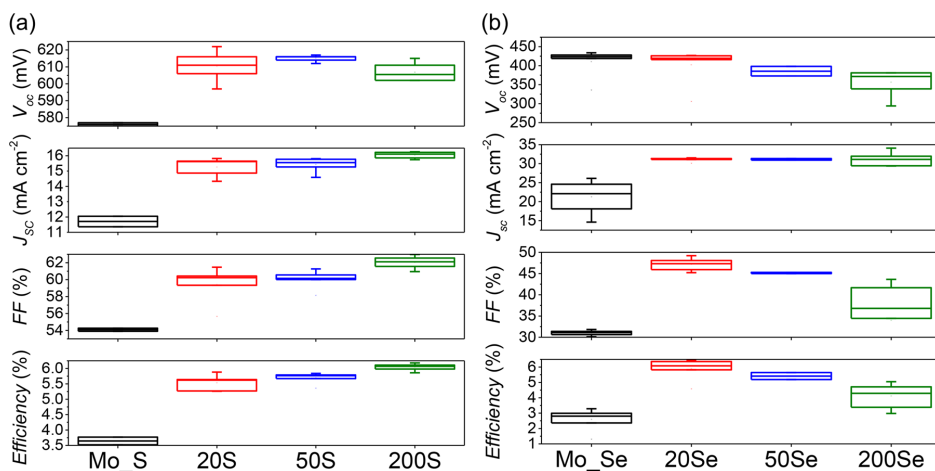


Figure 7. Box plots showing the solar cell parameters open circuit voltage (V_{oc}), short circuit current (J_{sc}), fill factor (FF) and efficiency (η) for (a) S-annealed samples and (b) Se-annealed samples.

Table 4. Bulk TiN back contacts and their related properties.

Sample ID	N ₂ /Ar [sccm]	thickness [nm]	R _{sheet} [Ω/sq ⁻¹]	P [μΩ cm]	stress [MPa]
2Mo_S	Mo	350	0.6	21	+550 (Tensile)
45/20S	45/20	350	2.9	104	-1450 (Compr.)
13/40S	13/40	350	7.5	263	+60/-100
8/40S	8/40	350	8.3	289	+160 (Tensile)
1 μ45/20	45/20	1000	-	-	-
1 μ8/40	8/40	1000	-	-	-

This time, the thickness of the TiN layers was kept the same as for the baseline Mo in the reference sample to possibly ease the Na diffusion.

A series of TiN layers were deposited directly on SLG to evaluate their properties. In accordance with the literature, the resistivity (and sheet resistance for the chosen thickness) decreased with increasing N₂/Ar flow ratio.^[43,44] However, it was also found that increased N₂/Ar ratio shifted residual stress to more compressive and in the end, the same sputter settings used in the interlayer study (flow ratio N₂/Ar = 45/20 sccm) were used for “low resistive” TiN. For N₂/Ar = 8/40 sccm, used for “high resistive” TiN, the film exhibited tensile stress. One film was also deposited chosen with residual stress in between the other two (N₂/Ar = 13/40 sccm). Lower values of resistivity were found in the literature,^[45] close to those for Mo used in this study, but this could not be reached in this study. Properties of the TiN layers are summarized in **Table 4**.

The Na diffusion was assessed using the same method as described in Englund et al.^[27], namely comparing the intensity of the XPS peaks of Na 1s of S-annealed back contacts. The method is only an indication, and the amount of Na in the absorber layer might differ. However, the correlation between the tendency of increased Na 1s XPS intensity in Englund et al.^[27] and the increased Na content the absorber measured by SIMS in the present study indicate some accuracy of the method. To improve statistics, around 18 spots where chosen for each sample, uniformly distributed over the sample area. The averaged XPS peaks are shown in **Figure 8**. The Na 1s peaks of 2Mo_S, 45/20S, and 8/40S all had a rather narrow spread, while 13/40S was rather scattered (maybe reflecting also the residual stress that was opposite in different directions, see Table 3). Significantly less Na had diffused through the TiN back contacts compared to the Mo reference (2Mo_S). This clearly differs from the situation when TiN is deposited on top of Mo, as discussed previously.

To further investigate thickness-dependence of the Na diffusion and the validity of the suggestion in Scragg et al.^[41] that the bad performance of bulk TiN back contacts was a result of blocking of Na, additional 1 μm films deposited with 8/40 sccm (named 1 μ8/40) and 45/20 sccm (named 1 μ45/20) N₂/Ar flow ratio were also investigated. 1 μ8/40 did indeed further reduce the Na diffusion, but increased TiN thickness seems not necessarily further reduce the Na diffusion, as the 1 μ45/20 sample actually had a stronger Na peak than the 350 nm samples. After the anneal however, the 1 μ45/20 sample bent the whole SLG substrate due to strong compressive residual stress. Only the TiN films with thickness of 350 nm were deposited with CZTS. Deposition of CZTS and annealing was done in identical

way as described in the Experimental section, but this time, the composition was measured to Cu/Sn = 1.88 and Zn/(Cu + Sn) = 0.40, i.e., Cu poor (Sn rich) and Zn rich. The morphology was examined by analysis of the cross-sections in SEM, which are shown in **Figure 9**. Despite the significantly reduced Na diffusion, the grain growth for these films all seem to be good and comparable to that of the Mo reference. The white areas, distributed more or less uniformly in the films are Zn rich secondary phases is expected due to the Zn rich composition. This was confirmed by TEM-EDS analysis.

The TEM-EDS was performed on FIB polished lamellae of annealed CZTS with the various TiN back contacts. Images are shown in **Figure 10**. Once again the TiN proves its chemical robustness in the tough chemical environment during the annealing and decomposition except some minor oxidation related to voids could be observed in the Ti map in Figure 10b. The maps are showing nearly identical trends when comparing the different samples. The Zn rich composition results in the random distribution of Zn rich secondary phases as also seen in the SEM images in Figure 9. In Figure 10a but especially (c) a small enrichment of Sn at the front and the back interface can be seen. The composition is Sn rich so it is expected, but in contrast to the Zn, this enrichment occurs preferentially at the interfaces. The Sn enrichment was not uniform, however, and when repeated with an even more Sn rich composition (Cu/Sn = 1.79, Zn/(Cu + Sn) = 0.39) the phenomena could not be observed again.

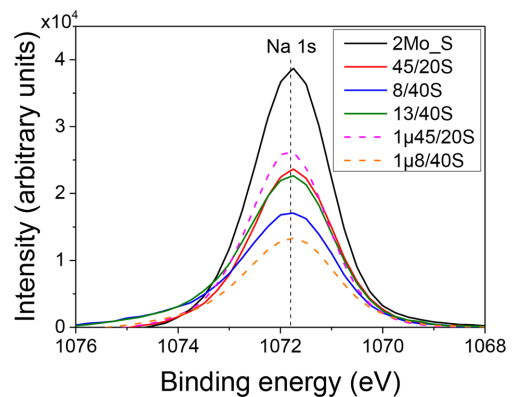


Figure 8. XPS signal from the Na 1S peak of annealed back contacts.

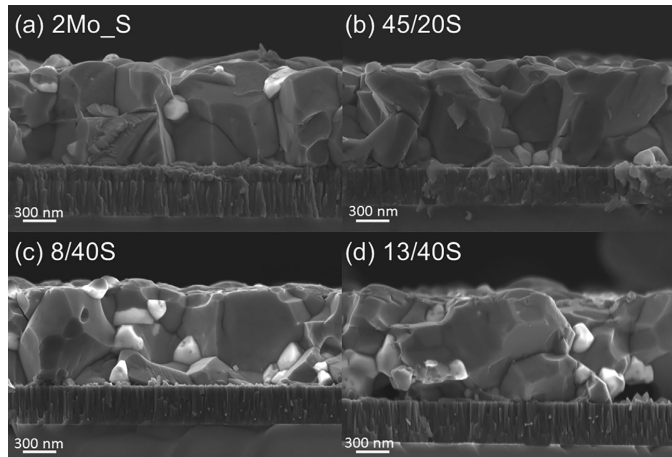


Figure 9. SEM images of cross-section of annealed samples. a) 2Mo_S; b) 45/20S; c) 8/40S; d) 13/40S.

Finally, JV was measured and the solar cell parameters extracted, see **Figure 11a**. None of the TiN bulk contacts performed better than the Mo reference (2Mo_S) in any aspect and clearly did not follow the trend seen in the interlayer study with improved solar cell performance with increased TiN thickness. One important reason is likely the reduced Na diffusion as discussed above, but this cannot alone explain the differences between the different TiN back contacts. The conclusion is that neither the amount of Na nor the resistivity (or sheet resistance) of the TiN are the most critical parameters as the 45/20S cells barely worked at all with several cells not showing rectifying diode behavior (the reason for the large spread for this sample in **Figure 11a**). However, the higher sheet resistance is likely contributing to the increased series resistance

when comparing to Mo. The superior performance of thick TiN interlayers on Mo might be due to the good lateral conductivity of the Mo beneath, which is lost to some extent in this case. One more possible reason can be the strong compressive stress (-1450 MPa) while the CZTS is optimized for the Mo with tensile stress ($+550$ MPa). The TiN samples have in common that the cells exhibit a high series resistance as well as shunt conductance (as seen in the IV curves), both contributing to the low FF. In **Figure 11b**, the JV curves of the best Mo reference and the best TiN bulk back contact sample (13/30S) are shown, having the typical characteristics of the TiN cells described above. The corresponding EQE spectra are shown in **Figure 11c**, showing a reduced collection over the whole spectrum for the sample with TiN back contact. Despite the drawbacks discussed,

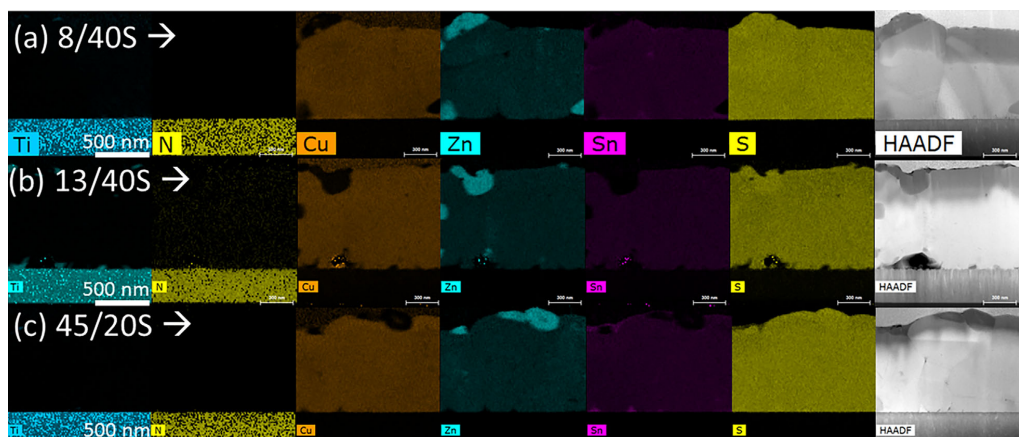


Figure 10. TEM-EDS maps for the samples with 350 nm TiN bulk back contacts deposited with varied flow ratios of N_2/Ar sccm and CZTS absorber. a) 8/40S; b) 13/40S; and c) 45/20S.

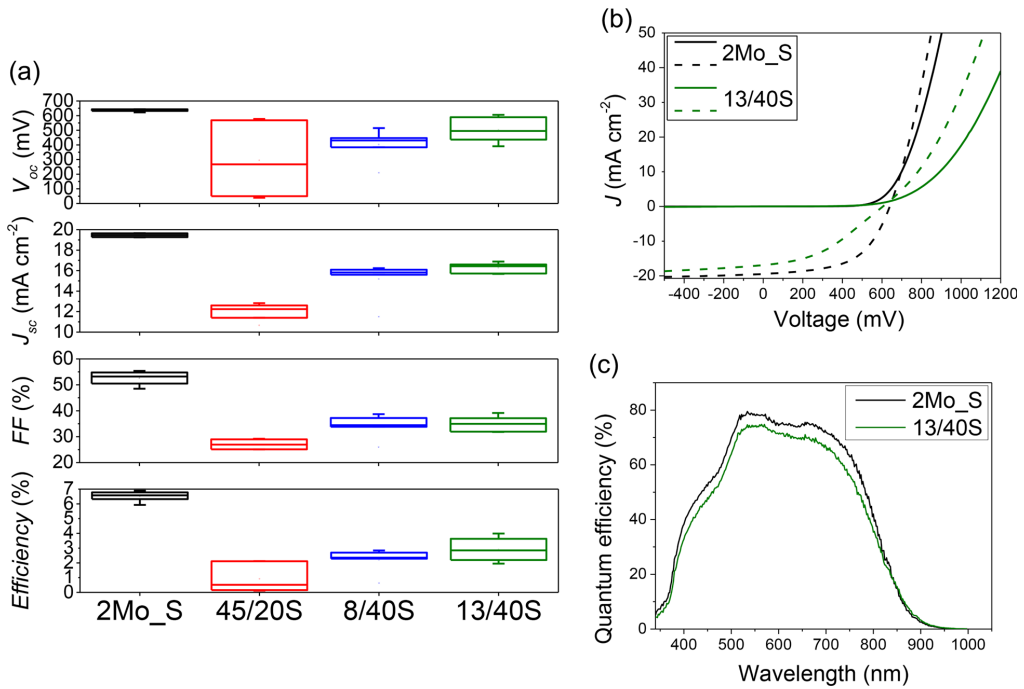


Figure 11. a) Summary of solar cell parameters extracted from JV. b) JV-curves of the Mo reference and the best cell with TiN bulk back contact 13/40S. Solid lines show dark JV, dashed line show light JV. c) EQE spectra.

the results show that bulk TiN back contacts is a promising highly inert alternative to Mo.

Several methods were tried to increase the Na content in the absorbers, namely addition of NaF at the back contact before CZTS deposition and pre-annealing of the TiN back contacts. In both cases adhesion was very poor and the cells bad. The same was the case when introducing of a sacrificial Mo layer of a few nanometers on top of the TiN. In the end, the best result was achieved with clean, untreated TiN back contacts. There is room for improvement, such as by optimizing stress in the bulk TiN back contacts (or re-optimizing CZTS deposition). Sheet resistance could be decreased by using thicker layers, and that would require careful optimization of residual stress and also assurance of sufficient supply of Na, possibly by using alternative strategies to supply of Na.

4. Conclusions

TiN interlayers, and the effects of varied thicknesses of TiN interlayers between the SLG/Mo were investigated for CZTS(e) thin film solar cells. The TiN interlayers are, except for some limited oxidation, related to the presence of voids, highly inert and does not degrade during the high temperature anneal. It was shown that openings exist in thin TiN interlayers, resulting from the surface roughness of Mo. Chalcogens from the precursor and Mo from the Mo substrate diffuses through the openings

and along grain boundaries in the TiN interlayers, resulting in formation of point contacts of $\text{MoS}(e)_2$ in case of thin TiN interlayers. Thick TiN interlayers facilitates Na diffusion into the absorbers. Also solar cell performance improves with increased TiN thickness in case of S-annealing, which questions the notion that $\text{MoS}(e)_2$ is necessary for good electrical contact between the absorber the BC. These findings open pathways to widen the anneal processing window for both higher or lower chalcogen pressures, facilitating the drive for highly efficient CZTS(e) thin film solar cells. The improved solar cell performance of sulfurized cells did not extend to bulk TiN back contacts, but still solar cells with cells having up to 4% efficiency were shown.

Acknowledgements

The authors want to thank Nils Ross for the deposition of CZTS precursor films, Lars Riekehr for the TEM-EDS analysis of the TiN bulk back contacts, and Yi Ren and Jes K. Larsen for valuable discussion. The Swedish Foundation for Strategic Research (FLL12-0178) is acknowledged for the financial support of this work.

Conflict of Interest

The authors declare no conflict of interest.

Keywords

back contacts, CZTS, interlayers, thin film solar cells, titanium nitride

Received: June 29, 2018

Revised: August 20, 2018

Published online: September 14, 2018

- [1] International Energy Agency (IEA), *Technology Roadmap Solar Photovoltaic Energy*. OECD/IEA, Paris **2014**.
- [2] International Energy Agency Photovoltaic Power Systems Programme (IEA PVPS), *2018 Snapshot of Global Photovoltaic Markets*. IEA PVPS, Paris **2018**.
- [3] W. Wang, M. T. Winkler, O. Gunawan, T. Gokmen, T. K. Todorov, Y. Zhu, D. B. Mitzi, *Adv. Energy Mater.* **2014**, *4*, 7.
- [4] X. Liu, Y. Feng, H. Cui, F. Liu, X. Hao, G. Conibeer, D. B. Mitzi, M. Green, *Prog. Photovolt. Res. Appl.* **2016**, *24*, 6.
- [5] A. Polman, M. Knight, E. C. Garnett, B. Ehrler, W. C. Sinke, *Science* **2016**, *352*, 6283.
- [6] T. J. Huang, X. Yin, G. Qi, H. Gong, *Phys. Status Solidi RRL* **2014**, *8*, 9.
- [7] S. Englund, N. Saini, C. Platzer-Björkman, *Solar Energy*, **2018**, <https://doi.org/10.1016/j.solener.2018.04.024>.
- [8] S. López-Marino, M. Placidi, A. Pérez-Tomás, J. Llobet, V. Izquierdo-Roca, X. Fontané, A. Fairbrother, M. Espíndola-Rodríguez, D. Sylla, A. Pérez-Rodríguez, E. Saucedo, *J. Mater. Chem. A* **2013**, *1*, 29.
- [9] H. Cui, X. Liu, F. Liu, X. Hao, N. Song, C. Yan, *Appl. Phys. Lett.* **2014**, *104*, 4.
- [10] H. Cui, C.-Y. Lee, W. Li, X. Liu, X. Wen, X. Hao, *Int. J. Photoenergy* **2015**, *2015*, 170507.
- [11] W. Li, X. Liu, H. Cui, S. Huang, X. Hao, *J. Alloys Compd.* **2015**, *625*, 277.
- [12] F. Liu, K. Sun, W. Li, C. Yan, H. Cui, L. Jiang, X. Hao, M. A. Green, *Appl. Phys. Lett.* **2014**, *104*, 5.
- [13] G. Altamura, L. Grenet, C. Roger, F. Roux, V. Reita, R. Fillon, H. Fournier, S. Perraud, H. Mariette, *J. Renew. Sust. Energy* **2014**, *6*, 1.
- [14] S. Oueslati, G. Brammertz, M. Buffière, H. ElAnzeery, D. Mangin, O. ElDaif, O. Touayar, C. Köble, M. Meuris, J. Poortmans, *J. Phys. D: Appl. Phys.* **2015**, *48*, 3.
- [15] F. Zhou, F. Zeng, X. Liu, F. Liu, N. Song, C. Yan, A. Pu, J. Park, K. Sun, X. Hao, *ACS Appl. Mater. Interfaces* **2015**, *7*, 41.
- [16] Z. Tong, K. Z., K. Sun, C. Yan, F. Liu, L. Jiang, Y. Lai, X. Hao, J. Li, *Sol. Energy Mater. Sol. Cells* **2016**, *144*, 537.
- [17] J. Kim, S. Park, S. Ryu, J. Oh, B. Shin, *Prog. Photovolt. Res. Appl.* **2017**, *25*, 4.
- [18] B. Vermang, Y. Ren, O. Donzel-Gargand, C. Frisk, J. Joel, P. Salome, J. Borome, S. Sadewasser, C. Platzer-Bjorkman, M. Edoff, *IEEE J. Photovolt.* **2016**, *6*, 1.
- [19] S. Lopez-Marino, M. Espíndola-Rodríguez, Y. Sánchez, X. Alcobé, F. Oliva, H. Xie, M. Neuschitzer, S. Giraldo, M. Placidi, R. Caballero, V. Izquierdo-Roca, A. Pérez-Rodríguez, E. Saucedo, *Nano Energy* **2016**, *26*, 708.
- [20] S. Ranjbar, G. Brammertz, B. Vermang, A. Hadipour, S. Cong, K. Suganuma, T. Schnabel, M. Meuris, A. F. da Cunha, J. Poortmans, *Phys. Status Solidi A* **2017**, *214*, 1.
- [21] T. Schnabel, Erik Ahlswede, *Sol. Energy Mater. Sol. Cells* **2017**, *159*, 290.
- [22] H.-J. Chen, S.-W. Fu, S.-H. Wu, T.-C. Tsai, H.-T. Wu, C.-F. Shih, P. Gouma, *J. Am. Ceram. Soc.* **2016**, *99*, 5.
- [23] M. Colina, I. Martin, S. Giraldo, Y. Sanchez-Gonzalez, R. Kondrotas, F. Oliva, V. Izquierdo-Roca, A. Perez-Rodriguez, A. Coll, R. Alcobilla, E. Saucedo, *IEEE J. Photovolt.* **2016**, *6*, 5.
- [24] J.-Y. Kang, G. Y. Baek, S. Gedi, Y. J. Song, C.-W. Jeon, *J. Alloys Compd.* **2018**, *748*, 188.
- [25] Z. Wei, C. M. Fung, A. Pockett, T. O. Dunlop, J. D. McGettrick, P. J. Heard, O. J. Guy, M. J. Carnie, J. H. Sullivan, T. M. Watson, *ACS Appl. Energy Mater.* **2018**, *1*, 6.
- [26] H. Ehira, K. Jimbo, H. Katagiri, *AIP Conf. Proc.* **2017**, *1865*, 050004.
- [27] S. Englund, V. Paneta, D. Primetzhofer, Y. Ren, O. Donzel-Gargand, J. K. Larsen, J. Scragg, C. Platzer Björkman, *Thin Solid Films* **2017**, *639*, 91.
- [28] J. A. Thornton, D. W. Hoffman, *Thin Solid Films* **1989**, *171*, 5.
- [29] T. Ericson, *Licentiate Thesis*, Uppsala University, June **2013**.
- [30] R. M. Langford, M. Rogers, *Micron* **2008**, *38*, 8.
- [31] M. K. Linnarsson, A. Hallen, J. Astrom, D. Primetzhofer, S. Legendre, G. Possnert, *Rev. Sci. Instrum.* **2012**, *83*, 9.
- [32] J. Park, J. Huang, K. Sun, Z. Ouyang, F. Liu, C. Yan, H. Sun, A. Pu, M. Green, X. Hao, *Thin Solid Films* **2018**, *648*, 39.
- [33] F. Liu, J. Huang, K. Sun, C. Yan, Y. Shen, J. Park, A. Pu, F. Zhou, X. Liu, J. A. Stride, M. A. Green, X. Hao, *NPG Asia Mater.* **2017**, *9*, 7.
- [34] K.-J. Yang, J. Hy. Sim, B. Jeon, D.-H. Son, D.-H. Kim, S.-J. Sung, D.-K. Hwang, S. Song, D. B. Khadka, J. Kim, J.-K. Kang, *Progr. Photovolt. Res. Appl.* **2015**, *23*, 7.
- [35] J. V. Li, D. Kuciauskas, M. R. Young, I. L. Repins, *Appl. Phys. Lett.* **2013**, *102*, 16.
- [36] B. Shin, N. A. Bojarczuk, S. Guha, *Appl. Phys. Lett.* **2013**, *102*, 9.
- [37] J. J. Scragg, J. T. Watjen, M. Edoff, T. Ericson, T. Kubart, C. Platzer-Bjorkman, *J. Am. Chem. Soc.* **2012**, *134*, 47.
- [38] V. Paneta, S. Englund, S. Suvanam, J. Scragg, C. Platzer-Björkman, D. Primetzhofer, *Nucl. Instrum. Methods B* **2018**, <https://doi.org/10.1016/j.nimb.2018.06.020>.
- [39] J. F. Moulder, F. S. Stickle, E. S. Sobol, K. D. Bomben, J. Chastain, R. C. King, *Handbook of X-ray Photoelectron Spectroscopy: A Reference Book of Standard Spectra for Identification and Interpretation of XPS Data*. Physical Electronics Division, Perkin-Elmer Corporation, Eden Prairie, Minnesota, USA **1992**.
- [40] S. S. Hegedus, W. N. Shafarman, *Prog. Photovolt. Res. Appl.* **2004**, *12*, 2.
- [41] J. J. Scragg, T. Kubart, J. T. Wätjen, T. Ericson, M. K. Linnarsson, C. Platzer-Björkman, *Chem. Mater.* **2013**, *25*, 15.
- [42] J. Malmström, S. Schleussner, L. Stolt, *Appl. Phys. Lett.* **2004**, *85*, 13.
- [43] F. Vaz, J. Ferreira, E. Ribeiro, L. Rebouta, S. Lanceros-Méndez, J. A. Mendes, E. Alves, P. Goudeau, J. P. Rivière, F. Ribeiro, I. Moutinho, K. Pischow, J. de Rijk, *Surf. Coat. Technol.* **2005**, *191*, 2.
- [44] N. K. Poonon, D. J. R. Appleby, E. Arac, P. J. King, S. Ganti, K. S. K. Kwa, A. O'Neill, *Thin Solid Films* **2015**, *578*, 31.
- [45] M. Kawamura, Y. Abe, H. Yanagisawa, K. Sasaki, *Thin Solid Films* **1996**, *287*, 1.